Impact and Crashworthiness Lab

2018 Annual Report

Vol. II: Battery Modeling

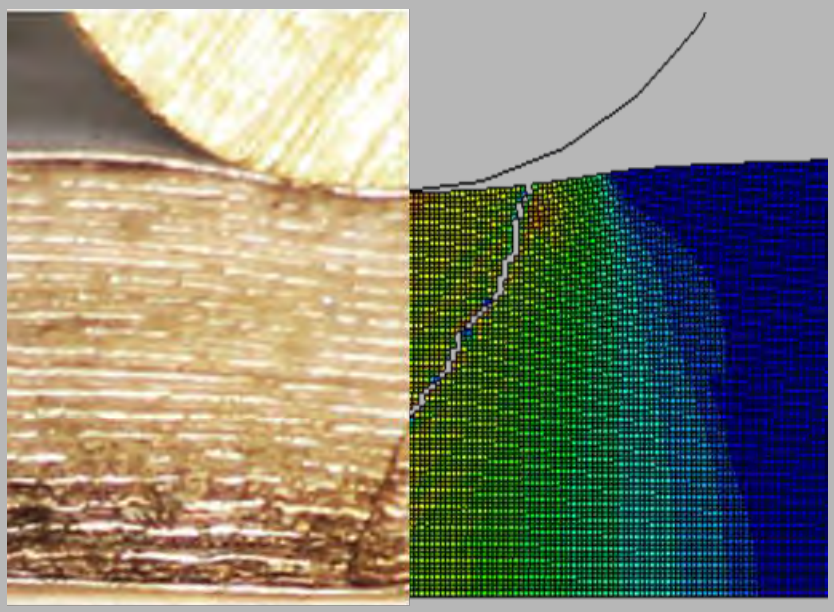

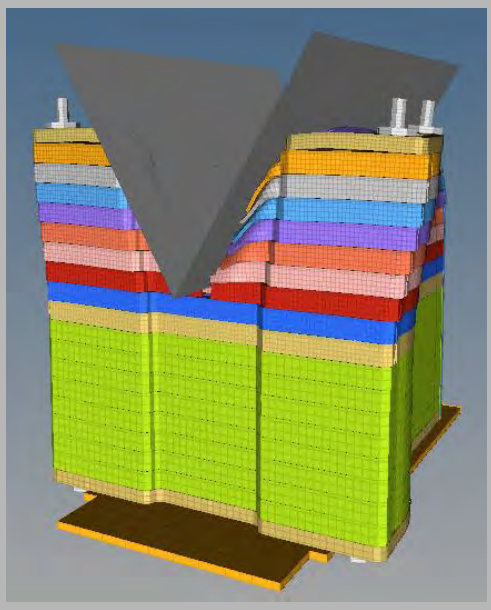

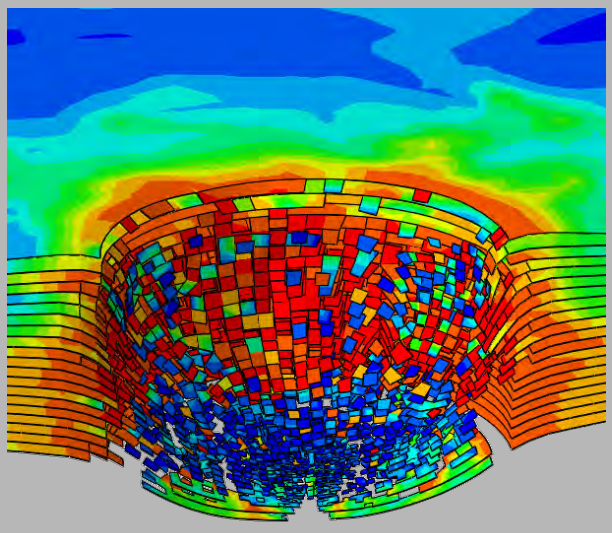

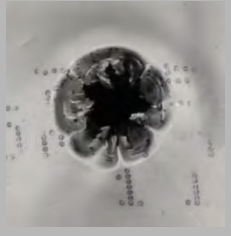

Compiled by: Juner Zhu, Elham Sahraei and Tom Wierzbicki

9th MIT workshop on

Computational Modeling of Lithium Ion batteries for crash safety

Impact and Crashworthiness Lab, MIT

Electric Vehicle Safety Lab, Temple University

Program director: Professor Tomasz Wierzbicki (wierz@mit.edu)
Program co-director: Professor Elham Sahraei (elham.sahraei@temple.edu)

November 9-10, 2018

TABLE OF CONTENTS

PROFESSOR TOMASZ (TOM) WIERZBICKI

DIRECTOR OF IMPACT AND CRASHWORTHINESS LAB

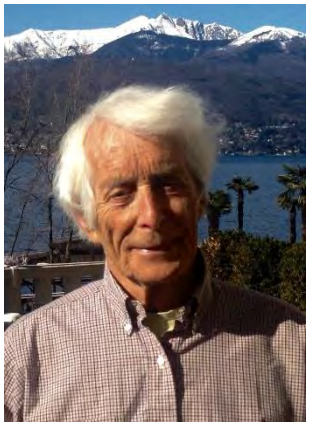

Professor Tomasz Wierzbicki received his MS degree from the Department of Mechanical Engineering of the Warsaw University of Technology. He earned his PhD degree from the Institute of Fundamental Technological Research. Soon after that, he left for a postdoctoral study at Stanford University. His innovative research in crashworthiness earned him invitation from Volvo where he worked over the years on various projects. In 1981, he was promoted to a Full Professor at the Polish Academy of Sciences and in the same year he left for the United States, which has become his home. In 1983, he was appointed as a full professor at MIT, where he is currently directing the Impact and Crashworthiness Lab. He is the author of over 200 papers published in major international journals. In 1986, he received the Alexander von Humboldt senior, US scientist award which started his long-lasting collaboration with the BMW R&D Department in Munich. It was here where he was exposed to the problem of fracture which became his main focus for the past two decades. His professional accomplishment can be followed by looking at the list of large industry-oriented programs that he established at MIT. Those programs were supported by over 50 major automotive, steel, aluminum and shipbuilding companies. Professor Wierzbicki's research and consulting interests are in the area of dynamic plasticity, structural failure, crashworthiness, ultralight material, and ductile fracture. More recently he established a unique program on modeling of lithium-ion batteries. He served for many years as an Associate Editor of the *International Journal of Impact Engineering*.

PROFESSOR ELHAM SAHRAEI

DIRECTOR OF ELECTRIC VEHICLE SAFETY LAB

Professor Elham Sahraei holds dual appointments in the Department of Mechanical Engineering at Temple University and in the Department of Mechanical Engineering at MIT. She is the co-director of the MIT Battery Consortium and director of Electric Vehicle Safety Lab (EVSL). She is the PI for an ONR Battery project and Technical Monitor of the USAID SHERA project. She earned her PhD degree from the George Washington University in 2011, and completed two years of post-doctoral training at Massachusetts Institute of Technology in 2013. Besides her research in Lithium-ion battery, her expertise includes full-scale vehicle crash analysis, occupant protection, and analysis of roadside safety structures. She is the recipient of SAE Myers award, Stapp student award, and WTS scholarship. She has served as a chair person and plenary speaker for multiple conferences including Battery Safety, Battery Congress, and ASME IMECHE.

ICL & EVSL TEAMS WORKING ON BATTERY PROJECTS

Professor Junhe Lian is currently a tenure-track assistant professor on Advanced Steels and Applications in the Department of Mechanical Engineering at Aalto University and he also has a joint appointment at the Steel Institute, RWTH Aachen University as the head of the Damage Tolerance Group. He has been a visiting scientist for multiple stays at the Impact and Crashworthiness Lab (ICL) in the Department of Mechanical Engineering at MIT focusing on the safety assessment of Lithium-ion batteries. His main research field lies in the ICME development and application on microstructure design and mechanical property optimization for engineering materials, including micro and macro plasticity and damage, microstructure synthetic model development for metals, multiscale modelling, and data-driven approach for ICME. He received the ESIS-Elsevier Young Scientist Award in 2018 and the Werner Koester Prize from DGM awarding the best paper on the International Journal of Materials Research (IJMR) in 2013.

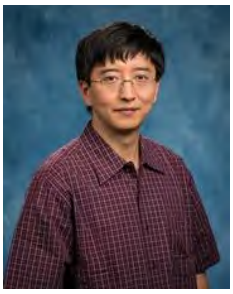

Professor Feng Zhu is an assistant professor in Mechanical Engineering Department, Embry-Riddle Aeronautical University (ERAU), in Daytona Beach, Florida. Prior to joining ERAU, he worked as a research faculty member at Automotive Safety Group and Bioengineering Center in Wayne State University. His research area is applied impact mechanics, injury biomechanics and safety product design. He has published 1 monograph and over 70 peer-reviewed journal papers. He is serving as an academic reviewer for 40 international journals and the U.S. Army. He is a member of the SAE Occupant Protection Advisory Committee and has served as organizers and chairs in a number of national and international conferences. Besides the primary appointment in ERAU, he is a visiting scholar in ICL working on the area of vehicle battery module crash safety.

Professor Yuanli Bai works at the Department of Mechanical and Aerospace Engineering (MAE) at the University of Central Florida (UCF). He obtained PhD degree in Mechanical Engineering from Massachusetts Institute of Technology (MIT) in 2008 under the supervision of Professor Tomasz Wierzbicki. Prior to joining UCF in January 2011, he was a mechanical engineer at the General Electric Global Research Center (GE-GRC) in Niskayuna, NY. Dr. Bai's current research is focused on plasticity, ductile fracture and reliability testing/analysis/simulation for various engineering materials and structures. He operates the Lab of Solid and Structure Mechanics at the MAE department. Dr. Bai has published over 60 papers in his fields most highly rated journals and conference proceedings.

Professor Yong Xia is an Associate Professor at the Automobile Crash Lab (ACL) of Tsinghua University in China. Dr. Xia studied Polymer physics for a B. S. degree and Solid Mechanics for a Ph. D. degree in University of Science and Technology of China. He continued his research work at the Department of Automotive Engineering in Tsinghua University since 2004, and was promoted to be an Associate Professor there in 2010. He was a Visiting Scholar at the impact and Crashworthiness Lab (ICL) of MIT. The research activities of Dr. Xia mainly focus on: (1) Characterizing large deformation and failure of lightweight materials, (2) Studying failure behaviors of adhesive-bonded joints and developing FE model of the joints for vehicle crash CAE, and (3) Analyzing pedestrian-vehicle impacts and designing pedestrian protection countermeasures. He also took charge of establishing the platform for testing dynamic properties of materials in ACL.

Dr. Maysam Gorji Bandpay received his Ph.D. from ETH in 2016, under the supervision of Prof. Pavel Hora and Prof. Frédéric Barlat. His research interests focused on theoretical and experimental aspects of forming technologies in real and virtual environments subject to information and complexity constraints. In September 2016, Dr. Maysam Gorji Bandpay is currently a Research Scientist in Prof. Wierzbicki's group. He also holds a dual appointment as a researcher at ETH's Chair of Computational Modeling of Materials in Manufacturing, supervised by Prof. Dirk Mohr. Dr. Gorji is responsible for conducting research in the area of Additive Manufacturing, Machine Learning, and Micro & Meso material forming. He is also applying the latest model of the material models developed at ICL to predict deformation and failure for many industrial processes such as cold and hot forming of a steel and aluminum sheets and strength and energy absorption of lightweight periodic cellular structures.

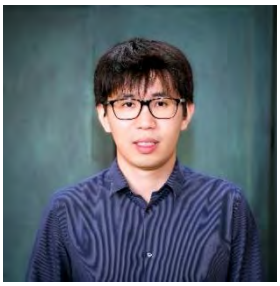

Juner Zhu is a fourth year PhD student at ICL. He received his Bachelor and Master's degrees from the Department of Automotive Engineering of Tsinghua University. His research at Tsinghua was on testing and modeling of the mechanical behaviors of High Strength Steel sheets, including plastic anisotropy and strain rate sensitivity. After he came to MIT in August 2015 for his PhD studies, Juner extended his research interest into crash safety of lithium-ion batteries in Electric Vehicles. So far, he has published nine journal articles in this area. He has finished two summer internships, one at Ford as a materials engineer in 2016 and the other at Apple as a battery engineer in 2018.

Thomas Tancogne-Dejean is a fourth year PhD student. He graduated from Ecole Polytechnique, where he completed studies focusing on mechanics, and from Ecole Nationale des Ponts et Chaussées for studies in homogenization of periodic and random media. His research focuses on two aspects of Additive Manufacturing technique. Firstly it aims at developing both plasticity and fracture models of an additive manufactured materials such as titanium alloy. Secondly, Thomas' work aims at design low relative density truss and plate lattices with isotropic elastic properties and low plastic anisotropy, while maintaining high specific stiffness and strength. He spent the summer 2016 as an intern in the additive manufacturing lab at GE Global Research in Niskayuna, NY.

Wei Li is a fourth year PhD student in Department of Automotive Engineering of Tsinghua University in China. He came to ICL as a visiting student in November 2017 and will stay for one year. He received his Bachelor Degree from Department of Automotive Engineering of Hunan University. His research in Tsinghua has been on testing and FE modeling of pouch and prismatic cells. He was also involved together with Dr. Marcelo Paredes in high strain rate plasticity and fracture tests on X65 offshore pipe steel. He is currently working on modeling the shear fracture of the multi-layer pouch cells using discrete particle method in Abaqus.

LT Nathaniel Byrd is a second year graduate student in the US Navy's 2N program at MIT. He graduated from North Carolina State University in 2007 with a B.S. in Mechanical Engineering. LT Byrd has over 15 years of experience in the Navy as a Surface Warfare Officer, Engineering Duty Officer, and as a Nuclear Electronics Technician. He graduated in 2018 with Master's degrees in Mechanical and Naval Engineering.

Marian Bulla joined the Electric Vehicle Safety Laboratory as a research fellow in November 2016. He obtained his Dipl.-Ing. (FH) at the university of applied science in Iserlohn (Germany). He started his career at the at LAT (chair of thermodynamics of University RWTH Aachen) and moved to the Fraunhofer ILT (Institute of LASER Technology) for 2 years. After that, he proceeded to the research institute for automotive, where he worked for 3 years as professor assistant. In the last 10 years he is working at ALTAIR Engineering in the core development team, where his topics are in new materials and failure criteria. He implemented the first failure model into RADIOSS, based on the work of Elham Sahraei. He was visiting the MIT during summer of 2018.

Dr. Golriz Kermani joined the Electric Vehicle Safety Laboratory (EVSL) as a postdoctoral fellow in September 2016. She accepted a faculty position at Temple University in September 2018, and now serves as an affiliate faculty with EVSL. Her research focuses on investigating the behavior of Li-Ion batteries under dynamic loading scenarios and developing models for in-plane loading of batteries. She has also developed a 3D micro model of the cell Representative Volume Element (RVE). She received her Ph.D. degree from Temple University in 2016. During her PhD, she characterized the rate dependency and inhomogeneity of aortic tissue and investigated their effects on the risk of traumatic aortic failure and/or injury. She was a visiting scholar at MIT during the summer of 2017

Dr. Mehdi Gilaki joined the Electric Vehicle Safety Laboratory (EVSL) as a postdoctoral research fellow in 2018. He earned his Ph.D from University of Wisconsin-Milwaukee in 2017 where he studied safety of Lithium-ion batteries used in electric vehicles under abnormal conditions. His research involved various experimental approaches as well as finite element simulations and high-performance computation to study impact on Li-ion cells and modules. Dr. Gilaki's research interests and expertise include crashworthiness analysis, Li-ion battery safety and advanced finite element simulations. The goal of his current research is to develop a framework to understand interactive effects of combined mechanical and electrical loading on safety and integrity of lithium-ion cells, modules, and packs.

Mohammad Mehdi Keshavarzi is a Graduate Research Assistant at Electric Vehicle Safety Lab (EVSL). He received his bachelor degree in Mechanical Engineering from Shiraz University and earned his Masters degree in Applied Mechanics from University of Tehran where he investigated the Fluid-Structure Interaction Phenomena in transonic flow. He has participated in numerous CFD and FEA projects with applications in Dental and Maxillofacial surgeries and has two year of work experience as a structural engineer in the R&D team of a private copper mine. He joined Electric Vehicle Safety Lab in Fall 2018.

Yihan Song is a PhD student at Temple Department of Mechanical Engineering. He joined the Electric Vehicle Safety Lab as a Graduate Research Assistant in Fall 2018. He earned his bachelor's degree in thermal energy and dynamic engineering from University of Science and Technology Beijing in 2016 and master's degree in mechanical engineering from George Washington University in 2018. He is proficient in finite element method and solid simulations. He will be working on thermal/structural modeling of lithium-ion batteries.

Gyuyoung Kim joined the Electric Vehicle Safety Lab in November 2017 as part of the Korea WEST exchange student program. He worked on modeling the volume change in battery cells due to charge and discharge cycles. Gyuyoung Kim is currently a senior studying Mechanical Engineering at Seoul National University of Science and Technology. He is interested in solid mechanics and computational analysis of structures.

Joseph Franke was a research assistant at Electric Vehicle Safety Lab (EVSL) in 2017-2018. He graduated from Mechanical Engineering Department at George Mason University and is joining TU Aachen for Masters' study. He has worked on material characterization of battery separators. His previous engineering experience comes from FIRST robotics and 2 years at INF robotics, a healthcare robotics startup. In both he was responsible for the design and coordination of manufacturing. Last year he interned at Williams Notaro, a MEP consulting firm in Fairfax, VA.

Luke T. Jameson was a research assistant at Electric Vehicle Safety Lab in 2017-2018. He is a Dean's List student studying Mechanical Engineering at George Mason University. His research is on design of a fixture for coupled electrical-mechanical testing of batteries. Born in US, he has attended schools in Singapore, Australia, and England and graduated from Langley High School in McLean, Virginia where he was an outstanding math and Latin honors student, and President of the Latin Honor Society. At George Mason, Luke is especially interested in solid mechanics and thermodynamics. His interest in vehicle safety was piqued when he was safely cushioned by a well-designed car and walked away from a serious, sometimes fatal collision.

SUMMARY OF RESEARCH ACTIVITIES IN 2018

The fast-growing market of electric vehicles demands further improvements in safety and crashworthiness of lithium-ion batteries. MIT Battery consortium has been leading the would-wide research in understanding and modeling of the mechanisms in deformation and failure of battery cells and components under various loading conditions. In January 2017, the new phase of MIT Battery Consortium was initiated for the period of three year. We are now at the end of the second year of the three years of Phase III. There are currently seven sponsors of the Consortium:

Altair
AVL
Daimler
Ford (sponsored by Ford-MIT alliance)
Jaguar-Land Rover
muRata
Peugeot-Citroen

The joint research team in 2018 including Impact and Crashworthiness Lab at MIT and Electric Vehicle Safety Lab at Temple University, consisted of eighteen people.

The annual funding of the battery modeling consortium is $360K. ICL also received $150K from Ford-MIT Alliance for battery research. In 2017-2018, EVSL has raised an additional $350K from the Office of Naval Research for investigation of electrical-mechanical coupling of failure in batteries. This project will be conducted in collaboration with MIT Electrical Engineering and Computer Science Department. In addition, the joint program between ICL and Bandung Institute of Technology started with $100K per year funding to ICL. This year, the interim meeting was held on June 19-20 in Warwick UK and was hosted by Jaguar-Land Rover. The agenda of the meeting as well as the list of participants are included in this volume. The annual meeting, for which we always prepare the present meeting material, will be held on Nov 9-10, 2018 in Boston.

Work in 2018 has proceeded in all six projects formulated in the research proposal for Phase III of Battery Consortium research. There were well-defined five projects in the proposal and Project 6 was added on the request of one of our sponsors. We believe that our joint team is current with work on all 6 projects. These projects are listed below with reference to the corresponding presentation at the annual meeting.

Project 1. Dynamic response: study of high strain rate effects (two presentations at 2017 Annual Review Meeting)

Project 2. Extension of micro model of the RVE for axial/in-plane and 3D loading (presentation by Golriz Kermani)

Project 3. Development of a general failure locus and programming in LS-DYNA (presentation by Marian Bulla and Elham Sahraei)

Project 4. Failure analysis at the cell level under axial/in-plane compression (presentation by Golriz Kermani and Elham Sahraei)

Project 5. Effect of aging on mechanical properties of cells & components (presentation by Elham Sahraei and Gyu Young Kim in interim meeting)

Project 6. Development and validation of strain-based and stress-based failure criterion (presentation by Jimmy (Junhe) Lian and Wierzbicki)

All presentations at the Consortium Review Meeting will be available to the consortium members through the password-protected website. Those type of deliverables will not be provided to potential sponsors and invited guests of this category of attendees, and we decided to include in the present meeting material full-versions of six recent publications of our joint team. The first paper is a review article which should be interested to a broad audience. Other five papers are very technical. A full list of published papers and presentations since the beginning of the battery safety program in our lab is included in next sections.

A number of perspective sponsors contacted me with a question what specialized program they would receive in case they join now the Battery Consortium. Such a list is presented below:

1. Homogenized mechanical deformation models for pouch and elliptical cells. This will include model description, calibration, and validation; Developments are available in LS Dyna, ABAQUS, and RADIOSS.

2. Homogenized mechanical failure models for pouch and elliptical cells. This will include model description, calibration, and validation; Developments are available in LS Dyna, ABAQUS, and RADIOSS.

3. Micro model of a Representative Volume Element (RVE), including properties of anode, cathode, and separator for compression and buckling simulations.

4. Detailed model of layered pouch cells with all components (separator, coatings of anode and cathode, current collectors, and pouch), currently for Abaqus.

5. Separate input parameters of constitutive models of all five component materials, with calibration and experimental validation (material cards).

6. Recommendation on mesh size for pouch batteries.

7. Machine learning data-driven mechanical failure model (ongoing).

8. Modeling of impact response of Chevy Volt modules (ongoing).

It should be noted that many of the above deliverables are available over and above what has been promised in the original proposal for Phase III research. We are wishing to all participants a very productive and enjoyable meeting!

Tom Wierzbicki

Elham Sahraei

BATTERY MODELING PUBLICATIONS OF THE MIT BATTERY CONSORTIUM TEAM

Submitted articles

1. Kermani G., Sahraei E., Dynamic Impact Response of Lithium-Ion Batteries, Constitutive Properties and Failure Model, Submitted to RSC Advances.
2. Zhu J., Luo H., Li W., Gao T., Xia Y., Wierzbicki T., Influence of electrolyte on the impact response of lithium-ion battery pouch cells, submitted to Joule.

Journal publications

1. Dixon B.,, Mason A, Sahraei E., "Effects of electrolyte, loading rate and location of indentation on mechanical integrity of li-ion pouch cells", Journal of Power Sources 396, 412–420, 2018
2. Zhu J., Wierzbicki T., Li W., "A review of safety-focused mechanical modeling of commercial lithium-ion batteries", Journal of Power Sources, 378, 153-168, 2018.
3. Zhu J., Li W., Xia Y., Sahraei E., Testing and Modeling the Mechanical Properties of the Granular Materials of Graphite Anode, Journal of The Electrochemical Society 165 (5), A1160-A1168, 2018
4. Li W., Xia Y., Zhu J., Luo H., State-of-Charge Dependence of Mechanical Response of Lithium-Ion Batteries: A Result of Internal Stress. Journal of The Electrochemical Society 165 (7), A1537-A1546, 2018
5. Zhu J., Zhang X., Luo H., Sahraei E., "Investigation of the deformation mechanisms of lithium-ion battery components using in-situ and interrupted micro tests". Applied Energy 224, 251-266, 2018
6. Luo H., Zhu J., Sahraei E., Xia Y., "Adhesion strength of cathode electrode in lithium-ion batteries under combinded tension/shear loadings". RSC Advances, 8 (8), 3996-4005, 2018
7. Chung S., Tancogne-Dejeanb T., Zhu J., Luo H., Wierzbicki T., "Plane-strain failure in lithium-ion batteries under transverse indentation loading", Journal of Power Sources, Vol 389, Pages 148-159. 2018
8. Zhang, X., J. Zhu, and E. Sahraei. "Degradation of battery separators under charge–discharge cycles." RSC Advances 7.88 (2017): 56099-56107.
9. Kisters T., Sahraei E., Wierzbicki T., "Dynamic impact tests on lithium-ion cells", International Journal of Impact Engineering, Vol. 108, Pages 205-216, October 2017.
10. Kermani G., Sahraei E., "Review: Characterization and Modeling of the Mechanical Properties of Lithium-Ion Batteries", Energies, 10(11), 1730, 2017
11. Zhu J., Zhang X., Sahraei E., Wierzbicki T., "A combined experimental/numerical study on deformation and failure of 18650 battery cells under axial compression", Journal of Power Sources vol. 336 pp 332-340, 2016
12. Zhang X., Sahraei E., Wang K., "Failure Mechanisms of Li-ion Battery Separators, Leading to Soft and Hard Internal Shorts", Nature Scientific Reports, vol. 6, 2016.
13. Zhang X., Sahraei E., Wang K., "Deformation and Failure Characteristics of Four Types of Lithium

ion Battery Separators", Journal of Power Sources, vol. 327, pp 693-701, 2016.

14. Sahraei E., Bosco E., Dixon B., Lai B.," Microscale failure mechanisms leading to internal short circuit in Li-ion batteries under complex loading scenarios", Journal of Power Sources, vol. 319, pp 56-65, 2016.
15. Bonatti C., Mohr D., "Anisotropic viscoplasticity and fracture of fine grained metallic aluminum foil used in Li-ion batteries", Materials Science and Engineering: A, vol 654, , pp 329–343, 2016.
16. Sahraei E., Kahn M., Meier J., Wierzbicki T., "Computed Tomography and Finite Element Modeling of Cracks Developed in Lithium-ion Cells under Mechanical Loading," RSC Advances (Impact Factor 3.84), 5, 80369 – 80380, 2015.
17. Zhang X., , Wierzbicki T., "Characterization of plasticity and fracture of shell casing of lithium-ion cylindrical battery", Journal of Power Sources, vol. 280, pp 47-56, 2015.
18. Sahraei E., Meier J., Wierzbicki T., "Characterizing Mechanical Properties and Onset of Short Circuit for Three Types of Lithium-ion Pouch Cells," Journal of Power Sources, vol.247, pp. 503-516, 2014.
19. Xia Y., Wierzbicki T., Sahraei E., Zhang X., "Damage of Cells and Battery Packs Due to Ground Impact," Journal of Power Sources, vol.. 267, pp. 78–97, 2014.
20. Wierzbicki T., Sahraei E., "Homogenized Mechanical Properties for the Jellyroll of Cylindrical Lithium-ion Cells," Journal of Power Sources, vol. 241, pp. 467-476, 2013.
21. Sahraei E., Campbell J., Wierzbicki, T., "Detection of Short Circuit in 18650 Li-ion Cells under Mechanical Abuse: Experiments, Finite Element Modeling, and Validation," Journal of Power Sources, vol. 220, pp. 360–372, 2012.
22. Sahraei E., Hill R., Wierzbicki, T., "Calibration and Finite Element Simulation of Pouch Li-ion Batteries for Mechanical Integrity," Journal of Power Sources, vol. 201, pp. 307– 321, 2012.

Conference Presentations of ICL on Battery Safety

23. Li W., Poster: "Mechnical modeling of lithium-ion battery pouch cells: state-of-charge and loading speed". Battery Safety Conference. Arlington VA, November 1-2, 2018
24. Sahraei E., "Failure Criterion for Lithium-ion Batteries, Implementation and Validation", CAE Grand Challenge, Hanua, Germany, April, 2018
25. Zhu J., "Modeling the Granular/Metal Multi-layered Structure of Lithium-ion Batteries", US National Congress of Theretical and Applied Mechanics. Chicago, June, 2018
26. Zhu J., "Structural Designs for Electric Vehicle Battery Pack against Ground Impact"., SAE World Congress and Experience. Detroit, MI, Apirl 2018
27. **Sahraei E**., Zhang X., "On Mechanics of Hard Versus Soft short Circuit in Lithium-ion Batteries", ASME IMECE 2017, *Tampa, Florida, Nov 3-9, 2017.*
28. **Sahraei E**., Wierzbicki T., Bulla M., "A Criterion to Predict Onset of Electric Short Circuit for Lithium-Ion Batteries Subjected to Mechanical Loads", Advanced Battery Power Conference, *Aachen, Germany, March 29-30, 2017.*
29. Zhu J., "Failure in Lithium-ion Batteries under Transverse Indentation Loading". International Mechanical Engineering Congress and Exposition 2017, Tampa, FL, Nov 9, 2017

30. Sahraei E., “Mechanical Crush and Internal Short Circuit Mechanisms”, Battery Safety Council, Jan. 13, 2017.
31. Sahraei E., “Optimization of Li-ion Battery Structures Using Computational Homogenization”, ASME IMECHE 2016, Phoenix, AZ, Nov 16, 2016.
32. Sahraei E., “Calibration of a Homogenized Jellyroll Model through Micro-Mechanical Tests”, Battery Safety 2014, Washington, DC, Nov. 13-14, 2014.
33. Sahraei E., Wierzbicki T., “Testing and Constitutive Modeling of Four Types of Lithium-ion Batteries,” Battery Safety 2013, San Diego, CA, Nov. 14-15, 2013.
34. Sahraei E., Wierzbicki T., “Crashworthiness and Internal Short Modeling for Pouch and Cylindrical Lithium-ion Cells,” Batteries 2013, Nice, France, Oct. 14-16, 2013.
35. Meier J., Sahraei E., Salk M., Kisters T., Huberth F., “State of Charge vs. Thermal Runaway for Lithium-Ion Large Pouch Cells,” 3rd Battery Congress, Troy, MI, Apr. 15-16, 2013.
36. Sahraei E., Wierzbicki T., “Characterizing Crash Safety of Cylindrical and Pouch Li-ion Batteries using Computational Modeling,” Battery Safety 2012, Las Vegas, NV, Dec. 6-7, 2012.
37. Campbell J., Sahraei E., and Wierzbicki T., “Detecting and modeling the onset of short circuit in a Li-ion cell under mechanical loading,” 2nd Battery Congress, Ann Arbor, MI, Apr. 23-24, 2012.
38. Sahraei E., Hill R., and Wierzbicki T., “Modeling of Lithium-ion Cylindrical Batteries for Mechanical Integrity: Experiments, Calibrations, and Validation,” 1st Battery Congress, Ann Arbor, MI, Apr. 11-12, 2011.
39. Sahraei E., Wierzbicki T., Hill R., Luo, M., “Crash Safety of Lithium-Ion Batteries, Towards Development of a Computational Model,” 2010 SAE World Congress, SAE Technical Paper # 2010-01-1078, Detroit, MI, Apr. 13-15, 2010.
40. Sahraei E., Hill R., and Wierzbicki T., “Modeling of Lithium-ion Batteries for Crash Safety,” Proceedings of International Auto Body Congress (IABC), Troy, MI, Nov. 3-4, 2010.

Agenda

Interim Meeting of MIT Program on Battery Safety and Crashworthiness

Hosted by: Jaguar_Land Rover

University of Warwick, Coventry CV4 7AL, UK

International Manufacturing Centre (IMC), Boardroom 2

Day 1: Tuesday, June 19, 2018

9:00-9:30	All participants	*Reception and Greetings*
9:30-9:45	Jim Hooper (JLR)	*Welcome Address*
9:45-10:00	Tomasz Wierzbicki (MIT) and Elham Sahraei (GMU/MIT)	*Current Status of Consortium and Projects*
10:00-10:30	Golriz Kermani (GMU) and Elham Sahraei (GMU/MIT)	*Progress on Modeling of In-plane Loading*
10:30-11:00	Juner Zhu (MIT), Wei Li (MIT/Tsinghua), Yong Xia (Tsinghua), and Elham Sahraei (GMU/MIT)	*Testing and modeling the mechanical properties of the granular materials of graphite anode*
11:00-11:30	**Coffee Break**	
11:30-12:00	Iain Masters (JLR/WMG)	*Mechanical Test Methods of Batteries*
12:00-12:15	Wei Li (MIT/Tsinghua), Yong Xia (MIT/Tsinghua), Juner Zhu(MIT), Hailing Luo (MIT/Tsinghua)	*SOC dependence of mechanical response of lithium-ion batteries: a result of internal stress*
12:15-12:30	Gyu young Kim (GMU) and Elham Sahraei (GMU/MIT)	*Modeling mechanical response of high SOC battery cells*
12:30-2:00	**Lunch**	
2:00-2:30	Elham Sahraei (GMU/MIT) and Marian Bulla (ALTAIR)	*Updates on User Defined Material and Failure Laws*
2:30-3:00	Juner Zhu, Wei Li, Tomasz Wierzbicki	*Reinforcing mechanisms of various granular materials*
3:00-3:30	Mark Amor Segan (JLR/WMG)	*Overview of Energy Innovation Center Research Activities*
3:30-4:00	Thomas Kisters (EMI)	*Impact tests on large prismatic Lithium-ion cell with various SOC*
4:00-5:00	*All*	*Feedback and Discussion*
6:00	**Group Dinner**	

Agenda

Interim Meeting of MIT Program on Battery Safety and Crashworthiness

Hosted by: Jaguar_Land Rover
University of Warwick, Coventry CV4 7AL, UK
International Manufacturing Centre (IMC)

Day 2: Wednesday, June 20, 2018

10:00 AM-12:30 PM	Tour of Warwick Manufacturing Group R&D Facility
12:30	**Lunch**

List of Participants of the Interim Meeting of Battery Consortium Meeting

Warwick, UK, June 2018, Hosted by Jaguar Land-Rover

	Guest	Company	Contact Details
1	Marian Bulla	Altair	bulla@altair.de
2	Bernhard Brunnesteiner	AVL	bernhard.brunnsteiner@avl.com
3	Martin Schwab	AVL	Martin.Schwab@avl.com
4	Johannes Irslinger	Daimler	johannes.irslinger@daimler.com
5	Thomas Kisters	EMI	thomas.kisters@emi.fraunhofer.de
6	Dr Yong-Hwan Choi	Hyundai	yonghwan.choi@hyundai.com
7	Balraj Ghataore	JLR	bghataor@jaguarlandrover.com
8	Dr James Hooper	JLR	jhooper@jaguarlandrover.com
9	Dr Roland Hin Kwan Wong	JLR	hwong1@jaguarlandrover.com
10	Ines Altubo Andres	JLR	ialtuboa@jaguarlandrover.com
11	Mark Tyler-Street	JLR	mtylerst@jaguarlandrover.com
12	Philip Mannock	JLR	pmanock@jaguarlandrover.com
13	Richard Brown	JLR	rbrow132@jaguarlandrover.com
14	Steve Hodbod	JLR	shodbod@jaguarlandrover.com
15	Jason Page	JLR	jpage3@jaguarlandrover.com
16	Arunn Thanikachalam	JLR / WMG	A.N.Thanikachalam@warwick.ac.uk
17	Dr Alon Ratner	JLR / WMG	A.Ratner@warwick.ac.uk
18	Dr Iain Masters	JLR / WMG	i.g.masters@warwick.ac.uk
19	Dr Lukasz Figiel	JLR / WMG	l.w.figiel@warwick.ac.uk
20	Dr Richard Beaumont	JLR / WMG	richard.beaumont@warwick.ac.uk
21	Mark Amor-Segan	JLR / WMG	mark.amor-segan@warwick.ac.uk
22	Steven Lucas	JLR / WMG	steven.lucas@warwick.ac.uk
23	Prof. Damoon Soudbakhsh	MIT / Temple	damoon.soudbakhsh@temple.edu
24	Prof. Elham Sahraei Esfahani	MIT / Temple	elham.sahraei@temple.edu
26	Wei Li	MIT / Tsinghua	weili17@mit.edu
27	Benoit Changeux	PSA	benoit.changeux@mpsa.com

Agenda

Annual Review Meeting of Battery Consortium

Impact and Crashworthiness Lab (ICL)

Day 1. Friday, November 9, 2018

Metro Meeting Center-Boston

101 Federal Street, 4th Floor, Downtown Boston

8:15-8:45	**Continental Breakfast**	
8:45-9:00	Tom Wierzbicki and Elham Sahraei	*Status Update on the Current Projects*
9:00-9:20	Elham Sahraei, Damoon Soudbakhsh, and Mehdi Gilaki	*Effects of Mechanical Damage on Electrical Properties*
9:20-9:50	Jimmy (Junhe) Lian and Wierzbicki	*Prediction of Shear Crack Formation: Comparison of four fracture criteria*
9:50-10:20	Juner Zhu and Wei Li	*Constitutive Modeling of Battery Coatings and FE Detailed Model of Pouch Cells*
10:20-10:40	Victor Oancea (SIMULIA)	*Computational Mechanics Methods for Li-ion Battery Cells*
10:40-11:00	**Coffee Break**	
11:00-11:30	Donal Finegan (NREL)	*Sequence of Battery Failure Using In-situ CT Scan*
11:30-11:50	Golriz Kermani and Elham Sahraei	*3D RVE and Failure Predictions*
11:50-12:10	Yuanli Bai and Jimmy (Junhe) Lian	*Anisotropic Plasticity Model of Lithium-ion Battery Cells*
12:10-12:30	Yong Xia/Qing Zhou	*Testing and Modeling of Battery Modules of Chinese EV*
12:30-1:45	**Lunch***	
1:45-2:15	Andrew Oury (GM)	*Current state of standards and regulations for battery pack underbody protection*
2:15-2:35	Golriz Kermani and Elham Sahraei	*In-plane Modeling from RVE to Cell Level*
2:35-2:55	Marian Bulla (Altair), Feng Zhu, Junhe Lian, Wei Li, Rui Luo, Juner Zhu, Tomasz Wierzbicki	*Testing and Simulation of Chevy Volt Module*
2:55-3:20	**Coffee Break**	
3:20-3:40	Mehdi Gilaki and Elham Sahraei	*Mechanical Properties of Cells under Operating Temperatures*
3:40-4:00	Wei Li and Juner Zhu	*Data-driven Failure Model of Li-ion Pouch Battery Cells based on Detailed FE Model*
4:00-5:00	Perspective of Sponsors and Planning for Next Phase	
5:00	**Adjourn**	

* All meals are catered-in and free of charge

Day 2. Saturday, November 10, 2018

A Lab Tour and Workshop on FE Implementation in Abaqus, LS-Dyna, and RADIOSS

Impact and Crashworthiness Lab, MIT

77 Mass. Ave., Room 5-011, Cambridge

10:00-11:00	**Lab Tour**	
11:00-11:30	Sigit Santosa (ITB, Indonesia)	*Experience in Large-scale Simulation of Electric Vehicles*
11:30-11:50	Marian Bulla and Elham Sahraei	*Validations of Failure Criteria in RADIOSS*
11:50-12:00	Jimmy (Junhe) Lian and Tom Wierzbicki	*Comparison of Prediction of LS-Dyna and Abaqus material models of battery deformation*
12:00-12:10	Jimmy (Junhe) Lian and Tom Wierzbicki	*Study of Mesh Size Effect on Crack Formation of Pouch Batteries in Abaqus*
12:10-12:30	Elham Sahraei	*Modeling Strategy in LS-Dyna*
12:30-12:50	Thomas Tancogne-Dejean and Tom Wierzbicki	*Checking the accuracy of simulation through closed-form solutions*
	Discussion	
1:00-	**Lunch***	

* Table reserve at Catalyst, 300 Technology Square, Cambridge, MA 02139

List of confirmed participants of the November 2018 Annual Review Meeting

1	Johannes Irslinger	Daimler	johannes.irslinger@daimler.com
2	Charles Patrissi	NUWC Newport	Charles.Patrissi@navy.mil
3	Lars Greve	Volkswagen AG	lars.greve@volkswagen.de
4	Peiran Ding	ESI	Peiran.Ding@esi-group.com
5	Thomas Kisters	Fraunhofer EMI	kisters@emi.fraunhofer.de
6	Pierre-Olivier Santacreu	Aperam	pierre-olivier.santacreu@aperam.com
7	Benoit CHANGEUX	PSA Groupe	benoit.changeux@mpsa.com
8	Gildas Delbeke	Dyson	gildas.delbeke@dyson.com
9	Donal Finegan	NREL	Donal.Finegan@nrel.gov
10	Keunhwan Pack	Apple	kpack@apple.edu
11	Xiaowei Zhang	Tesla	xiaowzhang@tesla.com
12	Andrew P. Oury	GM	andrew.p.oury@gm.com
13	Saif Siddiqui	GM	saif.siddiqui@gm.com
14	Tejas Bhavsar	GM	tejas.bhavsar@gm.com
15	Junhe Lian	Aalto University	Junhe.Lian@iehk.rwth-aachen.de
16	Marian Bulla	Altair	bulla@altair.de
17	Yuanli Bai	UCF	bai@ucf.edu
18	Feng Zhu	Embry-Riddle	fengzhume@gmail.com
19	Jean Michel Terrier	Altair	jmterrier@altair.com
20	John Kim	Toyota	john.kim@toyota.com
21	Eric Carlson	Independent	Ejcarlson1776@gmail.com
22	Jerome Rousseau	Altair	rousseau@europe.altair.com
23	Tobias Glossmann	Mercedes-Benz	tobias.glossmann@daimler.com
24	John Izzo	Naval Undersea Warfare Center	John.r.izzo@navy.mil
25	Victor Oancea	SIMULIA	Victor.OANCEA@3ds.com
26	Pierre L'Eplattenier	LSTC	pierre@lstc.com
27	Nory Ison	Apple	nison@apple.com
28	Dhaval Lokagariwar	Apple	dlokagariwar@apple.com
29	Sigit Santosa	IBT	sigit.santosa@itb.ac.id
30	Masatomo Tanaka	Murata	masatomo.tanaka@murata.com
31	Tatsushiro Hirata	Murata	tatsushiro.hirata@murata.com
32	Jaeyoung Lim	Hyundai	jytree@hyundai.com
33	Bernhard Brunnsteiner	AVL	bernhard.brunnsteiner@avl.com
34	Martin Schwab	AVL	martin.schwab@avl.com
35	Jonathon Harding	Exponent	jharding@exponent.com

2018 Featured Articles

Zhu J., Wierzbicki T., Li W., “A review of safety-focused mechanical modeling of commercial lithium-ion batteries”, Journal of Power Sources, 378, 153-168, 2018.

Dixon B.,, Mason A, Sahraei E., “Effects of electrolyte, loading rate and location of indentation on mechanical integrity of li-ion pouch cells”, Journal of Power Sources 396, 412–420, 2018

Zhu J., Li W., Xia Y., Sahraei E., Testing and Modeling the Mechanical Properties of the Granular Materials of Graphite Anode, Journal of The Electrochemical Society 165 (5), A1160-A1168, 2018

Li W., Xia Y., Zhu J., Luo H., State-of-Charge Dependence of Mechanical Response of Lithium-Ion Batteries: A Result of Internal Stress. Journal of The Electrochemical Society 165 (7), A1537-A1546, 2018

Luo H., Zhu J., Sahraei E., Xia Y., “Adhesion strength of cathode electrode in lithium-ion batteries under combinded tension/shear loadings”. RSC Advances, 8 (8), 3996-4005, 2018

Chung S., Tancogne-Dejeanb T., Zhu J., Luo H., Wierzbicki T., “Plane-strain failure in lithium-ion batteries under transverse indentation loading”, Journal of Power Sources, Vol 389, Pages 148-159. 2018

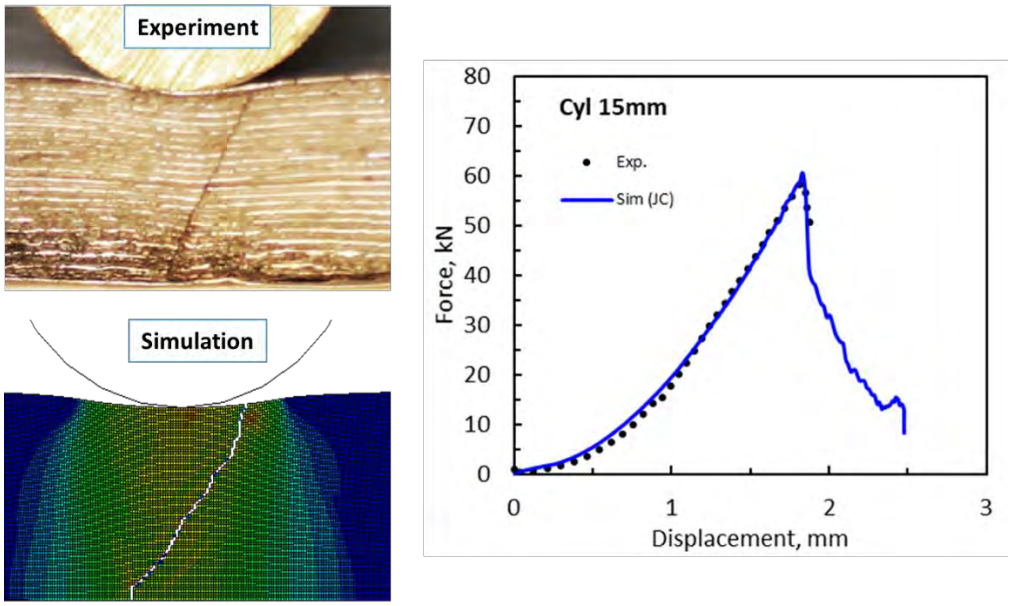

(Accuracy of MIT model prediction)

Journal of Power Sources 378 (2018) 153–168

Contents lists available at ScienceDirect

Journal of Power Sources

journal homepage: www.elsevier.com/locate/jpowsour

Review article

A review of safety-focused mechanical modeling of commercial lithium-ion batteries

Juner Zhu[a], Tomasz Wierzbicki[a,*], Wei Li[b]

[a] Impact and Crashworthiness Lab, Department of Mechanical Engineering, MIT, 77 Massachusetts Ave., Cambridge, MA 02139, USA
[b] State Key Lab of Automotive Safety and Energy, Department of Automotive Engineering, Tsinghua University, Beijing 100084, PR China

HIGHLIGHTS

- Recent progresses in the safety-focused mechanical modeling of LIBs are reviewed.
- Multi-scales: micro/meso (material), macro (cell), and macro-system (module, pack).
- Reviewing detailed/homogenized/RVE FE models, material models, & analytical models.
- Experiments at component/cell/module levels are summarized.

GRAPHICAL ABSTRACT

ARTICLE INFO

Keywords:
Lithium-ion battery
Safety
Mechanical modeling
Multi-scale
Short circuit

ABSTRACT

We are rapidly approaching an inflection point in the adoption of electric vehicles on the roads. All major automotive companies are having well-funded plans for mass market affordable branded EV product line models, which can open the floodgates. A rapid growth of battery energy density, accompanied by an aggressive progress of reduction of costs of lithium-ion batteries, brings safety concerns. While more energy stored in the battery pack of an EV translates to a longer range, the downside is that accidents will be more violent due to battery inevitable explosion. With today's technology, severe crashes involving intrusion into the battery pack will potentially result in a thermal runaway, fire, and explosion.

Most of research on lithium-ion batteries have been concerned with the electrochemistry of cells. However, in most cases failure and thermal runaway is caused by mechanical loading due to crash events. There is a growing need to summarize the already published results on mechanical loading and response of batteries and offer a critical evaluation of work in progress. The objective of this paper is to present such review with a discussion of many outstanding issues and outline of a roadmap for future research.

1. Introduction: study of mechanical properties of LIBs at multiple scales

The market of Electric Vehicles (EV) is no longer a matter of speculation and analysis predictions. The introduction in 2017 of Chevy Bolt and Tesla Model 3 marks a new era for the automotive industry. Both cars have over 200 miles range on a single charge and are affordable. According to the comprehensive report of the UBS [1], the cost parity of gasoline engine and EV will be reached 2–3 years earlier than originally believed. This trend is mostly due to the advances in the design of lithium-ion batteries in terms of energy capacity and simultaneous drop in the price of a battery pack.

The annual production of Tesla 3 is expected to reach 500,000 units while the output of GM's Bolt will be slightly less. All new Nissan Leaf

* Corresponding author.
E-mail addresses: zhujuner@mit.edu (J. Zhu), wierz@mit.edu (T. Wierzbicki), wei-l14@mails.tsinghua.edu.cn (W. Li).

https://doi.org/10.1016/j.jpowsour.2017.12.034
Received 3 November 2017; Received in revised form 6 December 2017; Accepted 13 December 2017
Available online 22 December 2017
0378-7753/

Nomenclature

E	Elastic modulus
ν	Poisson's ratio
$\bar{\varepsilon}_p$	Plastic strain
$\dot{\bar{\varepsilon}}_p$	Plastic strain rate
ε_{22}^p	Plastic strain in the transverse direction
ε_{33}^p	Plastic strain in the thickness direction
r_L	Lankford r-value
MD	Machine direction
TD	Transverse direction
DD	Diagonal direction
f	Yield function
$\sigma_{ij}(i,j=1,2.3)$	Stress component
$\bar{\sigma}_Y$	Equivalent flow stress, function of plastic strain
F, G, H, L, M, N	Coefficients of Hill48 yield function
σ_0	Yield stress
Q, β	Coefficients of Voce hardening law
η	Stress triaxiality
$\bar{\theta}$	Lode angle parameter
c_1 and c_2	Coefficients of Modified Mohr-Coulomb model
a and n	Coefficients of the power law
C	Coefficient of Johnson-Cook model
$\mathbf{E}$	Total strain tensor
$\mathbf{E}^e$, $\mathbf{E}^p$	Elastic and plastic strain tensor
μ	Friction coefficient of Drucker-Prager model
ϕ	Friction angle of Drucker-Prager model
c	Cohesion parameter of Drucker-Prager model
p	Pressure, first invariant of deviatoric stress
q	Mises equivalent stress, second invariant of deviatoric stress
r	Third invariant of deviatoric stress
$\mathbf{S}$	Deviatoric stress
ε_f	Normalized critical displacement (NCD) to short circuit
δ_f	Displacement to short circuit
l_c	Characteristic length in the loading direction
p_0	Center of the yield ellipse on the p-axis of crushable foam model
A	Size of the yield ellipse on the p-axis of crushable foam model
B	Size of the yield ellipse on the q-axis of crushable foam model
Φ	Void volume fraction of Gurson-Tvergaard-Needleman model
P	Load measured in abuse tests of cells
H_c	Thickness of cell
R	Punch radius in hemispherical punch test
N	Total number of electrodes in a cell
h_f	Thickness of current collector
m	Number of waves in the length
D	Bending rigidity of a plate

with 150–200 miles range will be available on the market in 2018. Altogether, the total stock of EV, which already crossed one million mark in 2016, is reaching now an inflection point. The International Energy Agency [2] predicts that by 2025, there will be up to 100 million cars on the roads world-wide. With such a large number, the law of statistics will apply and EV will experience a similar number of accidents as the gasoline-powered cars. The question that must be posed and answered is what new safety issues bring the EV as compared to the gasoline-powered cars.

It is generally recognized that if the battery pack is split-open or damaged in the accident, there is a potential of the so-called battery thermal runaway, fire, and explosion. The highly-publicized accident of

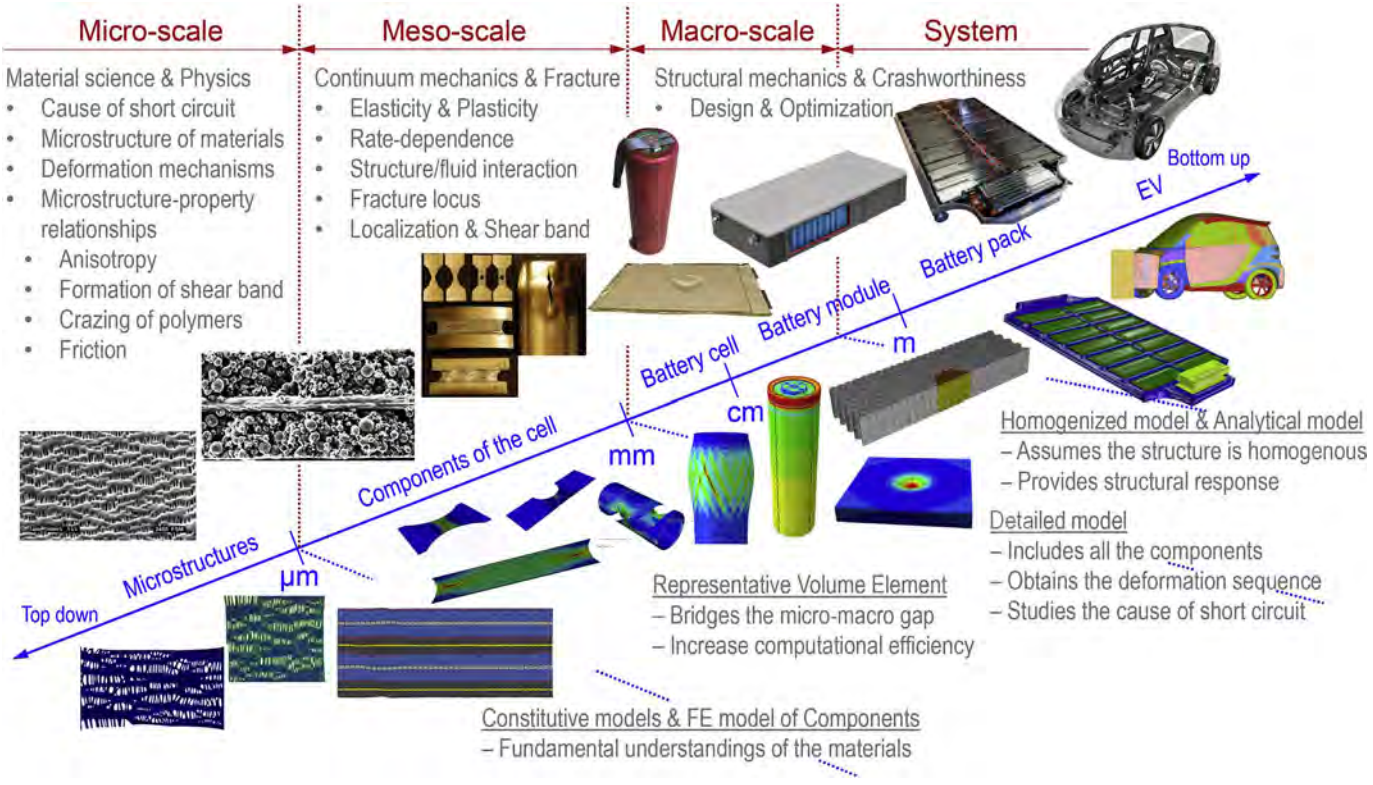

Fig. 1. The study of mechanical properties of LIBs involves multiple scales and disciplines, and various models have been proposed to characterize the mechanical behavior of LIBs at each length scale.

Tesla Model S that caught fire after hitting road debris illustrates the additional danger of driving EVs. This danger is being augmented by an ever-increasing capacity of lithium-ion cells and battery packs so that mere energy could be suddenly released during car crash. The automotive industry, battery manufacturers, the regulatory agencies such as NHTSA in the US or BAM in Germany, as well as the insurance industry should be prepared to deal with this eminent problem.

This article is reviewing the state-of-art in the specific problem of mechanical loading of batteries during crash events. While there is an enormous bulk of research on electro-chemistry of batteries as well as thermal management, studies on the response and failure of cells due to crash loading lags far behind in terms of available researches and number of publications. A part of the issue is a sensitivity of the word "safety" in terms of media exposure, public perceptions, and fear of litigation. This is especially true in the case of a new industry. But now, as EV industry has reached point of no-return, the crash safety of lithium-ion batteries should receive a proper attention.

Conditions and prevention of thermal overheating and electrical overcharging of batteries are covered extensively in the literature [3–7]. The focus of the present document is placed on intrusion of rigid objects into battery cells, modules, and packs. The battery packs are usually placed in the least deformable parts of a car. Still penetration may occur especially in side collisions, road debris impacts, and small overlap crash tests. Damage may also be caused by an external short circuit, due to deceleration forces during a collision. These types of failure modes are very much design-dependent and thus are covered by the electrical control system rather than by the law of mechanics.

The study of safety of batteries involves multiple scales [8,9] (see Fig. 1). Therefore, this paper is divided into three parts, each discussing advances in a given particular scale and on that base, indicates needs for further research. It also presents in an easy-to-follow tabular form the main finding of the last ten years of research, including typical parameters of commercial cells with different form factors. The objective of the review article is two-fold. First, it will explain how the damage and failure of individual cells is progressing and what are the main factors that influence the possibility of electrical short circuit and potential thermal runaway of batteries. Secondly, it will review progress in computational modeling and what type of tests are needed to generate input data to commercial Finite Element (FE) codes.

2. Part I. Micro-scale and meso-scale: constitutive models of components of battery cells

The jellyroll (or stack of electrodes) of commercial lithium-ion batteries in the current market is a multi-layered structure (see Fig. 2a), and a single repeatable unit consists of a cathode, an anode, and two layers of separator. Further, the cathode is made of an aluminum foil coated on both sides by an active material with a binder. Likewise, the anode is composed of a copper foil coated with graphite (or silicon) particles. All the components are immersed in electrolytes and covered by a pouch or a steel shell casing. The chemistry and materials of the components may differ among battery manufacturers, but the basic structure of such a repeatable unit is almost identical. The cross-sections of the components of a commercial lithium-ion battery with NMC (Nickel-Manganese-Cobalt) cathode, graphite anode and microporous polypropylene separators are shown in Fig. 2b–c. Table 1 describes qualitatively the mechanical characteristics of each component. In the remaining of this section, the mechanical properties of all the components will be described in details.

Table 1
Materials and general mechanical characteristics of each battery cell components.

Component	Material	Mechanical behavior	References
Current collector	Aluminum foil (cathode)	Anisotropy	[12–14]
	Copper foil (anode)	Strain hardening	[12,13]
		Ductile fracture	[12,24]
		Rate-dependence	[12,25,26]
Coating	Powders of graphite/ active particles and binders	Pressure-dependence	[13,51]
Separator	Porous polymer (with/without ceramic coating)	Orthotropy	[29,55–58]
		Elasto-viscoplasticity	[29,56,61,62]
		Temperature dependent	[29,57,58,69]
Shell casing or pouch	Steel or aluminum sheet	Anisotropy	[18,29,104]
		Strain hardening	[18,29,104]
		Ductile fracture	[18,29]

The term "form factor" distinguishes between pouch cells, prismatic cells, elliptical cells, and cylindrical cells. The pouch cells can vary in size from the tiny ones found in cellular phones to large secondary cells for EV applications. The most common cylindrical cells, 18650 used for example in Tesla Model S, is 18 mm in diameter and 65 mm in length. Tesla Model 3 uses slightly larger cylinders, the 2170 cell. Thus, the cells are not "micro" in size. What justifies the title micro-scale and meso-scale is a very small thickness of individual components and complex structure of the coating and separator.

2.1. Current collectors

The current collectors of commercial lithium-ion batteries are metal foils – aluminum for the cathode and copper for the anode. The

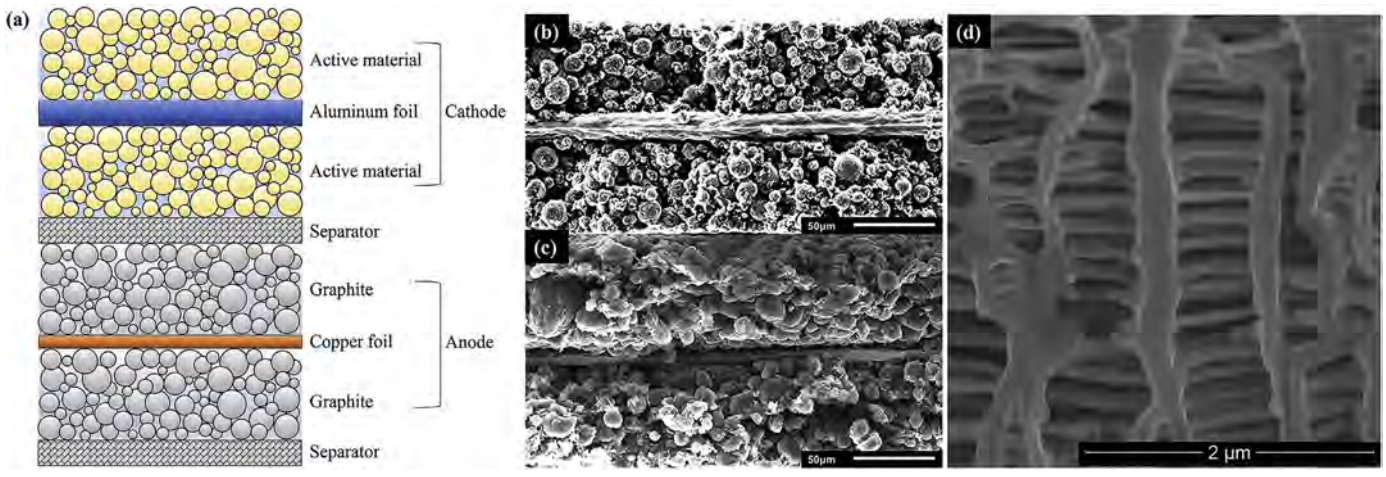

Fig. 2. (a) Repeatable unit (RVE) of a lithium-ion battery, and cross-sections of the components: (b) NMC cathode, (c) graphite anode, and (d) polypropylene separator (microporous polypropylene).

thickness of the foils is about 10–25 μm. The copper foil is usually slightly thinner than the aluminum foil. Both of these two materials exhibit typical elastic-plastic mechanical properties of metallic materials. The elastic properties of aluminum and copper – the elastic modulus E, and Poisson's ratio ν – are well known and given in Table 2. Plastic properties are defined by the coefficients of anisotropy and hardening curve.

2.1.1. Plastic anisotropy

During the manufacturing process, thin metal foils undergo multiple rolling operations, which introduce a certain amount of plastic anisotropy into the material. There are two concepts to quantify this property [10,11]. The first one is the ratio of the yield stresses in different directions, which indicates the anisotropy in material strength. According to existing tensile test results of the current collectors [12–14], the difference among yield stresses in machine direction (MD, 0°), transverse direction (TD, 90°), and diagonal direction (DD, 45°) is almost negligible (see Fig. 3a).

The second concept to describe the anisotropy of plastic flow of thin sheets is by means of the Lankford r-value, which is defined as

$$r_L = \mathrm{d}\varepsilon_{22}^p / \mathrm{d}\varepsilon_{33}^p, \tag{1}$$

where ε_{22}^p and ε_{33}^p are the transverse plastic strain and through-thickness plastic strain when the sample is loaded in x_1-direction, respectively. Materials are incompressible during plastic deformation. In order to deform material in tensile test, either the width or thickness of specimens must change. Physically, the Lankford parameter tells us what the ratio between these two deformations is. For the isotropic material, strain distributions in the width and thickness are the same and $r_L = 1$. The determination of the Lankford r-value requires a full-field measurement of the strain distribution, which is usually accomplished using the Digital Image Correlation (DIC) method. Fig. 3c shows the speckle pattern on a dog-bone specimen and the virtual cruciform extensometer. Fig. 3b plots the ε_{22}-ε_{33} curves in the three directions of the same aluminum foil as that in Fig. 3a, used as the current collector of a commercial LIB. The r-values of this material turn out to be 0.2 (MD), 1.5 (DD) and 1.1 (TD), which suggests a very severe anisotropy (see Table 2).

To sum up, existing test data of the current collector metal foils shows that they are almost isotropic in material strength, but highly anisotropic with respect to plastic flow. It is not sufficient to make a statement about anisotropy based on the stress-strain curves and ignore the r-value, which can greatly influence the distribution of plastic strain [10]. It should also be pointed out that the precise measurements of stress-strain curves and Lankford r-values require a delicate design of the testing setup. The biggest challenge is how to align the specimen without causing edge fracture, wrinkling, and buckling, which are very common for thin films (large length/thickness ratio). One of the approaches to overcome this difficulty is micro testing [12], for which the length and width of the specimen is designed to be of the same order as the thickness. Fig. 3d shows a loading device for micro testing used for battery study.

For mathematically modeling the plastic anisotropy, the Hill48 model [15] is the simplest and probably the most popular model in the metal forming field. Its yield function is given by

$$f = \sqrt{F(\sigma_{22}-\sigma_{11})^2 + G(\sigma_{33}-\sigma_{11})^2 + H(\sigma_{11}-\sigma_{22})^2 + 2L\sigma_{23}^2 + 2M\sigma_{31}^2 + 2N\sigma_{12}^2} - \bar{\sigma}_Y(\bar{\varepsilon}_p), \tag{2}$$

where σ_{ij} are the stress components, F to N are six coefficients to be calibrated, and $\bar{\sigma}_Y(\bar{\varepsilon}_p)$ describes the strain hardening of the material. There are other anisotropic yield functions that can be used to model the current collectors, such as the Yld series [12,16,17].

2.1.2. Strain hardening

According to the test results of the aluminum foil [12] and the copper foil [13], both of them have a relatively low hardening rate $\mathrm{d}\bar{\sigma}_Y/\mathrm{d}\bar{\varepsilon}_p$. In other words, the hardening curve $\bar{\sigma}_Y(\bar{\varepsilon}_p)$ tends to be flat as the plastic strain increases (see Fig. 3a). This special characteristic can be well captured by the Voce hardening law,

$$\bar{\sigma}_Y(\bar{\varepsilon}_p) = \sigma_0 + Q[1 - \exp(-\beta\bar{\varepsilon}_p)], \tag{3}$$

where σ_0, Q and β are the three parameters to be calibrated. Other hardening laws, such as the Swift law defined by power function $\bar{\sigma}_Y = a(\bar{\varepsilon}_p - \bar{\varepsilon}_0)^n$, are more suitable for describing higher hardening rate [20]. Typical values of the constants σ_0, Q, and β for both foils are given in Table 2. To increase the precision of characterization, two hardening laws could be combined with a weighting coefficient [10].

2.1.3. Ductile fracture

Fracture of aluminum and copper foils is proceeded by large plastic deformation, during which plastic strain increases rapidly but the flow stress keeps relatively stable. The fracture behavior of the current collectors falls in the category of ductile material, and therefore is described by a suitable strain-based failure criterion [21]. The simplest strain-based ductile fracture criterion is the constant equivalent plastic strain, in which fracture is assumed to occur in the material element where the equivalent plastic strain reaches a critical value [22]. This is a far reaching simplification because experiments show that the fracture strain depends on the stress state. Some metallic materials can undergo very large deformation under compression, while they fail very easily under tension. Table 2 lists the fracture strains of the aluminum foil and copper foil of a commercial LIB under tension, biaxial tension, and plane-strain tension [19]. Large difference can be observed among these values, which has been proven to obey the Mohr-Coulomb (MC) fracture model [12,21–25].

$$(\sqrt{1+c_1^2} + c_1)\sigma_1 - (\sqrt{1+c_1^2} - c_1)\sigma_3 = 2c_2, \tag{4}$$

where σ_1 and σ_3 is the maximum and minimum principal stresses, respectively, and c_1 and c_2 are the two unknown coefficients governing the fracture locus. The MC criterion can be transformed from the principal stress space into the $(\bar{\sigma},\ \eta,\ \bar{\theta})$ space. The equivalent stress can be expressed in terms of the stress invariants,

$$\bar{\sigma} = c_2\left[\frac{1+c_1^2}{3}\cos\left(\frac{\bar{\theta}\pi}{6}\right) + c_1\left(\eta + \frac{1}{3}\sin\left(\frac{\bar{\theta}\pi}{6}\right)\right)\right]^{-1}, \tag{5}$$

where η and $\bar{\theta}$ are the triaxiality and Lode angle parameter, respectively, defined by

Table 2
Elastic-plastic parameters of the current collector foils [12,13,19,24] and the steel shell casing of 18650 cell [18,29].

Components		Current collector		Shell casing
		Aluminum (cathode)	Copper (anode)	Mild steel
Thickness (μm)		15–25	10–15	260
Elastic modulus (GPa)		70	110	160
Poisson's ratio (−)		0.33	0.34	0.3
Yield stress σ_0 (MPa)		150	150	500
Ultimate tensile stress (MPa)		165	220	525
Strain hardening (Voce law)	Q (MPa)	143	87.2	195
	β (−)	48	344	360
Lankford-r value (−)	0°	0.2	/	0.77
	45°	1.5	/	0.62
	90°	1.1	/	0.66
Failure strains (−)	Tension	0.023–0.034	0.018–0.020	1.022
	Shear	/	/	1.030
	Biaxial tension	0.052	0.116	1.025
	Plane-strain	0.025	0.082	1.020

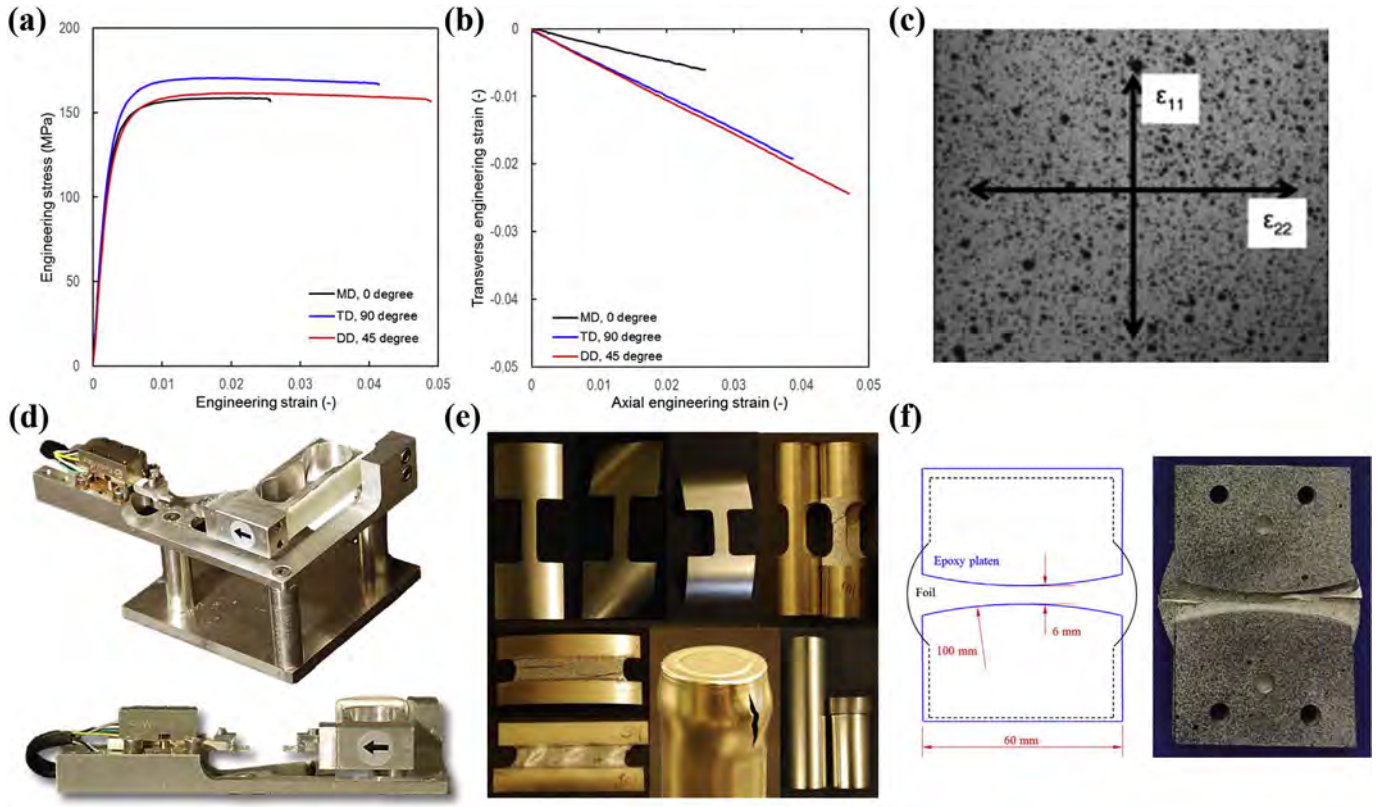

Fig. 3. Test results and setups of metal components [12,18,19]. (a) Engineering stress vs. strain curves in three directions (MD, TD and DD) of the aluminum foil used as the current collector of cathode, (b) transverse plastic strain vs. axial plastic strain of tensile tests of the aluminum foil, (c) illustration of transverse strain and axial strain on a speckled dog-bone sample, (d) loading device of micro tests, (e) designs of specimen in the study of the mechanical behavior of shell casing of 18650 cylindrical cell, and (f) plane-strain specimen of battery components.

$$\eta = -\frac{p}{q}, \tag{6}$$

$$\bar{\theta} = 1 - \frac{2}{\pi}\arccos\left(\frac{r}{q}\right)^3, \tag{7}$$

where p, q, and r are the three invariants of the stress tensor,

$$p = -\frac{1}{3}(\sigma_{11} + \sigma_{22} + \sigma_{33}), \tag{8}$$

$$q = \bar{\sigma} = \sqrt{\frac{1}{2}[(\sigma_{11} - \sigma_{22})^2 + (\sigma_{22} - \sigma_{33})^2 + (\sigma_{33} - \sigma_{11})^2]}, \tag{9}$$

$$r = \left[\frac{1}{2}(2\sigma_{11} - \sigma_{22} - \sigma_{33})(2\sigma_{22} - \sigma_{33} - \sigma_{11})(2\sigma_{33} - \sigma_{11} - \sigma_{22})\right]^{1/3}. \tag{10}$$

With a hardening curve $\bar{\sigma}(\bar{\varepsilon}_p)$, for example the power law $\bar{\sigma} = a(\bar{\varepsilon}_p)^n$, the failure plastic strain can be obtained,

$$\bar{\varepsilon}_p^{failure} = \left\{\frac{a}{c_2}\left[\frac{1 + c_1^2}{3}\cos\left(\frac{\bar{\theta}\pi}{6}\right) + c_1\left(\eta + \frac{1}{3}\sin\left(\frac{\bar{\theta}\pi}{6}\right)\right)\right]\right\}^{-1/n}, \tag{11}$$

where a and n are the two coefficients coming from the fitting of the power law. Using the values listed in Table 2, this MC model can be conveniently calibrated. A detailed calibration procedure for battery modeling can be found in Ref. [24]. In a simplified way, the two fracture constants can be determined from DIC strain measurements in the plane-strain and axi-symmetric punch tests [25]. This calibration technique has been developed by the present investigating team and reported in several earlier publications [21–23].

2.1.4. Strain rate dependence

The strain rate sensitivity of aluminum and copper has been investigated in a number of publications. High strain rate test on thin current collector foils was conducted by Bonatti and Mohr [12], Luo et al. [26], and Jiang et al. [27]. The strength of the two foils becomes significantly larger as the strain rate (or loading speed in the tests) increases. This trend of rate-dependence can be described by the Cowper-Symonds function [28] or by the well-known Johnson-Cook model [29],

$$\bar{\sigma}_Y(\bar{\varepsilon}_p) = [\sigma_0 + a(\bar{\varepsilon}_p)^n][1 + C\ln(\dot{\bar{\varepsilon}}_p/\dot{\bar{\varepsilon}}_p^{\text{ref}})], \tag{12}$$

where σ_0 is the quasi-static yield stress, $\dot{\bar{\varepsilon}}_p^{\text{ref}}$ is the reference strain rate, and C is the coefficient for strain rate dependence to be found from dynamic tests.

The tensile failure strain of the two current collector foils was also found to be rate-dependent, though the trend is a non-monotonic function of the strain rate [26]. Dynamic test data on thin foils is still very scant in open literature to draw a conclusion about the rate-dependence.

2.2. Shell casing and pouch

Besides the current collectors, the shell casing (or pouch for pouch cells) is another metal component in battery cells. Two common material choices are mild steel and aluminum. Their basic mechanical properties could be found in engineering handbooks, but the deep-drawing process of cylindrical shell leaves a non-uniform thickness. Zhang and Wierzbicki [18] carried out a comprehensive experimental/numerical study on the shell casing of a 18650 battery cell. A series of tests were specially designed for the cylindrical geometry of the cell, including uniaxial tension, shear, in-plane tension, central hole tension, axisymmetric punch, hydraulic bulge, and axial compression (see Fig. 3d). The Hill48 plasticity model and MC fracture criterion were calibrated according to the test results. The mechanical parameters of

18650 casing material are listed in Table 2.

2.3. Coating materials

The most essential component of LIBs is the active coating materials from the electrochemical point of view. The chemistry of the coating is different from one manufacturer to another and also is continuously changing to increase battery energy and power. In the current battery market, the most common material for anode is graphite, and for cathode, there are $LiCoO_2$ (LCO), $LiMn_2O_4$ (LMO), $LiNiMnCoO_2$ (NMC), $LiFePO_4$ (LFP), etc. The powders of the granular coating are held together by a binder which also serves to attach the coatings onto the current collectors. Therefore, the coating material of a practical electrode is very complicated and its overall mechanical behavior is a combined result of all the sub-components of the coating layer.

There have been a large number of studies at the nanoscale particle-level to investigate the coupled electrochemical-mechanical problems during charging-discharging processes. Zhao and co-workers [31–39] carried out a series of studies on the elasticity, plasticity, fracture, and debonding in electrodes at this scale and several models were proposed based on the behavior of a single particle. Leo and co-workers [40,41] investigated the plastic deformation mechanism of the amorphous silicon anodes and its effect on the electrochemical performance. However, at micro-scale and meso-scale, testing and modeling work about pure coating materials is absent, and the mechanism and constitutive law of the deformation remain unclear. At these two scales, the coatings can be visualized as a granular material like sands and concrete, from a structural point of view. One can easily understand this analogy by checking the cross-section of the electrodes shown in Fig. 2b and c as well as the manufacturing process of electrodes [42,43]. This can be further confirmed by Focused ion beam (FIB) SEM images [44] and the test results of nanoindentation [45], nano-scratch [46], and pealing [47,48] of the coating materials.

The history of mechanical modeling of granular materials can be traced back to the early and mid 19th century when the two classical models, Mohr-Coulomb [49] and Drucker-Prager [50], were developed. They have similar yield function, but Drucker-Prager is more convenient in computational applications because of the continuity in the yield surface [50–52]. The yield function of the Drucker-Prager plasticity model is

$$f = \overline{\sigma} - \mu p - c, \tag{13}$$

where μ is the friction coefficient and c is the cohesion of the material. The former controls the shape of the yield surface ($\mu = \tan\phi$, where ϕ is the friction angle) while the latter determines the magnitude (strength), as illustrated in Fig. 4. The most significant characteristic of the coating materials is the pressure-dependence – the strength of the material depends on the stress state. Fig. 4 shows five typical loading conditions in space of the Mises equivalent stress q vs. pressure p, i.e. uniaxial tension, shear, hemispherical punch, uniaxial compression, and plane-strain compression. Clearly, the difference among the Mises equivalent stresses for these five conditions measured at the same yield surface (also the same plastic strain) can reach more than several orders of magnitude. This prediction of the model is in very good agreement with the test results of tension and compression of coatings [13,53].

2.4. Separators

The separator is the most important inactive component in LIBs. It is either stacked between or wound together with the electrodes to form a jellyroll. In the current market, separators come in a variety of types and can be divided into molded, woven, nonwoven, microporous, bonded, papers, and laminates, in terms of the physical condition; dry-processed and wet-processed, in terms of the manufacturing process; PP, PE, PVC, PVdF, PTFE, etc., in terms of the chemical compositions [54–56]. Among all of these types, the most commonly-used ones are dry-processed PP and PE, tri-layer PP/PE/PP, ceramic coated PE, and nonwoven. Due to the distinctions in physical and chemical characteristics, the mechanical properties of these separators are significantly different. The basic mechanical properties of the four separators studied by Zhang and co-workers [30,57,58] are listed in Table 3 as typical examples.

2.4.1. Orthotropy of separator

During the manufacturing of dry-processed microporous polymeric separators, the original material is pre-stretched to obtain the microstructure with the desired thickness, porosity and pore size [59–61]. This process causes the crazing of polymers, which turns the crystal part of the material into amorphous. Eventually, the dry-processed polymeric separator is in a semi-crystal condition – lamellae, the crystal part, lie in the Machine Direction (MD), and fibrils, the amorphous part, lie in the Transverse Direction (TD). The degree of crystallinity could be evaluated by X-ray diffraction (XRD) [30,60]. Fig. 5a and b shows the microstructure of a dry-processed PP separator, which indicates a clear orthotropy of the material. Therefore, when the material is stretched in MD, the dominant deformation mode is the crazing of the lamellas, but when it is stretched in TD, the main deformation becomes the thinning of the lamellas. Controlled by the characteristic microstructure, the ultimate tensile stresses and elongations in the three directions (MD, TD and DD) are greatly different, as listed in Table 3. The engineering

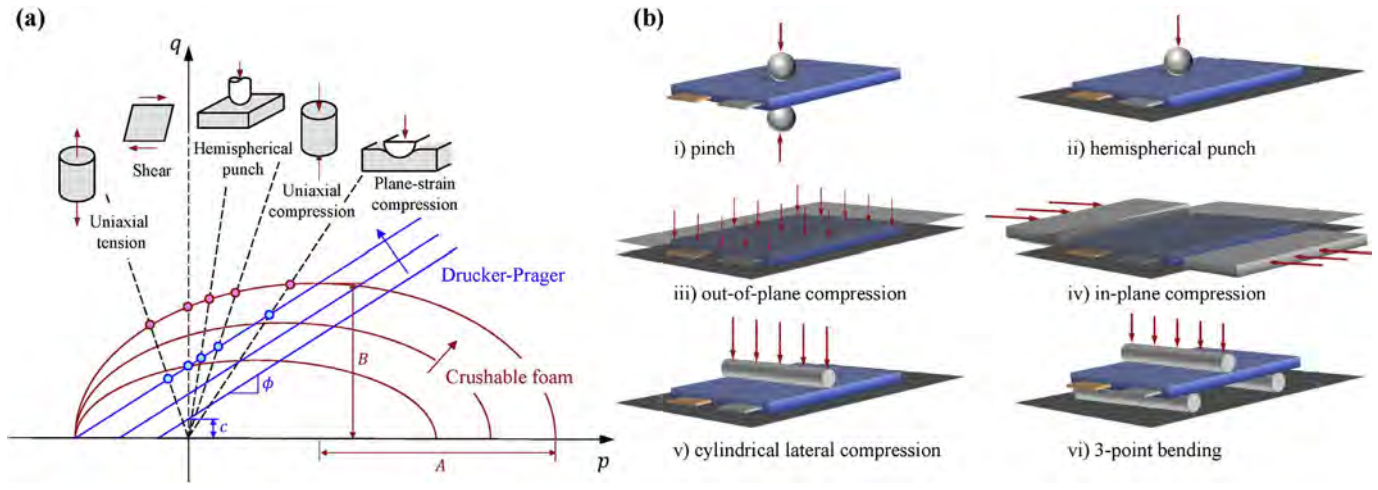

Fig. 4. (a) Stress states of different loading conditions and yield surfaces of Drucker-Prager model and crushable foam model, (b) various loading conditions for the mechanical abuse test of pouch cells: (i) pinch, (ii) hemispherical punch, (iii) lateral compression, (iv) in-plane compression, (v) cylindrical punch, (vi) 3-point bending.

Table 3
Mechanical properties of four commonly used separators [29,55,56].

Components		Separators			
		PP	PP/PE/PP	Al/PE/Al	Nonwoven
Process		Dry	Dry	Wet	Wet
Thickness (μm)		25	25	16 (2/12/2)	31
Porosity (−)		36%–46%	39%	37%	46%
Average pore size (μm)		0.01–0.1	0.05–0.21	0.1	0.2
Ultimate tensile stress (MPa)	MD	130	190	160	30
	TD	10	12	150	32
	DD	18	20	170	15
Tensile elongation (%)	MD	80	70	115	11
	TD	60	> 160	70	11
	DD	110	> 160	110	9

stress-strain curves of the three directions are plotted in Fig. 5d.

The market share of wet-processed separators is reported to be growing over the years and is predicted to exceed that of dry-processed in the next few years [62]. According to the test results, such wet-processed separators have much lower orthotropy than the dry-processed ones. This is also determined by its microstructure (see Fig. 5c). The ultimate tensile stresses and elongations of the two wet-processed separators studied by Zhang et al. [57] (ceramic-coated PE and nonwoven) are listed in Table 3, almost having the same values for different directions.

2.4.2. *Elasto-viscoplasticity and temperature-dependence*

In continuum mechanics, the mechanical behavior of such polymeric separators is categorized into the field of elasto-viscoplasticity, which combines of nonlinear elasticity-plasticity and strain rate dependence. The former characteristic can be clearly observed from the stress-strain curves in Fig. 5d. According to the nanoindentation tests of eight different types of separators carried out by Halalay et al. [63], the elastic modulus of existing polymeric separators varies from 50 MPa to 1 GPa. The response largely depends on the molecular weight of the polymer as well as whether the base material is coated with ceramics or not. The inelastic behavior of separators is highly nonlinear because of the presence of crazing of lamellae, which was nicely demonstrated by a series of tensile tests stopped at different strains carried out by Zhang [30]. Moreover, the strength of such semi-crystal polymers turns out to be strain rate dependent (see Fig. 5e). As the strain rate increases, the material strength becomes larger while the elongation becomes smaller. It was also reported that such rate-dependent property can lead to capacity fade of LIBs [64]. In addition, there is a clear temperature dependence on the mechanical property of semi-crystal polymers, as shown in Fig. 5f. Zhang's results show that the material becomes significantly softer when the temperature increases [30]. Investigating this property is of great importance from the point of safety in the thermal runaway scenarios.

Despite the great number of studies attempting to model the separators, the mechanical characterization work is still not fully settled. On the experimental side, the Dynamic Mechanical Analysis (DMA) [30,60] and the X-ray Diffraction (XRD) methods [60,61,65] are the two most effective techniques to investigate the strain-rate/temperature dependence and the microstructure of energy materials, respectively. However, in-situ evidence of the deformation mechanism of separators is still scant. On the modeling side, there have been many attempts to model such materials using molecular dynamics simulation and micromechanics theories [66–71], but those models could hardly be applied to large-scale industrial problems due to computational limitations. Under the framework of continuum mechanics, modeling the separators is even more challenging because: 1) the characteristic length of the materials (e.g. pore size and fiber length) is at nanoscale,

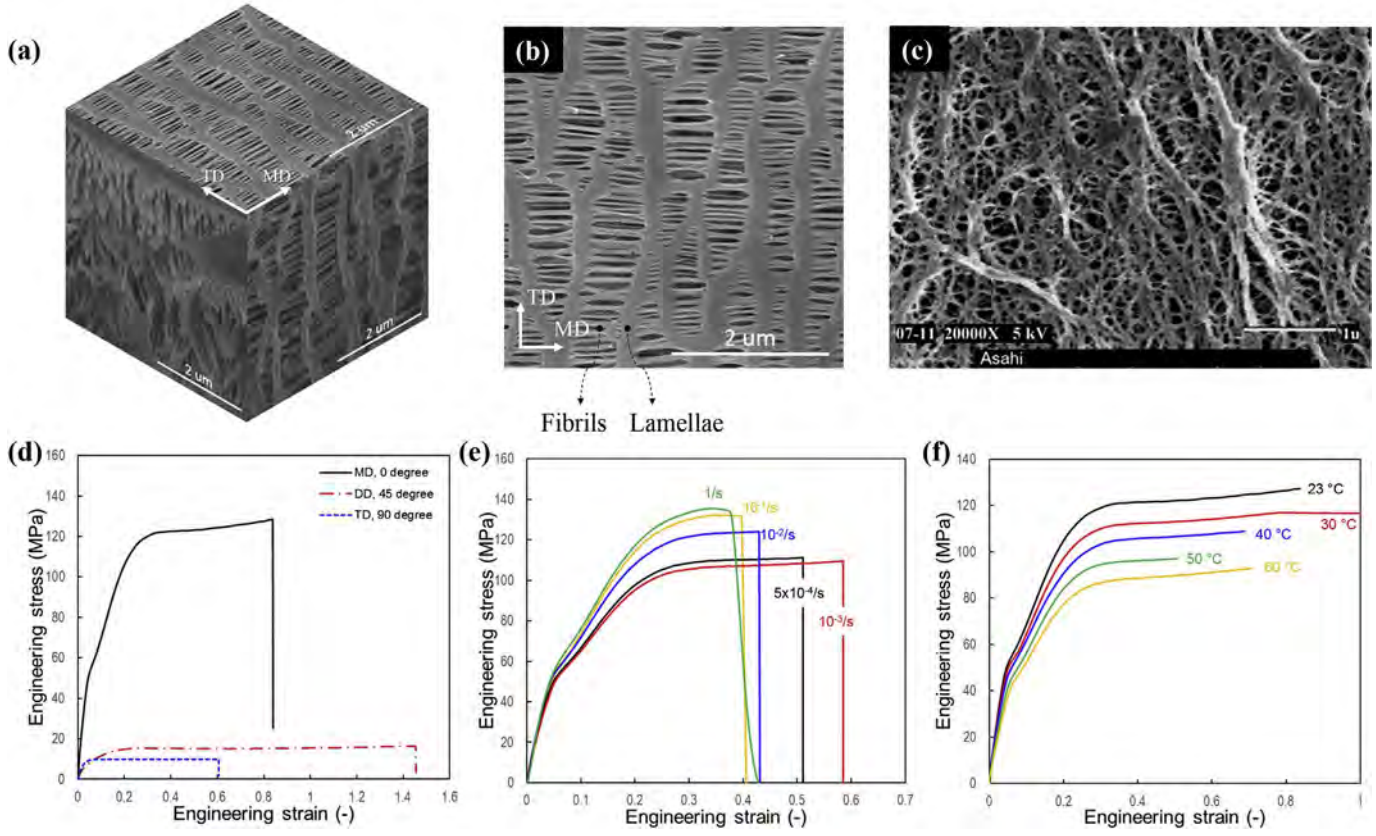

Fig. 5. Microstructure and mechanical behavior of separators (a) 3D view and (b) 2D top view of the microstructure of a dry-processed PP separator, (c) microstructure of a wet-processed separator in a more isotropic condition [54], and tensile stress-strain curves (d) in three directions (MD, DD and TD), (e) in MD under five different strain rates, (f) in MD under five different temperatures.

2) the material behavior is a combination of orthotropy, visco-plasticity and temperature dependence, and 3) the model have to cover both the microscopic physics and the macroscopic behavior. Existing constitutive models of polymeric materials are well established [72–75], but their suitability to model separators still remains to be validated. Moreover, to utilize those models, new user material subroutines (UMAT) must be developed because they are usually not available in commercial FE software, and a sophisticated calibration procedure has to be designed for the parameters of the models.

2.5. Adhesion strength between coating and current collector

During the long service life of LIBs, there are thousands of cyclic volume changes caused by the charge-discharge process. For graphite anodes, the volume change is about 10% [76], but for high capacity anode materials such as silicon and tin, it can reach as high as 300% [77–80]. A stress field will be generated by the volume change, leading to fade in cell capacity [79]. As a result, one common phenomenon is the delamination of coating and current collector [80,81], which could cause a fatal harm to batteries. Measuring the adhesion strength between the coating and the metal foil has been one of the necessary procedures in the manufacturing of battery cells. The peel test is the most frequently used experimental technique [82–85], in which the coating layer and the metal foil are clamped by two grips and tensile loading is applied to tear the sample. However, only the strength in 90° and 180° can be obtained in this peel test. For more orientations, one has to attach the electrode sample onto rigid substrates and apply combined tension/shear loads [48,86]. Alternatively, one can carry out the nano-scratch test on the electrodes, which utilizes a nanoscale probe to scratch the surface of the electrode through an inclined path into the thickness and measures the corresponding friction force. The advantage of the scratch test is that the depth for investigating is adjustable, thus making the measurement of different cross-sections possible.

The adhesion strength between coating and current collector is greatly dependent on the type and volume fraction of binders as well as the environmental parameters during the mixing and drying procedures [47]. According to the data reported by existing publications, the adhesion strength between coating and foil is in the range of several MPa [47,85,86]. This value is of the same order of magnitude as the strength of coatings, especially the graphite of the anode. Therefore, the fracture of anode is usually accompanied by the delamination phenomenon.

2.6. Electrode/separator assembly

The sequence of failure of coated electrode is a subject of current research of the present authors [19,25]. Plane-strain tension tests were carried out on copper foil, aluminum foil, separator, and an assembly of copper/separator/aluminum. Fig. 3f shows the specifications of the specimen. Two rigid epoxy platens are glued to the specimen to provide for large gripping area and to form a butterfly-shape gauge section. The fracture strain under plane-strain condition was determined to be 0.025 for aluminum foil, 0.082 for copper foil, and 0.151 for separator. In the plane-strain tension test of the assembly of copper/separator/aluminum, it appears that the fracture was triggered in the aluminum foil, which has the lowest fracture strain, and copper and separator failed soon after. The force level is continuously diminishing as the crack propagates from the initiation point to the boundary. Thus, the fracture strain of the assembly is 0.025.

2.7. Partial conclusions

Tests on cell components are by far the most demanding and difficult in the area of mechanical deformation and loading of LIBs. The main difficulty is the small size of all components of the stack of electrodes in the thickness direction. The internal structure of the separator and coating adds to the complexity of the problem and requires using experimental techniques of nano-technology. On the modeling side, it is necessary to include the effect of pressure, anisotropy, strain rate, and friction. The underlying constitutive models that accounts for all the above effects exist in the literature. The challenge is to derive practical calibration methods to determine free parameters entering these models. This can be done by direct measurements or by the inverse method that combines test results with Finite Element simulation of miniature test samples. The inverse method is the main tool employed in developing computational model at the cell level and will be extensively covered in Part II of this article.

Currently, little use is made of the growing understanding of the strength characteristics of cell components to improve safety of batteries subjected to mechanical loadings. While the choice of the main geometrical parameters and thickness of specific materials are made based on electro-chemical parameters, other parameters such as the amount and properties of binders, strength and friction of the interface between various layers can be adjusted to enhance safety. The main obstacle, as seen by the present investigating team, is lack of guidelines, if the cell should be made stiffer and stronger to reduce the amount of penetration or weaker and more compliant to delay or eliminate internal failure leading to electric short circuit and possible thermal runaway. This is a subject that must be resolved at the cell level by modeling the layered structure.

Finite Element simulation is a powerful tool that can be used to improve safety of batteries. Such tools would accelerate the design of optimum batteries and save months and years of the present trial-and-error approach. The main obstacle, for which no one should be blamed, is a limited power of the present generation of computers. Aluminum foil is the thinnest component of the electrode/separator assembly (10 μm) and this dictates the element size in the FE modeling. It might be 50,000 elements in the model of a micro-specimen cut from the foil and up to half a million elements in the model of a single repeatable electrode/separator assembly. Such a resolution will lead to 100 million elements in the cell module, which is too much to handle by a typical cluster of desktop workstations. A need of developing a homogenized material model of the electrode stack or jelly roll at the cell level is evident. This is the subject of Part II of this review article.

3. Part II. Macro-scale or cell level

At the macro-scale, the battery is a complex assembly, consisting of current collectors, active coating materials, separators, and shell casing, the mechanical properties of which have been described in Section 2. The mechanical behavior of a battery cell is not simply the sum total of the contributions of each component. Instead, it is greatly influenced by the interactions between them. On the experimental side, the cells should be tested under different loading conditions, which are known as mechanical abuse tests. Through these tests, information on the deformation mechanisms and structural responses is obtained for the establishment of deformation models and calibration procedures. On the modeling side, there are several different strategies: 1) detailed models, 2) Representative Volume Elements (RVE) approach, and 3) development of homogenized models. Detailed models include the most information about a real battery cell, but, as mentioned earlier, are computationally intensive. The homogenized models are most computationally efficient, and the RVEs approach is somewhere between these two strategies. In this section, a summary about the existing experimental results of the mechanical abuse tests is presented, and the three modeling strategies are reviewed.

3.1. Experimental results: mechanical behavior of cells subjected to various loading conditions

Currently, there is no existing standard or regulation about battery abuse tests that is accepted worldwide [87–91]. Besides, almost no recommendation specifies precisely loading and boundary conditions

[92]. Fig. 4b shows the six loading conditions for pouch cells reported in the open literature. i) Pinch test [93–97] applies concentrated coaxial loads onto the top and bottom surfaces of the cell by two rigid spheres. The radius of the rigid spheres can be several millimeters or several inches for different thickness of battery cells. ii) Hemispherical punch [13,14,26,53,98–102] is similar to the pinch test, but is easier to be carried out on universal testing machines. The difference is that the battery cell is placed on a rigid plate, instead of being subjected to two symmetric loadings on the two surfaces. iii) Out-of-plane compression [24,100,101,103–106] applies two uniform pressures onto the top and bottom surfaces, and the lateral surfaces are load free. The stress state of the cell is uniaxial compression. iv) In-plane compression test [99,105,107–115] applies two displacement boundary conditions onto the two sides of the battery cell. Depending on the design, the top and bottom surfaces are fully constrained by two rigid walls [110], or are subjected to a constant uniformly-distributed pressure [109,110]. v) Local lateral compression by a long cylinder [25], because of the large width/thickness ratio of the cells, prevails plane-strain condition in the central region. vi) 3-point bending test [24,99,100,106,112] places the cell onto two rigid supporters and applies punch loading at the center, thus creating a bending moment in the cell.

Among all these loading conditions, the out-of-plane compression (iii) and the in-plane compression (iv) are “material tests”, from which the compressive hardening curve $\overline{\sigma}_Y(\overline{\varepsilon}_p)$ can be calculated. The other four tests are “structural tests”, which have more complex stress states (see Fig. 4b). Still, they can be used to identify some material parameters (elastic modulus and hardening curve) when combined with a hybrid experimental/numerical method [116]. In the inverse method, numerical simulation of the test is conducted and the results of calculations are matched to the experimental data. An optimization procedure is then carried out to find the material parameters by minimizing the difference between simulation result and experimental data.

This section describes only the test methodology and some basic trends emerging from the experimental results. This is followed by computational modeling where a calibration procedure is explained with several examples.

3.1.1. Static tests of fully-discharged batteries

A number of studies have been carried out on the static tests of fully-discharged batteries over the past five years. All of the involved tests could be categorized into the six loading conditions shown in Fig. 4b. A majority of these studies have dealt with deformation (or crash) properties of cells, which is a relatively easy task. In the present article, only those experiments are described, which contribute to the development of criteria to predict the electric short circuit of cell subjected to indentation loadings. It is found that the onset of short circuit coincides with the drop of resistance force measured at the rigid indenters for most of the cases [24,100]. This is because the force drops when the separator is fractured, which immediately leads to short circuit of the cell [58]. The critical displacement δ_f of the rigid indenter to short circuit is collected from the test data of open literature. To eliminate the difference among batteries in geometry, it is proposed to introduce the normalized critical displacement ε_f (NCD), or average failure strain

$$\varepsilon_f = \delta_f / l_c, \tag{14}$$

where δ_f is the displacement of the indenter to failure, and l_c is the characteristic length in the loading direction (cell thickness for pinch, hemispherical punch, lateral compression, cylindrical punch, and 3-point bending; length or width for in-plane compression). The values of NCD are listed in Table 4. It should be noted that these values are usually dependent on the geometry of the rigid indenters. In this table, only the average values of each loading condition reported in literature are listed. One clear conclusion is that short circuit happens at different displacements under different loading conditions for the same battery cell.

Currently, the most studied battery cell and loading condition are the 18650 cylindrical cell under indentation of a hemispherical punch. For other batteries, especially the pouch cells for EV applications, there is still insufficient test data to draw general conclusions. From the existing data, it can be clearly seen that short circuit happens at a NCD of 0.20–0.70 for most of the batteries under all six loading conditions. In fact, this value of NCD could be used as a general indicator for commercial LIBs, and can also be implemented into Finite Element models as an artificial failure strain. It should be noted that the NCD value for the in-plane compression of cylindrical battery cells is usually smaller than that of others, because local buckling often happens in this situation [107]. Meanwhile, 3-point bending usually has higher tolerance for short circuit because the layers can slide on one another, resulting in less bending strain.

In some recent studies, a very interesting phenomenon about the failure of pouch cells was reported – when a pouch cell is subjected to lateral compression, strain localization happens and the cell fractures through a fault line that is inclined at a certain angle to the battery plane (see Fig. 6a–d). The angle is reported to be 45° for the battery cell in Ref. [93] and 62° for the battery cell in Ref. [25]. The underlying mechanism of this phenomenon is still not fully understood. It might come from the behavior of the granular active materials, or could be due to the multi-layered structure.

3.1.2. Dynamic tests and rate-dependence

In practical vehicle crash accidents, the deformation of materials is a dynamic process, the global strain rate of which can reach as high as 500 s^{-1} [117]. Studying the strain rate dependence of the mechanical properties of battery cells, therefore, is necessary. According to the data in existing publications [118–120], the strength of the battery cells increases under high loading speeds (high strain rate) compared with quasi-static situations. On one hand, most component materials of the battery cells have positive strain rate dependence, including steel, copper, separator, and coating, which was discussed in Section 2. On the other hand, there is the effect of electrolyte. Under dynamic

Table 4
Normalized critical displacement to short circuit of fully-discharged batteries under various static mechanical abuse loadings.

Form factor	Cell size[a]	Normalized critical displacement to short circuit (−)					
		Pinch	Hemispherical punch	Lateral compression	In-plane compression	Cylindrical punch	3-point bending
Pouch	59.5 × 34 × 5.35	/[b]	0.65 [96]	/	0.34 [108]	/	/
	129.5 × 43.5 × 8.2	/	0.61 [96]	/	/	/	/
	227 × 160 × 7.25	/	0.55 [96]	/	/	/	/
	232 × 153 × 7.5	/	0.40–0.47 [19]	/	/	0.27 [19]	/
Cylindrical	∅18 × 65	/	0.42 [98]	0.28 [111]	0.05 [106,111]	0.33 [98,111]	0.42 [98]
	∅60 × 203	/	/	0.40 [104]	/	0.33 [104]	0.75–0.92 [104]
Prismatic	43 × 34 × 4.3	0.47 [93]	/	/	/	/	/
Elliptical	∅18 × 65	/	0.23 [29]	0.39 [13]	/	/	/

[a] Length × Width × Thickness for pouch cells and prismatic cells, Diameter × Length for cylindrical cells and elliptical cells.
[b] / – Data not available.

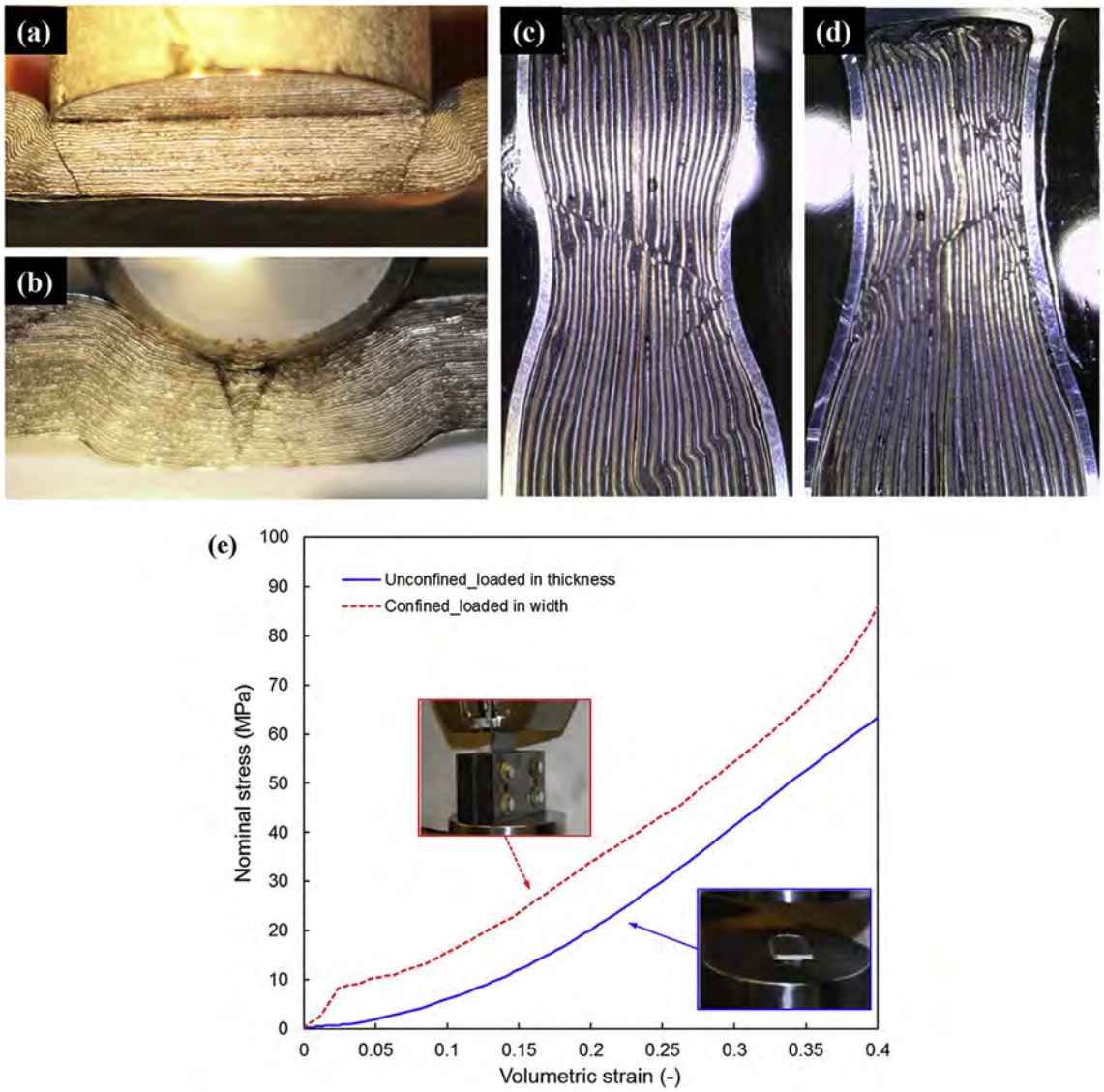

Fig. 6. Cross-sections of fractured pouch cells: (a) flat punch [25], (b) hemispherical punch [25], (c) pinch with 2″ punch head [93], (d) pinch with 3″ punch head [93]; and (e) stress-strain curve for confined compression in the width direction compared to unconfined compression.

loading, the viscous shear stress caused by the flow of electrolyte inside the battery is much larger, thus leading to larger energy dissipation.

The dynamic test results of two pouch cells and one elliptical cell reported by Kisters et al. [120] showed a very interesting rate-dependence on fracture behavior – mechanical failure of battery cell occurs at lower peak force and lower displacement as the loading speed increases. This phenomenon is very important for electric vehicle safety because it suggests that the deformation tolerance becomes lower under high-speed impact loading. The mechanisms for this counterintuitive phenomenon still remain unclear to the community, and more fundamental investigations are required to clarify and model it.

3.1.3. Effect of electrolyte and structure-fluid interaction

In a battery cell, all the components are immersed in the electrolyte. This special environment has a significant influence on the mechanical behavior of the microporous separators [71,121–123]. The difference between dry and wet separators comes from two mechanisms. The first one is the penetration of electrolyte molecules into the amorphous nanofibers of the separator. Molecular dynamics simulations [71] have shown that dimethyl carbonate (DMC) can increase the elastic modulus of amorphous PP but has no effect on that of the crystalline phase. The other mechanism is the structure-fluid interaction. When the separator is subjected to compressive loading, the volumetric deformation drives the electrolyte to flow through the micro-pores of the separator. This flow in turns provides an additional resistance force to the overall response of the material [122,123]. This structure-fluid interaction problem can be descried either with smooth particle hydrodynamics [51] or under the framework of poromechanics [123]. To the best knowledge of the authors, no investigation was reported into the similar environmental-dependence of other components.

The effect of the structure-fluid interaction exists not only at the component level, but also at the cell level. Under low speeds, this effect is not visible because the shear stress of a fluid is proportional to the velocity of the fluid. However, under high-speed dynamic loading, the difference between wet and dry cells is significant [120]. This is one of the possible mechanisms of the rate-dependence [124], discussed in Section 3.1.2.

3.1.4. State-of-charge dependence

To avoid the risk of severe thermal runaway at high state-of-charge (SOC) during mechanical abused test, most of the researches at the cell level are limited to a low SOC (close to zero), despite the fact that the in-service LIBs in electrical vehicles generally operate at a higher SOC when crash accidents happen. Thus, it is of great importance to

investigate the effect of SOC on mechanical integrity and onset of internal short circuit. Xu et al. [106,118] and Tsutsui et al. [119] have reported a significant SOC-dependence of mechanical integrity of 18650 cylindrical battery cell under compression and bending. The structural stiffness of 18650 cell increases and the displacement to short circuit decreases at higher SOC. In addition, soft or incomplete short circuit, which is reversible, was observed before the final complete short circuit [119]. However, for pouch cells, it was reported that there is almost no SOC-dependence of mechanical response under hemispherical punch loading [125]. At the current stage, with limited number of existing studies on the experimental side, it is hard to draw a general conclusion about the SOC-dependence of the mechanical behavior of LIBs. The answer largely depends on the compositions and properties of the active materials as well as the form factor of the cell.

There are two possible mechanisms through which the SOC of cell might have influence on its mechanical properties. The first one is the change of mechanical properties of active material particles during the charging process. According to existing publications, the elastic modulus of the graphite particles of anode increases during the lithiation process [76], while that of the NMC particles of cathode decreases due to de-lithiation [126]. Therefore, the overall tendency of the SOC-dependence cannot be explained simply by studying only one of the electrodes. The other mechanism is the volume change caused by the change of chemical compositions during the charging-discharging process [127–131]. At the cell level, this volume change can induce a local strain field into the active material particles, causing an internal stress field because the lithium-ion batteries usually operate under constrained boundary condition. This internal stress field could not only influence the mechanical behavior, but also cause the fade of LIB capacity [132].

3.2. Cell-level models

3.2.1. Detailed models

There is a bulk of experimental data on the material properties and constitutive models of the battery components, which makes it possible to develop Finite Element models covering all the detailed properties of the cell including all the components. Several detailed models have been established for 18650 cylindrical cell [100,107] and pouch cells [53]. These models are very useful to investigate the deformation sequence of the cell structure and the cause of internal short circuit [107]. However, the success of detailed models depends on computational resource and time. Usually, there are more than 100,000 elements in such a model, and even more to predict the local fracture behavior. For this reason, detailed models cannot be applied to large-scale simulations of modules, battery packs, and vehicle crash. Another challenge is to define proper contact conditions between different layers. So far, no study is carried out to investigate the real mechanical environment of the components, including but not limited to contact pressure, friction, and adhesion.

3.2.2. RVEs

Representative Volume Element (RVE) is defined as the smallest volume over which a measurement can be made that will yield a value representative of the entire cell [133]. The RVE for the jellyroll of battery cell is shown in Fig. 2a. It consists of two active material layers, two graphite layers, two separator layers, one copper foil, and one aluminum foil. Based on this fundamental structure, Sahraei et al. [13,19], Lai et al. [110,113,134], and Zhang et al. [53,135] developed RVE models for pouch cells and 18650 cylindrical cells, and the models are used for two functions. The first function is to investigate the deformation mechanism of the cell. There is a significantly smaller number of elements in RVE than a detailed model, thus reducing computational cost. However, its application is limited by the periodic boundary conditions and small strain gradients. For more complicated loadings like 3-point bending and cylindrical punch, the stress field is multi-axial and inhomogeneous, so it is very difficult to define accurate boundary conditions for the RVE. With improper boundary conditions, the RVE might display size effect on its mechanical behavior, which means that the volume can no longer represent the whole structure. Saharei et al. [13] is the earliest studies to discuss the effect of different boundary conditions on RVE by varying the ratio of tension and compression in the two directions. The second function of the RVE model is to obtain basic mechanical properties of the battery cell, such as the stress-strain curve [110,134]. It is useful to characterize the difference of mechanical behavior between tension and compression by different studies [53], but one should also be very careful about the contact definitions, which, similar to detailed models, includes the adhesion strength, friction, and contact pressure.

3.2.3. Homogenized models

Homogenized model, which for sure is the most computationally efficient among the three computational modeling strategies, treats the stack of electrodes or the jelly roll in a battery as a homogenized material. Thus, the task of the battery modeling is simplified to choosing a proper constitutive model and calibrate the unknown coefficients. Compared with other materials or structures, the commercial lithium-ion batteries exhibit four special mechanical properties:

1) Pressure dependence. The mechanical responses of tension and compression are greatly different [13,14,53,101,103,135].
2) Densification. When the cell is subjected to compressive loadings, it starts to densify and the hardening rate increases very rapidly [103,108,111].
3) Anisotropy. Due to multi-layered structure, the mechanical behavior of the in-plane direction is different from that of out-of-plane directions [13,24,53,94,97,112].
4) Shear band formation and fracture when subjected to compressive loading (see Fig. 6) [24,25,93,102,107].

Existing publications have come up with several constitutive models attempting to characterize these properties. The three most frequently used models are the crushable foam model, the honeycomb model, and the Gurson model, which will be reviewed next in this section.

3.2.3.1. Crushable foam model. Deshpande and Fleck [136] proposed two isotropic constitutive models for crushable metallic foams, which are based on the same yield function but have different hardening algorithms. Many research teams have applied these models to describe the mechanical behavior of battery cells [18,51,103,110,111,137]. The yield function of the model is elliptical (see Fig. 4a), expressed as

$$f = \sqrt{q^2 + (B/A)^2 p - p_0^{\,2}} - B, \tag{15}$$

where A and B are the sizes of the p-axis and q-axis of the yield ellipse, respectively. Recall that p and q are the pressure and Mises equivalent stress of the stress component, respectively. As shown in Fig. 4a, the crushable foam model is able to characterize the pressure-dependence of the plastic behavior of the material, which is similar to Mohr-Coulomb and Drucker-Prager. The difference among the three models is the shape of their yield function.

The reason for the applicability of the crushable foam model to battery cells is that the physical conditions of the active coating materials is very close to that of metallic foams. Both materials undergo a densification procedure when compressive loads are applied. As discussed in Section 2, certain types of separator are highly anisotropic and the foam material is intrinsically isotropic. In order to capture the anisotropic properties in the relations of a homogenized material, the honeycomb model can be used. Both the crushable foam and honeycomb models are available in the material model library of the general purpose software Abaqus [51] or LS-DYNA [137].

3.2.3.2. Honeycomb model. In the commercial FE software LS-DYNA, there is an option to describe a material as a honeycomb, which is called MAT_026_Honeycomb (or MAT_126_Modified_Honeycomb). In this material keyword, users are allowed to input different compressive hardening curves for each direction of the material, and these curves could be of very large hardening rates. These two important features make the material keyword very useful for modeling the anisotropic properties of battery cells which is due to structure anisotropy [53,135]. In other words, it was assumed that the compressive properties were similar in the MD and TD directions, and only different in the through-thickness direction. Sahraei et al. [14] performed a very comprehensive comparison of the crushable foam (isotropic material) and honeycomb model (anisotropic material) in the case of pouch and cylindrical batteries. It was pointed out that there are advantages and disadvantages of both models. The isotropic model is simpler and requires fewer tests for calibration, yet it gives reasonable results for most loading cases. At the same time, an anisotropic model improves the results for cases where unsatisfactory results were obtained with the isotropic model. Note that the anisotropic model is more complex and involves new material parameters that should be calibrated from additional testing.

3.2.3.3. Gurson model. The Gurson (or GTN) model [138] and its modified versions [139–141] have been widely accepted to characterize the plasticity and ductile fracture of metals. The yield function after the modification by Tvergaard and Needleman [141] is given as

$$f = \frac{q^2}{\overline{\sigma}_Y^2} + 2d_1\Phi\cosh\left(-d_2\frac{3p}{2\overline{\sigma}_Y}\right) - (1 + d_3\Phi^2), \tag{16}$$

where d_{1-3} are three material parameters to be calibrated, and Φ is the void volume fraction (0 for fully dense, 1 for completely void).

The Gurson model was applied to characterize the mechanical behavior of battery cells as well as the coating materials [108,134,142,143], and the simulation results turned out to be satisfactory. Moreover, it is a physics-based model for metals, which describes the nucleation, growth and interaction of voids. Therefore, the numerical simulation can predict crack initiation and propagation. However, its applicability to batteries is still questionable [144]. The Gurson model is developed for porous metals, so its physics meaning is fundamentally different with that of granular powders inside the battery cells, which is dominated by friction and interaction between particles. The upper limit of porosity for the Gurson model is approximately 10% [51,144], but the practical value for LIBs is usually 30%–40%. For these reasons, the failure characterization of battery cells using the Gurson model is not as reliable as it is for metals.

3.2.3.4. Summary on the three homogenized models. Altogether, each of the three models has certain advantages and disadvantages, but none of them can cover all of the four important properties mentioned previously (see Table 5). In particular, no work has been reported on the numerical characterization the formation and growth of shear band, which is shown in Fig. 6. Accurate characterization of the local failure of LIBs remains a formidable challenge for the mechanical/electrochemical community. The Mohr-Coulomb (M-C) model is adopted by Chung et al. [25] to characterize this special failure mode. In addition, the authors proposed a convenient calibration approach for this model, which depends on only one plane-strain test. The success of the M-C model stems from its capability of describing the inner friction of the particles, which is similar to the Drucker-Prager model shown in Fig. 4a. It can be derived from the constitutive relations of the model that the inclination angle of the fault line is $(\pi/4 + \phi/2)$ for granular materials with a friction angle of ϕ [145,146]. For an inclination angle of 62°, the friction angle of the coating materials is 34°.

Compared with Mohr-Coulomb and Drucker-Prager, the crushable foam model lacks the underlying physics of the coating layers, especially the inner friction between particles. Therefore, it is not capable to characterize the strain localization and the formation of shear bands across the thickness of pouch cells under compression, though several researches have adopted such foam models to simulate the tension/compression difference of electrodes and cells [53,100].

3.2.4. Analytical models

The previously described three modeling strategies (detailed model, RVE and homogenized model) rely heavily on computational approach. Each of them requires many input parameters to be obtained from a number of different tests. From the point of view of practical application, it will be highly desirable to develop approximate solutions of the problems that will bypass a need for time-consuming finite element simulations. A number of analytical studies have been carried out for cylindrical cells and pouch cells different loading conditions, including hemispherical punch [25,99,147], uniaxial in-plane compression [99,107,108], 3-point bending [99], and cylindrical punch [25,103]. For some of the cases, the full force-displacement curve can be predicted. For example, the model for pouch cells loaded in the transverse direction by hemispherical punch [99] yields the following load-displacement ($P - \delta$) relation

$$P_{h-p} = \frac{2\pi aR\delta^3}{3H_c^2} + \frac{2}{3}\pi\sigma_0 h_f N\delta, \tag{17}$$

where a is the coefficient of the parabolic fit of the compressive stress-strain curve, R is the punch radius, H_c is the thickness of the cell, δ is the displacement of punch, σ_0 is the average yield stress of aluminum and copper foil, h_f is the average thickness of a foil, and N is the total number of foils.

The power of such analytical solutions is that they could provide rapid estimations of cell resistance to out-of-plane and in-plane types of loading. At the same time, they usually require only one simple experiment for calibration, which is much less than that for numerical simulations. The beam-on-foundation model provides formulas for the local buckling wavelength and buckling load. The classical textbook solution by Timoshenko was applied for the first time by Sahraei et al. [99] to determine the magnitude of the buckling load $\Delta\sigma$ of the plane-strain in-plane compression with full lateral constraint.

$$\Delta\sigma = 2D\frac{m^2\pi^2}{l^2h}, \tag{18}$$

where D is the bending rigidity of a single foil, l and h denote the length and thickness of the pouch cell, and m is the experimentally measured number of waves of the length l. Substituting the actual values of all the parameters, the predicted buckling load was 9.03 GPa, which compares well with the measured buckling load in fully confined in-plane compression test, see Fig. 6e.

Another advantage of closed-form solutions is that they could be more easily embedded into system failure model consisting of modules and complete battery packs.

Table 5
Existing models to accounting for different features of the LIB cells.

Model	Pressure-dependence	Densification	Anisotropy	Shear fracture
Crushable foam	✓	✓		
Honeycomb	[a]	✓	✓	
Gurson	✓	✓		

[a] Depends on the curves input by users.

4. Part III. Macro system scale: battery modules and protective structures

The automotive industry is interested to see how the wealth of information on individual cell could be integrated into computational model of modules and battery packs. The difficulties here come from both experimental and computational sides. On the experimental side, there are many impact scenarios (side or bottom impact) as well as different designs of modules. Therefore, the cost of a comprehensive program on crush tests would be very time-consuming and expensive. There are only a few publications about the abuse tests of battery modules, covering a limited range of shapes and loading conditions. Xia et al. [148] performed drop tower tests on one type of modules consisting large-format pouch batteries. The test program included two different shapes of punch and three loading directions. In addition, modules were tested with 30% and 100% SOC. Measured in the tests were time history of load, displacement, and voltage. The photographs in Fig. 7a–c show a massive damage of modules subjected to cylindrical and wedge-type of punch loading.

It was interesting to see that the modules tolerated twice as much penetration in the in-plane X, Y -directions of cells than in the out-of-plane Z-direction. Only in one case of out-of-plane loading, smoke and fire started soon after the test. This leads to an interesting hypothesis that safety envelope of the module in terms of critical displacement under indentation is much larger than individual cells. This can be explained by additional degrees of freedom for individual cells to undergo rigid-body displacement and rotation without excessive internal damage.

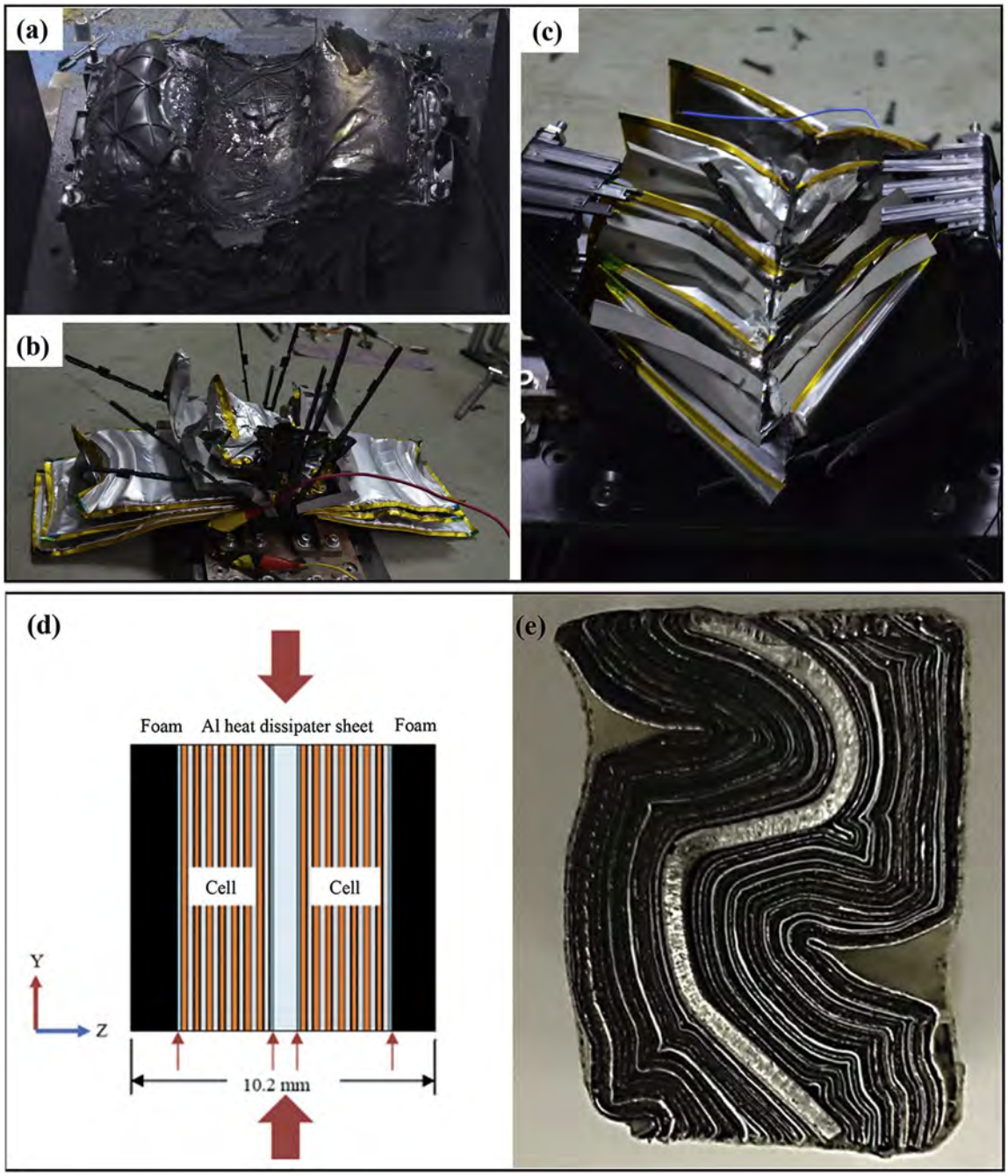

Fig. 7. Abuse tests of battery modules. (a–c) Photographs of the final damage patterns of modules subjected to 10 m/s impact of a rigid indenter in X direction, Y direction, and Z direction. (d & e) Sharp curvature bending pattern of thin aluminum plate heat dissipater sandwiched between two small pouch cells.

In-plane tests of an assembly of two pouch cells with heat dissipater in between was carried out with a series of papers from the Professor Jwo Pan's lab of the University of Michigan [108,110,113,114,134]. Experiments on fully-constrained system with thin aluminum plate heat dissipater sandwiched between two small pouch cells show very interesting deformation pattern, shown in Fig. 7d and e. The wavelength is seen to be of the order of the thickness of the system, and it looks that sharp curvature bending pattern was triggered by buckling of the heat dissipater plate resting on the cell foundation. An alternative mechanism of failure initiation was also proposed by the same team in the case of a single pouch cell without heat sink plate. The cells were fully discharged. Therefore, no conclusion could be drawn on the onset of electric short circuit and possible fire.

Recently, Tsinghua University and MIT joined forces to re-construct the highly publicized Tesla ground impact accident that resulted in a fire (see Fig. 8a) [147]. The damaged area at the bottom of the car was confined to one module, which contains about 400 cylindrical cells. The battery pack was protected by a 6.35 mm thick aluminum alloy armor plate. It was demonstrated through the detailed simulation that at approximately 25 mm penetration, the armor plate fractures exposing unprotected cells to further deformation and thermal-runaway. The computational model included all other components of the module with a complete material input data on each component. This is shown in Fig. 8a.

It appears that in further progress of testing and optimization of battery modules and packs should be performed with direct involvement of automotive companies because the computational models are so much dependent on the design. Some results on the integration of the battery pack into the vehicle body structure during crush events can be found in the following publications [149–154]. For example, the two EU projects, OSTLER (Optimized Storage Integration for the Electric Car) [149] and SmartBatt [150], studied the integration of EV subjected to different impact scenarios, including EuroNCAP pole side, offset deformable barrier, front impact, and rear impact. Out of those two, the report on the OSTLER project is the most comprehensive. It was shown that the floor mounted battery pack in the Toyota Yaris underwent severe intrusion (154 mm) during EuroNCAP pole side impact at 50 km/h (see Fig. 8b). The last figure underscores the importance of undertaking further studies on intrusions and deformations of modules and battery packs in everyday road accidents.

5. Summary and outlook

To summarize, this paper has reviewed the state-of-art techniques, theories and models for safety-focused mechanical characterization of commercial lithium-ion batteries at different scales. At micro-scale and meso-scale, the materials of battery cell components are being extensively investigated, and many useful material constitutive models have been well studied. The most important unsettled issue is the characterization of coating materials, the deformation mechanism of which is still not fully understood. At macro-scale or cell-level, different types of mechanical abuse tests were carried out to investigate the mechanical behavior of battery cells, and many detailed models, RVEs, and homogenized models have been proposed. However, still no homogenized model can characterize the four important mechanical properties at the same time, which includes pressure-dependence, material densification, anisotropy, and shear band failure. At the macro-system scale, there is still a lack of studies for both experimental and numerical investigations. Existing publications are focused on improving the crashworthiness of the protective structures of EVs and reducing the deformation of battery cells. A summary of some directions for the near future are as follows:

Providing in-situ experimental evidences. Currently, the two most useful tools for battery damage examination are cross-sectional cutting-polishing and micro CT scanning, both of which are post-mortem and can only provide the fracture information at the last moment. Recently, the X-ray technique has become mature enough so that in-situ micro CT and in-situ XRD tests are now available for real-time monitoring the deformation of materials during mechanical tests. Compared with post-mortem examinations, such in-situ tests can provide much more

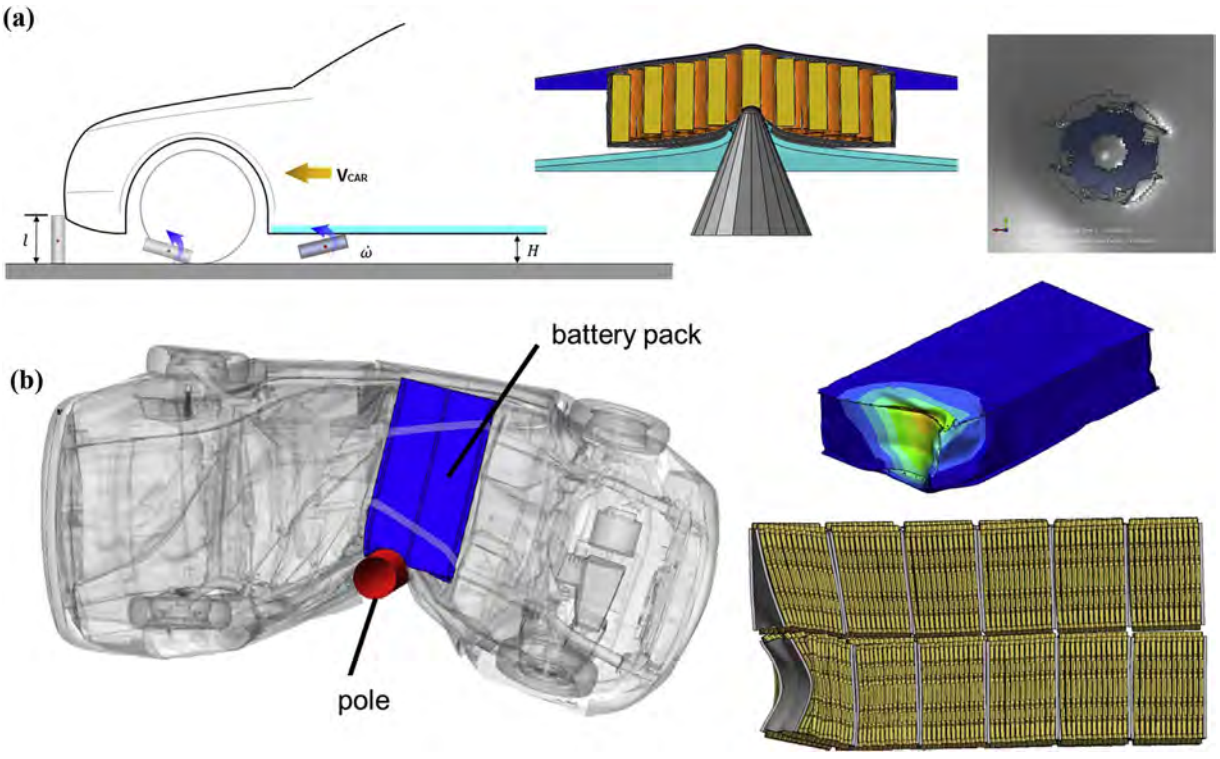

Fig. 8. Two scenarios of EV crash accidents (a) ground impact caused by road debris [147], impact object could intrude into the battery modules; (b) EuroNCAP pole side impact at 50 km/h [149], large deformation in battery module is observed and the maximum displacement can reach 154 mm.

information, especially the deformation sequences.

Standardizing the cell-level tests. The setup of cell-level tests varies greatly among different research teams, and there is no standard about the testing setup as well as the procedure for carrying out the test. To standardize the tests, the first thing that should be clarified is the function of different loading conditions. As summarized in this review, they can generally be categorized into two groups, material test and structural test. The material tests, such as in-plane and out-of-plane compressions, can be used for model calibration, and the structural tests, such as pinching and hemispherical punch, can be used for model validation. At the same time, the structural tests are usually closer to practical accident scenarios, thus can be used to investigate the safety tolerance of the battery cells.

Modeling the shear failure phenomenon. A number of models have been proposed, at both component level and cell level. However, none of them can characterize the shear failure phenomenon, which has been observed by many research teams. Greve and Fehrenbach [24] first attempted to apply the Mohr-Coulomb to battery modeling, and a recent work by Chung et al. [25] suggests that the Mohr-Coulomb model is effective in modeling such local failure mode. Therefore, future studies can be focused on implement the M-C model into computational codes.

Dynamic testing and strain rate dependence. Dynamic test data of both battery components and individual cells is greatly needed. For automotive industry use, the tests should cover the range from 0 (quasi-static) to 500 s^{-1} to meet the demand of crash simulation. Quasi-static tests (under 1 s^{-1}) can be conducted using universal test machine. For dynamic tests, hydraulic machine or split Hopkinson bar are two common choices. Abuse test at cell-level requires large kinetic energy to be input into the structure. Therefore, drop mass systems are more suitable [155].

Effective homogenized models for battery cells and modules. To the automotive industry, homogenized models are always preferable rather than detailed models and RVEs. For battery cells, existing models are still not sufficient to the characterize the shear failure. For battery modules, there is still no applicable model. To bridge the gap, both experimental and computational investigations are required.

Next-generation batteries. As the battery techniques are developing rapidly, new batteries were born in labs, and some of them have even come into market. The all-solid-state battery is believed to be the next generation after lithium-ion batteries [156]. A number of studies have been carried out on characterizing the mechanical properties of lithium metal [157] and solid electrolyte as well as establishing cell-level models for all-solid-state batteries [79,158]. However, there are still many safety-focused mechanical problems to be investigated, such as the deposition of lithium and growth of dendrites.

Acknowledgement

The support from the MIT Battery Modeling Consortium (Altair, AVL, Daimler, Jaguar-Land Rover, LG Chem, and Boston-Power) is gratefully acknowledged.

References

[1] P. Hummel, D. Lesne, J. Radlinger, C. Golbaz, C. Langan, K. Takahashi, D. Mulholland, A. Stott, G. Haire, M. Mittermaier, N. Gaudois, L. Chaw, Report: UBS Evidence Lab Electric Car Teardown - Disruption Ahead? (2017).
[2] International Energy Agency, Report: Global EV Outlook 2017-Two Million and Counting, (2017).
[3] X. Feng, M. Ouyang, X. Liu, L. Lu, Y. Xia, X. He, Energy Storage Mater. 10 (January 2018) 246–267.
[4] Q. Wang, P. Ping, X. Zhao, G. Chu, J. Sun, C. Chen, J. Power Sources 208 (2012) 210–224.
[5] S. Abada, G. Marlair, A. Lecocq, M. Petit, V. Sauvant-Moynot, F. Huet, J. Power Sources 306 (2016) 178–192.
[6] M.-T.F. Rodrigues, G. Babu, H. Gullapalli, K. Kalaga, F.N. Sayed, K. Kato, J. Joyner, P.M. Ajayan, Nat. Energy 2 (2017) 17108.
[7] D. Ren, X. Feng, L. Lu, M. Ouyang, S. Zheng, J. Li, X. He, J. Power Sources 364 (2017) 328–340.
[8] T. Wierzbicki, E. Sahraei, J. Zhu, The Mechanics of Lithium-ion Batteries, (2016).
[9] T. Wierzbicki, E. Sahraei, S. Dajka, G. Li, S. Santhanagopalan, C. Zhang, G.-H. Kim, M.A. Sprague, NREL (National Renewable Energy Laboratory (NREL)), Golden, CO (United States), 2015.
[10] J. Zhu, Y. Xia, H. Luo, G. Gu, Q. Zhou, Int. J. Mech. Sci. 89 (2014) 148–157.
[11] M. Luo, M. Dunand, D. Mohr, Int. J. Plast. 32–33 (2012) 36–58.
[12] C. Bonatti, D. Mohr, Mater. Sci. Eng. A 654 (2016) 329–343.
[13] E. Sahraei, E. Bosco, B. Dixon, B. Lai, J. Power Sources 319 (2016) 56–65.
[14] E. Sahraei, M. Kahn, J. Meier, T. Wierzbicki, RSC Adv. 5 (2015) 80369–80380.
[15] R. Hill, Proc. Roy. Soc. Lond. Math. Phys. Sci. 193 (1948) 281–297.
[16] J.W. Yoon, F. Barlat, K. Chung, F. Pourboghrat, D.Y. Yang, Int. J. Plast. 16 (2000) 1075–1104.
[17] J.W. Yoon, D.Y. Yang, K. Chung, F. Barlat, Int. J. Plast. 15 (1999) 35–67.
[18] X. Zhang, T. Wierzbicki, J. Power Sources 280 (2015) 47–56.
[19] S.H. Chung, J. Zhu, H. Luo, E. Sahraei, submitted for publication, (2017).
[20] P. Larour, Doctoral theis, Lehrstuhl und Institut für Eisenhüttenkunde, 2010.
[21] Y. Bai, T. Wierzbicki, Int. J. Fract. 161 (2010) 1–20.
[22] T. Wierzbicki, Y. Bao, Y.-W. Lee, Y. Bai, Int. J. Mech. Sci. 47 (2005) 719–743.
[23] Y. Bai, T. Wierzbicki, Int. J. Plast. 24 (2008) 1071–1096.
[24] L. Greve, C. Fehrenbach, J. Power Sources 214 (2012) 377–385.
[25] S.H. Chung, T. Tancogne-Dejean, J. Zhu, H. Luo, T. Wierzbicki, submitted for publication, (2017).
[26] H. Luo, X. Jiang, Y. Xia, Q. Zhou, International Mechanical Engineering Congress and Exposition, ASME, 2015 V009T012A052–V009T012A052.
[27] X. Jiang, H. Luo, Y. Xia, Q. Zhou, SAE Int. J. Mater. Manuf. 9 (2016).
[28] G.R. Cowper, P.S. Symonds, DTIC Document, Brown Univ, Providence Ri, 1957.
[29] G.R. Johnson, W.H. Cook, Proceedings of the 7th International Symposium on Ballistics, The Hague, The Netherlands, 1983, pp. 541–547.
[30] X. Zhang, Doctoral thesis, Massachusetts Institute of Technology, Cambridge, 2017.
[31] K. Zhao, M. Pharr, S. Cai, J.J. Vlassak, Z. Suo, J. Am. Ceram. Soc. 94 (2011) s226–s235.
[32] K. Zhao, M. Pharr, L. Hartle, J.J. Vlassak, Z. Suo, J. Power Sources 218 (2012) 6–14.
[33] K. Zhao, M. Pharr, J.J. Vlassak, Z. Suo, J. Appl. Phys. 108 (2010) 073517.
[34] K. Zhao, M. Pharr, J.J. Vlassak, Z. Suo, J. Appl. Phys. 109 (2011) 016110.
[35] K. Zhao, M. Pharr, Q. Wan, W.L. Wang, E. Kaxiras, J.J. Vlassak, Z. Suo, J. Electrochem. Soc. 159 (2012) A238–A243.
[36] K. Zhao, W.L. Wang, J. Gregoire, M. Pharr, Z. Suo, J.J. Vlassak, E. Kaxiras, Nano Lett. 11 (2011) 2962–2967.
[37] M. Pharr, Z. Suo, J.J. Vlassak, Nano Lett. 13 (2013) 5570–5577.
[38] M. Pharr, Z. Suo, J.J. Vlassak, J. Power Sources 270 (2014) 569–575.
[39] M. Pharr, K. Zhao, X. Wang, Z. Suo, J.J. Vlassak, Nano Lett. 12 (2012) 5039–5047.
[40] C.V. Di Leo, E. Rejovitzky, L. Anand, Int. J. Solid Struct. 67–68 (2015) 283–296.
[41] E. Rejovitzky, C.V. Di Leo, L. Anand, J. Mech. Phys. Solid. 78 (2015) 210–230.
[42] T. Günther, N. Billot, J. Schuster, J. Schnell, F.B. Spingler, H.A. Gasteiger, Adv. Mater. Res. (2016) 304–311. Trans Tech Publ.
[43] H. Bockholt, W. Haselrieder, A. Kwade, Powder Technol. 297 (2016) 266–274.
[44] J.M. Foster, X. Huang, M. Jiang, S.J. Chapman, B. Protas, G. Richardson, J. Power Sources 350 (2017) 140–151.
[45] L.A. Riley, A.S. Cavanagh, S.M. George, S.-H. Lee, A.C. Dillon, Electrochem. Solid State Lett. 14 (2011) A29–A31.
[46] J. Chen, J. Liu, Y. Qi, T. Sun, X. Li, J. Electrochem. Soc. 160 (2013) A1502–A1509.
[47] W. Haselrieder, B. Westphal, H. Bockholt, A. Diener, S. Höft, A. Kwade, Int. J. Adhesion Adhes. 60 (2015) 1–8.
[48] A.M. Gaikwad, A.C. Arias, ACS Appl. Mater. Interfac. 9 (2017) 6390–6400.
[49] O. Mohr, Abhandlungen aus dem gebiete der technischen mechanik, (1906).
[50] D.C. Drucker, W. Prager, Q. Appl. Math. 10 (1952) 157–165.
[51] Dassault Systèmes, Abaqus Analysis Use's Manual, Simulia Corp, USA, 2007.
[52] R.E. Miller, Int. J. Mech. Sci. 42 (2000) 729–754.
[53] C. Zhang, J. Xu, L. Cao, Z. Wu, S. Santhanagopalan, J. Power Sources 357 (2017) 126–137.
[54] P. Arora, Z. Zhang, Chem. Rev. 104 (2004) 4419–4462.
[55] X. Huang, J. Solid State Electrochem. 15 (2011) 649–662.
[56] H. Lee, M. Yanilmaz, O. Toprakci, K. Fu, X. Zhang, Energy Environ. Sci. 7 (2014) 3857–3886.
[57] X. Zhang, E. Sahraei, K. Wang, J. Power Sources 327 (2016) 693–701.
[58] X. Zhang, E. Sahraei, K. Wang, Sci. Rep. 6 (2016) 32578.
[59] G. Venugopal, J. Moore, J. Howard, S. Pendalwar, J. Power Sources 77 (1999) 34–41.
[60] C.T. Love, J. Power Sources 196 (2011) 2905–2912.
[61] S.H. Tabatabaei, P.J. Carreau, A. Ajji, J. Membr. Sci. 345 (2009) 148–159.
[62] K. Yuzawa, Y. Yang, N. Bhandari, M. Sugiyama, S. Nakamura, Goldman Sachs Report: Charging the Future: Asia Leads Drive to Next-generation EV Battery Market, (2016).
[63] I.C. Halalay, M.J. Lukitsch, M.P. Balogh, C.A. Wong, J. Power Sources 238 (2013) 469–477.
[64] C. Peabody, C.B. Arnold, J. Power Sources 196 (2011) 8147–8153.
[65] Y. Liang, L. Ji, B. Guo, Z. Lin, Y. Yao, Y. Li, M. Alcoutlabi, Y. Qiu, X. Zhang, J. Power Sources 196 (2011) 436–441.
[66] S. Lee, G.C. Rutledge, Macromolecules 44 (2011) 3096–3108.
[67] A. Sedighiamiri, L.E. Govaert, J.A.W. van Dommelen, J. Polym. Sci. B Polym. Phys. 49 (2011) 1297–1310.
[68] A. Sedighiamiri, D.J.A. Senden, D. Tranchida, L.E. Govaert, J.A.W. van Dommelen, Comput. Mater. Sci. 82 (2014) 415–426.

[69] J.A.W. van Dommelen, D.M. Parks, M.C. Boyce, W.A.M. Brekelmans, F.P.T. Baaijens, J. Mech. Phys. Solid. 51 (2003) 519–541.
[70] X. Xiao, W. Wu, X. Huang, J. Power Sources 195 (2010) 7649–7660.
[71] S. Yan, X. Xiao, X. Huang, X. Li, Y. Qi, Polymer 55 (2014) 6282–6292.
[72] G. Ayoub, F. Zaïri, M. Naït-Abdelaziz, J. Gloaguen, Int. J. Plast. 26 (2010) 329–347.
[73] C. Regrain, L. Laiarinandrasana, S. Toillon, K. Saï, Int. J. Plast. 25 (2009) 1253–1279.
[74] A. Rozanski, A. Galeski, Int. J. Plast. 41 (2013) 14–29.
[75] D.J.A. Senden, G.W.M. Peters, L.E. Govaert, J.A.W. Van Dommelen, Polymer 54 (2013) 5899–5908.
[76] Y. Qi, H. Guo, L.G. Hector, A. Timmons, J. Electrochem. Soc. 157 (2010) A558–A566.
[77] L.Y. Beaulieu, K.W. Eberman, R.L. Turner, L.J. Krause, J.R. Dahn, Electrochem. Solid State Lett. 4 (2001) A137–A140.
[78] A. Timmons, J.R. Dahn, J. Electrochem. Soc. 154 (2007) A444–A448.
[79] G. Bucci, T. Swamy, S. Bishop, B.W. Sheldon, Y.-M. Chiang, W.C. Carter, J. Electrochem. Soc. 164 (2017) A645–A654.
[80] L. Anand, J. Mech. Phys. Solid. 60 (2012) 1983–2002.
[81] X.-y. Zhang, F. Hao, H.-s. Chen, D.-n. Fang, Mech. Mater. 91 (Part 2) (2015) 351–362.
[82] H.-K. Park, B.-S. Kong, E.-S. Oh, Electrochem. Commun. 13 (2011) 1051–1053.
[83] J.-H. Lee, U. Paik, V.A. Hackley, Y.-M. Choi, J. Power Sources 161 (2006) 612–616.
[84] ASTM Committee D-14 on Adhesives, Standard Test Method for Peel Resistance of Adhesives (T-peel Test), ASTM International, 2015.
[85] D.S. Kim, S.W. Bae, D.H. Kim, J.M. Cho, M.S. Yu, Int. J. Precis. Eng. Manuf. 18 (2017) 1307–1311.
[86] H. Luo, J. Zhu, E. Sahraei, Y. Xia, submitted for publication, (2017).
[87] SAE International, Electric and Hybrid Electric Vehicle Rechargeable Energy Storage System (RESS) Safety and Abuse Testing, (2009).
[88] SAE International, Electric and Hybrid Vehicle Propulsion Battery System Safety Standard - Lithium-based Rechargeable Cells, (2011).
[89] ISO 12405-1, Electrically Propelled Road Vehicles - Test Specification for Lithium-ion Traction Battery Packs and Systems - Part 1: High-power Applications, (2011).
[90] UN/ECE Regulation No. 100.02, Uniform Provisions Concerning the Approval of Vehicles with Regard to Specific Requirements for the Electric Power Train, (2013).
[91] UL 2580, Batteries for Use in Electric Vehicles, (2013).
[92] V. Ruiz, A. Pfrang, A. Kriston, N. Omar, P. Van den Bossche, L. Boon-Brett, Renew. Sustain. Energy Rev. 81 (Part 1) (January 2018) 1427–1452.
[93] H. Wang, S. Simunovic, H. Maleki, J.N. Howard, J.A. Hallmark, J. Power Sources 306 (2016) 424–430.
[94] H. Maleki, J.N. Howard, J. Power Sources 191 (2009) 568–574.
[95] W. Cai, H. Wang, H. Maleki, J. Howard, E. Lara-Curzio, J. Power Sources 196 (2011) 7779–7783.
[96] F. Ren, T. Cox, H. Wang, J. Power Sources 249 (2014) 156–162.
[97] J.A.T. PI, S. Allu, S. Gorti, S. Kalnaus, A. Kumar, D. Lebrun-Grandie, S. Simunovic, S. Slattery, B. Turcksin, H. Wang, Oak Ridge National Lab Report: Crashworthiness Models for Automotive Batteries, (2016).
[98] E. Sahraei, J. Meier, T. Wierzbicki, J. Power Sources 247 (2014) 503–516.
[99] E. Sahraei, R. Hill, T. Wierzbicki, J. Power Sources 201 (2012) 307–321.
[100] E. Sahraei, J. Campbell, T. Wierzbicki, J. Power Sources 220 (2012) 360–372.
[101] W.-j. Zheng, F.-c. Lan, J.-q. Chen, Z.-j. Li, DEStech transactions on environment, Energy Earth Sci. ICEPEE (2017) 393–403.
[102] H. Wang, T.R. Watkins, S. Simunovic, P.R. Bingham, S. Allu, J.A. Turner, J. Power Sources 364 (2017) 432–436.
[103] T. Wierzbicki, E. Sahraei, J. Power Sources 241 (2013) 467–476.
[104] I. Avdeev, M. Gilaki, J. Power Sources 271 (2014) 382–391.
[105] I.V. Avdeev, M. Gilaki, ASME 2012 International Mechanical Engineering Congress and Exposition, American Society of Mechanical Engineers, 2012, pp. 461–467.
[106] J. Xu, B. Liu, D. Hu, Sci. Rep. 6 (2016) 21829.
[107] J. Zhu, X. Zhang, E. Sahraei, T. Wierzbicki, J. Power Sources 336 (2016) 332–340.
[108] M.Y. Ali, W.-J. Lai, J. Pan, J. Power Sources 242 (2013) 325–340.
[109] A. Mason, M.S. Thesis, Mechanical Engineering, Massachusetts Institute of Technology, Cambridge, MA, USA, 2017.
[110] W.-J. Lai, M.Y. Ali, J. Pan, J. Power Sources 248 (2014) 789–808.
[111] M.Y. Ali, W.-J. Lai, J. Pan, J. Power Sources 273 (2015) 448–459.
[112] M. Raffler, A. Sevarin, C. Ellersdorfer, S.F. Heindl, C. Breitfuss, W. Sinz, J. Power Sources 360 (2017) 605–617.
[113] S.-J. Sung, W.-J. Lai, M.Y. Ali, J. Pan, S. Barbat, SAE Int. J. Mater. Manuf. 7 (2014) 480–487.
[114] C.M. Amodeo, M.Y. Ali, J. Pan, Int. J. Crashworthiness 22 (2017) 1–14.
[115] E. Sahraei, T. Wierzbicki, R. Hill, M. Luo, SAE Int. (2010) 2010-01-1078.
[116] M. Dunand, D. Mohr, Int. J. Solid Struct. 47 (2010) 1130–1143.
[117] H. Huh, J. Lim, S. Park, Int. J. Automot. Technol. 10 (2009) 195–204.
[118] J. Xu, B. Liu, X. Wang, D. Hu, Appl. Energy 172 (2016) 180–189.
[119] W. Tsutsui, T. Siegmund, N.D. Parab, H. Liao, T.N. Nguyen, W. Chen, Exp. Mech. (2017) 1–6.
[120] T. Kisters, E. Sahraei, T. Wierzbicki, Int. J. Impact Eng. 108 (2017) 205–216.
[121] A. Sheidaei, X. Xiao, X. Huang, J. Hitt, J. Power Sources 196 (2011) 8728–8734.
[122] J. Cannarella, X. Liu, C.Z. Leng, P.D. Sinko, G.Y. Gor, C.B. Arnold, J. Electrochem. Soc. 161 (2014) F3117–F3122.
[123] G.Y. Gor, J. Cannarella, J.H. Prévost, C.B. Arnold, J. Electrochem. Soc. 161 (2014) F3065–F3071.
[124] H. Luo, J. Zhu, Z. Pan, Y. Xia, Q. Zhou, submitted for publication, (2017).
[125] H. Luo, Y. Xia, Q. Zhou, J. Power Sources 357 (2017) 61–70.
[126] S. Yang, J. Wu, B. Yan, L. Li, Y. Sun, L. Lu, K. Zeng, J. Power Sources 352 (2017) 9–17.
[127] R. Fu, M. Xiao, S.-Y. Choe, J. Power Sources 224 (2013) 211–224.
[128] J.H. Lee, H.M. Lee, S. Ahn, J. Power Sources 119 (2003) 833–837.
[129] E. Gibellini, C. Lanciotti, R. Giovanardi, M. Bononi, G. Davolio, A. Marchetti, C. Fontanesi, J. Electrochem. Soc. 163 (2016) A2304–A2311.
[130] S.A. Roberts, V.E. Brunini, K.N. Long, A.M. Grillet, J. Electrochem. Soc. 161 (2014) F3052–F3059.
[131] B. Rieger, S.V. Erhard, K. Rumpf, A. Jossen, J. Electrochem. Soc. 163 (2016) A1566–A1575.
[132] J. Cannarella, C.B. Arnold, J. Power Sources 245 (2014) 745–751.
[133] R. Hill, J. Mech. Phys. Solid. 11 (1963) 357–372.
[134] W.-J. Lai, M.Y. Ali, J. Pan, J. Power Sources 245 (2014) 609–623.
[135] C. Zhang, S. Santhanagopalan, M.A. Sprague, A.A. Pesaran, J. Power Sources 298 (2015) 309–321.
[136] V.S. Deshpande, N.A. Fleck, J. Mech. Phys. Solid. 48 (2000) 1253–1283.
[137] L.S.T.C. LS-DYNA, Keyword User's Manual, (2017).
[138] A.L. Gurson, Doctotral thesis, Brown University, 1977.
[139] K. Nahshon, J.W. Hutchinson, Eur. J. Mech A. Solid. 27 (2008) 1–17.
[140] L. Xue, Eng. Fract. Mech. 75 (2008) 3343–3366.
[141] V. Tvergaard, A. Needleman, Acta Metall. 32 (1984) 157–169.
[142] S.M. Khosrownejad, W.A. Curtin, J. Mech. Phys. Solid. 107 (2017) 542–559.
[143] J.A. Turner, S. Allu, S.B. Gorti, S. Kalnaus, A. Kumar, D.T. Lebrun-Grandie, S. Pannala, S. Simunovic, S.R. Slattery, H. Wang, Report: Crash Models for Advanced Automotive Batteries: a Review of the Current State of the Art, Oak Ridge National Lab. (ORNL), Oak Ridge, TN (United States), 2015.
[144] Z. Chen, X. Wang, A. Atkinson, N. Brandon, J. Eur. Ceram. Soc. 36 (2016) 3473–3480.
[145] L. Anand, C. Gu, J. Mech. Phys. Solid. 48 (2000) 1701–1733.
[146] K. Kamrin, M.Z. Bazant, Phys. Rev. E 75 (2007) 041301.
[147] Y. Xia, T. Wierzbicki, E. Sahraei, X. Zhang, J. Power Sources 267 (2014) 78–97.
[148] Y. Xia, G. Chen, Q. Zhou, F. Shi, X. Shi, Engineering Failure Analysis, (2017).
[149] M. Funcke, S. Schäfer, R. Wohlecker, D. Dufaut, D. Sturk, K. Vavalidis, EU Project Report: Optimised Storage Integration for the Electric Car, (2014), p. 123.
[150] H. Kapeller, The 27th International Electric Vehicle Symposium (EVS27), Barcelona, Spain, 17th–20th November, 2013.
[151] J. Kukreja, T. Nguyen, T. Siegmund, W. Chen, W. Tsutsui, K. Balakrishnan, H. Liao, N. Parab, Extreme Mech. Lett. 9 (2016) 371–378.
[152] T.N. Nguyen, T. Siegmund, W. Tsutsui, H. Liao, W. Chen, Mater. Des. 105 (2016) 51–65.
[153] W. Tsutsui, T. Nguyen, H. Liao, N. Parab, J. Kukreja, T. Siegmund, W. Chen, MRS Adv. 1 (2016) 381–388.
[154] P.D. Rawlinson, U.S. Patent: Vehicle Battery Pack Ballistic Shield, (2012).
[155] Y. Xia, J. Zhu, Q. Zhou, Int. J. Impact Eng. 86 (2015) 284–294.
[156] M. Braga, N. Grundish, A. Murchison, J. Goodenough, Energy Environ. Sci. 10.1 (2017) 331–336.
[157] C. Xu, Z. Ahmad, A. Aryanfar, V. Viswanathan, J.R. Greer, Proc. Natl. Acad. Sci. 114 (2017) 57–61.
[158] G. Bucci, T. Swamy, Y.-M. Chiang, W.C. Carter, arXiv preprint arXiv:1703.00113, (2017).

Journal of Power Sources 396 (2018) 412–420

Contents lists available at ScienceDirect

Journal of Power Sources

journal homepage: www.elsevier.com/locate/jpowsour

Effects of electrolyte, loading rate and location of indentation on mechanical integrity of li-ion pouch cells

Brandy Dixon[a], Amber Mason[a], Elham Sahraei[a,b,*]

[a] Impact and Crashworthiness Lab (ICL), Massachusetts Institute of Technology, Cambridge, MA, USA
[b] Electric Vehicle Safety Lab (EVSL), George Mason University, Fairfax, VA, USA

HIGHLIGHTS

- Analyzed effects of electrolyte presence on material properties of lithium ion cells.
- Examined effects of punch location on mechanical response of lithium-battery cells.
- Studied changes in cell response at various loading rate.
- Investigated repeatability of mechanical punch testing .

ARTICLE INFO

Keywords:
Lithium-ion cell
Mechanical abuse
Finite element modeling
Experiment set-up

ABSTRACT

The safety of lithium-ion batteries under mechanical abuse conditions is an essential feature where these cells are used in mobile applications such as electric vehicles. In recent publications, punch testing has been used as a benchmark to study the mechanical abuse tolerance of the cells. What has not been studied in depth is how various test conditions such as the loading rate or the location of indentation affect the response of the cell. This paper quantifies the effects of four important test variables on the results of mechanical indentation tests. The first factor studied was to what degree tests on dry dummy cells without electrolyte can predict the response of a production cell. Then the effects of loading location, center versus on the edge, was evaluated. The speed of the test, at quasi-static rates, was the third variable. The last test characteristic studied was the repeatability of punch loading experiments. After completing the test program, a finite element model was developed to simulate the response of all studied cases. The model showed good predictability of load-displacement response and the onset of short circuit under all loading scenarios studied in this research.

1. Introduction

Lithium-ion batteries have a high energy density and no memory effect, making them attractive for a variety of applications from small electronics to electric vehicles and airplanes. The safety of lithium-ion batteries is extremely important due to their widespread use in consumer products including vehicles. While much is understood about lithium-ion batteries, no comprehensive computational models exist to predict their safety and optimize these batteries before manufacture.

The battery research of the Impact and Crashworthiness Laboratory (ICL) at the Massachusetts Institute of Technology has been focused on understanding the lithium-ion battery's mechanical properties so that individual battery cells and battery packs can be characterized during crash events. This work began in 2010 with the mechanical testing of small cylindrical and pouch cells to develop a finite element model of a lithium-ion cells using representative volume elements (RVE). The first RVE models used an isotropic homogenized foam model to represent the interior of the battery [1–5], but subsequent models incorporated the characteristics of the individual layers [6–8]. Mechanical testing of batteries by the ICL included compression, indentation, and three-point bending of different sizes and types of batteries and at different states of charge (SOC). Tensile, biaxial punch, compression and other tests were performed on battery interior components, including individual anode, cathode, separator, and multilayer samples [7,9–12]. All test results were incorporated into new or existing computational models to further refine and validate them. A summary of the above research is published in a recent review paper by Kermani and Sahraei (2018) [13].

Studies on the mechanical properties of lithium-ion batteries has been conducted by other research groups as well. Researchers from the University of Michigan have studied the mechanical properties of large

* Corresponding author. Electric Vehicle Safety Lab (EVSL), George Mason University, Fairfax, VA, USA.
E-mail address: esahraei@gmu.edu (E. Sahraei).

https://doi.org/10.1016/j.jpowsour.2018.06.042
Received 10 October 2017; Received in revised form 29 May 2018; Accepted 10 June 2018
Available online 17 June 2018
0378-7753/

lithium-ion cells and modules under compressive loading scenarios and developed relevant computational models [14–16]. The mechanical properties of large cylindrical cells have been studied by Volkswagen [17] and researchers from the University of Wisconsin [18]. Additional research on 18650 cells and the effects of state of charge and dynamic loading on mechanical properties of these cells has been reported by researchers from Beihang University [19,20]. Despite the recent advances in research on the mechanical behavior of lithium-ion batteries, there are still many unknowns in understanding the complete properties of these cells. In this research, authors have focused on answering three major questions posed by industry: the effects of electrolyte, loading rate, and location of indentation on the mechanical integrity of lithium-ion pouch cells. In addition, the repeatability of punch tests was explored.

In many studies, researchers use a dry cell with no electrolyte or cut out a sample of a cell, allowing the electrolyte to evaporate resulting in a dry sample, to study the material properties of lithium-ion batteries [16,18]. However, there have not been any systematic studies to understand how the behavior of a dry cell replicates or differs from the response of a cell with electrolyte. This study sheds light on the points of similarity and differences between the two. Additionally, no investigation on how material properties may change when the indentation location changes from the center toward or at the edges of the cell has been conducted. In all publications focusing on the indentation of batteries, loading has been applied to the center of the cell. This research investigates the changes in material properties from center to edges of a pouch battery cell.

The effects of loading rate on the response of the cell is also explored in this research. Few recent studies report on the dynamic response of cylindrical and pouch cells [19,21]. Most previous research and modeling work used quasi-static loading scenarios [2,14,17,22] without analyzing effects of quasi-static loading rates on the response of the cell. Finally, repeatability of punch testing was studied. Punch testing is used as a benchmark to determine mechanical abuse tolerance of lithium-ion cells, but this testing is destructive, expensive, and poses safety concerns. Therefore, the testing is sometimes limited, making repeatability an important factor. To study the above topics, a series of experimental tests were completed. In each series, one factor was varied, and all other variables remained constant. The results were then used to develop a Finite Element model for the subject pouch cell to further analyze the changes in material properties due to changes in the specific cell or loading conditions.

2. Experiments

Commercially available pouch cells were used for testing with and without electrolyte (live cell and dry cell). The cells had Lithium Nickel Cobalt Oxide chemistry, a nominal capacity of 52 A h, and a volumetric energy density of 280 W h/l. Shape and dimensions of the cell are shown in Fig. 1. The live cells were discharged to 0% SOC for safe testing. Both dry cell and discharged live cells were used for compression and hemispherical punch testing with the MTS Loading Frame as shown in Fig. 1.

2.1. Test equipment

The primary test equipment used for this research was a displacement-controlled 200 kN MTS Loading Frame with a crosshead speed range of 0.1 mm/min to 1000 mm/min. The MTS machine was fitted with flat cylindrical punches for compression tests and hemispherical punches for indentation, or punch tests. Testworks© 4 software measured the force and recorded the displacement. In addition, an Imaging Retiga 1300i digital camera and Vic-Snap™ and Vic-2D™ digital image correlation (DIC) software recorded and calculated the displacement from test equipment that was marked. A RadioShack© 46-Range Digital Multimeter and Meterview software recorded voltage and resistance. In order to ensure safety during cell tests, a ventilated enclosure and an extension rod for the MTS machine were also used.

Tape with markings was attached to the MTS fixtures, and the DIC camera tracked the markings for comparison with the MTS displacement results. The voltage and resistance of the cells were recorded using a multi-meter. For the discharged live cells, a short circuit was detected in the cell when the voltage started to drop.

The experiments were designed to study effects of five variables on test results. First parameter studied was effects of electrolyte. For this purpose dry and live discharged cells were subjected to flat compression and punch indentation loads and the differences in the response of these cells were investigated. The tests were conducted on cells with pouch cover. However, previous research has shown that pouch cover, which is a thin foil of fused aluminum/polyester, do not add any strength to the cell under these loading scenarios [2], and the measured data directly reflects the properties of the electrode/separator stack. The second factor was the location of loading. For this purpose, hemispherical punch loading was applied to a matrix of points starting from center of the cell and moving toward the edges and the results were compared. The third factor studied was quasi static rate of loading, tests were performed at speeds of 0.2–20 mm/min. The last item was the repeatability of test results. For this purpose, indentation tests with three different punch diameters were conducted and the range of variability of repeated identical tests were identified.

3. Finite element modeling

Two types of models have been used to simulate through thickness behavior of pouch lithium-ion cells, using isotropic and anisotropic crushable foam materials [2,4,6]. The observation of an isotropic separator failure from the indentation tests of the pouch cells in this study indicates that the isotropic crushable foam model available from the library of LS Dyna software will be suitable for the simulation of this cell. This material model works in the plane of principal stresses and behaves differently in tension and compression. The behavior in tension is elastic until reaching a tensile cut-off value σ_{YT}, which caps the highest stress the material can tolerate in tension. A hardening stress-strain curve is defined in compression. Here the compressive hardening curve is calibrated from the flat cylinder punch shown in Fig. 1. A transition area between the compressed and free section of the cell have minimal contribution to the total force and can be neglected in calculation of stress-strain curves [4]. Therefore, compressive hardening stress (σ_{YC}) can be directly calculated by dividing total force (F) by punch cross sectional area (A), i.e. $\sigma_{YC} = \frac{F}{A}$. Compressive stresses for live and dry cells are shown in Fig. 2. The tensile response of the cell cannot be directly calculated from any of the punch cells. Therefore, tensile coupon tests were performed on all components of the cell, and the aggregated tensile curve was calculated as a weighted average of the system of layers undergoing same strain ($\sigma_{avg} = \frac{\Sigma \sigma_i t_i}{\Sigma t_i}$) where σ_i and t_i are the stress and thickness of each layer. The aggregated tensile curve was used to calculate the Young's Modulus (4200 MPa) and tensile cut-off stress, (18 *MPa*). Cell density was calculated from the mass and dimensions of the cell (2.530e-009 tonne/mm3).

A finite element model of the pouch cell was developed in LS Dyna explicit finite element code, using 31416 solid elements. All components of the pouch cell, including the cover were homogenized into a single part. A multi-step mesh was used to reduce number of elements and accelerate simulations. The mesh size used under the punch was $1.2 \times 1.2 \times 1$ mm and was increased to $2.5 \times 2.5 \times 1$ mm and $10 \times 10 \times 1$ mm when moving outside the loading area, as shown in Fig. 5.

4. Results and discussion

First set of results presented here are from variety of experimental

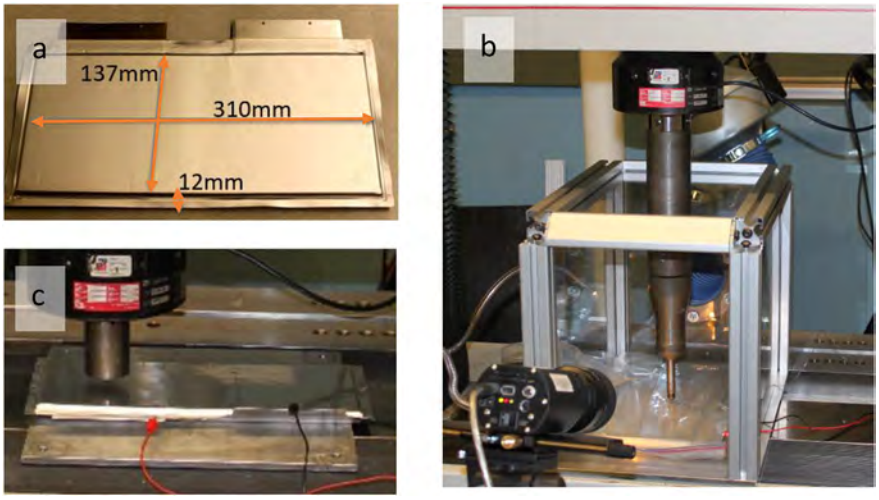

Fig. 1. Pouch cell dimensions (a), test set up with hemispherical punch (b), and flat cylindrical punch test (c).

evaluations to identify effects of four parameters on the test data: electrolyte, punch location, rate of loading, and repeatability. Each factor is studied separately and discussed in a subsection. After presentation of test outcomes, the simulation results are presented and discussed. The models verify the validity of material characterization and the trends observed under each loading condition.

4.1. Effect of electrolyte

To determine the effect of electrolyte on the cell's loading response, dry and discharged live cells were compression and punch tested. The compression tests were performed using a flat cylinder punch with a diameter of 44.64. The punch tests were conducted using a hemispherical punch with a diameter of 12.6 mm. All tests were conducted at a loading rate of 1 mm/min. The hemispherical punch test was repeated two times on each cell type, while the compression test was conducted twice on the discharged live cell and once on the dry one.

The dry cell has a slightly stiffer response and higher level of force compared to the discharged live cell. For comparison, the force recorded for the flat punch compression test of the dry cell at a displacement of 4 mm was 167 kN, while the force for the discharged live cell was 150 kN. The difference in peak force between dry and live cells during hemispherical punch loading is significant (dry cell has a 48% higher peak load). The hemispherical punch tests showed maximum force measurements of 7.7 kN at 4 mm displacement for the dry cell and 5.2 kN at 3 mm displacement for the discharged live cell. Fig. 3 shows the force-displacement curves for these tests.

The onset of short circuit is detected from the drop in voltage in the discharged live cell tests. For the flat cylindrical loading, short circuit happens at about 2 mm displacement, while for hemispherical punch test, it is at 3.3 mm. It appears that the sharp edge of the cylindrical punch initiates short circuit at a lower displacement. In case of the flat cylindrical punch loading, the short circuit does not initiate any drop in force. However, for the hemispherical punch, the onset of short circuit coincides with a drop in load. For the dry cell, no voltage measurement was available, but the resistance was measured during the flat cylindrical compression and a drop in resistance from 1000 Ω to 0 was recorded at a displacement of 2.2 mm which coincides with the onset of short circuit for the discharged live cell. The failure for dry hemispherical punch test was only recorded through a drop in force at 4 mm displacement.

These results are aligned with findings of Sheidaei et al. (2011) and Yan et al., 2014 that report on effects of electrolyte on polymeric separator [23,24]. Their findings suggest that polymeric separators fail earlier when they are soaked in electrolyte as opposed to when tested in dry state. In the current research, the effects of electrolyte on each of the micro components (separator, coating and metal foils) were not studied separately. However, the homogenized response of the cell follows the same trend and becomes softer in wet state. Also, the onset of failure is earlier when a live cell is tested in comparison to a dry cell.

4.2. Effect of loading location

The effects of loading location were studied using punch testing with a 12.6 mm hemispherical punch. A series of hemispherical punch tests were performed at varying locations on the dry pouch cell. The first test was located in the center of the cell, approximately 65 mm from the cell's long edge. The second test was 30 mm from the long

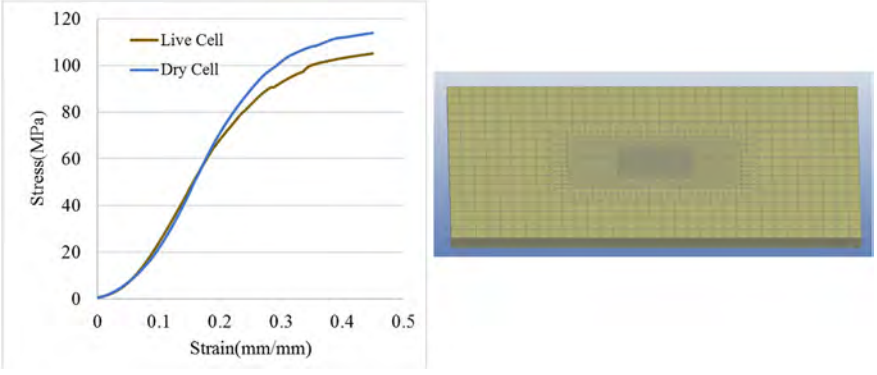

Fig. 2. Compressive stress-strain curve (left), and Finite Element Mesh (right).

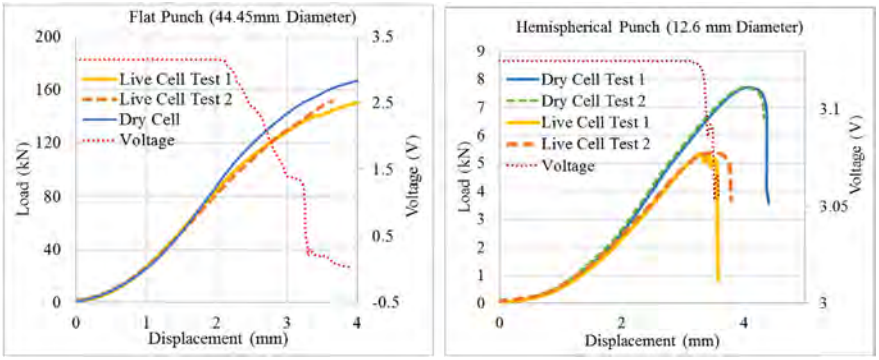

Fig. 3. Compressive Load-Displacement under flat cylindrical loading (left) and hemispherical punch indentation (right) for dry cells and live discharged cells.

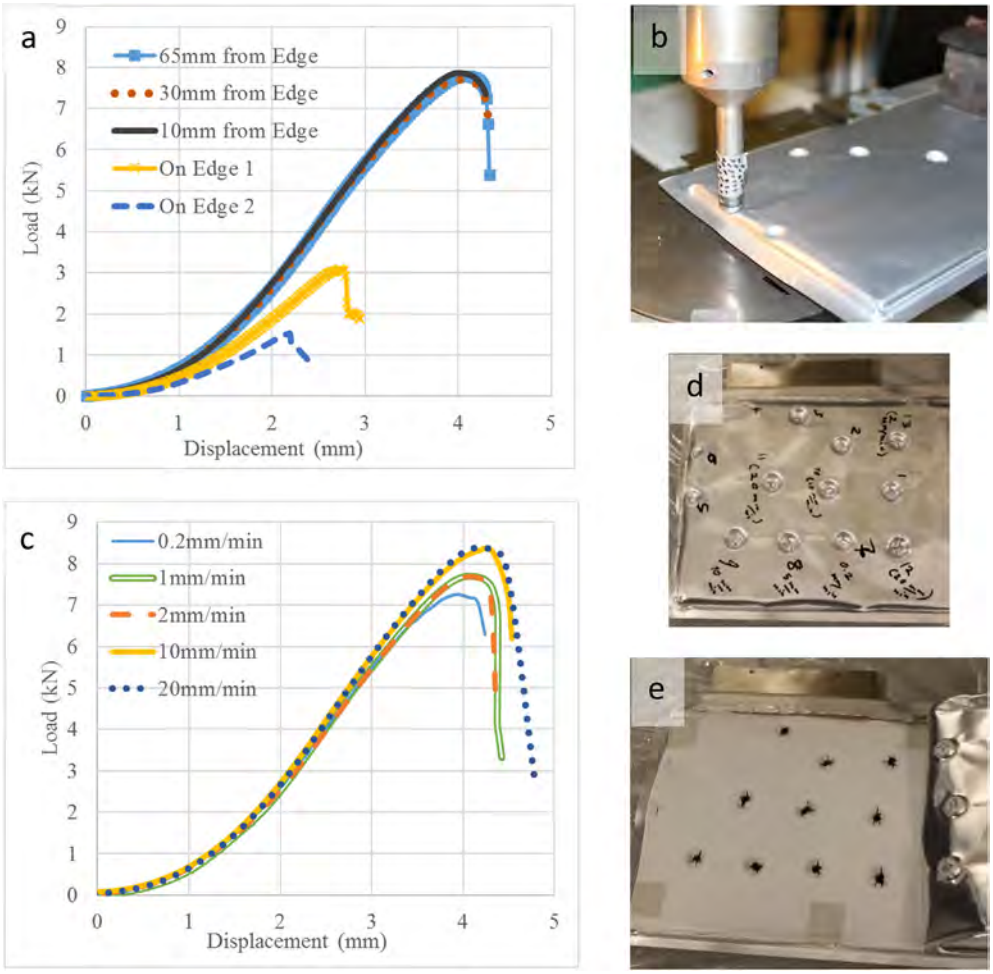

Fig. 4. Load-displacement results from punch loading at different locations (a), location of punch tests presented in Graph a (b), load-displacement results from tests at various speeds (c), location of additional punch tests with varying speeds (d), and a view of separator layer under the pouch cover after completion of tests (e).

edge, and the third was 10 mm from the long edge. The fourth test was performed on the edge of the cell. And the fifth test was also on the cell edge, but with the punch centered on the edge. The test locations can be seen in Fig. 4. The plots of the three tests that were not on the cell edge were consistent, and all had maximum force measurements around 7.6 kN at a crosshead of 4.1 mm. The two tests on the edge had much lower maximum force results, which was expected since the edge of the cell had less material than the cell interior. The first test performed on the cell edge had a maximum force of 3.1 kN at a crosshead of 2.8 mm, while the second had a maximum force of 1.5 kN at 2.2 mm.

The study of the effect of testing location demonstrated that only tests on the cell edge had a significant decrease in maximum force and displacement. Changing the punch location from a central point of 60 mm from the edge to any other point where the punch is not touching the edge does not produce any difference in the load displacement results. This gives researchers freedom to use a single cell for performing multiple tests without concern that punch location will affect the results.

4.3. Effect of loading rate

The effects of loading rate were also studied using punch testing with a 12.6 mm hemispherical punch. This second set of hemispherical punch tests was performed at varying speeds from 0.2 mm/min to

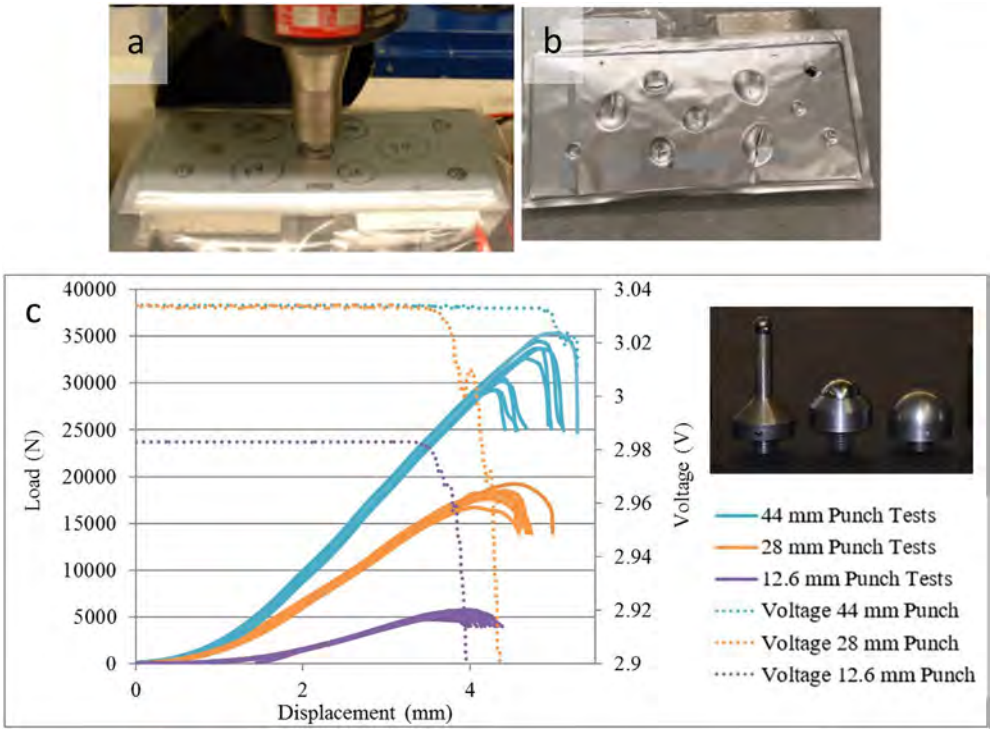

Fig. 5. Repeatability of punch test results, using three hemispherical punch sizes. Test set up (a), cell deformation after repeated tests (b), and load-displacement results for three punch sizes (c).

20 mm/min. To ensure accurate displacement results, the MTS measurements were verified with the displacement data obtained from the DIC analysis. Increasing speeds produced increasing maximum force and displacement measurements, as shown in Fig. 4. Tests conducted at speeds of the same order of magnitude had similar results, but the tests at speeds of different orders of magnitude had considerable differences in maximum force measurements. The 20 mm/min punch test had the highest maximum force of 8.4 kN, and the 0.2 mm/min test had the lowest maximum force of 7.3 kN. The maximum force measurements occurred at approximately 3.6–4.4 mm punch displacements.

After the test, the exterior cover was removed to investigate the shape of failure in the separator layer. Except the tests on the cell edge, all tests at different speeds and locations on the cell showed a similar pattern of deformation and failure as shown in Fig. 4. The separator layer was a nonwoven type and showed an axisymmetric failure pattern, indicating an isotropic separator material.

4.4. Repeatability of test results

Because of the cost and safety precautions required when testing automotive size lithium-ion batteries, often mechanical tests are only repeated 1–2 times. To understand the repeatability of the tests, three live cells were discharged and subjected to a number of punch tests with three hemispherical punches (Dimeters 12.6 mm, 28 mm, and 44 mm). The first test on each cell allowed for the recording of voltage, while in subsequent tests only load-displacement could be measured. The test matrix and the order of tests on each cell is shown in Appendix Table 1. There were total 12 tests with the small punch (12.6 mm), and nine tests with the medium (28 mm) and large (44 mm) punches each. Fig. 5 shows the load-displacement curves for all tests, and Appendix Table 2 shows the peak force and associated displacement for each test. The peak force and displacement increased as the punch size increased. For the small punch, the average peak force was 5.3 kN at 3.8 mm displacement. The average peak force increased to 18.2 kN at 5.5 mm displacement for the medium punch and to 32.1 kN at 6.3 mm for the large punch.

In terms of repeatability, the load-displacement curves were highly repeatable for the tests with all three-punch sizes studied. There was a slight variation in peak force and the associated displacements, especially as the punch size increased. The small hemispherical punch tests of 12.6 mm diameter had the highest repeatability of the results with a standard deviation of 0.3 kN in peak force and 0.15 mm in displacement. This suggests that punch tests can be used as a benchmark to compare various cells. Still it should be noted that normalizing the errors over magnitude of the peak force shows similar variability (< 10%) for all punch sizes.

4.5. Finite element simulation results

The first loading scenario studied was the indentation of a cell in the central area using 12.6 mm hemispherical punch on dry and discharged live cells. This simulation was used to calibrate the failure strain (principal strain to failure in tension). The calibration for the discharged live cell was completed by choosing the failure strain that causes element failure at the onset of short circuit, as determined by a corresponding voltage drop (see Fig. 3). This point is slightly before the peak load. For the dry cell, failure strain was chosen to create element failure when reaching peak load in the test. The failure strain for the dry cell was 0.105 mm/mm, and for the discharged live cell was 0.1 mm/mm. Fig. 6 shows the results of the small hemispherical punch simulation for both dry and discharged live cell models. Force-displacement and the onset of failure are predicted closely in both simulations.

The second case studied was loading at the edge. In this case, the punch was located at the boundary of the cell in a way that only 50% of the punch was located on the cell and the other half of the punch was unsupported. The model predicted the load displacement and onset of short circuit with very good accuracy for this case as well, as shown in Fig. 6. It should be noted that the material model and calibration parameters for hardening curves and element failure was not modified for this simulation. Therefore, this result shows that material properties do not have a significant change on the edge of the cell.

Fig. 7 shows the results for medium (28.6 mm) and large (44 mm)

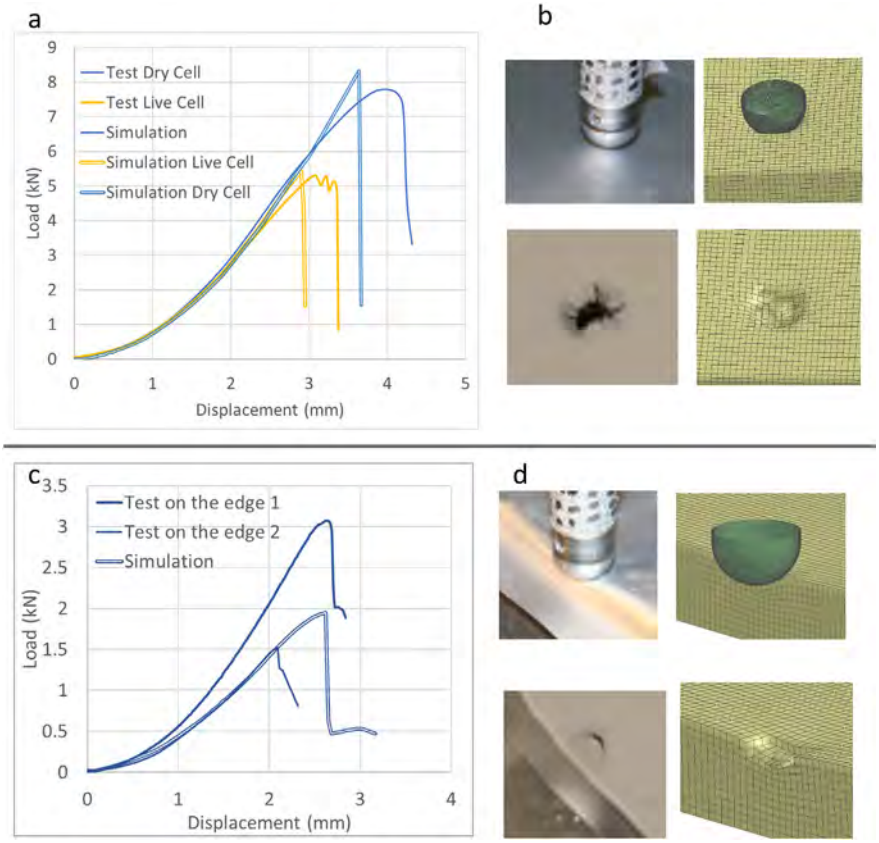

Fig. 6. Simulation of 12.6 mm punch indentation, in the center (1st row): load-displacement (a), comparison of test and simulation set up and final shape of damage (b). Simulation of loading on the edge (2nd row): load-displacement (c), and comparison of simulation set-up and deformation (d).

hemispherical punch loading. Both models predict load-displacement curves with great accuracy. The onset of element failure coincides with onset of short circuit in the tests. The fracture pattern in the simulations also resembled the one in the tests and had a cross shape in both cases. This is because the material was isotropic. Again, no adjustment of material properties or failure strain was needed to achieve these results.

Fig. 8 shows the results for flat cylindrical punch loading simulation. The model predicts the load displacement curve very well. The onset of failure from the simulation is showed with first element deletion, which is discernible from a small local peak after 2 mm displacement. This point coincides with the onset of voltage drop from the tests, and this indicates that the model is predicting the onset of failure correctly for this case as well. Neither test nor simulation showed a global peak force at onset of failure, which is contrary to the case of hemispherical punch loadings. The failure strain used here is the same as used for hemispherical punch cases, indicating both types of loading scenarios were successfully simulated with the original model.

It should be noted that all tests and analysis conducted in this paper were performed at room temperature. Material properties can change significantly under extreme cold or hot temperatures. Considering the operating range of temperature for batteries (−20 °C to 60 °C), it is important that the above characterization and analysis be conducted also at a range of variable temperatures. This topic will be investigated in future publications.

In summary, the finite element model showed that using an isotropic crushable foam material model calibrated with only a few parameters including Young's Modulus, density, stress-strain curve in compression, tensile cut-off value, and principal strain to failure, one can successfully predict the response of the cell in the various loading conditions studied here. The model should be calibrated separately for a dry versus discharged live cell. No changes in parameters were needed to simulate flat punch versus hemispherical punches or loading location on the edge versus in the center of the cell. The latter means that although the configuration of electrode and separator layers change from flat stacks in the center to folded separator around electrodes at the edge, the homogenized material properties of the cell are not different on the edge of the cell compared to its center. Therefore, one model is valid to simulate the different loading scenarios that were presented here.

5. Conclusion

In this research, several issues affecting test response of lithium-ion batteries were investigated, including the effects of electrolyte, indentation location, and loading rate, as well as repeatability of the punch test. These are factors not generally well defined or controlled in current test procedures. Therefore, researchers or industrial users may rely on test results in a specific configuration and falsely consider them comparable with other test scenarios. This research explains what factors should be closely controlled in comparable tests and what could be left open for operator convenience. It was found that the presence of electrolyte has a significant impact on the response of the cell. The pouch cells with electrolyte had lower force and displacement measurements compared with dry pouch cells in both compression and punch loading scenarios studied. Therefore, researchers should pay extra attention when evaluating the mechanical response of a cell from a dummy test or dry components. In the quasi-static range of speeds studied in this research, the higher speed/strain rate tests of the pouch cells showed a higher maximum force and displacement measurements when the difference in speed was at least one order of magnitude. However, there was no significant difference in the response of the cell if the test speeds were within the same order of magnitude. For example, no difference was observed between 1 and 2 mm/min tests or 10 and 20 mm/min tests. It was also noted that the hemispherical punch

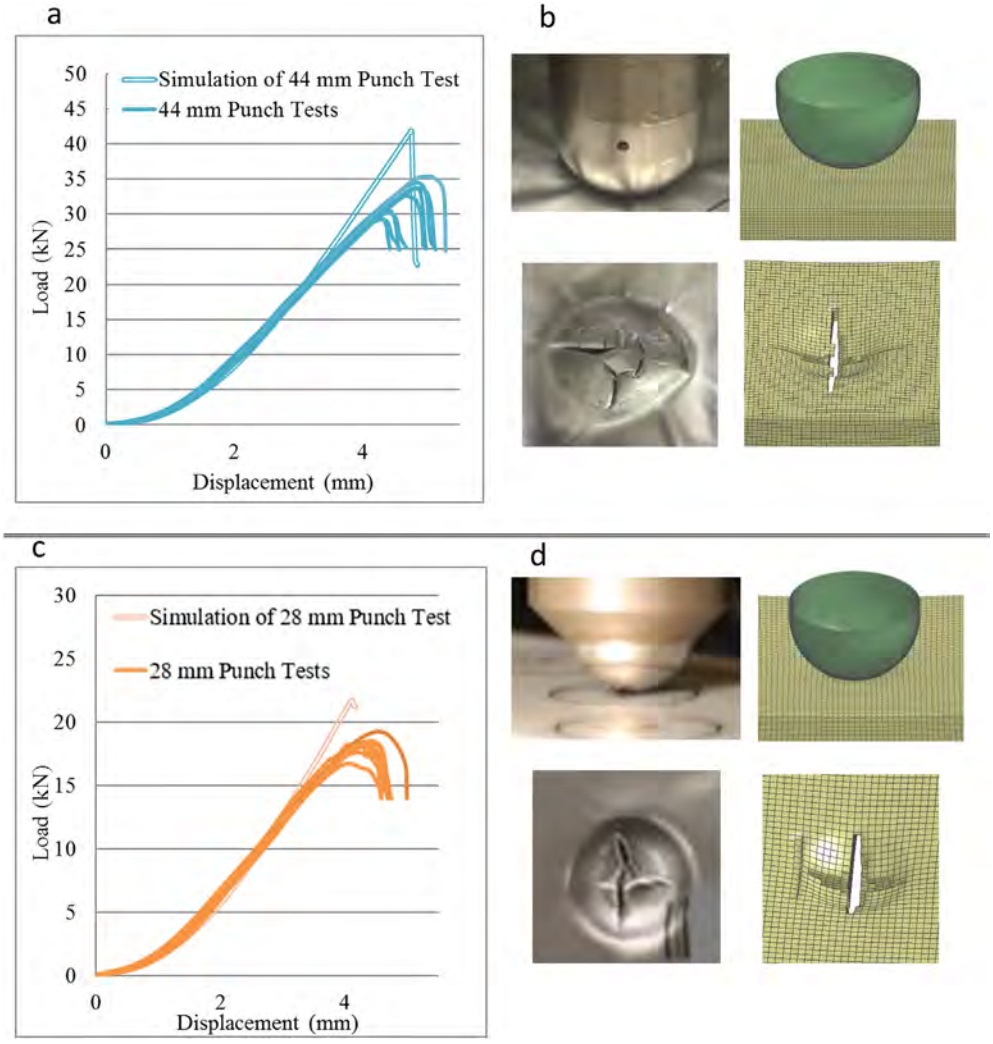

Fig. 7. Simulation of 44 mm punch loading (1st row): load-displacement curve (a), and comparison of test and simulation in set-up and failure patterns (b). Simulation of 28 mm punch loading (2nd row): load-displacement (c), and comparison of test and simulation set up and fracture patterns (d).

testing produces highly repeatable results and the data will not be affected by the location of the punch, as long as the deformation area is not on the edge of the cell.

Acknowledgement

This work has been supported by Industrial MIT Battery Consortium with sponsorship of Daimler, Jaguar-Land Rover, LG Chem, and Boston Power. The authors would like to thank Mr. Benjamin Lai for collaboration in the test program. Also, the authors acknowledge support of ALTAIR for providing HyperWork software for this study. Authors appreciate review and comments of Professor Tomasz Wierzbicki on this manuscript.

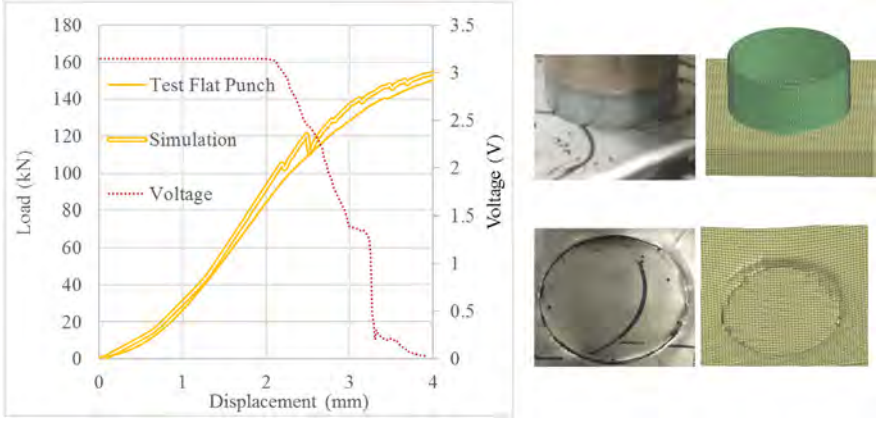

Fig. 8. Simulation of flat cylindrical punch loading, load-displacement (left) and comparison of set up and failure mode between test and simulation (right).

Appendix

Table 1
Repeatability Tests on Three Pouch Cells

Test Cell	Number and Order of Tests Performed
1	a. 3 medium punch indentation, 1 with Voltage b. 3 large punch indentation c. 4 small punch indentation
2	a. 4 small punch indentation, 1 with Voltage b. 3 medium punch indentation c. 3 large punch indentation
3	a. 3 large punch indentation, 1 with Voltage b. 3 medium punch indentation c. 4 small punch indentation

Table 2
Peak force and associated displacement for punch test

Cell	Punch Test	Peak Force (kN)	Disp. (mm)
1	12.6mmT7	5.4	3.9
1	12.6mmT8	5.3	3.8
1	12.6mmT9	5.8	4.0
1	12.6mmT10	5.4	3.9
2	12.6mmT1	5.7	3.8
2	12.6mmT2	5.0	3.7
2	12.6mmT3	4.9	3.6
2	12.6mmT4	4.8	3.5
3	12.6mmT7	5.2	3.8
3	12.6mmT8	5.4	4.1
3	12.6mmT9	5.6	4.0
3	12.6mmT10	5.2	3.8
Average =		5.3 (SD 0.3)	3.8 (SD 0.16)
1	28mmT1	18.5	5.4
1	28mmT2	17.6	5.4
1	28mmT3	18.2	5.5
2	28mmT5	18.4	5.6
2	28mmT6	19.2	5.7
2	28mmT7	18.3	5.6
3	28mmT4	18.5	5.6
3	28mmT5	16.7	5.2
3	28mmT6	18.1	5.6
Average =		18.2 (SD 0.7)	5.5 (SD 0.15)
1	44mmT4	32.6	6.4
1	44mmT5	30.2	6.1
1	44mmT6	29.3	6.0
2	44mmT8	34.5	6.5
2	44mmT9	30.5	6.1
2	44mmT10	29.3	5.9
3	44mmT1	35.3	6.8
3	44mmT2	33.7	6.6
3	44mmT3	33.7	6.5
Average =		32.1 (SD 2.3)	6.3 (SD 0.29)

References

[1] E. Sahraei, T. Wierzbicki, R. Hill, M. Luo, Crash safety of lithium-ion batteries towards development of a computational model, Soc. Automot. Eng, 2010.

[2] E. Sahraei, R. Hill, T. Wierzbicki, Calibration and finite element simulation of pouch lithium-ion batteries for mechanical integrity, J. Power Sources 201 (2012) 307–321, http://dx.doi.org/10.1016/j.jpowsour.2011.10.094.

[3] E. Sahraei, J. Campbell, T. Wierzbicki, Modeling and short circuit detection of 18650 Li-ion cells under mechanical abuse conditions, J. Power Sources 220 (2012) 360–372, http://dx.doi.org/10.1016/j.jpowsour.2012.07.057.

[4] E. Sahraei, J. Meier, T. Wierzbicki, Characterizing and modeling mechanical properties and onset of short circuit for three types of lithium-ion pouch cells, J. Power Sources 247 (2014) 503–516, http://dx.doi.org/10.1016/j.jpowsour.2013.08.056.

[5] Y. Xia, T. Wierzbicki, E. Sahraei, X. Zhang, Damage of cells and battery packs due to ground impact, J. Power Sources 267 (2014) 78–97, http://dx.doi.org/10.1016/j.jpowsour.2014.05.078.

[6] E. Sahraei, M. Kahn, J. Meier, T. Wierzbicki, Modelling of cracks developed in lithium-ion cells under mechanical loading, RSC Adv. 5 (2015) 80369–80380.

[7] E. Sahraei, E. Bosco, B. Dixon, B. Lai, Microscale failure mechanisms leading to internal short circuit in Li-ion batteries under complex loading scenarios, J. Power Sources 319 (2016) 56–65, http://dx.doi.org/10.1016/j.jpowsour.2016.04.005.

[8] J. Zhu, X. Zhang, E. Sahraei, T. Wierzbicki, Deformation and failure mechanisms of 18650 battery cells under axial compression, J. Power Sources 336 (2016) 332–340, http://dx.doi.org/10.1016/j.jpowsour.2016.10.064.

[9] X. Zhang, E. Sahraei, K. Wang, Li-ion battery separators mechanical integrity and failure mechanisms leading to soft and hard internal shorts, Nat. Sci. Reports (2016), http://dx.doi.org/10.1038/srep32578.

[10] X. Zhang, E. Sahraei, K. Wang, Deformation and failure characteristics of four types of lithium-ion battery separators, J. Power Sources 327 (2016) 693–701, http://dx.doi.org/10.1016/j.jpowsour.2016.07.078.

[11] X. Zhang, J. Zhu, E. Sahraei, Degradation of battery separators under charge–-discharge cycles, RSC Adv. 7 (2017) 56099–56107, http://dx.doi.org/10.1039/C7RA11585G.

[12] H. Luo, J. Zhu, E. Sahraei, Y. Xia, Adhesion strength of the cathode in lithium-ion batteries under combined tension/shear loadings, RSC Adv. 8 (2018) 3996–4005, http://dx.doi.org/10.1039/c7ra12382e.

[13] G. Kermani, E. Sahraei, Review: characterization and modeling of the mechanical properties of lithium-ion batteries, Energies 10 (2017), http://dx.doi.org/10.3390/en10111730.

[14] W.-J. Lai, M.Y. Ali, J. Pan, Mechanical behavior of representative volume elements of lithium-ion battery cells under compressive loading conditions, J. Power Sources 245 (2014) 609–623, http://dx.doi.org/10.1016/j.jpowsour.2013.06.134.

[15] M.Y. Ali, W.-J. Lai, J. Pan, Computational models for simulations of lithium-ion battery cells under constrained compression tests, J. Power Sources 242 (2013) 325–340, http://dx.doi.org/10.1016/j.jpowsour.2013.05.022.

[16] W.J. Lai, M.Y. Ali, J. Pan, Mechanical behavior of representative volume elements of lithium-ion battery modules under various loading conditions, J. Power Sources 248 (2014) 789–808, http://dx.doi.org/10.1016/j.jpowsour.2013.09.128.

[17] L. Greve, C. Fehrenbach, Mechanical testing and macro-mechanical finite element simulation of the deformation, fracture, and short circuit initiation of cylindrical Lithium ion battery cells, J. Power Sources 214 (2012) 377–385, http://dx.doi.org/10.1016/j.jpowsour.2012.04.055.

[18] I. Avdeev, M. Gilaki, Structural analysis and experimental characterization of cylindrical lithium-ion battery cells subject to lateral impact, J. Power Sources 271 (2014) 382–391, http://dx.doi.org/10.1016/j.jpowsour.2014.08.014.

[19] J. Xu, B. Liu, X. Wang, D. Hu, Computational model of 18650 lithium-ion battery with coupled strain rate and SOC dependencies, Appl. Energy 172 (2016) 180–189, http://dx.doi.org/10.1016/j.apenergy.2016.03.108.

[20] J. Xu, B. Liu, D. Hu, State of charge dependent mechanical integrity behavior of 18650 lithium-ion batteries, Sci. Rep. 6 (2016) 21829, http://dx.doi.org/10.1038/srep21829.

[21] T. Kisters, E. Sahraei, T. Wierzbicki, Dynamic impact tests on lithium-ion cells, Int. J. Impact Eng. 108 (2017) 205–216, http://dx.doi.org/10.1016/j.ijimpeng.2017.04.025.

[22] T. Wierzbicki, E. Sahraei, Homogenized mechanical properties for the jellyroll of cylindrical Lithium-ion cells, J. Power Sources 241 (2013) 467–476, http://dx.doi.org/10.1016/j.jpowsour.2013.04.135.

[23] A. Sheidaei, X. Xiao, X. Huang, J. Hitt, Mechanical behavior of a battery separator in electrolyte solutions, J. Power Sources 196 (2011) 8728–8734, http://dx.doi.org/10.1016/j.jpowsour.2011.06.026.

[24] S. Yan, X. Xiao, X. Huang, X. Li, Y. Qi, Unveiling the environment-dependent mechanical properties of porous polypropylene separators, Polymers 55 (2014) 6282–6292, http://dx.doi.org/10.1016/j.polymer.2014.09.067.

Journal of The Electrochemical Society, **165** (5) A1160-A1168 (2018)
0013-4651/2018/165(5)/A1160/9/$37.00 © The Electrochemical Society

Testing and Modeling the Mechanical Properties of the Granular Materials of Graphite Anode

Juner Zhu,[1,=,z] **Wei Li,**[1,2,=] **Yong Xia,**[2] **and Elham Sahraei**[1,3]

[1]*Impact and Crashworthiness Lab, Massachusetts Institute of Technology, Cambridge, Massachusetts 02139, USA*
[2]*State Key Lab of Automotive Safety and Energy, Department of Automotive Engineering, Tsinghua University, Beijing 100084, People's Republic of China*
[3]*Electric Vehicle Safety Lab, The George Mason University, Nguyen Engineering Building, Fairfax, Virginia 22030, USA*

The graphite anode of commercial lithium-ion batteries is a typical granular material embedded in a soft binder. To investigate its mechanical properties, a combined experimental/theoretical/numerical study is proposed and performed. On the experimental side, a systematic procedure is established, including graphite anode slurry preparation, cylindrical sample manufacturing, axial/lateral compression tests of the sample, and data analysis. On the theoretical side, the Drucker-Prager cap model, which has been widely used in the powder industry, is adopted. The inter-particle portion of the yields surface of the model is calibrated using the experimental results. On the numerical side, a model in Abaqus/explicit is established with the discrete element method. The Young's modulus of particles and the surface energy per unit area are identified as the two dominant factors that control the contact property of the particles in the discrete element method simulation. By adjusting the two factors together with iterations, a set of optimal values are determined so as to render satisfactory simulation result that can predict the deformation pattern as well as the strength of the granular anode material. At last, the deformation mechanisms of the material are discussed based on the experimental and numerical results.
 [DOI: 10.1149/2.0141807jes]

Manuscript submitted February 26, 2018; revised manuscript received April 9, 2018. Published April 18, 2018.

The mechanical properties of lithium-ion batteries are drawing more attention from the electrochemical community as the markets of electric vehicle (EV) and consumer electronics keep growing. It has been found that the stress field and mechanical failure of the battery components can influence its electrochemical properties.[1–4] Moreover, large deformation of the battery pack and module of EVs subjected to lateral collision[5] or ground impact[6] could expose the battery cells to electric short circuit, thermal runaway, fire, and even explosion.[7–10] The automotive manufacturers, academic and industrial teams, and battery suppliers have jointly attempted to characterize the mechanical behavior of battery cells and design safer batteries. Developing an accurate mechanical model for battery cells has been the subject of a large number of theoretical and numerical investigations.

Existing modeling strategies can be classified into two categories: analytical modeling[11,12] and numerical modeling. The latter includes homogenized models,[13–15] Representative Volume Elements,[16–18] and detailed models.[19,20] The accuracy of these models largely depends on the fundamental understanding of the deformation mechanisms of the components inside a battery, including current collectors, electrodes, and separators. While the aluminum and copper foils and the separators have been extensively studied,[21–24] the electrodes are more complicated because of the granular microstructure, which consists of large number of active particles bonded by the polymeric binder. Two independent deformation mechanisms exist in such materials – sliding and compaction.[25] The former is at inter-particle level for describing the relative movement and rearrangement of two particles, while the latter is at inner-particle level for describing the deformation of an individual particle.

The behavior of granular materials in general is a classical subject in mechanics that has been studied by a large number of theoretical investigations.[26–28] However, it has been a big challenge to perform numerical studies that can well capture the movement of particles. Fortunately, over the past two decades, the computational technology has improved so significantly that it is now possible to carry out particle-by-particle simulation for granular materials.[29,30] The discrete element method (DEM) in Abaqus[31] has become a very powerful numerical tool to characterize the mechanical behavior of granular materials. The advantage of such DEM simulation is that they are based on physical mechanisms and therefore can well predict the pattern of local deformation, such as the shear bands.

The electrodes of lithium-ion batteries are typical granular materials. In order to have a fundamental understanding of their mechanical behavior, joint effort has been made by the mechanical and electrochemical communities. Riley, et al.[32] is perhaps the first study that carried out nanoindentation tests on electrode material to obtain its elastic mechanical property. This type of test was later adopted by Gao, et al.[33] and Zhu, et al.[34] for different materials of cathode and anode, respectively. It turned out to be an effective approach for investigating the elastic deformation of an individual particle or a small area on the surface of an electrode, but with its current analysis procedure, the nanoindentation approach has not been capable of identifying the inter-particle movements. Chen, et al.[35] performed nano-scratch test for graphite anode materials with different binder content, thereby establishing a simplified particle model based on the experimental results. The nano-scratch test can only provide quantitative measurement for the friction coefficient and that it is not effective for studying plastic flow and failure of coated electrodes.

The task of the present paper is to develop a methodology for testing and modeling the mechanical properties of granular materials of electrodes, especially the plastic and fracture behavior. For this purpose, some existing knowledge of the powder metallurgy industry, such as the metal powder technology[36] and pharmaceutical tablets manufacturing,[37–41] are utilized. First, electrode slurry is prepared by mixing the dry graphite powders with PVDF binder according to a recipe of a commercial battery cell, and cylindrical samples are made by filling the slurry into a mold, drying it under fixed environmental conditions, and pre-compacting it to a standard density. Subsequently, the samples are subjected to axial compression and lateral compression, and the force-displacement responses of the samples are obtained. Using the experimental results, the deformation and failure mechanisms of the material are analyzed. To verify these analyses, a numerical model is established using the discrete element method in Abaqus/explicit. Force-displacement response obtained from simulation turned out to have good correlation with the experimental results. The theoretical and numerical work of the paper is based on the assumption that the existence of binder only affects the contact property between particles and its load-bearing contribution by deformation is negligible.

Material and Sample Preparation

Fig. 1 shows the entire sample preparation procedure of the studied anode, which started from dry powders – graphite powders MGP from

[=]These authors contributed equally to this work.
[z]E-mail: zhujuner@mit.edu

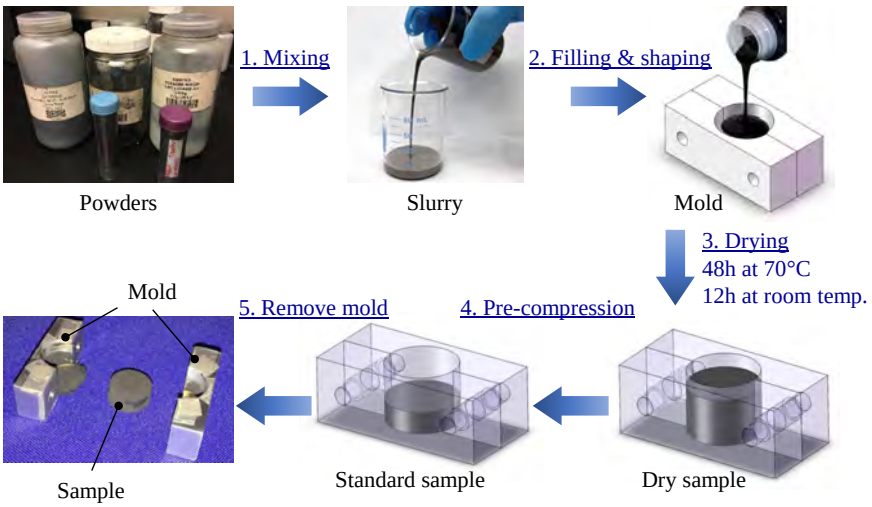

Figure 1. Entire procedure of standard sample preparation for the studied graphite anode granular material.

China Steel Chemical Co. and MAGD from Hitachi Chemical Co., Ltd., and Super P carbon black powder. Solef 6020 PVDF binder (provided by Solvay Specialty Polymers) was dissolved in 1-Methyl-2-pyrrolidone (NMP) to obtain 8.2 wt% PVDF solution. Homogeneous slurry was made by mixing the powders with the PVDF solution, and the final binder content was 4.2 wt%.

An aluminum mold was designed and manufactured to shape cylindrical anode samples. For the convenience of sample removal, the mold was divided into two separate parts that are connected by two bolts. Moreover, low-friction high-temperature-resistance tape made with Teflon PTFE was attached to the surface of the mold for lubrication. Filled with slurry, the mold was moved into an oven at 70°C for 48 hours, and was subsequently put under room temperature for 12 hours. After this process, a dry sample was obtained. To mimic the real situation of the electrodes of commercial batteries, the dry sampled was pre-compressed to a standard density of 3.5 g/cm^3 approximately. Finally, the mold could be disassembled and removed from the standard sample, which was about 16 mm in diameter and 5.1 mm in thickness.

Experimental Investigations

The standard samples were subjected to two typical mechanical loadings, axial compression and lateral compression (Brazilian test). An Instron loading device was employed to deform the sample and measure the force, and the deformation of the samples was recorded by a CCD camera simultaneously with a sampling frequency of 2 images/second.

Axial compression test.—The force-displacement curve of the axial compression test is plotted in Fig. 2, where a clear multiple-stage process is observed. Final shape of the compressed sample is shown in Fig. 3. To better understand the process, the slope (first derivative) of the curve is calculated and plotted in Fig. 2, and at the same time, the deformation sequence recorded by the CCD camera is shown in Fig. 4. In the beginning of the test (Displacement < 1.8 mm, Photo #1 & #2), the main deformation mode is the densification of the granular material, and the first turning point of the force-displacement curve (near to 1.5 mm) marks the start of large plastic deformation, which will be discussed in Discussions: inter-particle sliding and particle compaction and fragmentation section. Displacement 1.8 mm is the inflection point of the force-displacement curve (Photo #3). At this point, the slope stops increasing, and therefore, the force-displacement curve gradually enters a plateau. From Photo #3 in Fig. 4, it is found that this inflection point (1.8 mm) denotes the onset of macroscale cracks at the top of the sample. Interestingly, as the cracks propagate from top to bottom, the granular sample does not totally lose its load bearing capacity. Instead, the force-displacement curve still increases

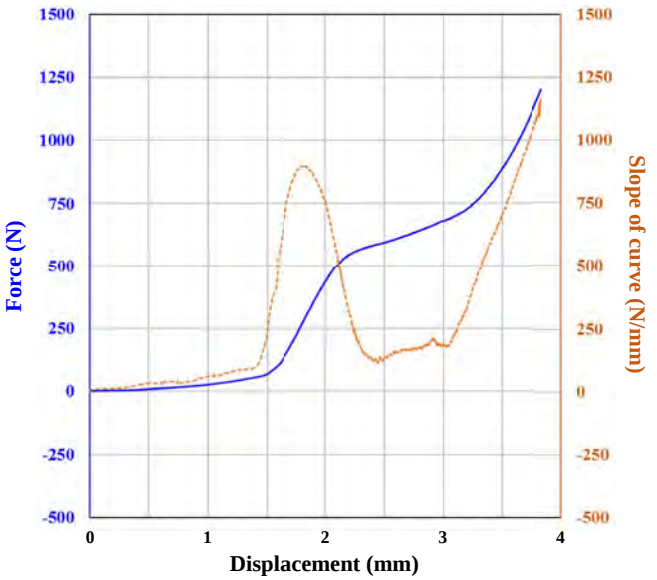

Figure 2. Force-displacement curve and its first derivative of axial compression test.

slowly (2.5 mm – end). This is because the central region with no crack undergoes a compaction process, in which the inner-particle deformation is the dominant deformation mechanism and bears a

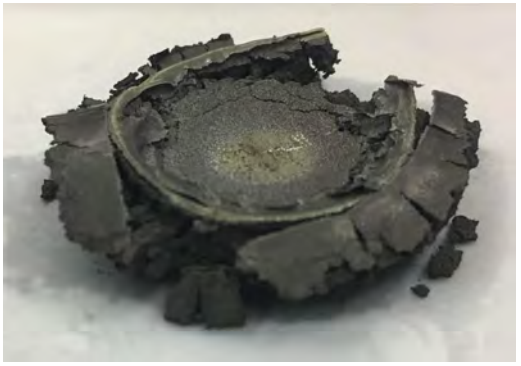

Figure 3. Cylindrical sample after axial compression test.

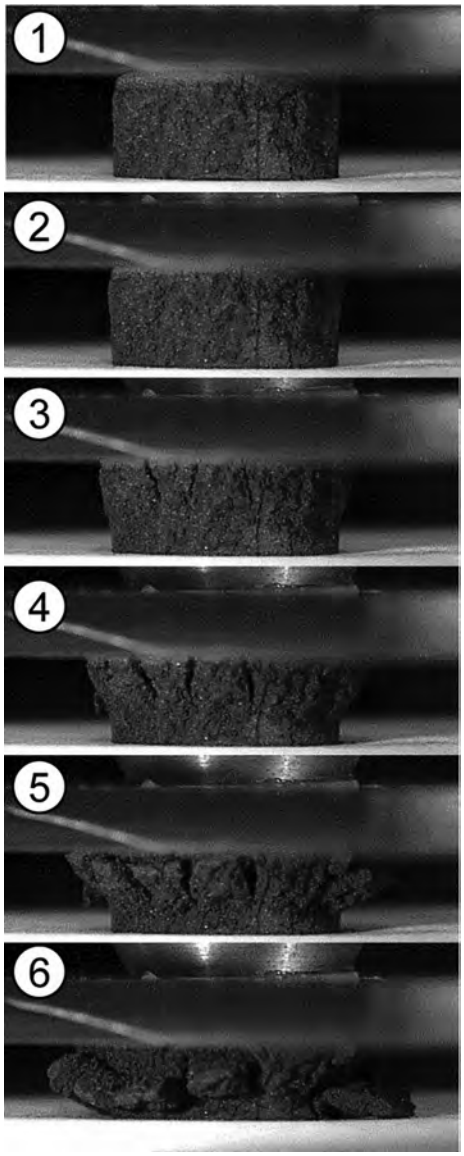

Figure 4. Deformation sequence of the compression test of the cylindrical graphite anode sample.

large force.[27] Photo #4 to #6 in Fig. 4 shows the crack propagation process.

Lateral compression (Brazilian) test.—The lateral compression test, also called Brazilian test, is a classical and useful tool for modeling the mechanical behavior of granular material.[41–43] The cylindrical sample is placed vertically between two rigid plates, which applies compressive load to the sample. Fig. 5 shows the force-displacement curve of the test as well as the slope of the curve. Similar to the axial compression case, there is an inflection point, which denotes the formation of macroscale cracks. Before that, only densification at microscale is evident. After the test, a radial crack through the sample is observed (see Fig. 6).

Experimental data analysis.—The stress state of the granular sample under axial loading is sketched in Fig. 7. Granular materials are commonly not good load bearing media subjected to shear loading, so it is usually assumed that the shear components of the stress tensor are negligible. Hence, two stress invariants are calculated to describe the plastic behavior of granular materials. p is the pressure

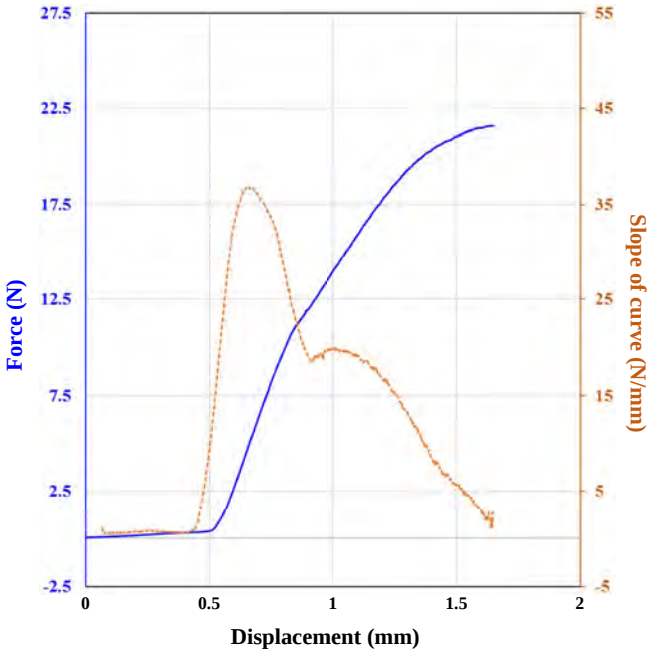

Figure 5. Force-displacement curve and its first derivative of lateral compression test.

(first invariant),

$$p = -(\sigma_{zz} + 2\sigma_{rr})/3. \quad [1]$$

and $\bar{\sigma}$ (or denoted as q in some publications) is the Mises equivalent stress (second invariant),

$$\bar{\sigma} = |\sigma_{zz} - \sigma_{rr}|. \quad [2]$$

For both studied loading cases, there is a linear relation between pressure p and Mises equivalent stress $\bar{\sigma}$ in the sample – $\bar{\sigma} = 3p$

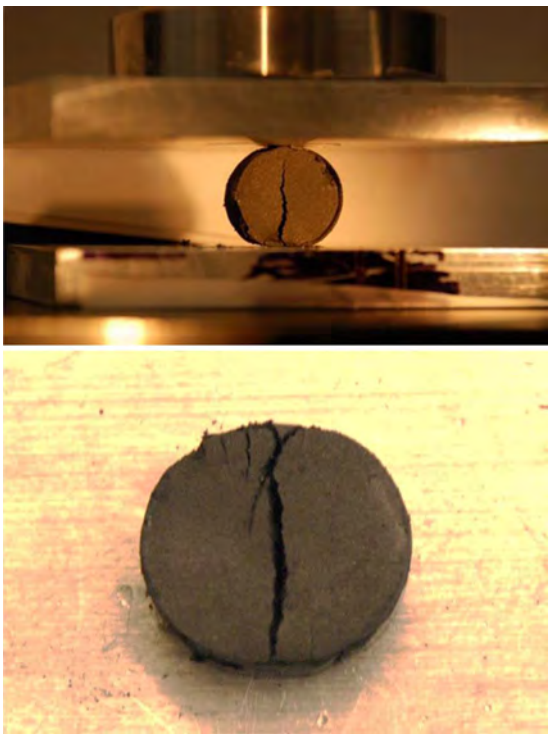

Figure 6. Cylindrical sample after lateral compression test.

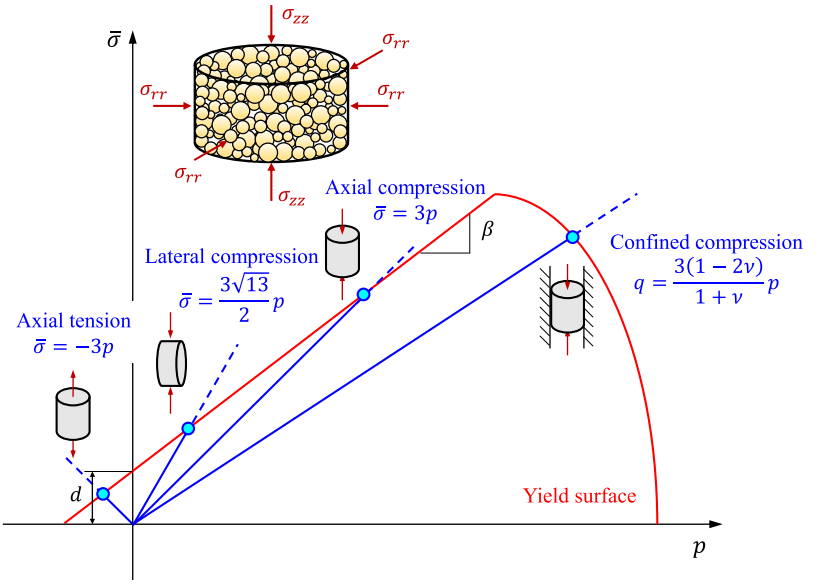

Figure 7. Yield surface and stress states of the graphite anode sample. Red solid curve is the yield surface of Drucker-Prager cap model. Blue dashed curves starting from the origin are the stress state of axial tension, lateral compression, axial compression, and confined compression.

for axial compression and $\bar{\sigma} = (3\sqrt{13}/2)p$ for lateral compression. The lateral compression test is not as straightforward as the axial compression. A detailed derivation for the stress state can be found in open literature.[41,44,45] The two linear relations are plotted in the $(p, \bar{\sigma})$ space as blue dashed straight lines starting from the origin of the coordinate in Fig. 7. In a practical test, the sample deforms elastically until the stress meets the yield surface, which is represented by the red solid curve. Here, the yield surface of the Drucker-Prager cap model[25,31,40,44] is adopted for the studied anode material. The model consists of two separate parts, covering the two deformation mechanisms at inter-particle and inner-particle levels. At the inter-particle level, the deformation of material is the sliding and shear failure between particles, which is described by the yield function

$$F_s = \bar{\sigma} - p\tan\beta - d = 0, \qquad [3]$$

where β is the friction angle and d is the cohesion between particles. At the inner-particle level, the deformation happens in individual particles, which is known as compaction and is represented by

$$F_c = \sqrt{(p-p_a)^2 - (Rq)^2} - R(d + p_a\tan\beta) = 0, \qquad [4]$$

where R is the eccentricity of the ellipse, and p_a is the critical pressure that leads to compaction of material.

The two parts of the yield surface, F_s and F_c, are sketched in Fig. 7. It is clear that F_s is a straight line, while F_c is one quadrant of an ellipse, known as the "cap" of the model. p_a is the p-axis of the intersection point of the shear failure and cap surfaces.

Usually, the friction angle of granular materials is low, and the axial compression and lateral compression curves can only meet the inter-particle yield surface F_s for the first yield, as shown in Fig. 7. In other words, samples in these two tests will result in inter-particle failure, which is sliding followed by macroscale cracks. This agrees well with the experimental observations of the present study. As mentioned in Axial compression test section, at the late stage of the axial compression test, the material continues to harden after a short plateau. This post-yield behavior is due to the compaction of the central core of the sample, which will be further discussed in Numerical simulation with discrete element method section and Discussions: inter-particle sliding and particle compaction and fragmentation. Here, for the calibration of F_s, only the first yield behavior will be analyzed (before 2 mm displacement in Fig. 2).

The experimental data of the axial and lateral compression tests can be used to determine the friction angle β of the graphite anode material. It is worth noting that no simple stress-strain curve could be determined explicitly from either of these two tests, because of the non-uniformity of the deformation field in the sample. A common practice for the calibration of friction angle in the powder industry is adopting the maximum force of the curves as the characteristic point to calculate the "crush stress". However, for the studied graphite material, it is found that the force keeps increasing due to the compaction process. Therefore, alternatively, the inflection points that denote the onset of macroscale cracks are utilized as the first yield points. The forces at the two inflection points with maximum slope of curve, F_y^a and F_y^l, are determined from Fig. 2 and Fig. 5, respectively. Hence, the yield stresses for the two cases are calculated. For the axial compression, we have

$$\bar{\sigma}_y^a = \frac{4F_y^a}{\pi D^2}, \qquad [5]$$

and for lateral compression, it can be derived following Refs. 41–43,

$$\bar{\sigma}_y^l = \frac{2F_y^l}{\pi Dt}, \qquad [6]$$

where $D = 16$ mm is the diameter, and $t = 5.13$ mm is the sample thickness.

As shown in Fig. 7, these two yield stresses are the intersection points between the blue dashed straight lines ($\bar{\sigma} = 3p$ and $\bar{\sigma} = 3\sqrt{13}p/2$) and red solid yield surface. Using the geometric relations, cohesion d and the friction angle β can be determined:

$$d = \frac{\bar{\sigma}_y^a\bar{\sigma}_y^l\left(\sqrt{13}-2\right)}{\bar{\sigma}_y^a + 2\bar{\sigma}_y^l}, \qquad [7]$$

$$\beta = \tan^{-1}\left[\frac{3\left(\bar{\sigma}_y^a + d\right)}{\bar{\sigma}_y^a}\right]. \qquad [8]$$

For the studied anode material, it is determined as $d = 59.5$ kPa and $\beta = 70.9^\circ$. Thus, the sliding part of the yield surface F_s is calibrated.

To calibrate the "cap" surface of F_c, a third test is needed. A common choice in open literature is the confined loading test, in which the sample is put into a rigid die and thus cannot expand transversely. Using elasticity theory, the linear relation between $\bar{\sigma}$ and p can be obtained: $\bar{\sigma} = 3(1-2\upsilon)p/(1+\upsilon)$, where, υ is the Poisson's ratio. This linear path is plotted in Fig. 7 as well. It is clearly dependent on the Poisson's ratio of the material. For example, incompressible materials, whose υ is 0.5, shall have an equivalent stress of zero when subjected to confined compression. For the studied granular material for anode, it is difficult to obtain the Poisson's

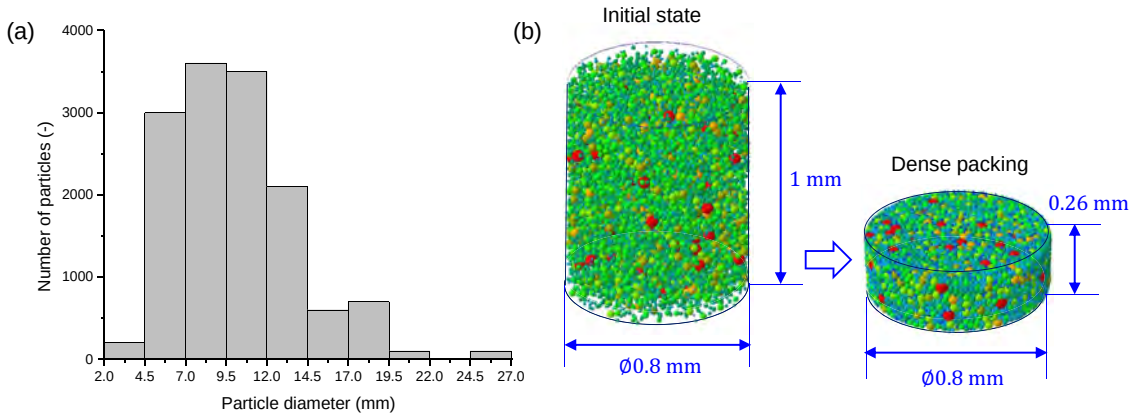

Figure 8. Geometry preparation (a) particle size distribution (b) initial state and dense packing of particles.

ratio accurately from the axial compression test because of the non-uniform displacement field. For this reason, $\bar{\sigma}$ and p has to be measured directly from the confined loading test, which requires at least one pressure sensor embedded in the rigid wall to obtain a history of σ_{rr}. Moreover, the probe of the sensor has to be small enough to fit the size of sample without bringing extra influence. At the stage of this present study, due to the lack of such device, confined compression test has not been covered. As a result, the inner-particle level yield surface F_c cannot be fully calibrated. More discussions about it will be provided in Discussions: inter-particle sliding and particle compaction and fragmentation section.

Predicting the tensile strength of the anode material.—The calibration results in the above section could be used to predict the strength of other loading conditions. A typical example is the axial tension condition, in which the linear relation between $\bar{\sigma}$ and p is: $\bar{\sigma} = -3p$. In the $\bar{\sigma} - p$ coordinate, this curve is a flip of the curve of axial compression over the $\bar{\sigma}$-axis (see Fig. 7). Substituting this relation into Eq. 3 gives

$$\bar{\sigma}_y^{tension} = \frac{d}{1 + \tan\beta/3}. \quad [9]$$

Plugging $d = 59.5$ kPa and $\beta = 70.9^\circ$ into Eq. 9, $\bar{\sigma}_y^{tension}$ turns out to be 30.3 kPa.

In reality, it is difficult to carry out axial tension test on pure anode material because of the lack of effective grippers. For such granular materials, the gripping pressure cannot be too large to crack the sample, which is a big challenge to also confirm reliable boundary condition. Most of the existing experimental data reported by open literature is from tensile tests of the entire anode (an assembly of graphite/copper/graphite) and subtracting the stress-strain curve of copper from the overall response of the assembly.[14] It has been known that the tensile strength is significantly dependent on the binder content. Recently, an graphite anode with a binder content of 5% wt was tested by the authors' team.[34] The tensile strength turned was estimated to be around 100 kPa, which is close to the $\bar{\sigma}_y^{tension}$ obtained in the present study. The main discrepancy comes from two sources. One is the measurement of strength. In the assembly of graphite/copper/graphite, the strength of graphite is almost negligible compared to that of the copper, which makes it very difficult to accurately obtain the contribution from the graphite coating. The other is the calibration of the DPC model. Only two tests, axial compression and lateral compression, were used to determine the linear portion of the yield surface. From Fig. 7, it can be seen that these two points are very close to each other in the $\bar{\sigma} - p$ coordinate, thus limiting the accuracy of the calibration.[44]

Numerical Simulation with Discrete Element Method

A numerical simulation is conducted using discrete element method (DEM) in Abaqus/Explicit. To increase the computational efficiency but keep the same deformation pattern as that of the experiments, the geometry of the simulation model is scaled down 20 times of the size of the test sample without changing the height/diameter ratio (5/16). To mimic the practical powder material of the graphite anode, it is required that the model is a random dense packing of sphere particles, which has to be realized in Abaqus by two separate steps. At the first step, a "cloud" of spherical particles were generated and distributed within a cylindrical space (1 mm height, 0.8 mm diameter), and the particles have no initial contact between one another. There are 13900 particles following a size distribution as shown in Fig. 8a, which is suggested by Ref. 46, to achieve an initial density of 0.1625. In the second step, a pre-simulation is run to let the particles settle under gravity load and then a uniaxial compression load is applied. The pre-simulation stops when the particles establish initial contacts with each other without noticeable penetration.[47,48] As a result, a random dense packing of sphere particles is obtained, as shown in Fig. 8b. All the particles are contained in a cylindrical space (0.26 mm height, 0.8 mm diameter) with a relative density of 0.625, which is close to the practical anode material. Note that the height to diameter ratio (0.26/0.8) of the simulation geometry is also close to that of samples in the experiments (5/16).

In DEM, the binder between particles is not described as real elements. Its tensile property is characterized as the cohesion in the contact algorithm in the FE model. Meanwhile, the particles are assumed to be non-deformable in geometry, and the compressive deformation of particles are controlled by the contact properties, which in this study is described by the Johnson-Kendall-Roberts (JKR) adhesive normal contact model.[31] It relates the contact force P to the contact area A, as follows

$$P = \frac{4E^* \cdot A^3}{3R^*} - \sqrt{8\pi\Gamma \cdot E^* \cdot A^3} \quad [10]$$

The effective Young's modulus E^* and effective radius R^* can be determined by

$$\frac{1}{E^*} = \frac{1 - {v_1}^2}{E_1} + \frac{1 - {v_2}^2}{E_2} \quad [11]$$

$$R = \frac{R_1 R_2}{R_1 + R_2} \quad [12]$$

where v_i, E_i, R_i $(i = 1, 2)$ denote the Poisson's ratio, the Young's modulus, and the radius of two contacting particles. In this study, it is assumed that all the particles have identical mechanical properties, $v_1 = v_2$ and $E_1 = E_2$. Γ is the surface energy per unit area of the two contacting particles. Note that the Young's modulus and Poisson's

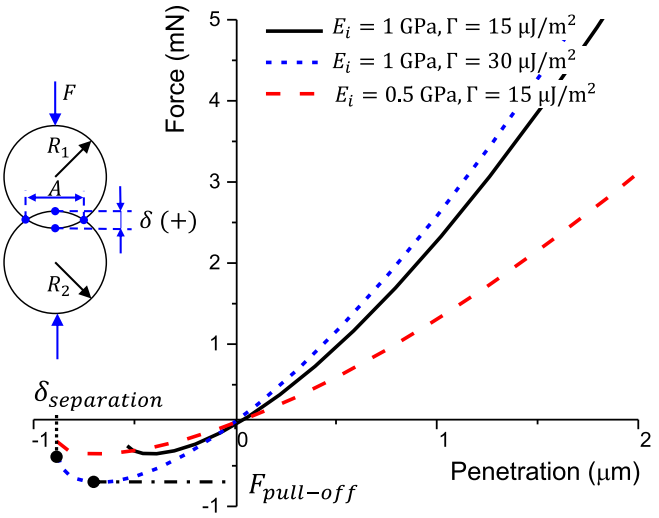

Figure 9. The normal contact behavior of the shifted-JKR model.

ratio here refer to the properties of individual particles, instead of those of the granular material consisting of myriads of particles.

In the JKR model, the approaching distance δ for two contacting particles is also related to the contacting area A by

$$\delta = \frac{A^2}{R^*} - \sqrt{\frac{2\pi\Gamma \cdot A}{E^*}} \quad [13]$$

With Equations 10 and 13, the contact area A can be eliminated and thus the force-penetration relation of normal contact can be determined. Simulations with the Poisson's ratio of particles of 0.05, 0.2, 0.3 and 0.4 were carried out, respectively, while keeping the other parameters unchanged. It was found that the Poisson's ratio of particles has an almost negligible contribution to the force P, and therefore it is set to 0.3 according to existing publications.[49] The effective Young's modulus E^* and surface energy density Γ are two dominant factors. Fig. 9 shows the force-penetration relation for different Young's Modulus and surface energy density. Note that the curves are shifted horizontally to have zero forces under zero penetration, which is also referred to as the shifted-JKR model.[32] A positive penetration (inner-particle deformation) renders a compressive force in the contacting surface, and a negative penetration (i. e. separation of two particles) results in a tensile force, which can describe the adhesion of the binder between particles. As the separation increases to reach the pull-off force, the tensile force starts to drop and finally becomes zero at a critical separation distance. Comparing the three cases in Fig. 9, it can be clearly seen that surface energy density controls the pull-off force or the cohesive property and the Young's modulus largely determines the contacting force or the inner-particle deformation. This conclusion will be utilized to calibrate the two coefficient for the studied graphite anode material.

Table I. Material parameters of the DPC model and DEM model and calibration results.

Parameter	Value
Cohesion, d	59.5 kPa
Friction angle, β	70.9°
Friction coefficient, tan β	2.88
Effective Young's modulus, E^*	1 GPa
Surface energy density, Γ	15 μJ/m²
Poisson's ratio of single particle, v	0.3

The friction coefficient is determined from the experimental results in Experimental data analysis section as 2.88 (tan 70.9°). However, attaining the Young's modulus and surface energy density of a micro size graphite particle from experiment is tricky – various values of modulus of graphite powder have been reported in existing publications, ranging from 1–50 GPa.[49–51] At the same time, it is difficult to find a reference value for the surface energy density Γ between graphite particles. Therefore, simulations with various coefficients are conducted and optimized to inversely calibrate the two values. Simulation results with three different sets of parameters are plotted in Fig. 10, and it is found that a Young's modules of 1 GPa and a surface density of 15 μJ/m² can provide the best prediction of the experimental results. The calibrated material parameters of DPC model and DEM model are listed in Table I.

The gradual force increases at the initial deformation stage of experiments cannot be observed in the simulation because the numerical model is developed with initial contact between particles fully established. Thus, the simulation results are shifted horizontally for comparison with experiments, and the figure therefore starts from 1 mm. From Fig. 10, we can see that the simulation result with E = 1 GPa and Γ = 15 μJ/m² well matches the experimental result up to the peak stress in axial compression case. It is expected that the discrete particle model cannot characterize the compaction behavior (after 2 mm) in the axial compression test. This is because the particles in the discrete element method are assumed to be non-deformable. For this reason, the inner-particle portion of the experimental curve

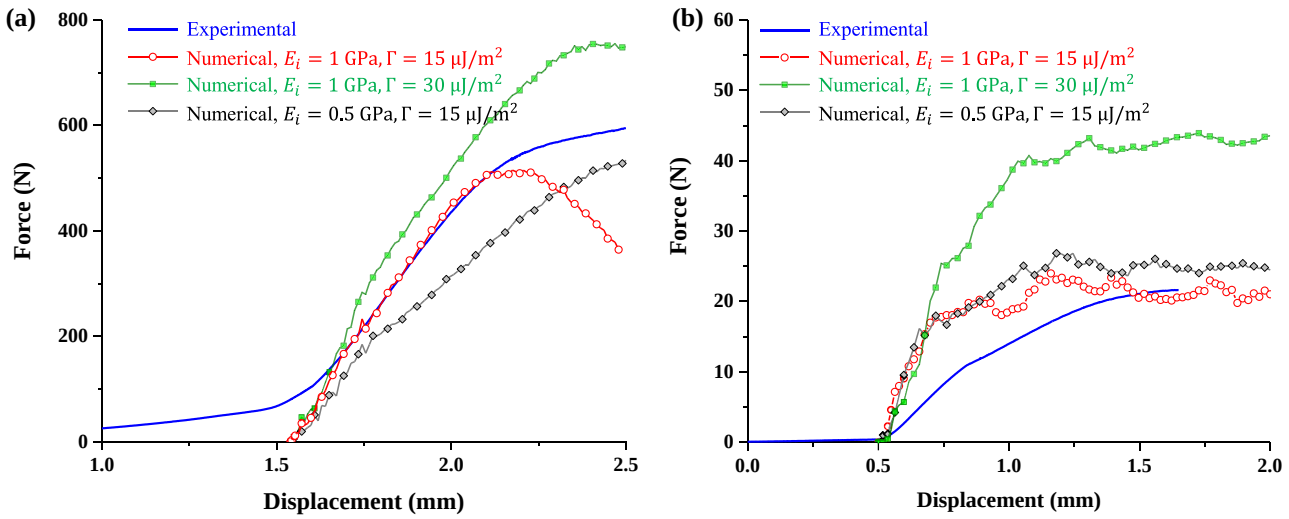

Figure 10. Simulation results with DEM (a) axial compression (b) lateral compression.

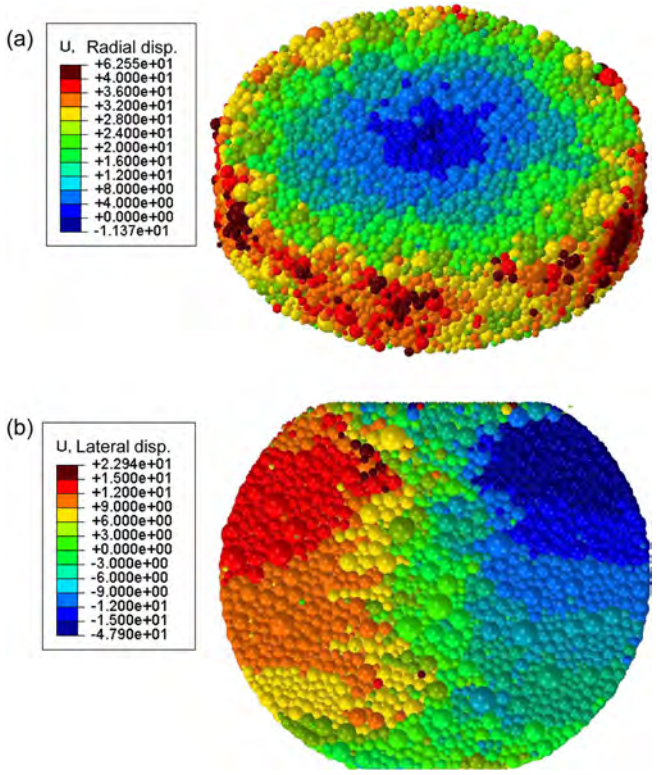

Figure 11. Deformed configurations of (a) axial compression and (b) lateral compression.

is not plotted in Fig. 10a. In the lateral loading case, it turns out that the force-displacement curve cannot be described accurately, but the force level and overall trend can be well predicted. The reason also lies in the fact that there is no initial gap between particles in the numerical model, which is different from the experimental case.

Comparing the predictions by the three sets of parameters, it is found that under axial compression the slope of stress-strain curve is mainly controlled by the Young's modulus of single particle and the surface energy density only affects the peak stress, while under lateral loading, the stress-strain response is largely determined by surface energy density and Young's modulus has a negligible influence. Here, it should be pointed out that these two coefficients of material properties do not reflect the real deformation of individual particles. In the discrete element method, the deformation of particles is considered only in the contact algorithm. Therefore, it is hard to evaluate the dominant deformation mechanism in the tests like what is done in Experimental data analysis section using the continuum model.

The deformed configuration are extracted at the displacement of 2 mm and 1.5 mm for axial compression and lateral compression, respectively, as shown in Fig. 11. In the axial compression case (Fig. 11a), the radial displacement of the free surface is much larger than that of the inner core and the particles at the edge appear to separate. It means that the edge surface may have cracks while the inner core undergoes consolidation, which is consistent with experimental observations (Fig. 3). In the lateral compression case (Fig. 11b), the contour of lateral displacement is presented. It can be seen that the left part of sample moves leftward and right part moves rightward, which means that the sample is being tore apart through the middle axis, as observed in experiment. However, it is worth noting that no clear cracks are observed in both cases of simulation. This is due to the difference between the contact algorithm of the simulation and the practical structure of the anode material. The bonding strength between two particles goes to zero once sliding happens, but in the simulation, the cohesive force is a function of contact area and thereby always exists unless the distance between the two particles becomes sufficiently large. How to modify the contact algorithm to include the effect of sliding should be an important task for further improvement of the numerical model.

Discussions: Inter-Particle Sliding and Particle Compaction and Fragmentation

Due to the lack of confined compression test in this study, it is not possible to fully calibrate the inner-particle level yield surface, which describes the deformation of an individual particle. However, it was found that compaction of particles happened in the axial compression tests at a late stage. This can be clearly observed from the cracked sample after test shown in Fig. 3 as well as the force-displacement curve after 2 mm in Fig. 2. In this section, the compressive deformation mechanism of the anode graphite material will be discussed.

Fig. 12a shows the surface of the original graphite anode tilted at 52°, which clearly shows the configuration of the particles. Focused ion beam (FIB) was used to obtain a cross-sectional view of the original graphite anode sample (see Fig. 12b). It is worth noting that the image is from an electrode film of a commercial battery with same materials and similar binder content, instead of the large bulk sample that were tested. This operation is because of the size limit of the FIB device. It can be seen that the anode is composed of particles with similar diameters. There is already some contact among the particles before compression because of the low binder content. Moreover, a number of initial cracks exist inside the particles. When subjected to compression, some of these cracks will be closed first. This observation can explain why there is a relatively slow increasing stage in the force-displacement curve before 1.5 mm compression. Fig. 12c shows the cross-section of the fully-compressed graphite anode. It can be seen that most of the initial cracks are closed and only some fault lines are visible.

Based on these cross-sectional views of the graphite anode material, the deformation sequence can thereby be speculated, as shown in the schematic of Fig. 13. Overall, it is a combined result of inner-particle and inter-particle deformation, which compete with each other and the weaker one dominates the deformation. At the start of the test,

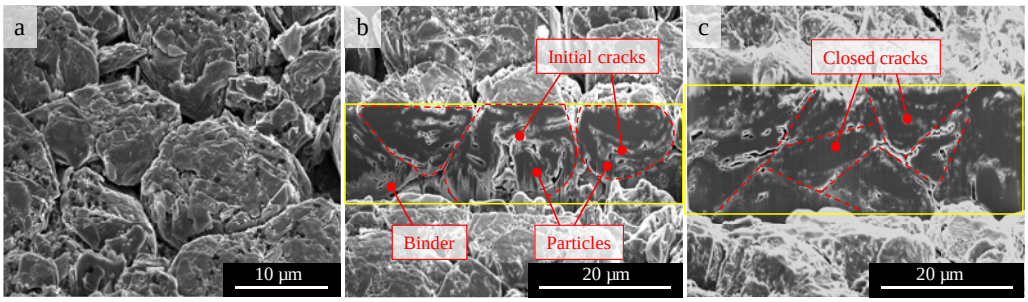

Figure 12. (a) Surface view tilted at 52° and (b) cross-sectional view cut by focused ion beam of the original graphite anode, (c) cross-sectional view of the fully-compressed graphite anode.

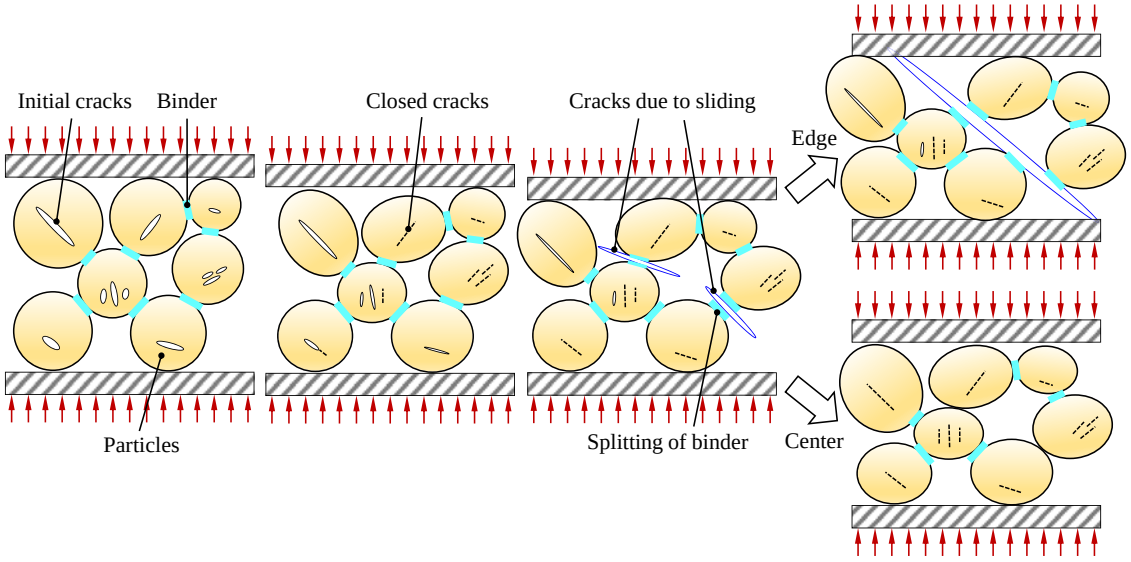

Figure 13. Schematic of the deformation sequence of the axial compression test, which is a combined result of inner-particle and inter-particle deformation.

the major deformation happens inside the highly porous particles, which is comparatively weak. As a result, some of the initial cracks are closed, and the force starts to increase rapidly. During this stage, some particles slide over one another, causing some micro cracks to appear. At the edge of the sample, it is easy for these micro cracks to coalesce and form macroscale cracks, but in the central region, the material is in a state of confined condition and therefore a compaction process goes on. In the compaction process, almost all the cracks inside the particles are closed.

In most conventional continuum mechanical models for granular materials like the Drucker-Prager cap model that was used in the present study, it is always presumed that there is no initial crack in the particles and the particles are stiff and hard. For metal powders, this presumption is true. However, for the studied graphite particles that are porous, it is not valid. During the deformation process, inter-particle and inner-particle deformation happens almost simultaneously. This unique mechanism may have an influence on the yield behavior, which is out of the capability of the Drucker-Prager cap model. How the model should be modified to cover this mechanism has to be further investigated.

Concluding Remarks

This study presents a combined experimental/theoretical/numerical investigation into the mechanical properties of the granular material of a graphite anode. The major contributions of the study are: 1) establishing a systematic experimental procedure that includes sample preparation and testing for investigating the mechanical properties of the graphite anode, especially, plasticity and failure behavior under mechanical loading, 2) proposing the use of the Drucker-Prager cap model for the characterization of anode material, and 3) developing a discrete particle model in Abaqus/explicit to simulate the deformation of the graphite anode.

The main conclusions about the mechanical properties of the studied anode material can be summarized as follows. 1) There are two deformation mechanisms governing the plastic behavior, inter-particle sliding and particle compaction. 2) The critical deformation mode that leads to failure in the axial/lateral compression tests is inter-particle sliding, but at the late stage of axial compression, there is large amount of compaction. 3) The Drucker-Prager cap model is suitable for the characterization of the granular graphite anode material, and it can be calibrated by three tests, axial compression, lateral compression, and confined compression. 4) The discrete element method is an effective tool to simulate the anode material. It can well predict the inter-particle deformation pattern as well as the strength level of the material, but cannot provide insights into the inner-particle compaction.

The methodologies and conclusions of the present study can be generalized to other granular materials used for anodes and cathodes. Meanwhile, we have to acknowledge that, as the first study that applies these methodologies and models from powder technology area to battery research, this is a preliminary work and can be further improved. Future directions should provide more information from confined compression tests to fully calibrate the DPC model. The DEM model should be improved to properly describe the failure of cohesion due to sliding. Finally, the deformation of the particles in the DEM model should be taken into account.

Acknowledgment

The authors are grateful to the MIT Battery Modeling Consortium (Altair, AVL, Boston-Power, Daimler, Jaguar-Land Rover, LG Chem, Murata, and PSA Groupe) and Ford-MIT Alliance for the financial support. Thanks are due to Professor Tomasz Wierzbicki for the constructive comments about this paper. J.Z. thank Dr. Ankita Shah Faulkner, Dr. Qina Sa, Ms. Ruolin Zhou, and Dr. Joanna Turteltaub for their valuable advices on the preparation of anode slurry and dry anode samples. Financial support provided by China Scholarship Council (CSC) during the visit of W.L. to MIT is acknowledged. This work made use of the Shared Experimental Facilities supported in part by the MRSEC Program of the National Science Foundation under award number DMR – 1419807.

ORCID

Juner Zhu https://orcid.org/0000-0001-7072-2293
Yong Xia https://orcid.org/0000-0002-9586-9678

References

1. G. Bucci, T. Swamy, S. Bishop, B. W. Sheldon, Y.-M. Chiang, and W. C. Carter, *Journal of The Electrochemical Society*, **164**(4), A645 (2017).
2. G. Bucci, T. Swamy, Y.-M. Chiang, and W. C. Carter, *arXiv preprint arXiv:1703.00113*, (2017).
3. B. Wu and W. Lu, *Journal of The Electrochemical Society*, **163**(14), A3131 (2016).
4. B. Wu and W. Lu, *Journal of Power Sources*, **360**(Supplement C), 360 (2017).
5. M. Funcke, S. Schäfer, R. Wohlecker, D. Dufaut, D. Sturk, and K. EU Report, Optimised Storage Integration for the Electric Car. 2014.
6. Y. Xia, T. Wierzbicki, E. Sahraei, and X. Zhang, *Journal of Power Sources*, **267**, 78 (2014).

7. S. Abada, G. Marlair, A. Lecocq, M. Petit, V. Sauvant-Moynot, and F. Huet, *Journal of Power Sources*, **306**, 178 (2016).
8. V. Ruiz, A. Pfrang, A. Kriston, N. Omar, P. Van den Bossche, and L. Boon-Brett, *Renewable and Sustainable Energy Reviews*, **81**(1) 1427 (2018).
9. X. Feng, M. Ouyang, X. Liu, L. Lu, Y. Xia, and X. He, *Energy Storage Materials*, **10**, 246 (2018).
10. J. Zhu, T. Wierzbicki, and W. Li, *Journal of Power Sources*, **378**, 153 (2018).
11. E. Sahraei, J. Meier, and T. Wierzbicki, *Journal of Power Sources*, **247**, 503 (2014).
12. E. Sahraei, R. Hill, and T. Wierzbicki, *Journal of Power Sources*, **201**, 307 (2012).
13. T. Wierzbicki and E. Sahraei, *Journal of Power Sources*, **241**, 467 (2013).
14. E. Sahraei, M. Kahn, J. Meier, and T. Wierzbicki, *RSC Advances*, **5**, 80369 (2015).
15. E. Sahraei, J. Campbell, and T. Wierzbicki, *Journal of Power Sources*, **220**, 360 (2012).
16. W.-J. Lai, M. Y. Ali, and J. Pan, *Journal of Power Sources*, **248**, 789 (2014).
17. W.-J. Lai, M. Y. Ali, and J. Pan, *Journal of Power Sources*, **245**, 609 (2014).
18. E. Sahraei, E. Bosco, B. Dixon, and B. Lai, *Journal of Power Sources*, **319**, 56 (2016).
19. J. Marcicki, M. Zhu, A. Bartlett, X. G. Yang, Y. Chen, T. Miller, P. L'Eplattenier, and I. Caldichoury, *Journal of The Electrochemical Society*, **164**(1), A6440 (2017).
20. J. Zhu, X. Zhang, E. Sahraei, and T. Wierzbicki, *Journal of Power Sources*, **336**, 332 (2016).
21. X. Zhang, E. Sahraei, and K. Wang, *Journal of Power Sources*, **327**, 693 (2016).
22. X. Zhang, E. Sahraei, and K. Wang, *Scientific Reports*, **6**, 32578 (2016).
23. X. Zhang, J. Zhu, and E. Sahraei, *RSC Advances*, **7**(88), 56099 (2017).
24. C. Bonatti and D. Mohr, *Materials Science and Engineering: A*, **654**, 329 (2016).
25. C. Gu, M. Kim, and L. Anand, *International Journal of Plasticity*, **17**(2), 147 (2001).
26. A. Schofield and P. Wroth, *Critical state soil mechanics*, McGraw-Hill London (1968).
27. L. Anand and C. Gu, *Journal of the Mechanics and Physics of Solids*, **48**(8), 1701 (2000).
28. K. Kamrin and M. Z. Bazant, *Physical Review E*, **75**(4), 041301 (2007).
29. R. Kawamoto, E. Andò, G. Viggiani, and J. E. Andrade, *Journal of the Mechanics and Physics of Solids*, **111**, 375 (2018).
30. L. Sibille, N. Hadda, F. Nicot, A. Tordesillas, and F. Darve, *Journal of the Mechanics and Physics of Solids*, **75** (Supplement C), 119 (2015).
31. Dassault Systèmes, *Abaqus analysis users' manual*, Providence, RI, USA, (2017).
32. L. A. Riley, A. S. Cavanagh, S. M. George, S.-H. Lee, and A. C. Dillon, *Electrochemical and Solid-State Letters*, **14**(3), A29 (2011).
33. X. Gao, Z. Ma, W. Jiang, P. Zhang, Y. Wang, Y. Pan, and C. Lu, *Journal of Power Sources*, **311**, 21 (2016).
34. J. Zhu, X. Zhang, H. Luo, and E. Sahraei, submitted for publication, (2018).
35. J. Chen, J. Liu, Y. Qi, T. Sun, and X. Li, *Journal of The Electrochemical Society*, **160**(9), A1502 (2013).
36. B. Zhang, M. Jain, C. Zhao, M. Bruhis, R. Lawcock, and K. Ly, *Powder Technology*, **204**(1), 27 (2010).
37. C. Shang, I. C. Sinka, and J. Pan, *International Journal of Pharmaceutics*, **445**(1), 99 (2013).
38. A. Baroutaji, K. Bryan, M. Sajjia, and S. Lenihan, *Reference Module in Materials Science and Materials Engineering*, (2017).
39. T. Sinha, J. S. Curtis, B. C. Hancock, and C. Wassgren, *Powder Technology*, **198**(3), 315 (2010).
40. I. C. Sinka, J. C. Cunningham, and A. Zavaliangos, *Powder Technology*, **133**(1), 33 (2003).
41. L. H. Han, J. A. Elliott, A. C. Bentham, A. Mills, G. E. Amidon, and B. C. Hancock, *International Journal of Solids and Structures*, **45**(10), 3088 (2008).
42. S. Garner, J. Strong, and A. Zavaliangos, *Powder Technology*, **283**(Supplement C), 210 (2015).
43. H. Y. Li and G. Y. Shi, *International Journal of Impact Engineering*, **89**, 38 (2016).
44. C. Shang, I. C. Sinka, and J. Pan, *Experimental Mechanics*, **52**(7), 903 (2012).
45. S. Timoshenko and J. N. Goodier, *Theory of elasticity*, McGraw-Hill book Company (1951).
46. S. A. Roberts, V. E. Brunini, K. N. Long, and A. M. Grillet, *Journal of The Electrochemical Society*, **161**(11), F3052 (2014).
47. C. L. Martin, D. Bouvard, and S. Shima, *Journal of the Mechanics and Physics of Solids*, **51**(4), 667 (2003).
48. P. Pizette, C. L. Martin, G. Delette, P. Sornay, and F. Sans, *Powder Technology*, **198**(2), 240 (2010).
49. X. Xiao, W. Wu, and X. Huang, *Journal of power sources*, **195**(22), 7649 (2010).
50. K. Takahashi, K. Higa, S. Mair, M. Chintapalli, N. Balsara, and V. Srinivasan, *Journal of The Electrochemical Society*, **163**(3), A385 (2016).
51. Y. Qi, H. Guo, L. G. Hector, and A. Timmons, *Journal of The Electrochemical Society*, **157**(5), A558 (2010).

Journal of The Electrochemical Society, **165** (7) A1537-A1546 (2018)
0013-4651/2018/165(7)/A1537/10/$37.00 © The Electrochemical Society

State-of-Charge Dependence of Mechanical Response of Lithium-Ion Batteries: A Result of Internal Stress

Wei Li,[1] Yong Xia,[1,z] Juner Zhu,[2] and Hailing Luo[1]

[1]*State Key Laboratory of Automotive Safety and Energy, Tsinghua University, Beijing 100084, People's Republic of China*
[2]*Department of Mechanical Engineering, Massachusetts Institute of Technology, Cambridge, Massachusetts 02139, USA*

Effect of state-of-charge on the mechanical response of lithium-ion batteries subjected to mechanical abuse loading are studied. Indentation tests are performed on a cylindrical cell and a pouch cell at different states-of-charge. The test results evidence that the mechanical behavior of the cylindrical cell is significantly state-of-charge dependent, while for the pouch cell it is almost state-of-charge independent. To clarify the cause of such a difference in state-of-charge dependence, two control tests are designed and executed. Based on the control test results, we conclude that the internal stress to resist the charging-induced volume expansion of jellyroll is the major reason for state-of-charge dependence of the mechanical behavior. We also conclude that the difference in state-of-charge dependence between the two types of cells is closely associated with the casing stiffness (stiff metallic casing vs. soft pouch) and the construction method of jellyroll (winding versus stacking), which together create different conditions of resisting the volume expansion and retaining the internal stress. A supplementary test is carried out on the pouch cells under a normal cyclic charging-discharging condition to measure the volume expansion and the reaction force of the unconstrained and constrained pouch cell respectively.
 [DOI: 10.1149/2.0051809jes]

Manuscript submitted March 5, 2018; revised manuscript received May 9, 2018. Published May 22, 2018.

Lithium-ion batteries have been widely used as the power source of electric vehicles due to their high energy and power densities. However, more and more catastrophic accidents of electric vehicles have been reported, in which the battery smoked, fired, and even exploded under severe mechanical deformation. A large number of studies have been conducted to investigate the mechanical response and the short circuit induced by mechanical loading.[1–15] However, most of them are limited to a low state of charge (SOC) or a discharged state, despite the fact that the electric vehicles normally operates at a higher SOC when a crash accident happens. Thus, it is of great importance to figure out the influence of SOC on the mechanical behavior and the onset of the internal short circuit to improve the battery safety design of electric vehicles. Xu et al.[12] reported a significant SOC-dependence of mechanical integrity of the 18650 cylindrical cell, which was later supported by the work of Tsutsui et al.[8] However, for pouch cells, it was reported by Meier et al.[5] that the SOC-dependence is not significant under spherical punch head indentation loading. This conclusion was further verified by the present authors' team in a recent publication.[4] Thus, existing studies by different investigating teams appear to conflicts with each other, and the mechanisms of SOC-dependence still remain to be clarified.

During charging and discharging, the lithium ions move between cathode and anode, which involves a series of chemical reactions accompanied by the mass transfer process. The chemical compositions of the active material of cathode and the graphite coating of anode change due to lithium-ion intercalation and deintercalation. This can affect the mechanical properties of the anode and cathode coatings, which may further influence the overall mechanical performance of battery cell. Another fact is that the graphite (especially with silicon) structure expands and shrinks significantly during charging and discharging process, thereby resulting in the volume expansion of the cell.[16–20] Considering that the lithium-ion batteries usually operate under constrained conditions such as being wrapped with a plastic pouch or a metallic shell casing, the volume expansion in a constrained space may induce a field of internal stress and subsequently influence the mechanical and electrical behaviors of the cell.[21–25]

In summary, the mechanical response of battery cell subjected to external loading could vary with SOC in two possible mechanisms: (1) the change of mechanical properties of cathode and anode coatings, and (2) internal stress induced by the volume change during charging. On the first mechanism, Qi[26] used a density function theory to reveal an increasing compressive Young's modulus of graphite particles (anode coating) during the charging process due to lithium ion intercalation, and Yang[27] reported a decreasing Young's modulus of the active particles (cathode coating) due to lithium-ion de-intercalation. As an assembly, a battery cell consists of the same number of anodes and cathodes, and it has not been ensured whether a simple superstition can be applied to such a situation. Therefore, how the property changes in the electrode materials can contribute to the overall compressive behavior of a charged cell remains unclear. To clarify it, more test data at the macro level are greatly needed. On the second mechanism (the effect of expansion-induced internal stress), Cannarella et al.[22] ran a cyclic charging-discharging of a battery cell under an external constraint condition and found that the reaction force changed dynamically during the process and increased gradually over a long time, which also leads to a high rate of chemical degradation.

The purpose of this study is to investigate the SOC-dependence of the response of lithium-ion batteries under mechanical abuse. In the first section, mechanical abuse tests under different SOCs are performed on cylindrical cells and pouch cells to observe their SOC-dependence. The following section presents two control tests investigating the effect of the internal stress caused by volume expansion, which is speculated to be the main reason for the SOC-dependent behavior. Firstly, the jellyrolls of the cylindrical cell and pouch cell were obtained by removing the casing or pouch and tested under different SOCs. Secondly, a sandwich-like fixture was designed to conduct mechanical abuse tests on pouch cell with external constraints at different SOCs. The last section delivers a supplementary study under the normal operation condition. Experimentally, the deformation of unconstrained pouch cell is measured, and the reaction force of constrained pouch cell is recorded, which together with an analytical model helps to understand the volume expansion-induced internal stress.

Mechanical Abuse Tests of Cylindrical Cells and Pouch Cells at Different SOCs

To investigate the effect of SOC on the mechanical performance, indentation tests of two different types of commercial lithium-ion battery cell under different SOCs were conducted. One is a commercial Samsung 18650 cylindrical cell of 3300 mAh and the other is a commercial pouch cell of 20 Ah for electric vehicle use. The cathode active materials of the cylindrical cell and the pouch cell are Lithium Nickel Cobalt Aluminum Oxide (NCA) and Lithium Nickel Manganese Cobalt Oxide (NMC), respectively, and both cells have graphite anodes. Figs. 1a–1b show the main components of

[z]E-mail: xiayong@tsinghua.edu.cn

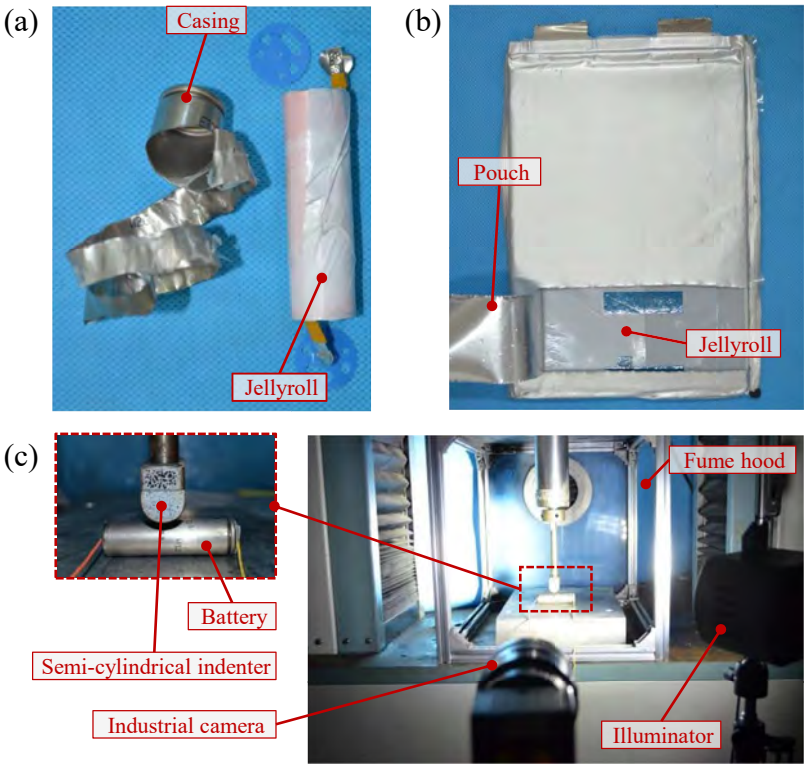

Figure 1. Disassembled (a) cylindrical and (b) pouch cell, the main parts are jellyroll and casing/pouch; (c) Indentation test setup of the cylindrical cell.

the disassembled cylindrical cell and pouch cell, for more detailed information, readers can refer to reference.[4,15] In general, both types of battery cells consist of a jellyroll and a casing. The main difference between the two types lies in two aspects: (1) the steel casing of the cylindrical cell is thicker and stronger than the aluminum pouch of the pouch cell, and thus has a stiffer structural performance; (2) the jellyroll of the cylindrical cell is winded with pre-stretched single whole films of components, while for the jellyroll of the pouch cell, the stacks of components are piled up layer by layer, and an internal pressure is subsequently imposed by vacuuming the pouch.

Cylindrical cells at different SOCs.—Lateral indentation tests with a 20 mm diameter semi-cylindrical steel bar were performed at four SOCs. The dimension of 20 mm is chosen as the same order of the diameter of the cylindrical cell (18 mm). With this dimension, the mechanical property under indentation can be well reflected according to the results presented in the following. Out of the same consideration, the diameter (12.7 mm) of the hemispherical punch head for the pouch cell is also chosen as the same order of the cell thickness (8 mm). The test setup is shown in Fig. 1c. All the tests were conducted in a universal test machine equipped with a 50 kN load sensor under a loading speed of 6 mm $\cdot$ min^{-1} (0.0001 m $\cdot$ s^{-1}). The sample and fixture were placed in a fume hood for safety consideration. The indentation displacement was recorded by a CCD camera and the data was processed by digital image correlation (DIC) method. The open circuit voltage (OCV) was recorded by a digital data acquisition device.

First, two repeats of indentation tests on the 0% SOC cells were carried out until 20 kN to obtain a preliminary understanding of the entire deformation process. The force and OCV responses are shown in Fig. 2a. Two local force peaks are observed. The first force peak corresponds to the local buckling of the casing and the damage initiation of the jellyroll. The battery keeps bearing load until the second peak when the terminal end fractures and the jellyroll is squeezed out. The force then drops again until the battery is fully compacted. The whole deformation process is shown in Fig. 2a. On the other hand, it can be seen that the OCV drops shortly before the first peak force. According to an observation in a previous publication of the authors' team,[4] it is inferred that the voltage drop corresponds to the inflection point in the force-displacement curve when the internal damages start to accumulate. The inflection point can be identified by calculating the slope of the force-displacement curve and finding the peak value. Change of the slope reflects the change of the local stiffness under indentation loading. Fig. 2b is the zoom-in around the peak slope in Fig. 2a, clearly showing the change of the slope and the drop of OCV. It implies that the inflection point can be chosen as an indicator of the internal short circuit in this loading condition.

Indentation tests were conducted on the cylindrical cells charged to SOCs of 10%, 30%, and 50%, respectively. The test results including those at 0% SOC are shown in Figs. 2c–2f, where all of the curves are plotted until the displacement of 8 mm to clearly present the responses at the early stage. Observed from the tests, no explosion occurs at 0% and 10% SOC, while two out of the three samples at 30% SOC suffer an explosion. For the samples at 50% SOC, severe thermal runaway happens followed by an explosion, and the jellyrolls are ejected out and burned. Therefore, 30% SOC appears to be a transition point, at which the risk of explosions starts to increase. Interestingly, the cases with severe explosion can be easily distinguished from the force-displacement response, where a quick drop of force takes place (see Figs. 2e and 2f). On the side of electrical response, the OCV of the cases without explosion (either without quick force drop) starts to drop before the peak force and around the inflection point. For the cases with an explosion (also with quick force drop), the OCV drops simultaneously with the force drop.

Fig. 3a shows a comparison of the mechanical response before displacement of 5 mm (the drop of voltage in the case of 50% SOC) for the cells at different SOCs. A significant SOC-dependence is observed, – the battery tends to be stiffer as the SOC increases. The force at 5 mm intrusion under 50% SOC increases around 20% compared with that under 0% SOC. Fig. 3b shows the intrusion displacements at the drop of voltage – a tendency of decrease is observed along with the increase of SOC. In other words, as the SOC increases, the internal short circuit of the 18650 battery cell under indentation is more likely to occur. One possible explanation is that under a higher SOC the mechanical damage initiates earlier due to the higher internal stress and with

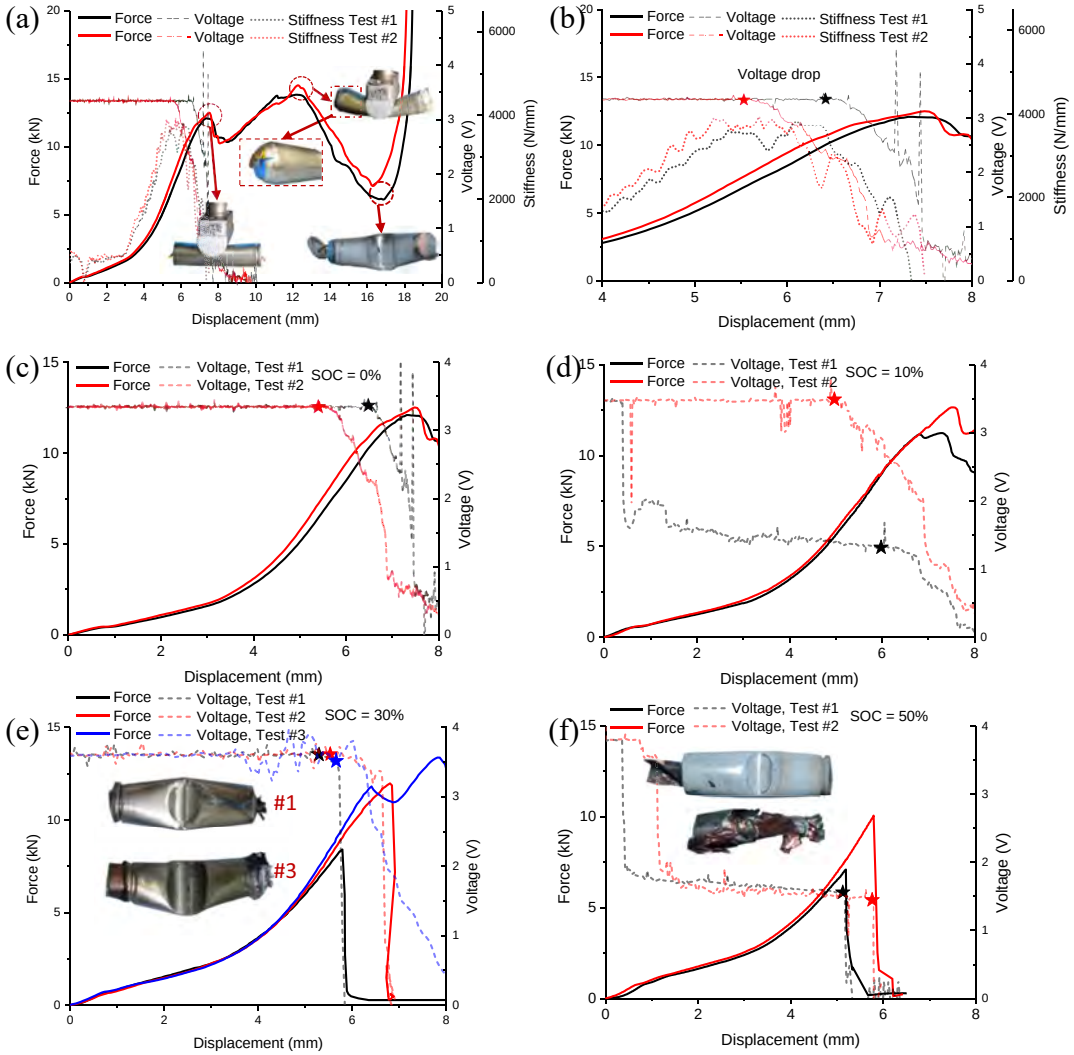

Figure 2. Test results at 0% SOC: (a) mechanical response and featured events along with increasing indentation, and (b) correlation between voltage drop and the inflection point in force-displacement curve; and test results at four different SOCs: (c) 0%, (d) 10%, (e) 30%, and (f) 50%.

higher electric energy, a slight damage is likely to trigger the internal short circuit.

Pouch cells at different SOCs.—Indentation tests of the pouch cells were performed with a 12.7 mm diameter hemispherical punch head and a 24 mm diameter flat-end cylinder, respectively, under a loading speed of 1 mm · min^{-1}. The test setup was the same as described previously for the cylindrical cell except for the type of punch head. As the capacity of the pouch cell is much larger than that of the cylindrical cell, it is dangerous to conduct abuse tests of pouch cells at very high SOC. Therefore, the hemispherical indentation tests, which cause very severe deformation in a local region, were only performed at two relatively low SOCs (0% and 30%). However, the flat-end indentation tests were performed at three different SOCs up to 100%, because no short circuit occurs within 50 kN (i.e. the loading capacity of the test machine in the present study) in this case. This gives us a chance to observe the influence of SOC on mechanical performance of the pouch cell within a large range of SOC without inducing uncontrollable thermal runaway.

The test results of hemispherical indentation at different SOCs are shown in Fig. 3c. No apparent change in mechanical performance is observed, especially before the inflection point of the force-displacement curve. The same observation can be found for flat-end indentation (Fig. 3d). Therefore, we can safely conclude that the mechanical performance of the pouch cell under each of the two loading cases is insensitive to SOC. On the side of electrical response, it can also be observed that SOC has no apparent influence. Besides, it can be observed that the voltage drops around the peak force, lagging behind the occurrence of the inflection point, which is different from the observation of the cylindrical cell. For pouch cells under indentation, the internal damage does start to accumulate at the inflection point,[4] but has not been severe enough to trigger the internal short circuit until the peak force.

Summary on SOC-dependence for the two cell types.—According to the test results, the SOC effects on the mechanical abuse response of the cylindrical cell and the pouch cell are clearly different. The former shows a strong SOC-dependence of both electrical and mechanical response, but the latter has no apparent SOC-dependence. The observations are in good agreement with existing publications.[4,5,8,12]

As described in Introduction, there are two possible reasons for the SOC-dependence. The first one is the change of material properties due to the intercalation of lithium in the graphite and deintercalation in the lithium-ion metal oxide. This characteristic was used to explain the experimental results in.[12] However, it is questionable according to the test results in the present study. If the change of material properties due to charging-discharging is the dominant cause, a clear SOC-dependence should have been observed in the

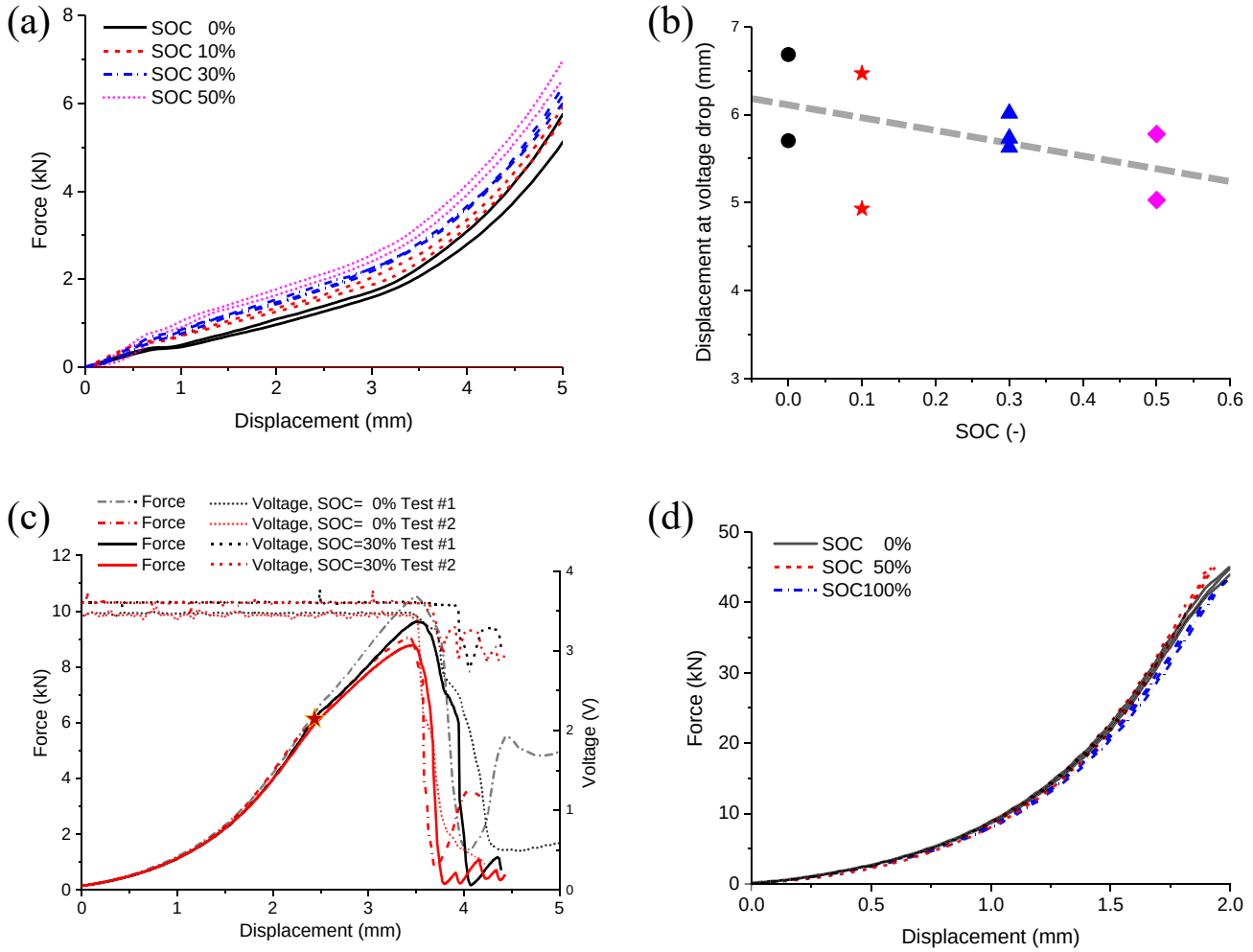

Figure 3. SOC-dependence of the cylindrical cell: (a) force-displacement responses before voltage drop, and (b) intrusion displacements at voltage drop; and SOC-dependence of the pouch cell under (c) hemispherical punch head indentation, and (d) flat-end cylinder indentation.

force-displacement curves of the pouch cell. However, the experimental evidence shows the contrary. In addition, we have verified that the difference in cathode materials is not the primary source of the SOC-dependence (see Appendix). Therefore, the first possible mechanism is excluded.

The second possible mechanism is the internal stress induced by volume expansion of the jellyroll. According to the results of the current study, this should be the main cause leading to the two different SOC-dependences. For the two cell types, the major differences in the structure are the construction form of jellyroll and the stiffness of casing, as described above. As illustrated in Fig. 4a, a high internal stress can easily develop within the cylindrical cell when the volume expansion during charging is strongly limited by the metallic casing and the winding jellyroll structure, while the internal stress in the pouch cell is almost negligible because it is difficult to restrict the volume expansion with the relatively flexible pouch and the stacking jellyroll structure. As validation, two control tests were performed which are presented in the following section.

Experimental Analysis on the Effect of Internal Stress

Indentation tests on jellyrolls of cylindrical cell and pouch cell.— To evaluate the influence of the internal stress caused by the jellyroll construction, the jellyrolls of two studied types of cells were prepared by dismantling the cylindrical or pouch cells, and then the mechanical abuse tests were conducted on the jellyrolls. The cylindrical cell was charged to a desired SOC at first, and then carefully disassembled to get the inside winding jellyroll with terminals remained, as shown in Fig. 1a. The winding jellyrolls at different SOCs were laterally loaded with the semi-cylindrical bar. The pouch cell was fully discharged at first. A window was then opened on the pouch (see Fig. 1b) and the packaging stress upon the stacking jellyroll was released. Indentation test with the flat-end cylinder was performed on the stacking jellyroll in this window area up to 20 kN, which ensures not causing damage to the jellyroll. After that, the tested stacking jellyroll was charged to a higher SOC, which was then subjected to the indentation of the flat-end cylinder at another position in the window area.

The test results shown in Figs. 4b–4c manifest that the cylindrical winding jellyroll has a remarkable SOC-dependence while the flat stacking jellyroll has no apparent SOC-dependence. For the stacking jellyroll, the volume expansion during charging is prominent, corresponding to sufficient release of the internal stress (a further demonstration is provided in Section Supplementary study: volume expansion of unconstrained cell and reaction force of constrained cell). Therefore, its SOC independence is understandable. Again, it demonstrates that the overall mechanical behavior of the jellyroll is less affected by the property change of the individual component materials due to charging.

Comparatively, the winding jellyroll cannot expand freely when charged due to the tightly rolling structure, so the internal stress remains at a high level even though the metallic shell casing has been removed. It is observed that in the indentation test of the winding jellyroll at a higher SOC (30%), an explosion occurs, which is a much violent response compared with the fracture propagation at the

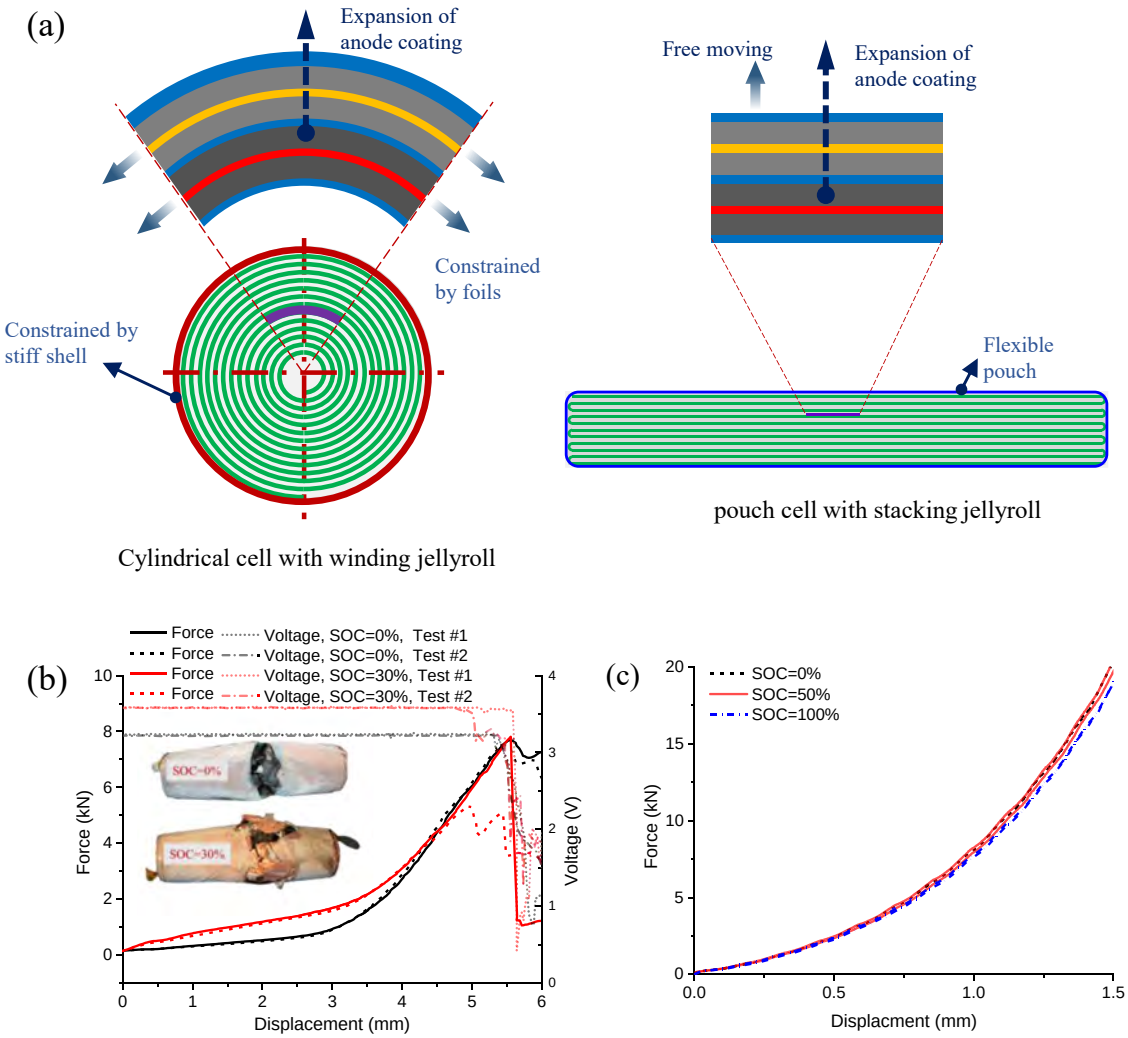

Figure 4. a) Schematic illustration of the structural differences between cylindrical cell and pouch cell and the different constraint effects on volume expansion. Test results of jellyroll at different SOCs: (b) jellyroll of cylindrical cell, (c) jellyroll of pouch.

bottom side of the jellyroll at 0% SOC, as shown in Fig. 4b. It indirectly demonstrates that a higher internal stress is kept inside the winding jellyroll at the higher SOC.

The control test on the two types of jellyroll demonstrates that a different jellyroll construction may have a different capacity to retain the internal stress due to charging, and subsequently result in different SOC-dependence of its mechanical abuse response. On the other hand, it should be noted that the SOC-dependence of the winding jellyroll is somewhat different from that of the integrated cylindrical cell, which means that the constraint from the shell casing also has a considerable contribution to the SOC-dependence of the cylindrical cell.

Indentation test of pouch cell under external constraint.—The other control test is designed to study the effect of the internal stress because of external constraints. The idea is applying constraints to the upper and lower surfaces of the pouch cell with rigid plates. It is expected that a remarkable internal stress can develop when the jellyroll inside tends to expand, unlike what happens in the unconstrained pouch cell. The rigid plates function like the shell casing of the cylindrical cell. To achieve this goal, a sandwich-like fixture was designed and fabricated, as shown in Fig. 5a.

In the fixture, the pouch cell is placed between the lower and middle plates, while the eight bolts connecting the two plates to assemble the fixture and applying the constraining force. Four strain gauge-based force sensors distributed between the upper and middle plates are used to measure the force applied to the pouch cell when the bolts are fastened or the jellyroll expands during charging. Circular holes are left in the centers of the upper and the middle plates, through which the flat-end indentation test can be performed on the pouch cell.

To study the effect of internal stress under different levels of external constraints, four loading cases were performed (see Fig. 5b). In Case A and Case B, the cells at 0% SOC were charged to 100% SOC at first without being constrained beforehand. After that, the cell of Case A was subjected to indentation loading without the fixture, while the cell of Case B was constrained by the fixture with zero pre-tightening force and then subjected to indentation loading. In Case C and Case D, the cells at 0% SOC were constrained at first by the fixture with 0 kN and 5 kN pre-tightening force, respectively, and then charged to 100% SOC. After that, all the fully charged cells of Case C and Case D were subjected to indentation loading. Note that in Case D, the pre-tightening force was applied by the fastening bolts and the punch head together. Appropriate proportion and increment of the forces were adopted to apply the pre-tightening as evenly as possible.

The results of this control test are shown in Fig. 5b. We can see that the response of Case B is in accordance with that of Case A, which means that the fixture design is reasonable and does not affect the mechanical response. Besides, a significant increase in force can be observed from Case B to Case C and to Case D. This indicates that when the pouch cell is constrained to prevent free volume expansion,

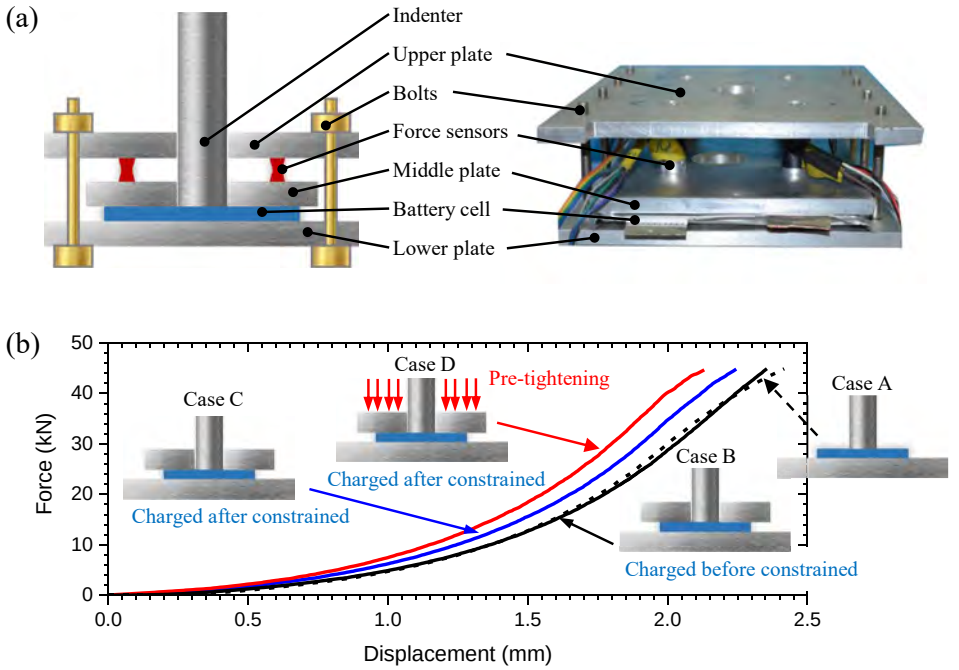

Figure 5. (a) Fixture design for indentation test of constrained pouch cell. (b) Indentation test results of constrained pouch cell under four different loading conditions.

the mechanical response becomes stiffer as the SOC increases, and a higher pre-tightening force, which means a stronger constraint, leads to a stiffer response.

This phenomenon can be explained as follows. The internal stress of the constrained cell develops during charging, and a stronger constraint results in a higher internal stress. With this internal stress, the constrained cell sustains a higher force under the same indentation compared with the unconstrained cell. Another aspect to understand this phenomenon is that the internal stress reduces the initial slack inside the cell and a smaller indentation is required to reach the same force. Therefore, the constrained cell has a stiffer mechanical response after charging.

Supplementary Study: Volume Expansion of Unconstrained Cell and Reaction Force of Constrained Cell

To support the above discussions on the effect of the volume expansion-induced internal stress on the SOC-dependence, two issues will be further explored in this section, the volume expansion of an unconstrained pouch cell and the reaction force of a constrained pouch cell under normal operating (charge/discharge) condition. A simple analytical model is then utilized to predict the reaction force during charging and to illustrate the relationship between the internal stress and the external constraint that limits the volume expansion.

Measurement of volume expansion of unconstrained cell.—In literature, various methods have been employed to measure the thickness change of batteries during charge-discharge, such as high accuracy displacement sensor[28] and 3D DIC method.[29] The 3D DIC method utilized in this study is an efficient and accurate way. The test system is shown in Fig. 6a. The 3D-camera system consists of two cameras facing downward at the cell's upper surface at a certain angle. The cell was placed on the horizontal ground, and the two edges of the pouch are fixed by a fixture to avoid possible rigid movement due to non-uniform deformation. The battery was firstly fully charged with the constant current following constant voltage method (constant current of 0.6C to 4.2 V and then constant voltage of 4.2 V to 1200 mA current), after standing for 90 minutes, it was then discharged with a constant current of 0.6C to 2.75V, and stood for another 90 minutes. Five cycles were performed and the displacement field of the cell's upper surface was measured.

The displacement fields under different SOCs along different directions are presented in Fig. 6c. X and Y directions are along the length and width directions, respectively. A positive value along Z-axis corresponds to an expansion along the thickness direction. From Fig. 6c, it can be seen that the displacement along the thickness direction (Z direction) is the most significant, while displacement along the width direction (Y direction) is much smaller, and the displacement along the length direction (X direction) can be neglected. The displacement field is not uniform and is concentrated in the area close to the terminals. In addition, the displacement increase along thickness direction is not significant before 70% SOC and quickly goes up to the maximum value in the later charging process.

The time history of the displacement along thickness direction is shown in Fig. 7a. The average displacement is calculated over the whole displacement field and the maximum displacement is extracted from a small area (10 mm × 10 mm) in the displacement concentration area. The peak to valley value of displacement (relative change) during charging was extracted in Fig. 7b. We can see from Fig. 7a and Fig. 7b that the cell experienced a large expansion during the first cycle, and the peak displacement gradually increases with cycles and approaches a steady state after 4th cycle. This trend is consistent with the results reported by Leung et al.[29] The residual displacement after each charge-discharge cycle is due to the less reversible binder expansion and particle stacking,[29] and the internal gas evolution[30] might contribute to the increasing peak displacement with cycles. Assuming the displacement fields of the upper surface and bottom surface of pouch cell are symmetric, the volume expansion during first charging cycle is around 6.5% and approaches a steady value of 2.8% after 4 cycles. Fig. 7c shows the thickness expansion with SOC during the charging stage of the last (#5) cycle. It can be observed that the thickness expansion is not linear to SOC. As mentioned before, the thickness starts to increase significantly after 60% SOC.

Measurement of the reaction force of constraint cell.—To measure the reaction force of a constrained cell during charging and discharging, the same fixture in the previous section (Fig. 5a) was adopted, except that there was no central hole in this case. The cell was cycled five times according to the same procedure described in Fig. 6b, under three different constraint conditions by applying

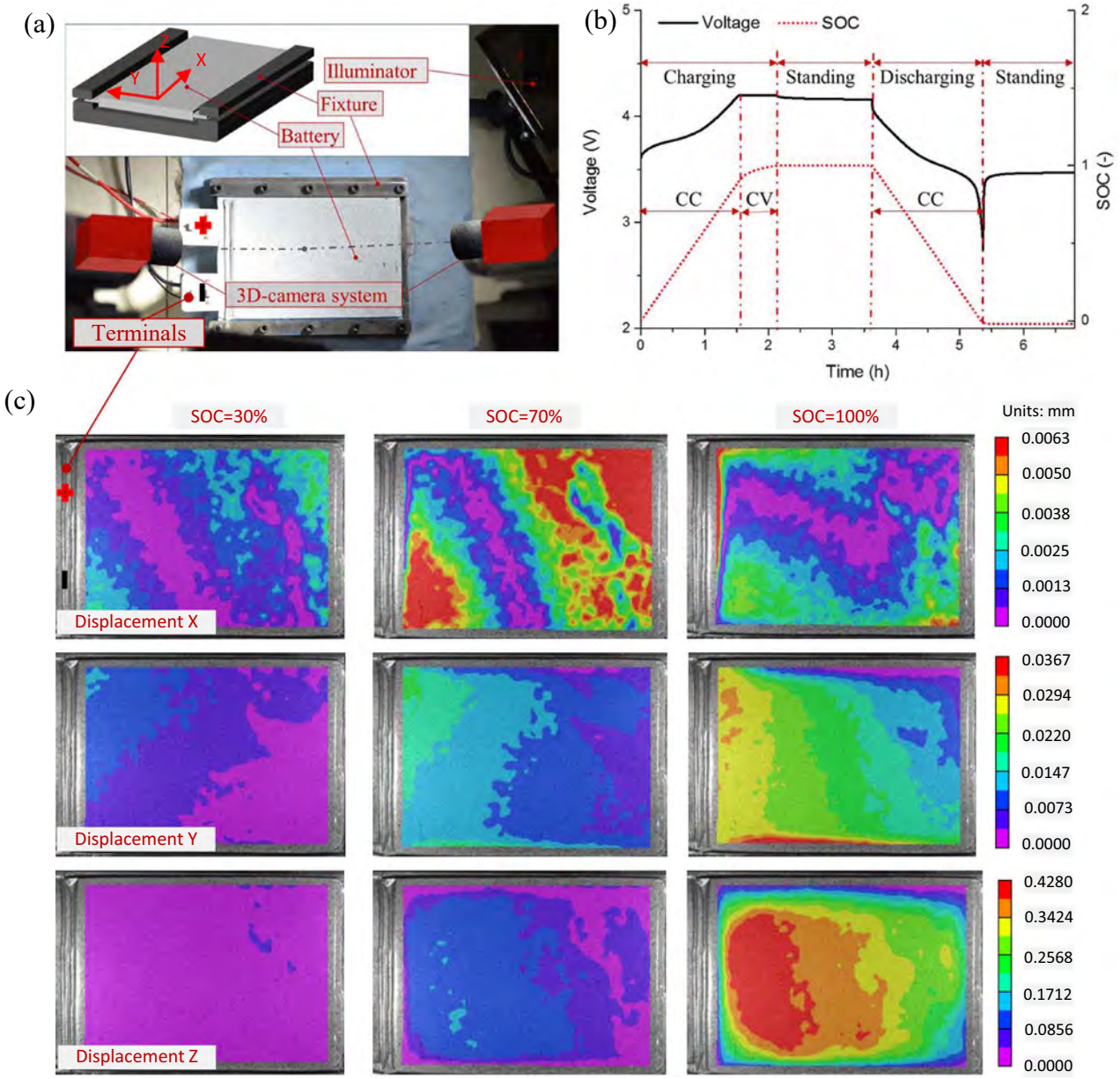

Figure 6. (a) Test setup for the 3D measuring system. (b) Charging and discharging cycle. (c) Deformation field at different SOCs.

different levels of pre-tightening force (0 kN, 1 kN, 5 kN). The reaction force due to the resistance to the volume expansion was recorded, and the results under 1kN pre-tightening force were presented in Fig. 7c. The reaction force increases during charging, and the peak force tends to decrease and reaches a steady state after 4 cycles, which is similar to the phenomenon observed in Figs. 7a–7b. The force decreases during the standing stage, which indicates that the mechanical property of the cell includes viscous effect due to the internal stress relaxation.

To compare the reaction force responses under the three different constraint conditions, the changes in force (excluding the pre-tightening force) are plotted in Figs. 7d and 7e. Note that under 0 kN pre-tightening condition, the reaction force does not show a consistent pattern, but there is still a cyclic change. A possible reason is that the force is not well detected due to the non-uniform deformation of the cell. Similar to the change of thickness expansion, the change of reaction force is also not linear to the SOC change (see Fig. 7c). The peak to valley value (relative change of force) during charging is extracted and compared in Fig. 7f. The relative change of force under 5 kN constraint is larger than that under 1 kN constraint.

Analytical model for estimating reaction force.—An analytical model[31] is adopted and modified to describe the internal stress induced by volume expansion within the constrained cell. The volume expansion can lead to a decrease in porosity and increase in the dimensions of electrodes. As illustrated in Fig. 8a, we can imagine an intermediate state, where the cell is freely expanded due to charging, and then it is compressed to the final state due to the constraint. The compressive deformation (Δl_{por}), which decreases the porosity,[32] subtracts a remarkable proportion of the free expansion (Δl_{exp}), while the remaining part is the dimensional change of cell (here we only consider the thickness change and neglect the change along width and length directions). The thickness change (Δl_{dim}) is also the elongation of the bolts. The relation can be expressed as follows.

$$\Delta l_{por} + v l_{dim} = \Delta l_{exp} \quad [1]$$

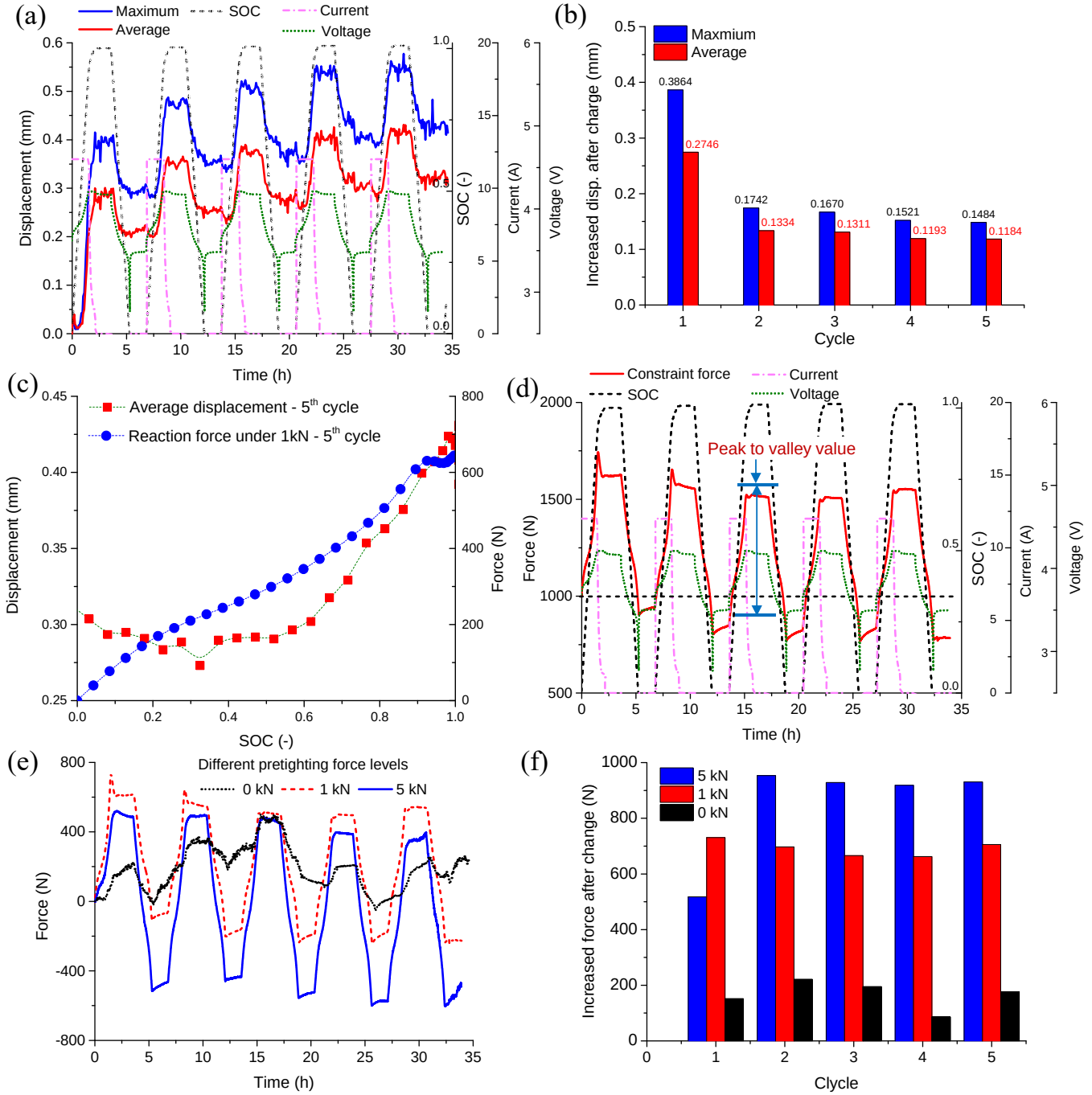

Figure 7. (a-b) Unconstrained cell: displacement-time history along thickness direction and the relative change of thickness for each charging cycle. (c) Average thickness expansion and relative increase of reaction force versus SOC at the last cycle. (d-f) Constrained cell: reaction force-time history and the relative increase of force for each charging cycle.

with

$$\Delta l_{por} = \left(T + \Delta l_{exp}\right) \cdot \varepsilon_{por} \quad [2]$$

$$\Delta l_{dim} = L \cdot \varepsilon_{dim} \quad [3]$$

where T is the thickness of pouch cell, and ε_{por} is the compressive nominal strain due to the decrease of porosity. L is the length of bolt constraining the cell. ε_{dim} is the nominal strain of bolt, which is equal to the dimension change of pouch cell. Since the reaction force acting on the cell and bolts are in equilibrium, we have

$$F_r = \sigma_c A_c = E_b \varepsilon_{dim} A_b \quad [4]$$

where F_r is the reaction force, σ_c and A_c are the internal stress and surface area of the constrained cell. E_b and A_b are the elastic modulus and total cross-section area of the eight bolts.

Assuming that the compressive behavior of the cell follows the power hardening law as follows

$$\sigma_c = B \cdot \left(\varepsilon_{por}\right)^n \quad [5]$$

This relation yields an increasing inelastic modulus $E_i = d\sigma_c/d\varepsilon_{por} = Bn(\varepsilon_{por})^{n-1}$ with an increasing compressive strain,

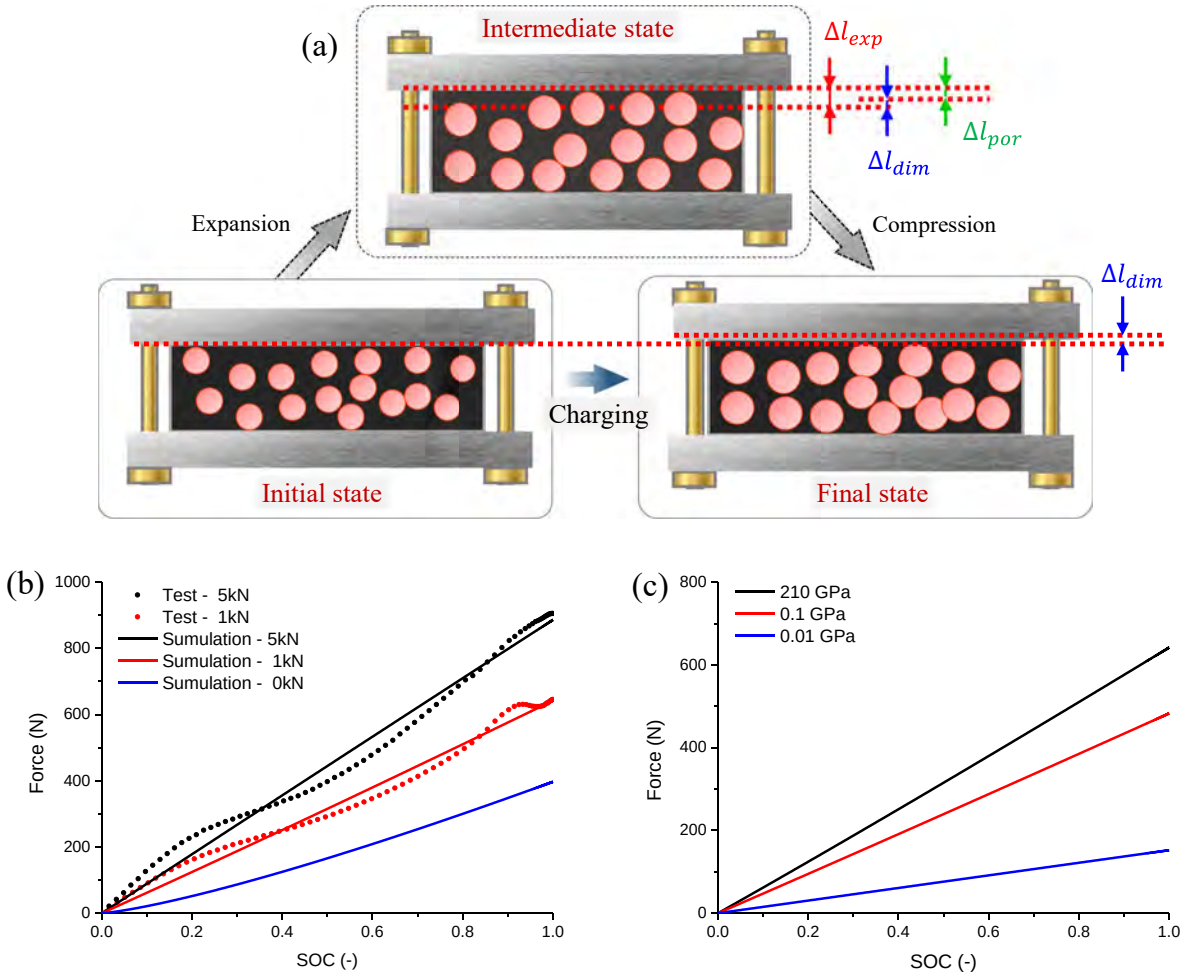

Figure 8. (a) Schematic description of the development of internal stress. (b-c) Results of the analytical model under different pre-tightening force levels and different Young's modulus of constraint bolts.

which is consistent with the fact that the stiffness of porous media tends to increase with an increase of compressive strain due to a more compacted structure. The thickness expansion is assumed to change linearly with SOC, as follows.

$$\Delta l_{exp} = T \cdot \varepsilon_{exp} \cdot \tau \quad [6]$$

where ε_{exp} is the nominal free expansion strain along the thickness direction of the cell after fully charged, and τ denotes the SOC.

With Eqs. 1–6, we have

$$\left(1 + \varepsilon_{exp} \cdot \tau\right) \cdot (\sigma_c / B)^{1/n} + \sigma_c A_c / (E_b A_b) \cdot L / T = \varepsilon_{exp} \upsilon \tau \quad [7]$$

The pre-tightening effect can be incorporated by adjusting the compressive strain as follow.

$$\varepsilon_{por} = (\sigma_c / B)^{1/n} - \varepsilon_0 \quad [8]$$

And the increased internal stress is $\sigma_{inc} = \sigma_c - \sigma_0$, where $\sigma_0 = B \cdot (\varepsilon_0)^n$. ε_0 is the pre-tightening strain corresponding to the pre-tightening stress σ_0.

Eq. 7 can be numerically solved for the internal stress σ_c after determining the three unknowns B, n, ε_{exp}. Then, we can get the reaction force with Eq. 4. The last charging cycle (#5) is simulated, when the force or displacement change reaches the steady state. ε_{exp} is directly determined from the deformation measurement (Fig. 7b), which is $0.118 \cdot 2/8.4 = 2.8\%$. The other two unknowns are optimized by matching the simulated results with test results under 1 kN and 5 kN pre-tightening force. The results are shown in Fig. 8b, and Table I lists all the parameters used. The results cannot precisely predict the complex change of experiment results, but the increasing trend is captured. This is due to that the assumption of linear thickness change with SOC in the analytical model is not consistent with experiment results. To evaluate the effect of constraint, two cases with a smaller elastic module (0.01 GPa and 0.1 GPa) of bolts are simulated, which represents the case of a weak constraint. The results (Fig. 8c) show a smaller increase in force under a weaker constraint.

To sum up, the experimental results show a noticeable volume expansion of an unconstrained cell and a significant internal stress in a constrained cell during charging. A simple analytical model is developed to capture the internal stress change with a changing SOC and to illustrate that a stronger constraint results in a higher internal

Table I. Parameters used in the analytical model.

Parameter	Value
Length of bolt constraining the cell, L	20 mm
Thickness of cell, T	8 mm
Surface area of cell, A_c	130×210 mm^2
Total cross-section area of bolts, A_b	$8 \times \pi \times 3^2$ mm^2
Elastic modulus of bolt, E_c	210 GPa
Free expansion strain of cell, ε_{exp}	2.8%
Hardening parameter, B	1.5 MPa
Hardening parameter, n	1.28

stress, which is consistent with the experiment results. These results support the conclusion in the previous section that the internal stress develops inside the pouch cell due to the external constraint, which results in a SOC-dependence of mechanical behavior under abuse loading.

Conclusions

In this study, the effect of SOC on the mechanical response of lithium-ion batteries subjected to external constraint is investigated under both mechanical abuse loading and normal charge/discharge condition. The major conclusion of the study is that the SOC-dependence of the mechanical behavior of lithium-ion battery cells is a result of the internal stress induced by volume expansion, instead of the material change of anode and cathode. This conclusion was derived by a series of control tests carefully, including the comparisons between cylindrical and pouch cells, between the winding jellyroll of the cylindrical cell and the stacking jellyroll of pouch cell, and between pouch cells with and without external constraints. Some other conclusions drawn based on this study are listed below:

1. The cylindrical cell has a significant SOC-dependent mechanical and electrical response, but the pouch cell shows a negligible SOC-dependence.
2. Both the constraint from the cylindrical winding structure of the jellyroll due to the roll-up process and the constraint from the stiff shell casing contribute to the internal stress development.
3. When the pouch cell is constrained to prevent free expansion, the mechanical response becomes stiffer as the SOC increases. A stronger constraint induces a stiffer response.
4. A simplified analytical model is applied to reveal the relationship between the internal stress and the external constraint that limits the volume expansion.

Acknowledgments

This study is supported by International Science & Technology Cooperation Program of China (contract No. 2016YFE0102200), National Natural Science Foundation of China (grant No.51675294 and No. U1564205). A part of the technical work is also sponsored by Ford URP (University Research Program). Financial support provided by China Scholarship Council (CSC) during the visit of W. Li to MIT is acknowledged.

Appendix

Influence of the difference in cathode materials.—In this study, the cathode materials of the tested cylindrical cell and pouch cell are NCA and NMC, respectively. Considering the same type of anode and similar active material of cathode, the electrode material should not be the main factor contributing to the different mechanical responses between cylindrical and pouch cell. Furthermore, we verified this by conducting the same lateral indentation tests on a NMC cylindrical cell. The result shows a significant SOC-dependent mechanical response (see Fig. A1), which is consistent with the results in the manuscript. Since we have reported that the NMC pouch cell has no apparent SOC-dependence, if the electrode material is the dominant factor, the NMC cylindrical cell should not have SOC-dependence either, which is the opposite of what we observed. Therefore, the difference of electrode materials is not the primary factor contributing to the different SOC-dependent mechanical responses between cylindrical and pouch cell.

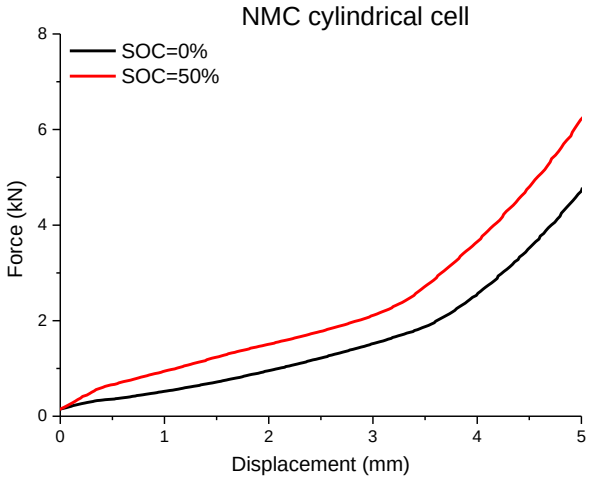

Figure A1. Results of lateral indentation on a NMC cylindrical cell under different SOCs.

ORCID

Yong Xia https://orcid.org/0000-0002-9586-9678
Juner Zhu https://orcid.org/0000-0001-7072-2293

References

1. L. Greve and C. Fehrenbach, *J. Power Sources*, **214**, 377 (2012).
2. T. Kisters, E. Sahraei, and T. Wierzbicki, *Int. J. Impact Eng.*, **108**, 205 (2017).
3. H. Luo, X. Jiang, Y. Xia, and Q. Zhou, *ASME 2015 Int. Mech. Eng. Congr. Expo.*, (2015).
4. H. Luo, Y. Xia, and Q. Zhou, *J. Power Sources*, **357**, 61 (2017).
5. J. D. Meier, E. Sahraei, M. Salk, T. Kisters, and F. Huberth, in *In Proceedings of the Battery Congress*, Troy, MI, USA.
6. E. Sahraei, J. Meier, and T. Wierzbicki, *J. Power Sources*, **247**, 503 (2014).
7. E. Sahraei, J. Campbell, and T. Wierzbicki, *J. Power Sources*, **220**, 360 (2012).
8. W. Tsutsui et al., *Exp. Mech.*, 1 (2017).
9. T. Wierzbicki and E. Sahraei, *J. Power Sources*, **241**, 467 (2013).
10. Y. Xia, G. Chen, Q. Zhou, X. Shi, and F. Shi, *Eng. Fail. Anal.*, **82**, 149 (2017).
11. Y. Xia, T. Wierzbicki, E. Sahraei, and X. Zhang, *J. Power Sources*, **267**, 78 (2014).
12. J. Xu, B. Liu, and D. Hu, *Sci. Rep.*, **6**, 21829 (2016).
13. J. Xu, B. Liu, X. Wang, and D. Hu, *Appl. Energy*, **172**, 180 (2016).
14. J. Zhu, T. Wierzbicki, and W. Li, *J. Power Sources*, **378**, 153 (2018).
15. J. Zhu, X. Zhang, E. Sahraei, and T. Wierzbicki, *J. Power Sources*, **336**, 332 (2016).
16. R. Fu, M. Xiao, and S. Y. Choe, *J. Power Sources*, **224**, 211 (2013).
17. J. H. Lee, H. M. Lee, and S. Ahn, *J. Power Sources*, **119–121**, 833 (2003).
18. E. Gibellini et al., *J. Electrochem. Soc.*, **163**, A2304 (2016).
19. S. a. Roberts, V. E. Brunini, K. N. Long, and a. M. Grillet, *J. Electrochem. Soc.*, **161**, F3052 (2014).
20. B. Rieger, S. V. Erhard, K. Rumpf, and A. Jossen, *J. Electrochem. Soc.*, **163**, A1566 (2016).
21. G. Bucci et al., *J. Electrochem. Soc.*, **164**, A645 (2017).
22. J. Cannarella and C. B. Arnold, *J. Power Sources*, **245**, 745 (2014).
23. X. M. Liu and C. B. Arnold, *J. Electrochem. Soc.*, **163**, A2501 (2016).
24. S. P. V. Nadimpalli, V. A. Sethuraman, D. P. Abraham, A. F. Bower, and P. R. Guduru, *J. Electrochem. Soc.*, **162**, A2656 (2015).
25. W. Zhou, *Electrochim. Acta*, **185**, 28 (2015).
26. Y. Qi, H. Guo, L. G. Hector, and A. Timmons, *J. Electrochem. Soc.*, **157**, A558 (2010).
27. S. Yang et al., *J. Power Sources*, **352**, 9 (2017).
28. B. Rieger, S. V. Erhard, K. Rumpf, and A. Jossen, *J. Electrochem. Soc.*, **163**, A1566 (2016).
29. P. K. Leung et al., *J. Power Sources*, **271**, 82 (2014).
30. B. Michalak et al., *Sci. Rep.*, **5**, 1 (2015).
31. T. R. Garrick, K. Kanneganti, X. Huang, and J. W. Weidner, *J. Electrochem. Soc.*, **161**, E3297 (2014).
32. J. Zhu, W. Li, Y. Xia, and E. Sahraei, *J. Electrochem. Soc.*, **165**, A1160 (2018).

RSC Advances

PAPER

View Article Online
View Journal | View Issue

Cite this: *RSC Adv.*, 2018, **8**, 3996

Adhesion strength of the cathode in lithium-ion batteries under combined tension/shear loadings

Hailing Luo,[ab] Juner Zhu,[b] Elham Sahraei [bc] and Yong Xia *[a]

Received 13th November 2017
Accepted 16th January 2018

DOI: 10.1039/c7ra12382e

rsc.li/rsc-advances

To understand the failure mechanism and establish reliable deformation tolerances for lithium-ion batteries under mechanical loading, accurate testing and modeling of individual components are indispensable. This paper is focused on one of the most common failure scenarios, which is the de-bonding between the coating material and the current collector. A new specimen is carefully designed to measure the failure strength of the coating-foil interface. The electrode is bonded to two acrylic substrates using liquid formula glue for one side and gel formula glue for the other. Compared with conventional peeling tests using double-sided tape, the major advantage of this new specimen is that it realizes conducting shear tests. Using this special specimen, the failure strength of the coating-foil interface is obtained under combined tension/shear loadings. The new method is less susceptible to the testing conditions such as loading rate. For the cathode studied in this paper, the shear strength of the coating-foil interface turns out to be almost twice its tensile strength, which emphasizes the necessity of carrying out combined tension/shear loading tests. Moreover, a combined adhesion and cohesion failure mode is observed at the failure interface, where with larger shear component, the adhesion failure becomes dominant.

1. Introduction

Lithium-ion batteries have been widely deployed in powering consumer electronics, and now their application has been extended to large-scale transportation. In the automotive industry, high energy density and long cycle life are always the two most essential design objectives, while the safety issue is of equal importance. During the charge–discharge cycles, the active coatings of electrodes have to endure pronounced volume change. This periodic volume change induces an alternating internal stress, which may lead to initiation of cracks inside the active material coating as well as a delamination between the coating and the current collector if the adhesion strength is unsatisfactory. Such damage is irreversible and can result in capacity loss.[1] Therefore, to ensure a long cycle life for the batteries, achieving and maintaining good adhesion conditions between active coatings and their interface with current collectors is very important.

On the other hand, the application to Electric Vehicles (EV) has put the lithium-ion batteries into a tougher situation – they may undergo large mechanical deformation that result in damage due to complicated external loads and intrusions during vehicle operations. It remains a big challenge to estimate the risk of failure of the batteries during a vehicle crash. Both experimental and numerical efforts have been made to investigate the fracture mechanisms of batteries under mechanical abuse loadings.[2–9] Based on careful and precise characterizations of the properties of the components of the cells, developing a finite element (FE) model covering the details of the jellyroll can largely help analyze and predict the damage evolution inside the batteries. Among those characterizations at the component level, the mechanical properties of various interfaces inside the multi-layered structure of jellyroll, *e.g.* the interface adhesion strength, have not been studied so far. These forces are important as they can significantly affect the global and local mechanical responses of the batteries subjected to external loads. Therefore, for modeling, it is necessary to develop appropriate approaches to measure the adhesion strength of electrode and to predict adhesive failure at the interface between the coating and the current collector.

Peel test is a conventional method in battery industry for ranking the adhesion strength of electrodes, which separates the active material coating from the current collector using bond tapes. Park, *et al.*[10] and Lee, *et al.*[11] applied the peel test with bond tapes to evaluate the electrodes with various binders and constituents, and demonstrated that polyvinyl alcohol (PVA) binder or certain additives like poly (acrylic acid) (PAA) could enhance the adhesion strength of the anode. However, the measurement of such peel test is highly influenced by the additional adhesion introduced by the bond tapes. The strength of bond tape is determined by the surface quality of the active

[a]State Key Laboratory of Automotive Safety and Energy, Department of Automotive Engineering, Tsinghua University, Beijing, 100084, China. E-mail: xiayong@tsinghua.edu.cn; Tel: +86-10-62789421

[b]Department of Mechanical Engineering, Massachusetts Institute of Technology, 77 Massachusetts Ave, Cambridge, MA, 02139, USA

[c]Electric Vehicle Safety Lab, The George Mason University, Nguyen Engineering Building, 4400 University Dr, Fairfax, VA 22030, USA

material coatings, unless a very strong bond tape such as the so-called VHB (Very High Bond) tape is used. Many other test procedures have been established for the purpose of measuring the adhesion strength of electrodes. Son, *et al.*[12] managed to measure the peel strength at a specific depth to the surface of the active coating on a device named the Surface and Interfacial Cutting and Analysis System (SAICAS). Scratch tests were carried out to estimate the adhesion strength of different interfaces (binder/binder, particle/binder and current collector/binder) inside electrodes.[13] *In situ* testing technique could also be adopted to study the crack evolution of the electrodes.[14] To directly measure the tensile strength (adhesion strength in normal direction) of the electrode, Haselrieder, *et al.*[15] customized a pull-off test to separate active material coatings from current collectors under tensile loading with double-sided bond tapes. However, the test results in the aforementioned studies are difficult to be utilized straightforwardly, and the analyses cannot cover the complicated loading states that the interface experiences in realities.

In the present paper, a new test method is proposed to realize direct measurement of the adhesion strength of the electrode under a combined tension/shear loading for different stress states. Detailed descriptions of the specimen preparation and the testing procedures are presented and thereafter, test results of cathode electrodes are presented to demonstrate reliability of the method.

2. Experiments

2.1 Specimen preparation

In this research a lithium–nickel–cobalt–oxide cathode from a commercial pouch cell without electrolyte (referred to as "dry cell") was studied. From a mechanical point of view, it is a simple sandwich structure, consisting of two layers of porous active material coatings (the blend of active particles, binders and conductive additives) and one aluminum foil (the current collector) in between. Since the thickness of an electrode is less than 200 μm, it is difficult to directly apply boundary

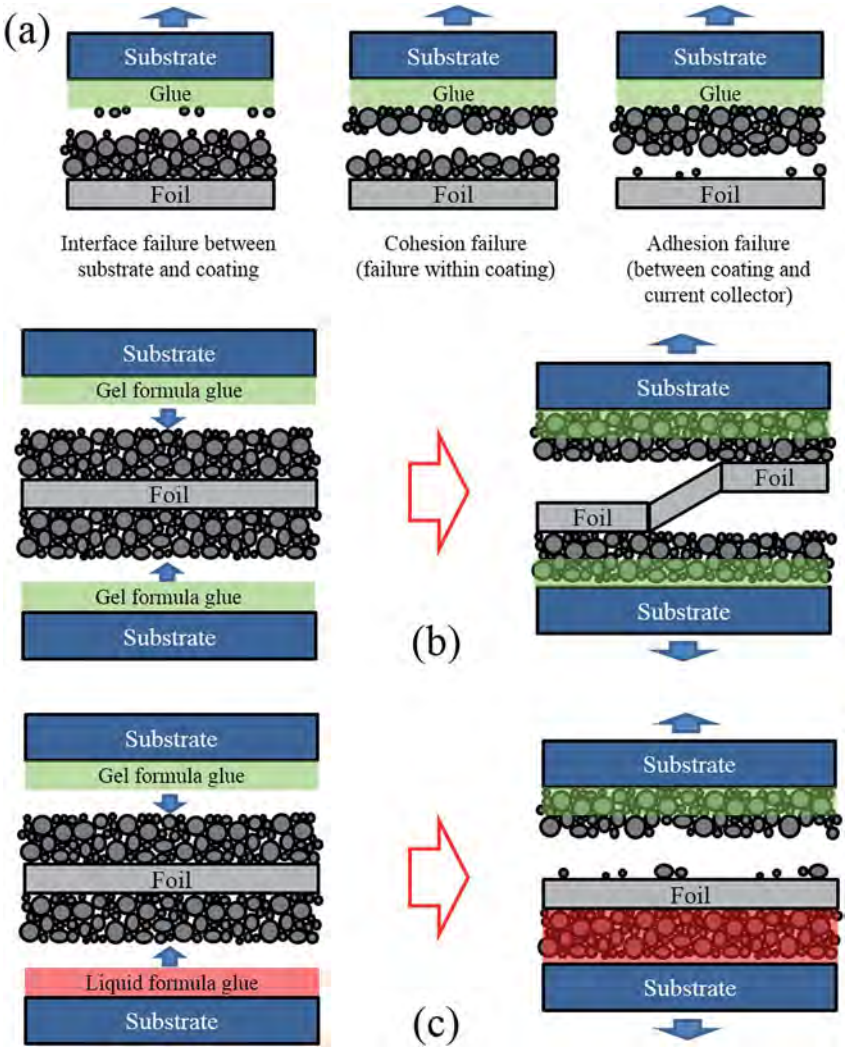

Fig. 1 (a) Different failure mechanisms, (b) specimen with gel glue on both side (the interface failure randomly occurs on either side of the electrode or switches from one side to another), and (c) specimen with gel glue on one side and liquid glue on the other side (the failure only occurs at one side).

constraints or loads to such a thin layer in a mechanical test to measure its interface strength. Therefore, each side of the electrode was bonded to an acrylic substrate (see Fig. 1) for the convenience of clamping.

In the multi-layered specimen, there are three critical cross-sections where fracture might happen, as shown in Fig. 1a. One is the interface between substrate and coating, second is the internal cross-section of coating, and the last one is the interface between coating and current collector. The failure scenarios that happen at the second and the third critical cross-sections are called "cohesion failure" and "adhesion failure", respectively. The present work aims to investigate the adhesion strength between coating and current collector. Thus, fracture is expected to happen in the third cross-section, instead of the other two. The interface failure between substrate and electrode can be prevented by applying high bonding glue instead of conventional double-sided tape. For the other two cases, since the amount of binder decreases from the top surface of the coating to the bottom,[16] the adhesion strength between the active material coating and the current collector is usually lower than the cohesion strength within the coating. Thus, the desired failure mode (fracture in the interface between coating and current collector) could be realized in experiments.

Moreover, the interface failure could randomly occur on either side of the electrode, or switch from one side to another, as shown in Fig. 1b. To control the failure only occurring at one side, we applied a liquid formula glue (Super Glue 15187, referred to as liquid glue in this paper) on one side of the electrode and a gel formula glue (Loctite Super Glue, referred to as gel glue in this paper) on the other side, to bond the electrode with the acrylic substrates, as shown in Fig. 1c. At the side with liquid glue, since the liquid glue permeates the entire thickness of the active material coating and enhances the original strength of both coating and coating-foil interface, both the coating material and the coating-foil interface were strengthened. At the other side with the gel glue, the gel formula glue only stays at the top of the porous coating material rather than permeating through the thickness. Thus, the original coating-foil interface remains intact. In this way, the coating-foil interface at the side with gel glue became the weakest location, making the failure occurrence and growth more controllable in the subsequent mechanical tests.

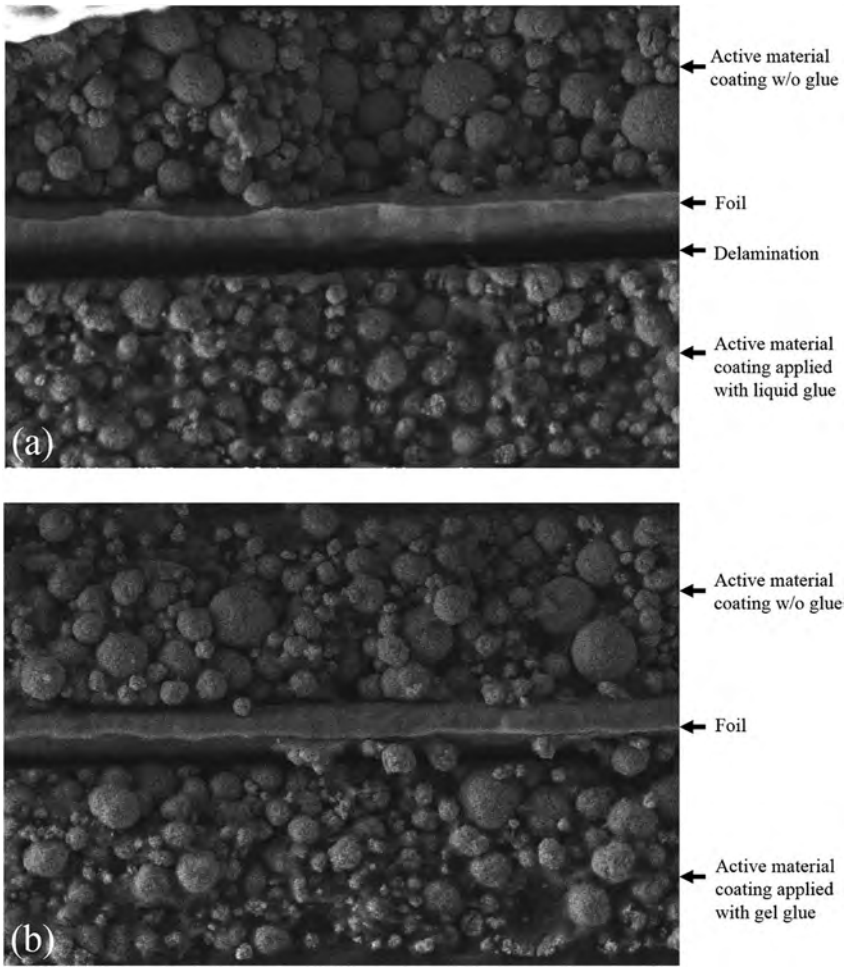

Fig. 2 Cross-sectional view of cathode fractured in uniaxial tensile test: (a) electrode with liquid glue on one side, and (b) electrode with gel glue on one side.

To validate the design of the specimen, dog-bone shaped cathode specimens were made using a razor blade and added glue, with two different strategies for comparison. The liquid glue and the gel glue were applied on one side of the cathode in Group A and Group B, respectively, while the other side of the cathode in each group were kept unstained. Then, tensile tests to fracture were performed on the specimens. Following the tests, the fracture cross sections were analyzed using SEM to identify the depth of the glue penetrating into the coating layer. As shown in Fig. 2a, for specimens of Group A, all the interspace between particles is filled with the liquid glue and delamination between coating and current collector is observed at the side where the liquid glue was applied. However, for specimens of Group B (Fig. 2b), less than half of the active material coating along the thickness direction is soaked with the gel glue. As shown with the morphology of Group B, the boundaries of the particles in the active material coating near the foil were kept as clear as those at the other side that were not subjected to any glue, while the boundaries of the particles close to the gel glue become blurry.

2.2 Setup of combined tensile and shear tests

To explore the adhesion strength of electrode under different stress states, a series of combined tensile and shear tests were designed. Fig. 3 shows the test setup and the dimensions of the specimens. The clear cast acrylic sheet with a thickness of 4.45 mm was used as the substrate and the specimens were manufactured by laser cutting, following the designed shapes. For each specimen, the electrode was placed between two substrates (one on each side of the electrode) with a predefined angle to the axial direction, every 15° from 0° to 90°. For the 0° test, the electrode was loaded along the normal direction of the current collector, thus the tensile strength of the coating-foil interface was measured. As the tilt angle becomes larger, the shear component increases. For the 90° test, the loading direction is parallel to the current collector. Therefore, the strength value is determined by the shear strength of the failure interface. To minimize the bending moment that might exist on the electrode, the specimen is fixed by a pin–pin boundary. An Instron uniaxial tensile machine with 2 kN load cell was used to perform all the tests. The velocity of the cross head was 1.0 mm min^{-1} and each test was repeated 3 times.

3. Results and discussion

3.1 Failure interface

The failure interface of each specimen was examined using SEM. Fig. 4 shows the SEM images of failure surface (current collector side) of specimens from 0°, 45° and 90° tests. For all the specimens, failure occurred at the side with gel glue just as expected. However, a combined adhesion and cohesion failure mode is observed for all the specimens. From 0° to 90°, the percentage of adhesion failure mode increases. For 0° specimen, cohesion failure is the dominant failure mode that one

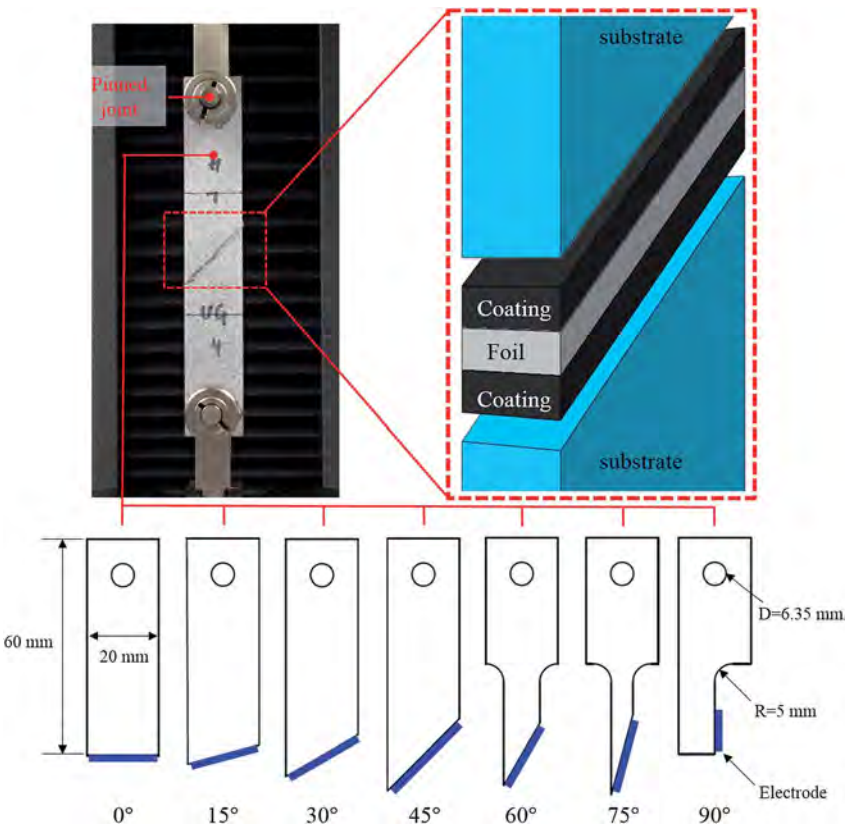

Fig. 3 Test setup of combined tensile and shear test.

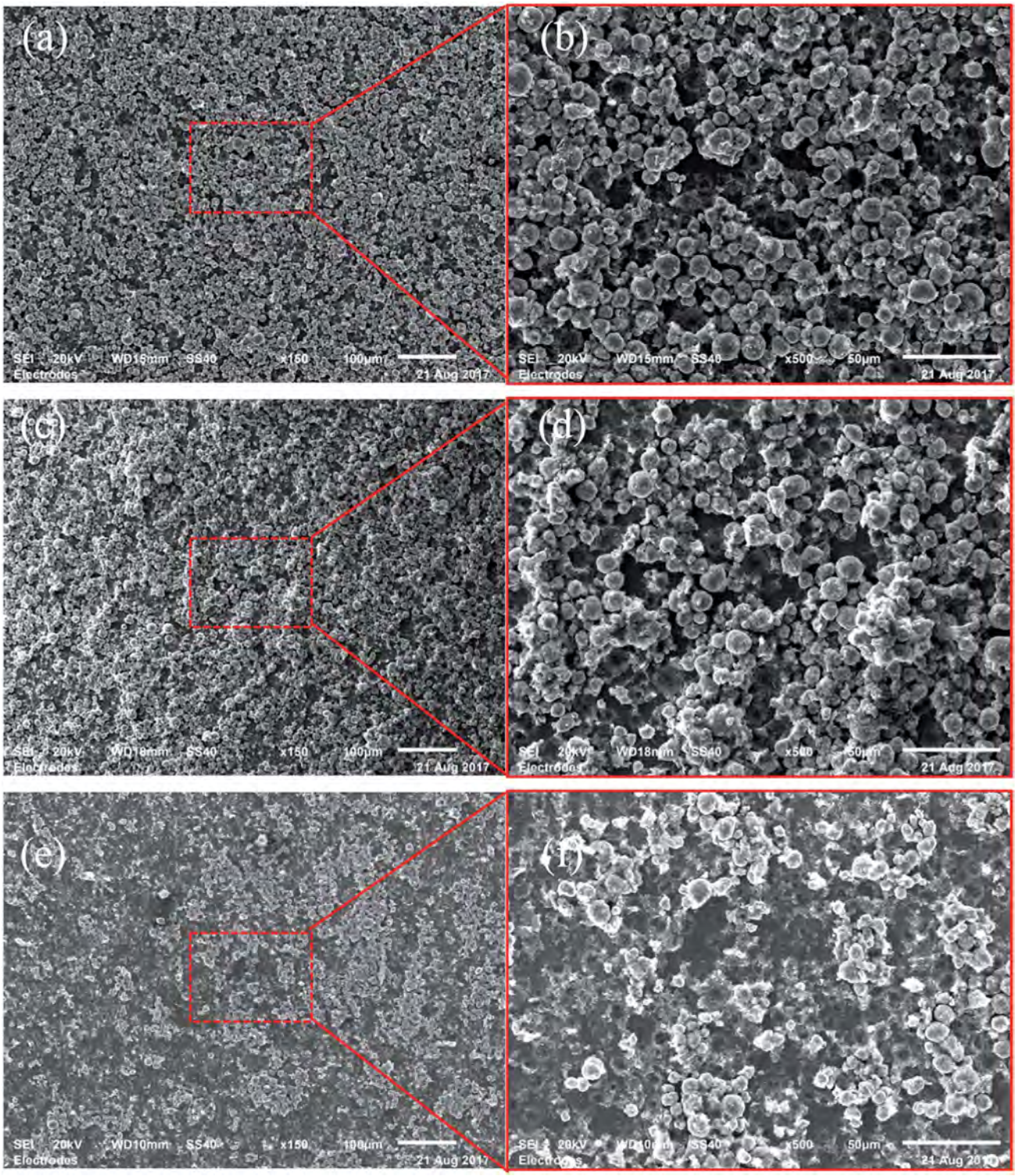

Fig. 4 SEM images of the failure interface of specimens from (a), (b) 0°, (c), (d) 45° and (e), (f) 90° test.

layer of active particles still covers most part of the current collector and only a small portion of the current collector is visible. However, for 90° specimen, only a few particles remain bonded to the current collector and adhesion failure becomes dominant. According to ref. 16, there is less amount of binder on the surface of the particles close to the coating-foil interface. For all the specimens, adhesion failure on the coating-foil interface is supposed to be the dominant failure mode. However, in fact the feature of the particle stacking structure could lead to a certain difference between the results at different loading angles. As shown in Fig. 5a, the thickness of the binder coated on the particles on the bottom layer is thinner than other

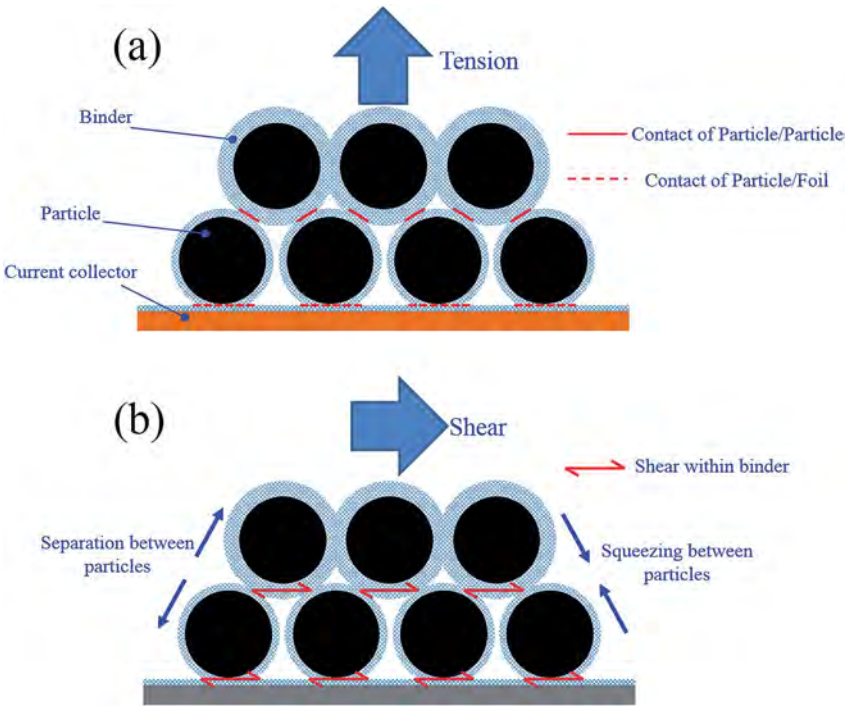

Fig. 5 Schematic of failure mechanism under (a) tension and (b) shear.

layers. However, the contact area between a particle and the surface of the current collector could be much larger than the contact area between a particle and the adjacent particles. Therefore, for 0° specimen, the effective adhesion strength of the coating-foil interface could be stronger than the cohesion strength between the bottom particle layer and the upper particle layer. That is why relatively large amount of particles remain on the surface of foil after 0° loading. When the specimen is loaded with larger proportion of shear component, the relative sliding between different particle layers leads to more squeezing between particles (shown in Fig. 5b). The resistant force caused by squeezing additionally contributes to the effective shear strength between particle layers. In the meantime, the shear strength of the coating-foil interface is only sustained by the binder itself. Therefore, the effective cohesion shear strength between particle layers could be larger than the adhesion shear strength of the coating-foil interface. That is why adhesion failure becomes dominant for 90° specimen.

3.2 Adhesion strength under different stress state

For each type of the specimens, it is assumed that the stress distribution is uniform across the failure interface, so the effective adhesion strength could be calculated as following:

$$\sigma_{\mu} = F_f/A \tag{1}$$

where F_f is the magnitude of the peak axial force, A is the area of the failure interface of the electrode. The results are shown in Fig. 6a. For each tilt angle, the failure strength is ranged between 3.0 MPa and 4.5 MPa. From 0° to 60°, the effective adhesion strength increases first and reaches its peak value for 60° specimen, indicating that electrode has a higher strength under larger proportion of shear component. However, the strength value of 75° and 90° specimen decreases. The failure strength is further decomposed into its tensile component and shear component by:

$$\sigma_n = \sigma_{\mu} \sin\theta \tag{2}$$

$$\sigma_S = \sigma_{\mu} \cos\theta \tag{3}$$

where θ is the tilt angle, σ_n is the tensile component and σ_S is the shear component. The results are plotted on the $\sigma_n - \sigma_S$ plane (as shown in Fig. 6b). The quadratic failure criterion of cohesive zone model[17] was adopted to predict the adhesion failure:

$$\left(\frac{\sigma_n}{\mathrm{NFLS}}\right)^2 + \left(\frac{\sigma_S}{\mathrm{SFLS}}\right)^2 = 1 \tag{4}$$

where NFLS is the normal tensile stress at failure and SFLS is the shear stress at failure. This two values (NFLS = 3.16 MPa, SFLS = 3.27 MPa) were calibrated from the average value of adhesion strength from 0° test and 90° test, respectively. As shown in Fig. 6b, the quadratic failure criterion underestimates the failure strength of most of the test results, especially tests with large shear component.

In order to refine the failure criterion of the coating-foil interface, explicit finite element (FE) models of the combined tensile and shear test (0°, 45°, and 90°) were established using LS-DYNA. Since the thickness of the electrodes is negligible compared with the sizes of the substrate, it is assumed that the neglecting the material property of the electrode would not

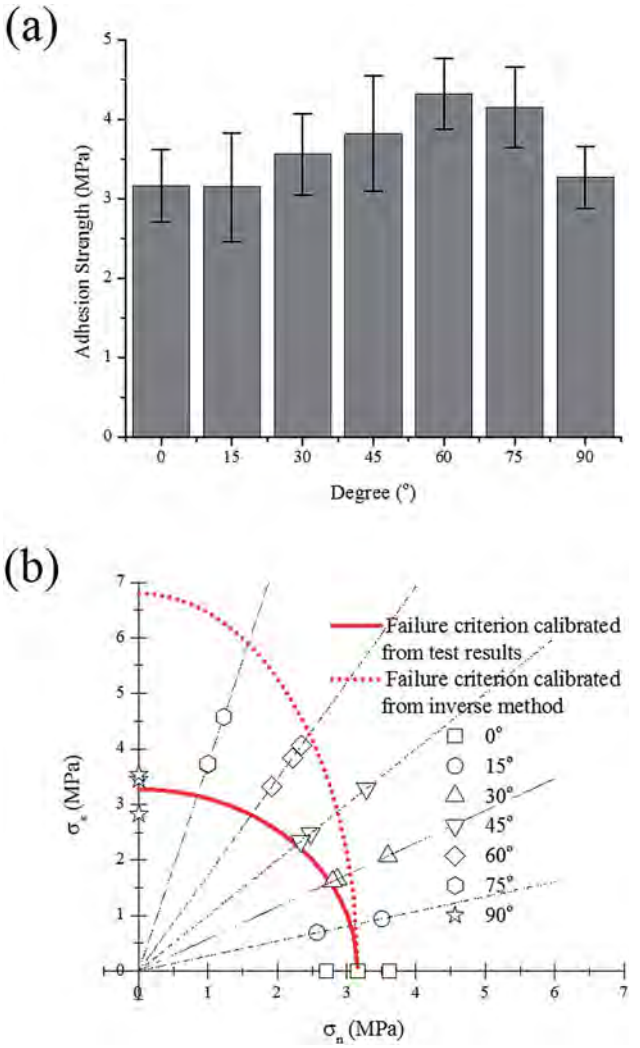

Fig. 6 Test results of combined tensile-shear test, (a) adhesion strength and (b) tensile and shear component of each test.

change the stress distribution at the failure interface. For simplicity, only the substrate was modeled using elasto-plastic material model (MAT_Piecewise_Linear_Plasticity in LS-DYNA) with Young's modulus $E = 3.1$ GPa and Poisson's ratio $\nu = 0.3$. The Young's modulus of the substrate was measured from uniaxial tensile test. A contact property (TIED_SURFACE_TO_SURFACE_FAILURE) was defined between two substrates to predict the adhesion failure, and failure occurs when the aforementioned quadratic failure criterion is met. First, the simulations were conducted with failure criterion calibrated from the test results. The peak forces from both simulation and test are plotted in Fig. 7(b), (d) and (f) for 0°, 45° and 90°, respectively. For 0°, the simulation result matches well with the test results. However, the simulation of 45° and 90° test underestimated the test results. The color-coded Von-Mises stress contours of each test at the moment right prior to fracture are also plotted in Fig. 7. The stress distribution across the failure interface is almost uniform for 0° and 45° test, while for 90° test, stress concentration could be identified at the edge of the failure interface. This stress concentration is mainly due to the asymmetry of the specimen. Since the assumption that stress distribution is uniform is no longer valid, the shear stress at failure should be recalibrated by inverse method. Thus, the shear strength (SFLS) in the failure criterion was tuned manually to match the peak force with test result in 90° test and the updated shear strength is 6.8 MPa. Again, the peak forces from simulations using the new set of parameters (NFLS = 3.16 MPa, SFLS = 6.8 MPa) are plotted in Fig. 7(b), (d) and (f), and a good agreement between simulation and test is achieved for each of the tests (0°, 45°, and 90° test). The failure criterion with the updated set of parameters is also plotted in Fig. 6b. The shear strength calibrated from inverse method is almost twice over the previous value. We also calculate the cohesion strength of the active material coating by subtracting the contribution of the current collector from the response of the entire electrode under uniaxial tensile test, this process has been described in ref. 3. The value calculated from this method is 8.0 MPa which is even larger than the shear strength obtained from the inverse method. Given the fact that the former one is mainly derived from the bulk material of the coating which usually has a higher failure strength than the foil-coating interface, this difference is still acceptable.

3.3 Comparison with double-sided tape

For comparison, a 0° test using double-sided adhesive tape (3M VHB 4950 foam tap) was also conducted. The gel formula glue was replaced with the tape, while the other side was still glued with the liquid formula glue. Besides 1 mm min^{-1}, both specimens with gel glue and double-sided tape were also conducted under a higher rate (100 mm min^{-1}) which is suggested by in ref. 15.

As shown in Fig. 8a, under both 1 mm min^{-1} and 100 mm min^{-1}, the tensile strengths derived from the specimens with gel formula glue are almost identical (3.16 MPa for 1 mm min^{-1} and 3.56 MPa for 100 mm min^{-1}), showing no apparent strain rate effect. However, the results from the test with double-sided adhesive tape is significantly influenced by the test rate. For 1 mm min^{-1} test, the failure was progressive and no peak force could be identified on the force-displacement curves. For 100 mm min^{-1} test, the tensile strength determined from the peak force is roughly 1.0 MPa which is significantly lower than the value obtained from tests of specimen with gel formula glue. This difference is probably attributed to the deformation of the substrate which will largely affect the stress state inside the electrode. In particular, due to its larger thickness and lower stiffness compared with the electrode, the adhesive tape is subjected to large deformation during the test. The large deformation of substrate may result in a non-uniform stress distribution, *i.e.* significant stress concentration in the electrode. In contrast, the stiffness of the gel formula glue is quite high after curing, bringing less effect on the uniformity of stress distribution inside the electrode. As shown in Fig. 8b, the force *versus* displacement curves from tests of specimen with adhesive tape is always lower than those with gel formula glue. This difference in global response should be a direct result of the

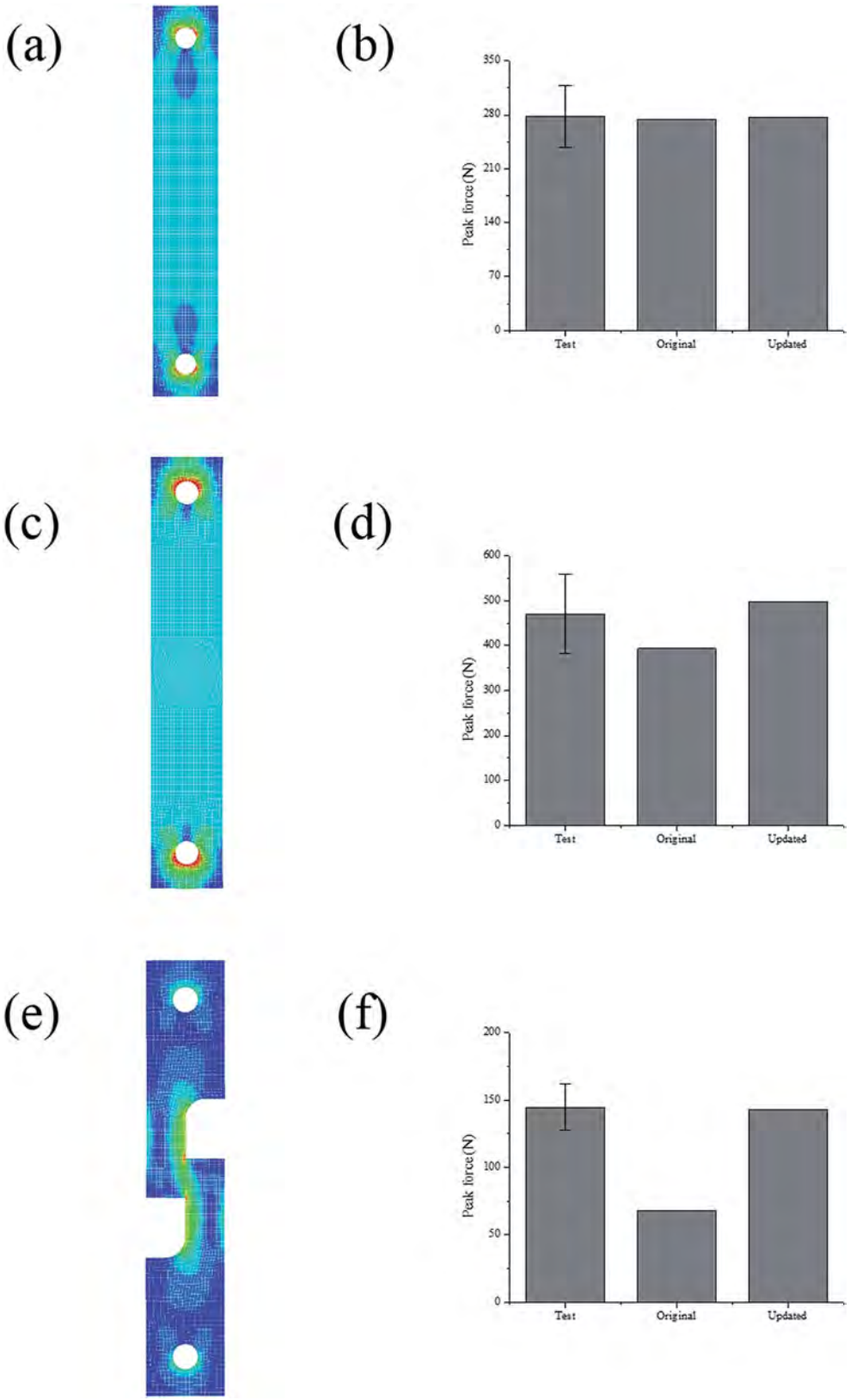

Fig. 7 Color-coded Von Mises stress contours of (a) 0°, (c) 45°, and (e) 90° test; comparison of peak force in experiment and simulation (with original set of parameters calibrated from test results and updated set of parameters calibrated by inverse method) for (b) 0°, (d) 45°, and (f) 90° test.

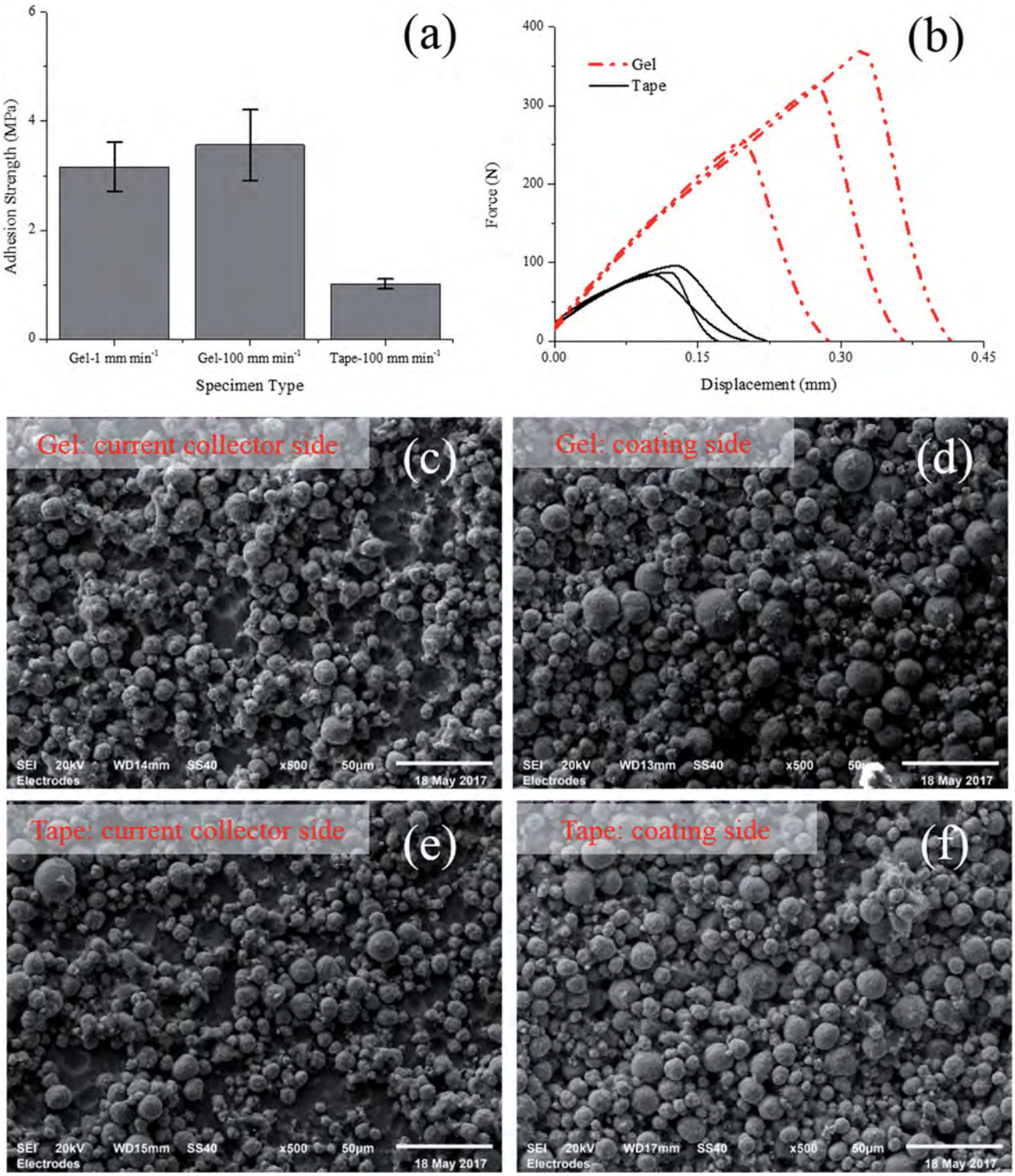

Fig. 8 (a) Test results of 0° test under 100 mm min^{-1}, (b) force *versus* displacement curves of test under 100 mm min^{-1}, SEM images of failure interface of (c), (d) specimens with gel glue and (e), (f) specimens with double-sided adhesive tape.

different stress distribution in the electrode. The SEM images of the fracture interface of specimens under 100 mm min^{-1} test are shown in Fig. 8, where a mixed failure mode is observed again and the cohesion failure is dominant. On the current collector side, most region of the foil is still covered by one layer of active particles, while most of the active particles remains staying on the coating side. In spite of the difference in test result of average strength, the morphology of the surfaces is almost identical, no matter the specimen was bonded with gel glue or double-sided tape.

4. Conclusion

A new test method has been specially designed to allow direct measurement of the adhesion strength of the electrodes. This new method has a major advantage over the conventional test methods with double-sided tape: the tests under large shear component could be conducted and the test results were less susceptible to the testing conditions such as loading rate. For the cathode studied in this paper, the strength results obtained from the inversed method indicated that the shear strength of the coating-foil interface is almost two times of its tensile strength. Moreover, a combined adhesion and cohesion failure mode was observed at the failure interface, where with larger shear component, the adhesion failure became dominant. While the tests were generally repeatable, a distribution of up to 25% was observed in the measured peak force. This will be improved in future extension of this research.

Conflicts of interest

There are no conflicts of interest to declare.

Acknowledgements

This study is supported by International Science & Technology Cooperation Program of China (contract No. 2016YFE0102200), National Natural Science Foundation of China (Grant No. 51675294 and No. U1564205), and the MIT Battery Modeling Consortium. A part of the technical work is also sponsored by Ford URP (University Research Program). Support of Altair Company with providing Hyperworks software for our research is greatly appreciated. H. L. thanks Mr Shaoting Lin of the MIT SAMs Lab for the help to cut the test samples. Dr Xiaowei Zhang is gratefully acknowledged for his constructive comments about the experimental work. Financial support provided by China Scholarship Council (CSC) during the visit of H. L. to MIT is acknowledged.

References

1 J. Vetter, P. Novák, M. Wagner, C. Veit, K.-C. Möller, J. Besenhard, M. Winter, M. Wohlfahrt-Mehrens, C. Vogler and A. Hammouche, *J. Power Sources*, 2005, **147**, 269–281.
2 E. Sahraei, M. Kahn, J. Meier and T. Wierzbicki, *RSC Adv.*, 2015, **5**, 80369–80380.
3 E. Sahraei, E. Bosco, B. Dixon and B. Lai, *J. Power Sources*, 2016, **319**, 56–65.
4 X. Zhang, E. Sahraei and K. Wang, *Sci. Rep.*, 2016, **6**, 32578.
5 H. Wang, S. Simunovic, H. Maleki, J. N. Howard and J. A. Hallmark, *J. Power Sources*, 2016, **306**, 424–430.
6 H. Luo, Y. Xia and Q. Zhou, *J. Power Sources*, 2017, **357**, 61–70.
7 C. Zhang, J. Xu, L. Cao, Z. Wu and S. Santhanagopalan, *J. Power Sources*, 2017, **357**, 126–137.
8 J. Zhu, X. Zhang, E. Sahraei and T. Wierzbicki, *J. Power Sources*, 2016, **336**, 332–340.
9 J. Zhu, T. Wierzbicki and W. Li, *J. Power Sources*, 2018, **378**, 153–168.
10 H.-K. Park, B.-S. Kong and E.-S. Oh, *Electrochem. Commun.*, 2011, **13**, 1051–1053.
11 J.-H. Lee, U. Paik, V. A. Hackley and Y.-M. Choi, *J. Power Sources*, 2006, **161**, 612–616.
12 B. Son, M.-H. Ryou, J. Choi, T. Lee, H. K. Yu, J. H. Kim and Y. M. Lee, *ACS Appl. Mater. Interfaces*, 2013, **6**, 526–531.
13 J. Chen, J. Liu, Y. Qi, T. Sun and X. Li, *ACS Appl. Mater. Interfaces*, 2013, **160**, A1502–A1509.
14 M. B. Gorji and D. Mohr, *Acta Mater.*, 2017, **131**, 65–76.
15 W. Haselrieder, B. Westphal, H. Bockholt, A. Diener, S. Höft and A. Kwade, *Int. J. Adhes. Adhes.*, 2015, **60**, 1–8.
16 M. Müller, L. Pfaffmann, S. Jaiser, M. Baunach, V. Trouillet, F. Scheiba, P. Scharfer, W. Schabel and W. Bauer, *J. Power Sources*, 2017, **340**, 1–5.
17 J. O. Hallquist, *LS-DYNA theory manual*, Livermore Software Technology Corporation, 2006.

Journal of Power Sources 389 (2018) 148–159

Contents lists available at ScienceDirect

Journal of Power Sources

journal homepage: www.elsevier.com/locate/jpowsour

Failure in lithium-ion batteries under transverse indentation loading

Seung Hyun Chung[a,b,*], Thomas Tancogne-Dejean[b], Juner Zhu[b], Hailing Luo[b,c], Tomasz Wierzbicki[b]

[a] Battery R&D, LG Chem Research Park, 188 Munji-ro, Yuseong-gu, Daejeon 34122, Republic of Korea
[b] Impact and Crashworthiness Laboratory (ICL), Massachusetts Institute of Technology, Cambridge MA, USA
[c] State Key Laboratory of Automotive Safety and Energy, Tsinghua University, Beijing 100084, China

HIGHLIGHTS

- Unique failure patterns under transverse punch loadings are observed.
- Closed-form solution is derived for traverse loadings on Li-ion cells.
- Proposed Mohr-Coulomb fracture criterion predicts well failure of lithium-ion cells.

ARTICLE INFO

Keywords:
Lithium-ion battery
Safety
Failure
Fracture
Internal short circuit

ABSTRACT

Deformation and failure of constrained cells and modules in the battery pack under transverse loading is one of the most common conditions in batteries subjected to mechanical impacts. A combined experimental, numerical and analytical approach was undertaken to reveal the underlying mechanism and develop a new cell failure model. When large format pouch cells were subjected to local indentation all the way to failure, the post-mortem examination of the failure zones beneath the punches indicates a consistent slant fracture surface angle to the battery plane. This type of behavior can be described by the critical fracture plane theory in which fracture is caused by the shear stress modified by the normal stress. The Mohr-Coulomb fracture criterion is then postulated and it is shown how the two material constants can be determined from just one indentation test. The orientation of the fracture plane is invariant with respect to the type of loading and can be considered as a property of the cell stack. In addition, closed-form solutions are derived for the load-displacement relation for both plane-strain and axisymmetric cases. The results are in good agreement with the numerical simulation of the homogenized model and experimentally measured responses.

1. Introduction

Development of reliable deformation and failure models of lithium-ion cells relies heavily on a good set of experimental data. At a level of individual cells, a choice of tests is limited to compression, indentation, and bending. Tensile and shear tests cannot be performed because cells do not have rigid shoulders to allow for firm mounting in the mechanical, hydraulic or pneumatic grips. Sahraei et al. [1–4] in a series of papers established a set of experiments needed to calibrate a homogenized model of batteries subjected to out-of-plane and in-plane compression. Also, a procedure of predicting failure of cells, understood as an onset of an electric short circuit, was developed by means of an inverse experimental/computational approach. Bending tests were performed by Sahreai et al. on small flat cells with and without pouch cover [2]. It was found that the pouch cover, that contributed little to the resistance to indentation, has a major effect on the bending strength. A simple model of the multilayered beam was able to explain the source of these differences. Greve et al. [5] performed a similar type of tests to establish failure limit by means of a coupled experimental/computational method. Zhang et al. [6,7] developed a lumped mechanical model for a coupled modeling methodology encompassing the mechanical, electrical and thermal response. Wang et al. [8] studied in-plane confined compression of pouch cells and explained a regular buckling pattern through the development of shear localization. Mason [9] constructed an apparatus to perform in-plane compression tests with controllable through thickness confinement force. Zhu et al. [10] subjected 18650 cylindrical cells to axial compression and developed a detailed computational model. The prediction of this model agrees

* Corresponding author. Battery R&D, LG Chem Research Park, 188 Munji-ro, Yuseong-gu, Daejeon 34122, Republic of Korea.
E-mail addresses: shchung@lgchem.com, shchung7@gmail.com (S.H. Chung), tancogne@mit.edu (T. Tancogne-Dejean), zhujuner@mit.edu (J. Zhu), luohl13@mails.tsinghua.edu.cn (H. Luo), wierz@mit.edu (T. Wierzbicki).

https://doi.org/10.1016/j.jpowsour.2018.04.003
Received 15 September 2017; Received in revised form 19 March 2018; Accepted 1 April 2018
Available online 11 April 2018
0378-7753/

closely with post-mortem tomography of damaged cells. Kisters et al. [11] recently reported dynamic impact tests on the pouch and elliptic cells with axisymmetric punches.

The question that must be posed is whether all these types of tests correspond to typical accidental loading pattern of various cells in everyday situations. The answer is no. For example, while the indentation of cells by an axisymmetric punch with different tip radius is widely used to calibrate battery models, it is also only one type of load application. Equally important is a plane-strain loading where a pouch or prismatic cell is loaded transversely by a long cylinder. Actually, in a number of tests proposed by various standards [12,13], loading is applied through rigid cylinders. Recent work on fracture of metallic material has proven that the plain strain is the most constrained case among all possible stress states and the corresponding equivalent failure strain is the lowest. Understanding and quantification of plain-strain failure of batteries will always provide the lower bound or worst case scenario. Still, a rigorous analysis of deformation and failure of cells under such loading is missing.

The objective of the present paper is to close the gap in our current experimental practice by characterizing the failure patterns under the various loading conditions and developing the failure criterion at the cell level. The results obtained have proven that the Mohr-Coulomb (MC) failure criterion [14], used in many branches of solid mechanics is also applicable for predicting failure of lithium-ion cells. A simple set of tests is then proposed to calibrate the two-parameters of the MC model. The present model is physically based and could replace the inverse experimental/numerical methodology that has dominated the current literature on cells failure.

Another major new result reported here is the derivation of the closed-form solution for the load-displacement relationship of cells subjected to lateral indentation by hemispherical and cylindrical punches. Both solutions compare well with the experimental results and finite element (FE) simulation. So, it can be used instead of a numerical method with no compromise in accuracy. It is believed that the present paper is putting the development of mechanical models of batteries on a firmer theoretical foundation and is providing new analytical and numerical tools for more reliable prediction of strength and onset of an electric short circuit for large format lithium-ion pouch cells.

2. Cell-level test and modeling

The lithium ion cell studied here is a 26.3 Ah large pouch-type cell with $LiMn_2O_4/LiNi_{1/3}Co_{1/3}Mn_{1/3}O_2$ - graphite chemistry and carbonate-based liquid electrolyte. The cell dimensions are 232 mm (L) x 153 mm (W) x 7.5 mm (T). The architecture of the cell consists of alternating layers of 20 anodes, 19 cathodes and separators in between them. All the cathodes and anodes are double-side-coated and the thicknesses of electrodes are 171 μm for cathode and 143 μm for anode. The current collectors are 20 μm aluminum foil for cathode and 10 μm copper foil for anode. The separator (27 μm) is dry-processed polypropylene (PP) with ceramic coatings on both sides. The exterior of the cell is an aluminum laminated film with 150 μm thickness. Except the materials mentioned here, there is no other material layer affects the mechanical strength of the lithium ion cell.

Cells were tested to evaluate load-displacement response and short circuit initiation under transverse punch loadings. All tests were performed at room temperature. Flat, hemispherical and cylindrical punches were used for tests and the list of punches are as follows:

- Flat punch (ø44.5 mm)
- Hemispherical punch (ø12.6 mm/ø28.6 mm/ø44.5 mm/ø90 mm)
- Cylindrical punch (ø15 mm/ø28.6 mm)

The strain state under flat and hemispherical punches are axisymmetric and that of lithium-ion cylindrical punch is predominantly plane-strain. The cylinders were aligned with the machine direction (MD) of the electrodes and the separator, so the plain strain cross section became transverse direction (TD). The experimental results were also compared to the results from a global homogenized computational model.

2.1. Experimental results

All cells were tested at 0% state of charge with open circuit voltage of about 3 V. The indentation rate of the punch was 1 mm/min (quasi-static) using a 200 kN loading frame (MTS Systems Corporation). The cell voltages were monitored during the tests to identify an internal short circuit where the voltage starts to drop from the initial value. The tests were stopped after observing peak load and voltage drop. Should the tests be continued, there will be a progressive compression of the coated material until full densification. In the final phase, the load will rapidly increase. Details of experimental method can also be found in the study by Sahraei et al. [4], which reported the characterization of lithium-ion pouch cells using the same method.

Load-displacement curves and voltage changes are shown in Fig. 1. Comparisons between the load-displacement curves and the voltage curves show that the force drops match with where the voltage drops, implying that initiation of inner mechanical failure triggers a short circuit in all test cases. For ø44.5 mm and ø90 mm hemispherical punch tests, only load-displacement responses were measured without voltage profile because, due to the shortage of cells available to test, we used already short-circuited cells by other indentation tests. (The locations of indentations were far enough not influencing each other.)

2.2. Finite element simulations

Finite element models were developed using LS-DYNA with a similar procedure developed by Sahraei et al. [3,4]. There were 16 elements through the cell thickness in all FE simulations giving the mesh size 0.469 mm. The cell stack was described by the compressible foam model (MAT 63) from the library of LS-DYNA materials and the compressive curve calculated from 44.5 mm flat punch is used for the input. The properties in tension are assumed to be linear up to a tensile cut-off value of $\sigma_f = 21$MPa. This value was obtained from a composite tensile curve calculated from the uniaxial tensile test results of cathode, anode, and separator. The compression curve was obtained from the 44.5 mm flat punch test (Fig. 1 (a)) with the assumption that there was a negligible edge effect. The edge effect of a flat punch is previously calculated by Sahraei et al. [4] and was shown to be less than 5% for a 25.3 mm diameter flat punch, and smaller for larger punch sizes. The punches were treated as rigid bodies because the strength of steel punches is more than an order of magnitude larger than that of the battery. Two different failure criteria were used in the numerical simulations. The initiation of failure in this section is assumed to be controlled by maximum principal strain ε_f and this value is calibrated by comparing experimental and modeling results. The application of the MC criterion is covered in Section 4. Also, it should be noted that a model is expected to be realistic until one of its elements reaches to the failure criterion. The physics after failure is not considered in this model, which is aimed at predicting load-displacement and failure (the first peak).

Modeling results are plotted in Fig. 1 in addition to the experimental data. Their force-displacement curves match generally well with the experimental results. However, the magnitude of the maximum principal strains ε_f was found to be different for the axisymmetric and the plane-strain conditions to match the failure points. For the axisymmetric tests (flat and hemispherical punches), the model was calibrated with the maximum principal strain $\varepsilon_f = 0.1$ and, for the plane-strain tests, the maximum principal strain was lowered to $\varepsilon_f = 0.043$ in order

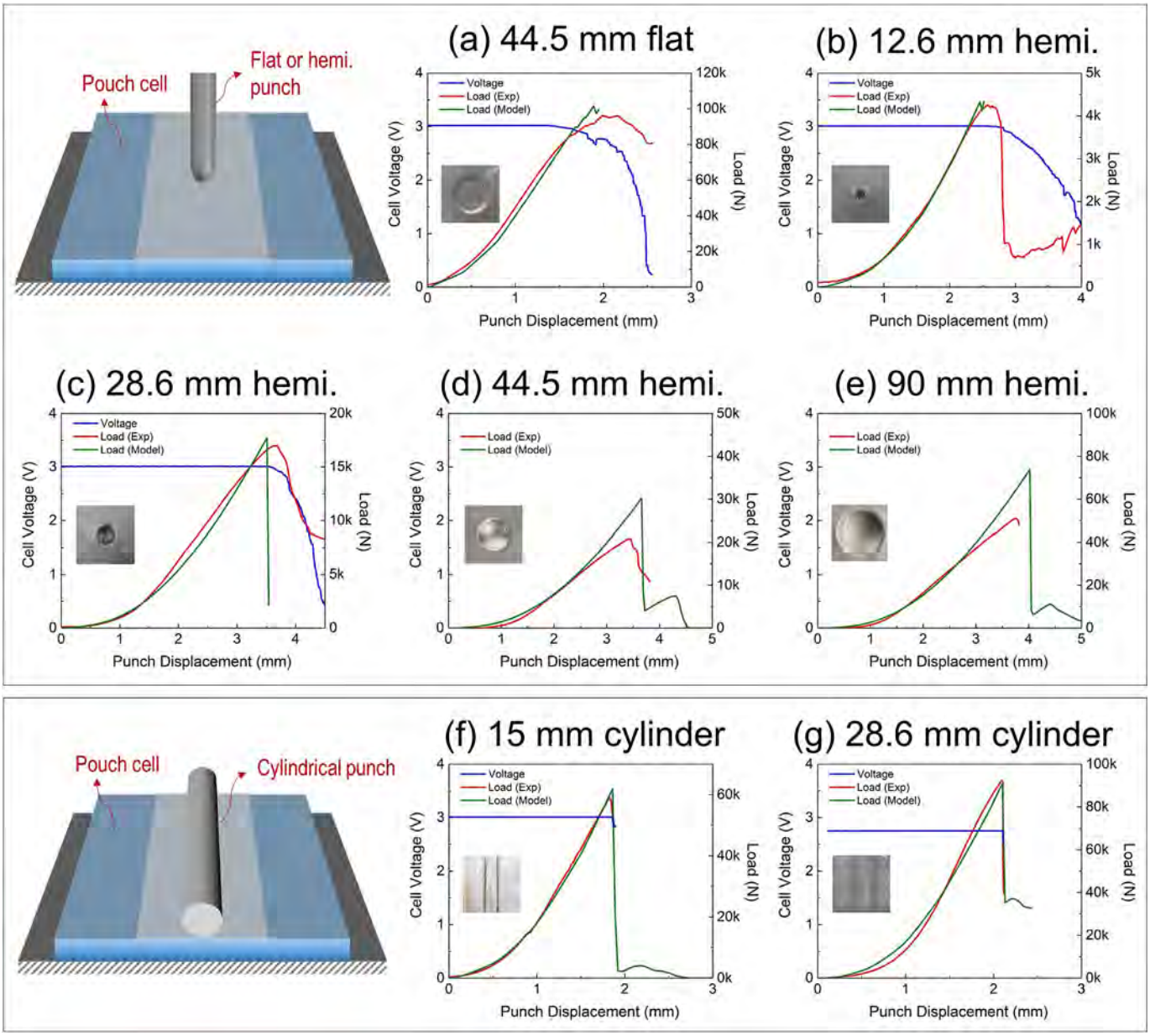

Fig. 1. Cell indentation test results of (a) ø45.5 mm flat punch, (b) ø12.6 mm, (c) ø28.6 mm, (d) ø44.5 mm and (e) ø90 mm hemispherical punches, and (f) ø15 mm and (g) ø28.6 mm cylindrical punches. Voltage and load-displacement results from experiments are plotted in blue and red colors and load-displacement results from finite element simulations are plotted in green color. The inserts inside the plots are the compressed areas of the cells after the tests. For ø44.5 mm flat and ø12.6 mm hemispherical punch simulations, the model plots (green) were drawn up to the point when one of the elements reaches to the failure criterion for the first time. For all the other cases in the figure, failure starts at a peak load value. Details of experimental method can also be found in the study by Sahraei et al. [4]. (For interpretation of the references to color in this figure legend, the reader is referred to the Web version of this article.)

to match the modeling result with the experimental results. With these two maximum principle strain values, the punch displacements at the time of failures predicted by the models match with the displacements by the experiments generally very well as shown in the graphs in Fig. 1. There were some discrepancies for ø44.5 mm and ø90 mm hemispherical punches. For these punches, there was an overprediction in force-displacement curves, but not in the failure locations. The punch displacements at the time of failure are very close between the models and the experiments.

Above results show that, while a fixed maximum principle strain value can be a useful indicator of initial failure at least for similar shape-type of punch loads with different sizes, it is also apparent that the value is not universally applicable and should be adjusted for different punch loading types.

2.3. Post mortem examination

Observing cell's inner structures is important to analyze the complex sequence of crack formation and global failure. We performed post mortem examinations to visually observe inner cell structures in order to understand how the inner electrode and separator layers are deformed and reach the failure point. In all the damaged batteries subjected to the hemispherical and cylindrical punch indentations, mechanical cuts were made to reveal the internal fracture patterns. In the case of axisymmetric tests, specimens were cut in half along the symmetry TD plane and the surfaces were ground mechanically. In the case of plane-strain tests, specimens were cut perpendicular to the cylinder direction and the resulting cut plane is also TD.

As shown in Fig. 2, for all the cross sections, alternating layers of

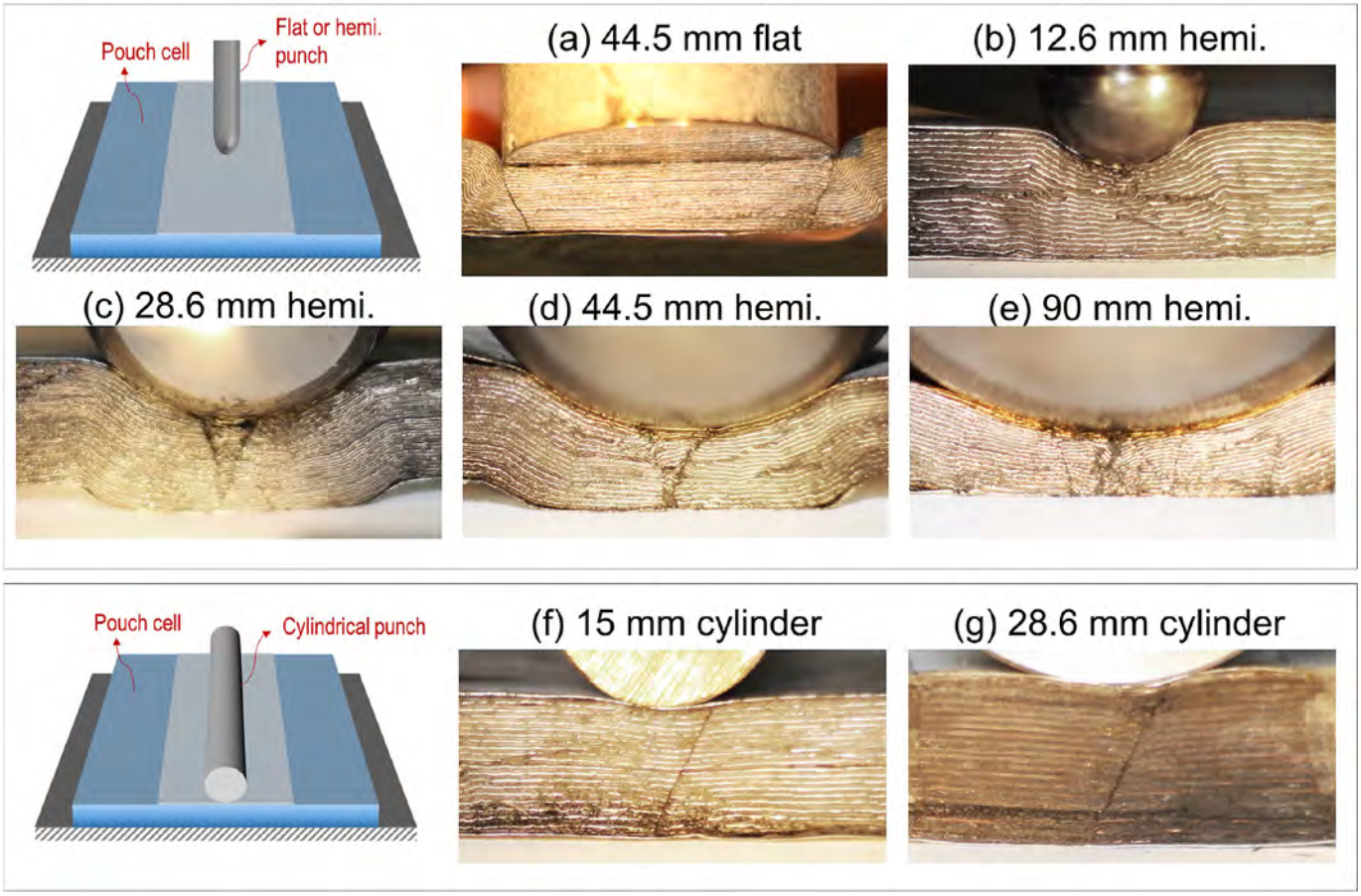

Fig. 2. Cell cross-section pictures (TD) from the tests of (a) ø45.5 mm flat punch, (b) ø12.6 mm, (c) ø28.6 mm, (d) ø44.5 mm and (e) ø90 mm hemispherical punches, and (f) ø15 mm and (g) ø28.6 mm cylindrical punches. Visible alternating layers are aluminum foil and copper foil and all specimens developed clear shear faults across layers of electrodes and separators.

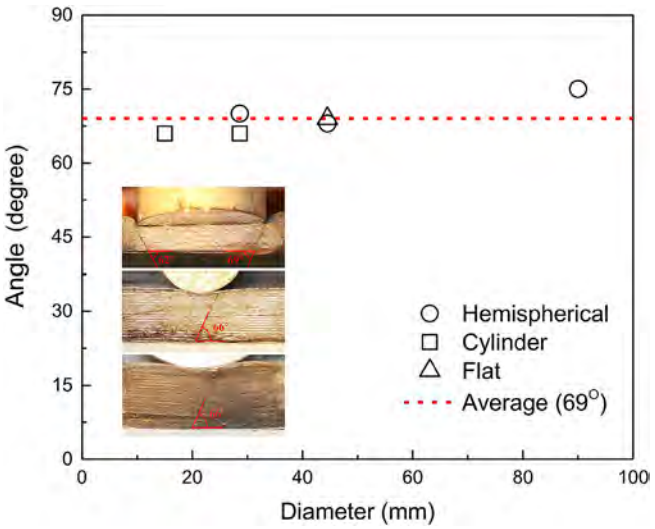

Fig. 3. The angles of the fault lines directly measured from Fig. 2. The inserted pictures inside the plot show some of the actual measurements of the angles shown in the plot. The red dotted line is the average value for all the angles measured. (For interpretation of the references to color in this figure legend, the reader is referred to the Web version of this article.)

aluminum foil and copper foil are clearly visible and all specimens developed clear shear faults across layers of electrodes and separators. This may imply that the electric short circuit occurs after multi-layer shear fractures instead of a single point failure brought about by global homogeneous compression. The similar phenomenon is also observed and discussed by Wang et al. [8] for the pinching tests of prismatic lithium-ion cells.

The fault lines form differently for the different sizes and types of the punches. For the flat punch (ø 44.5 mm in Fig. 2(a)), it is obvious that the fracture starts from the edge of the punch, where has the highest strain, and progressed toward the bottom and is slanted toward the inner area. For the hemispherical punches, the location and the shape of fault lines depend on the size of a punch. In case of the ø 28.6 mm and ø 44.5 mm hemispherical punch (Fig. 2(c and d)), the fault lines form “V” or “Y” shape, while in the case of ø 12.6 mm (Fig. 2(b)), the fault is concentrated adjacent to the interface between the cell and the punch, but does not go all the way to the bottom. The trend is different for the ø 90 mm punch because its radius is too large and forms initial fault lines that already extend to the bottom of the cell. In this case, there are multiple facets of fault lines and these lines form a “W” shape as shown in Fig. 2(e). There are also many additional smaller fault lines in the middle location and they may be generated when the structure collapsed after “W” shape fault lines were formed. For the cylindrical punches, the fault lines reach both the top and the bottom of the cell, as shown in Fig. 2(f and g). They are very straight and extend from the lower center to the punch interface on the side. They likely have run almost instantaneously, rather than progressed over the time scale of seconds, since our repetitive attempts to verify incompletely progressed fault line by stopping the indentation tests at the exact time of failure initiation were not successful. The fracture patterns observed in Fig. 2 have fault lines are almost straight across the thickness, and their orientations are independent of the radius of the indentation. The orientation of the fault line was carefully measured in all axisymmetric and plane-strain tests and is presented in Fig. 3. It can be concluded

that the development of the slant fracture at 69°is invariant with respect to all punch radii, size, and orientation, and it is a property of the cell stack. These fracture angles were measured after unloading of the specimen. A correction for the spring back is approximately 7° so that the corrected angle of slant fracture becomes 62°. This value will be used in the subsequent sections in developing the failure criterion.

3. Closed-form solution for the load-displacement relationship

From the point of view of practical application, an approximate solution of the problem can be used to bypass a need for time-consuming finite element simulation. The computational model in Section 2 requires many input parameters to be obtained from a number of different tests. In this section, we present the analytical solution requires one simple experiment for calibration of both deformation and failure of the cell stack. The advantage of closed-form solutions is that they could be more easily embedded into system failure model consisting of modules and complete battery packs.

3.1. Assumptions

The present analytical solution for the deformation and failure of pouch cell requires a number of simplified assumptions. Those assumptions can be justified by a careful analysis of both the experiments and numerical solutions.

The input for that model is the measured stress-strain relation both in compression and tension. The compressive part of the curve in the out-of-plane direction was calculated from the indentation test on flat 44.45 mm punch reported in Fig. 1(a). It was found that the following parabolic relation

$$\sigma = B\varepsilon^n \tag{1}$$

can be used to fit the measured curve. In this equation, σ is stress tensor, ε is strain tensor, and B and n are coefficients of hardening law. Two different sets of material constants were chosen to fit the measured curve. The best agreement with the test is achieved with the exponent n = 1.5. At the same time, the analytical solution of the plane-strain indentation problem can only be obtained for the integer value of the exponent, and the closest value is n = 2.0. Comparison between the measured stress-strain curve and the analytical representation is shown in Fig. 4(a). All other material properties including the constant B, Youngs Modulus E and the cut-off stress σ_{cut} in tension are given in Table 1. In the above formulation, the tensile failure strain ε_f is not the material constant but material/structure property and is to be determined by the inverse method, see for example Sahraei et al. [4].

Table 1
Material parameters of the cell stack.

	B [MPa]	n [-]	E [MPa]	σ_{cut} [MPa]	ε_f [-]
Exponent	500	1.5	4200	21	Stress state dependent
Parabolic	1200	2	4200		

It should be noted that metallic foils do not contribute to the compressive stress-strain curve in the through-thickness direction. However, in the in-plane compression, the buckling stress should be added to the compressive stress of the coating [2]. This is shown schematically in Fig. 4(b).

The color-coated plot of the compressive stress through the thickness under ø28.6 mm cylindrical punch is shown in Fig. 4(c). There is a clear boundary between the much larger value of the stress directly under the punch and much smaller outside zone on the right of the inflection point. In order to identify the correct kinematics of the indentation problem in the analytical solution, through-thickness profiles of the three component of the stress tensor at the cross section on the inflection point $x = \xi$ were extracted from the numerical solution and plotted in Fig. 5. Because of the presence of the shear stress, the principal direction of the stress tensor is slightly tilted to the global coordinate system. The maximum rotation of the principal directions at the punch/cell interface is about 14 °and rapidly diminishes to zero at the bottom. At the same time, the compressive stresses are almost constant through the thickness. The above results will be used in deriving the analytic solution, to be presented in the next section.

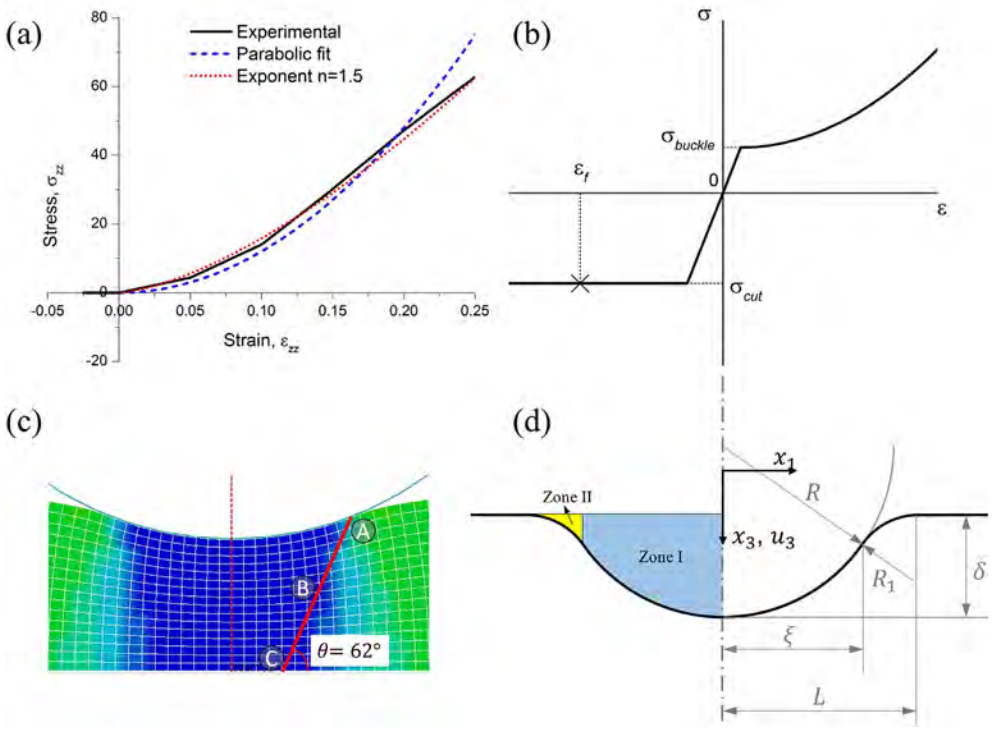

Fig. 4. (a) Measured through-thick stress strain curve from flat punch compression test and two analytical fits with parameters in Table 1. (b) Conceptual stress strain curve for in-plane tension/compression. (c) Deformed mesh under ø28.6 mm cylindrical punch and color-coated plot of the compressive stress. (d) Schematic of the analytical kinematics of the structure. The deformed profile of the cell consists of two zones divided by the inflection point $x = \xi$. (For interpretation of the references to color in this figure legend, the reader is referred to the Web version of this article.)

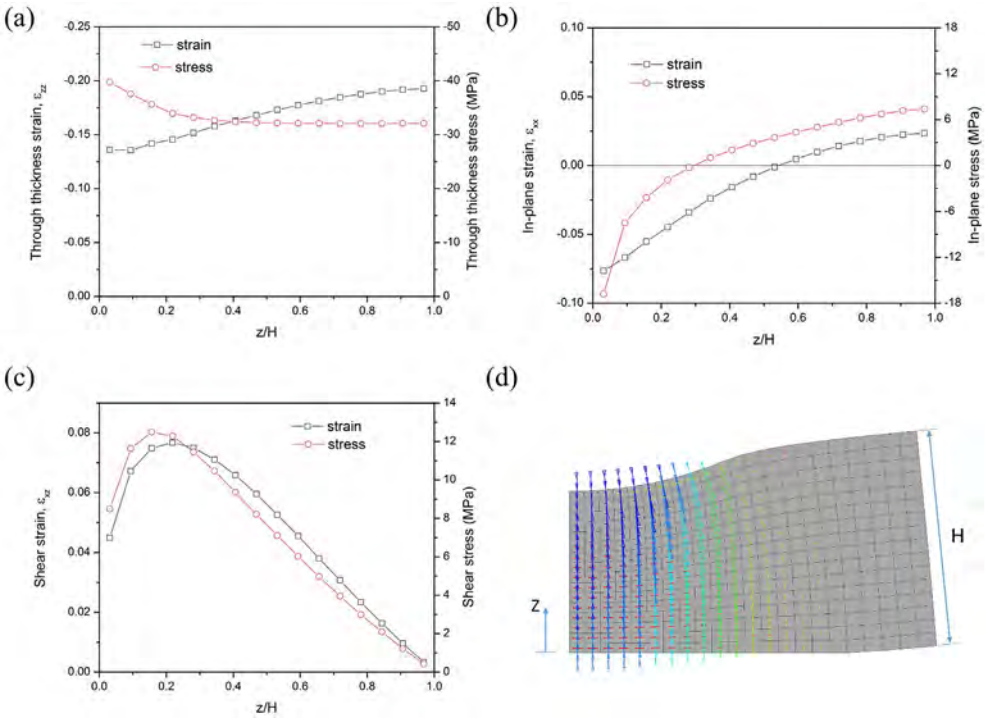

Fig. 5. Stress and strain profiles of (a) out-of-plane, (b) in-plane and (c) shear stresses across the thickness, and (d) the deformed mesh under ø28.6 mm cylindrical punch plane-strain indentation and direction of principal stresses.

3.2. Model hypothesis and justification

In the problem of lateral indentation of a cell by a long rigid cylinder, the strain state is predominantly plane. This condition is valid when the deformation zone is of the same order of magnitude as the thickness of the structure. In the present test, the maximum punch displacement never exceeded 3 mm and the resulted width of the indented zone stays below 9 mm. Referring to the undeformed coordinates system, this means that $\varepsilon_{2\alpha} = 0$, where $\alpha = 1$ is the longitudinal direction, $\alpha = 2$ is the transverse direction, and $\alpha = 3$ is the through-thickness direction. Thus, the non-zero components of the strain tensor are ε_{11}, ε_{22} and ε_{33}. The corresponding components of the stress tensor are σ_{11}, σ_{22} and σ_{33}. The transverse component σ_{22} becomes a reaction and does not induce any rate of deformation. Furthermore, the component σ_{33} under the punch is compressive while σ_{11} can be compressive or tensile.

The mathematical model for the present closed-form solution makes use of the highly asymmetric strength of the anode and cathode coating discussed in the previous sections. The shear and tensile strength of the coatings comes solely from the strength of the binder which is several orders of magnitude smaller than the compressive strength of the coating. Therefore, with a high degree of approximation, $|\sigma_{33}| \gg |\sigma_{11}|$. The contribution of the aluminum and copper foils adds to the tensile and shear strength of the homogenized model through the concept of the effective shear in the theory of moderately large deflection of plates.

Equilibrium in the punch loading problem, that is the expression between of the load P and punch rate of displacement $\dot{\delta}$ can be derived from the principle of virtual work.

$$\int_S T_3 \dot{u}_3 dS = \int_V \sigma_{ij} \dot{\varepsilon}_{ij} dV \tag{2}$$

where dS is a surface element on the punch cell interface (1,3 plane) and $dV = HdS$ is a volume element. For a rigid punch, $\dot{u}_3$ is constant and equal to $\dot{\delta}$. Therefore the integration on the left-hand side of Equation (2) can be readily performed when the integrated surface traction is equal to the total load P. Under the previously discussed assumptions, only two terms survive in the integrand of the right-hand side of the above equation

$$P\dot{\delta} = \int_V (\sigma_{33}\dot{\varepsilon}_{33} + \sigma_{13}\dot{\varepsilon}_{13}) dV \tag{3}$$

The contribution of the second term in the integrand of Equation (3) is always much smaller than the first term. A solution will be derived first by neglecting the shear term. Then, the contribution of the shear term will be evaluated and compared with the leading term.

For the axisymmetric problem, it is possible to derive the closed-form solution for any value of the exponent n. For plane-strain case, the derivation is carried out only in the case of $n = 2$, which applies to the presently studied cells.

3.3. Kinematics

Referring to the global coordinate system (x_1, x_2, x_3), the components of the displacement vector are $(u_1, u_2 = 0, u_3)$. It is assumed that the deformed profile of the cell consists of two zones. In the inner zone, the cell stack confirmed to the radius of the hemispherical punch R. Outside the contact area, the outer profile follows a circular arch of the radius R_1, see Fig. 4(d). It should be noted that the punch radius R is given, while the transition radius is unknown. Such a simple kinematics ensures deflection and slope continuity at the inflection point $x = \xi$ and the outmost region of the deformation zone $x = L$. It is also observed in the post-mortem examination. For relatively small deflections, the circular arches are approximated by parabolas. Accordingly, the expressions for the vertical components of the displacement vector u_3 is

$$u_3(x_1, x_3) = \begin{cases} \frac{x_3}{H}\left(\delta - \frac{x_1^2}{2R}\right) & \text{for } 0 < x_1 \le \xi \\ \frac{x_3}{H}\left(\frac{(x_1 - L)^2}{2R_1}\right) & \text{for } \xi \le x_1 \le L \end{cases} \tag{4}$$

where ξ is the coordinate of the inflection point. The horizontal component of the displacement vector u_1 is assumed to vanish and the justification is given in the next section.

A linear dependence of u_3 on the through-thickness coordinates x_3 ensures a constant magnitude of stresses and strains through the thickness.

Using continuity of the displacement at $x_1 = \xi$ and its slope

$$\frac{(\xi - L)^2}{2R_1} = \delta - \frac{\xi^2}{2R} \tag{5}$$

$$\frac{\xi - L}{R_1} = -\frac{\xi}{R} \tag{6}$$

This gives

$$L = \xi(1 + k) \tag{7}$$

$$\xi = \sqrt{\frac{2R\delta}{(1 + k)}} \tag{8}$$

where $k = R_1/R$

T velocity field is given by

$$\dot{u}_3(x_1, x_3) = \begin{cases} \frac{x_3}{H}\dot{\delta} & \text{for } 0 < x_1 \le \xi \\ \frac{x_3}{H}\dot{\delta}\left(\frac{1+k}{k}\right)\left(1 - \frac{x_1}{L}\right) & \text{for } \xi \le x_1 \le L \end{cases} \tag{9}$$

The strain and strain rates in zone 1 and 2 are

Zone 1: $0 < x_1 \le \xi$

$$\varepsilon_{33}(x_1) = \frac{\partial u_3}{\partial x_3} = \frac{1}{H}\left(\delta - \frac{x_1^2}{2R}\right) = \frac{\delta}{H}\left(1 - \frac{1}{1 + k}\left(\frac{x_1}{\xi}\right)^2\right) \tag{10a}$$

$$\dot{\varepsilon}_{33}(x_1) = \frac{\dot{\delta}}{H} \tag{10b}$$

Zone 2: $\xi \le x_1 \le L$.

$$\varepsilon_{33}(x_1) = \frac{L^2}{2HR_1}\left(1 - \frac{x_1}{L}\right)^2 \tag{10c}$$

$$\dot{\varepsilon}_{33}(x_1) = \frac{\dot{\delta}}{H}\left(\frac{1 + k}{k}\right)\left(1 - \frac{x_1}{L}\right) \tag{10d}$$

3.4. Upper-bound solution

The above expressions are substituted into the equation of virtual work, Equation (3), in order to derive solutions for both the plane-strain case and the axisymmetric case. The integration is performed over the surface area $dS = Wdx$. Details of the derivation are presented in the Appendix.

The normalized indentation force $\overline{P} = \frac{P(k)}{P_0}$ is

$$\overline{P}(k) = \left(\frac{5}{16}k^3 + \frac{5}{8}k^2 + \frac{5}{2} + 1\right)(1 + k)^{-3/2} \tag{11}$$

where $P_0 = \frac{16\sqrt{2}}{15}WB\sqrt{RH}\left(\frac{\delta}{H}\right)^{5/2}$. It can be shown that $\overline{P}(k)\overline{P}(k)$ is almost constant. A very weak dependence on k confirms that for plane-strain indentation, the transition radius $R_1 = R$, meaning $k = 1$.

The comparison between the calculated and measured load-displacement relation is shown in Fig. 6(a and b) for two values of the cylindrical punch radius, $R = 7.5$ mm and 14.3 mm. The correlation is good considering a number of simplifying assumptions made in the derivation. The theory predicts slightly small resistance force in the beginning and then overshoots the experimental curve later. The prediction could be improved by taking alternative parameters of the compression curve, $B = 500$ MPa and $n = 1.5$. However, a simple algebraic expression can be only derived for the parabolic fit with $n = 2$ for the plane-strain case.

The analytical solution for the axisymmetric punch follows the same procedure except for the rectangular coordinate x is replaced by the radial coordinate r and the surface element is $dS = rdrd\theta$. Leaving the derivation to Appendix only the final results are stated.

The expression for the dimensionless indentation force is

$$\overline{P}(k, n) = \frac{P}{P_0} = 1 + \frac{k^n}{(1 + k)^{n+1}}\left(\frac{k(2n + 3 + k)}{(n + 1)(2n + 3)} - 1\right) \tag{12}$$

where $P_0 = [2\pi/(n + 1)]BRH(\delta/H)^{n+1}$. For the axisymmetric problem, it is possible to derive the closed-form solution for any value of the exponent n. With $n = 1.5$ and $n = 2$, Equation (12) reduces to

$$\overline{P}(k, n = 1.5) = 1 + \frac{k^{3.5} + 6k^{2.5} - 15k^{1.5}}{15(1 + k)^{2.5}} \tag{13}$$

and

$$\overline{P}(k, n = 2) = 1 + \frac{0.05k^4 + 0.33k^3 - k^2}{(1 + k)^3} \tag{14}$$

The dependence of the solution on k is again very weak. The post-mortem examination of the deformed profile of the cell under the hemispherical punch confirms that the transition region, defined by R_1 is very small so one can take $k = 0$ without loss of accuracy. The predicted load-displacement curves, given by Equations (13) and (14) are compared with experimentally measured function in Fig. 6(c and d) for two values of hemispherical punch radius $R = 12.7$ mm and 28.6 mm. While Equation (14) shows a considerable difference between the analyzed and experimental results at the point of experimental failure location, Equation (13) is seen to compare very favorably with the experimental results.

It is recommended to use the above Equations (11) and (13) for plane-strain and axisymmetric punch indentation for rapid estimation of the resistance of the battery cells to localize indentation loading. It is recognized that the numerical solution slightly improves the accuracy of calculations, but the simplicity of closed-form solution makes in some cases the FE analysis not necessary. Additionally, the contribution of the discrete aluminum and copper foils to the closed-form solutions is negligible and the proof is presented in the Appendix.

4. Prediction of global failure

4.1. Failure model

One of the most important experimental observations is the inclination of the fault line at 62° to the battery plane. The independence of this angle on the type of loading and shape of an indenter means that this angle is a material constant and invariant for a given type of cell stack. According to the maximum shear failure hypothesis $max(\tau) = c_2$, the shear plane is inclined at 45° to the direction of the maximum principal stress σ_1. One possibility is that the departure from that angle is caused by the effect of the normal stress σ_n, as proposed by the Mohr-Coulomb (MC) failure criterion

$$\max(\tau + c_1\sigma_n) = c_2 \tag{15}$$

The MC fracture model is applicable to a wide range of materials from soil and rocks to ductile metals. Bai and Wierzbicki [15] showed that the orientation of the shear plane, defined by the unit normal vector (n_1, n_2, n_3) with respect to the direction of principal stresses $(\sigma_1, \sigma_2, \sigma_3)$ is uniquely related to the material constant c_1.

$$n_1^2 = \cos^2\theta = \frac{1}{1 + \left(\sqrt{1 + c_1^2} + c_1\right)^2} \tag{16}$$

Solving the above equation for c_1 gets a simple expression for the "friction" constant in terms of the orientation of the fracture surface θ.

$$c_1 = -\cot 2\theta, \text{ for } \frac{\pi}{4} < \theta < \frac{\pi}{2} \tag{17}$$

This equation is plotted in Fig. 7(a).

It should be noted that the value of c_1 is a strong nonlinear function of the angle θ. For example, taking the measured angle before unloading $\theta = 69°$, the constant $c_1 = 1.1$. The correction for unloading,

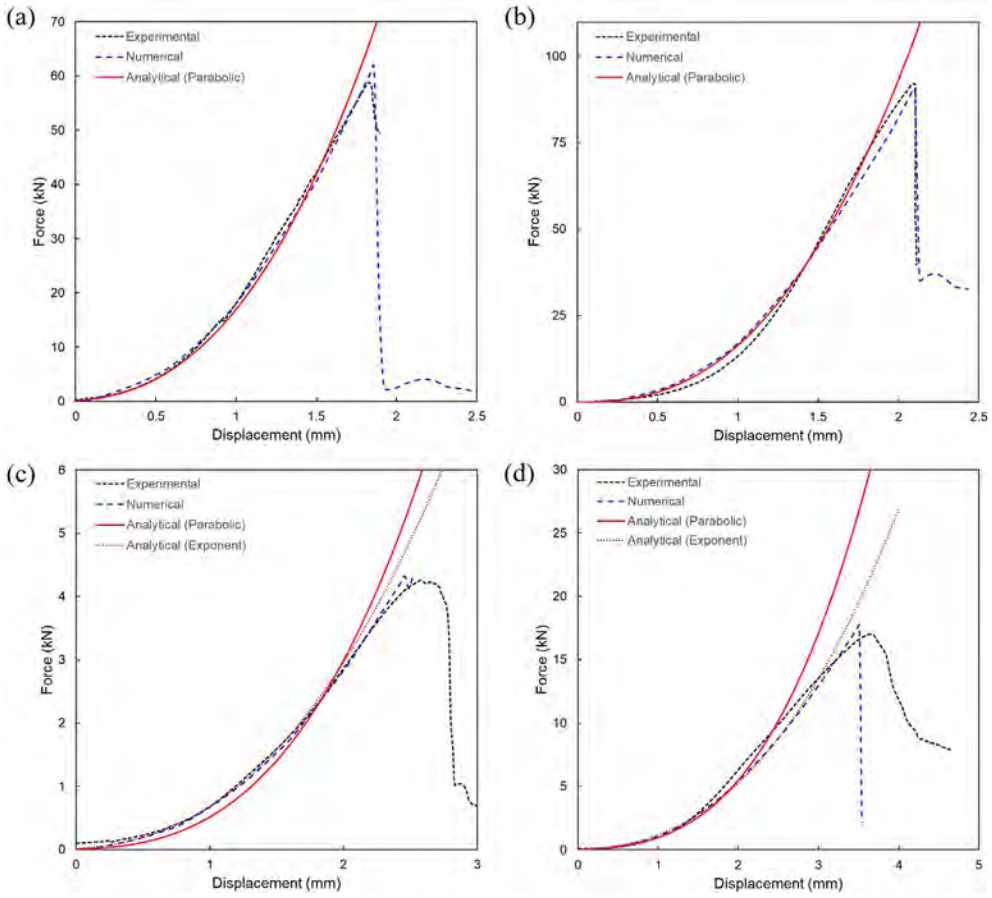

Fig. 6. Predictions of indentation by analytical model (red) compared with numerical (blue) and experimental (black) data (a) ø15 mm cylindrical punch, (b) ø28.6 mm cylindrical punch, (c) ø12.6 mm hemispherical punch, (d) ø28.6 mm hemispherical punch. For plane-strain case, a simple algebraic expression can be only derived for the parabolic fit with n = 2, so only parabolic analytical solutions were plotted in (a) and (b). However, for the axisymmetric problem, it is possible to derive the closed-form solution for any value of the exponent n. Therefore, two analytical cases were plotted for (c) and (d) - parabolic (B = 1200 MPa and n = 2) and exponent (B = 500 MPa and n = 1.5). For numerical solutions of cylindrical punches, For ø12.6 mm hemispherical punch, the numerical plot (blue) was drawn up to the point when one of the elements reaches to the failure criterion for the first time. For all the other cases in the figure, failure starts at a peak load value. (For interpretation of the references to color in this figure legend, the reader is referred to the Web version of this article.)

$\theta = 62°$, brings the value of the friction constant to a much lower value, $c_1 = 0.67$. The strong nonlinear dependence of c_1 on the angle θ will be studied in the continuation of the present research. One way of overcoming this difficulty would be to determine c_1 not only from the orientation of the fracture plane but also from the magnitude of the peak force and the corresponding measured displacement to failure. In this case, two, instead of one, tests will be needed for calibration. It was not possible to find from the tests alone if, in fact, the crack started at the bottom, center or the top, or at the cell-punch interface. In most cases, fracture should initiate at one point and then propagate down along the fault line. In the space of principal stresses, Equation (15) can be rewritten [15] as

$$(\sqrt{1 + c_1^2} + c_1)\sigma_1 - (\sqrt{1 + c_1^2} - c_1)\sigma_3 = 2c_2 \tag{18}$$

where σ_1, σ_2 and σ_3 are ordered principal stresses. The above equation can be transformed to the form involving the fracture angle θ

$$c_2 = \frac{1}{2}\left(\frac{1}{\sin 2\theta} - \cot 2\theta\right)\sigma_1 - \frac{1}{2}\left(\frac{1}{\sin 2\theta} + \cot 2\theta\right)\sigma_3 \tag{19}$$

In the coordinate system of principle stresses, the above equation

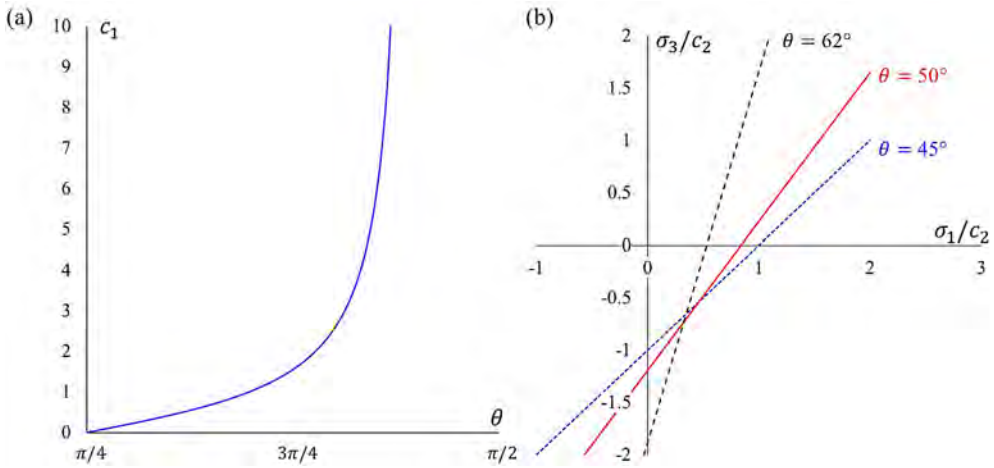

Fig. 7. (a) Dependence of the friction constant c_1 of the fracture surface θ in Equation (17). (b) Dependence of the fracture envelop on the orientation angle of the fracture surface θ in Equation (19).

Table 2
Values of principal stresses at onset of crack formation.

Points along fault line	Top, A	Middle, B	Bottom, C
σ_1(MPa)	−0.58	7.10	11.65
σ_3(MPa)	−32.54	−44.89	−48.06
c_2(MPa)	8.11	18.61	23.73

represents a straight line with a slope of $\sigma_3/\sigma_1 = \tan^2\theta$. A plot of this equation for three different orientations of the fracture surface is shown in Fig. 7(b). In particular, for the measured angle of the fracture surface, $\theta = 62°$, Equation (19) for the cohesion constant c_2 reduces to

$$c_2 = 0.94\sigma_1 - 0.27\sigma_3 \quad (20)$$

In order to evaluate the cohesion constant, information is needed on the magnitude of the local stresses (σ_1, σ_3) in the deforming region under the punch. Those stresses cannot be measured directly, and can only be provided by numerical simulation. For that purpose, an inverse experimental/numerical method must be used. A numerical study was completed to track down the evolution of the principal stresses and the resulting constant c_2 at three points along the fault line, defined in Fig. 4(c). The values of the principal stresses corresponding to the maximum measured failure load (P_{max} = 91.6kN) are shown in Table 2 in the case of the ø28.6 mm punch.

Failure will start at the point of the largest value of the cohesion constant c_2 = 23.73MPa, which is point C at the bottom of the cell, referred to Fig. 4(c). This prediction is consistent with the simulation result showing the distribution of stress components through the thickness of the cell in Fig. 5(b). The in-plane stress is compressive at the punch/cell interface. It changes its sign around point B and goes to full tension at point C. In the inverse calibration procedure, a numerical simulation is run and the right-hand-side of Equation (19) is evaluated in all FE elements along the prospective fault line. The element with the largest value triggers the shear band formation and the second material constant c_2 is evaluated from that point. In the present formulation, only one plain-strain test is needed to calibrate the MC fracture model. From the post-mortem examination, one can find the orientation angle θ of the fault line and the associated friction constant c_1. From the recorded peak force, the second constant c_2 is then found. The proposed Mohr-Coulomb failure criterion is stress-based. Fracture is controlled by the difference between the maximum and minimum principal stresses with suitable weighting functions. In the formulation due to Sahraei et al. [1], a fracture is triggered by reaching the critical value of the maximum principal strain. The difference between the above two approaches to failure predictions of batteries and some difficulties in properly formulating the local and global boundary-value problems are discussed in the last section of this paper.

4.2. Validation

In the previous part, the cohesion parameter c_2 was determined from the measured indentation depth corresponding to the peak load for the ø28.6 mm cylindrical punch. If the parameter c_2 is actually representing the fracture property of the cell material (stack of electrodes), it is supposed to give a good prediction of battery failure for different geometries of the punch and different loading conditions. On the experimental side, there were two plane-strain indentation tests with different radii. Therefore, it will be possible to predict initiation of failure corresponding to the second test not used for calibration. According to the proposed hybrid experimental/numerical procedure, the finite element simulation on the lateral indentation of the same cell with a ø15 mm cylindrical punch was performed to get values of principal stresses σ_1 and σ_3, and calculated the right-hand side of Equation (19). That function depends on the position of a given point within the cell. Calculations were run for several points at the symmetry axis along the thickness of the cell. The evolutions of that function at the top, middle and bottom points are shown in Fig. 8. The maximum value always reached at the bottom point and this is where fracture will start.

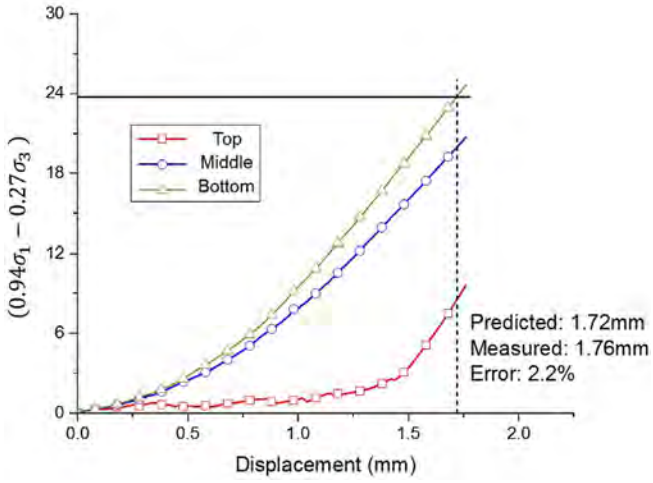

Fig. 8. Evolution of the right-hand side of Equation (20) at three points along the thickness of the cell under the ø15 mm cylindrical punch. The intersection point of the curve corresponding to the bottom point with the constant value of the parameter c_2 = 23.73MPa gives the predicted displacement to failure of 1.72 mm.

The intersection point of the curve corresponding to the bottom point with the constant value of the parameter c_2 = 23.73MPa gives the predicted displacement to failure. It is equal to 1.72 mm. At the same time, the measured displacement to the peak load and battery failure was 1.76 mm. Therefore, the present Mohr-Coulomb failure criterion predicted fracture initiation with an accuracy of 97.8%. Further tests and FE simulation will be performed in the further to provide additional evidence of the suitability of the present stress-based failure criterion.

5. Discussion and conclusion

Development of internal cracks in the cell stack is a precursor of an electric short-circuit under mechanical loading. The drop of voltage in the indentation occurs at the same time as the peak force in the load-displacement curve. Two approaches to predict failure of cells have emerged over the last several years. One is the inverse method involving FE simulation of the entire cell. The other one is a micro-mechanical approach in which a representative volume element (RVE) is introduced to study the sequence of failure of individual layers [1]. In this section, a brief overview of these two methods is offered and then advantages of a new way of predicting local and global failure of cells by means of the Mohr-Coulomb criterion are discussed.

5.1. Inverse method

In the existing approach to cell failure, the parameters of the homogenized constitutive model responsible for fracture are determined by the inverse method in which experimental and predicted displacement to failure are correlated [4,5,8]. The stress-strain curve on which the numerical simulations is based is shown in Fig. 4. On the tensile side of that curve, an elastic perfectly plastic model is assumed, where the cut-off stress σ_{cut} is found experimentally. During the deformation process, the maximum principal tensile strain is increasing until it reaches a critical value ε_f at a certain point under the punch. The

corresponding element is then deleted and crack will propagate. The element deletion technique will define the fracture surface. In the inverse method, the magnitude of ε_f is adjusted such that the measured and calculated displacement to fracture coincide. This method has been proved to be working well in many practical situations involving cylindrical and pouch battery under a transverse punch loading. For example, in the present problem, the critical strain value determined for axisymmetric punch is $\varepsilon_f = 0.1$ and for plane-strain case is $\varepsilon_f = 0.043$. In each case, the calculated of ε_f results in a good prediction for both displacement at fracture and maximum force. However, those values are case dependent and thus lack generality because the assumed tensile behavior is not physical and it does not correspond to the actually measured strain response of a typical assembly, which was discussed, for example in Ref. [1]. The difference between the axisymmetric and plane-strain fracture strain can be explained by considering the triaxiality and Lode angle dependence of the fracture strain brought up to the community first time by Bao and Wierzbicki [16], Xue [17] and Bai and Wierzbicki [15]. Clearly, the maximum principal fracture strain should be extended and made stress-state dependent. This deficiency has been removed in the proposed MC fracture model.

5.2. Micromechanical model

Sahraei et al. [1] proposed computational homogenization approach to predict the sequence of failure by means of an RVE of lithium-ion batteries. This model consists of one assembly of cathode and anode with a periodic boundary condition and simulated under the loading scenarios of various combinations of constant tensile and compression strains on both axes. This method goes one step further because the maximum principal failure strain is not constant but depends on the strain ratio in the in-plane and through-thickness direction. Work is in progress to verify experimentally this new failure model.

5.3. Stress-based failure model

In this paper, an alternative approach to failure and short circuit of batteries is proposed based on the observation during the axi-symmetric and plane-strain experiments. The key new finding is that there is a through-thickness fracture of the cell stack in the form of a flat surface crack with a consistently constant inclination to the battery plane. The angle is the same for the axisymmetric and the plane-strain punch indentation. This type of behavior can be conveniently explained by critical fracture plane theory, known as the Mohr-Coulomb failure criterion, Eq. (15). A distinguished feature of this criterion is that the fracture is controlled by both the hydrostatic pressure and the Lode angle, according to the formulation of Bai and Wierzbicki [15]. The present paper was concerned mainly with the formulation and not the solution of many different loading cases. At the same time, a thorough analysis of this criterion presenting in the previous section provides much-needed understanding of the physics of the failure phenomenon. Section 4 on validation provides a promising data, showing a predictive power of the new MC failure criterion.

Acknowledgement

The work presented herein was supported by the MIT Battery Modeling Consortium, especially by LG Chem, Ltd. with the extensive supports, and a separate grand from the Ford-MIT Alliance. Thanks are due to Professor Elham Sahraei for constructive comments on the early version of the manuscript. In the numerical simulation part of the paper, Altair software Hypermesh was used.

List of Symbols

σ	Stress tensor [MPa]
ε	Strain tensor [-]
u	Displacement field [mm]
x	Coordinate of an element [mm]
B, n	Coefficient of hardening law [MPa],[-]
α	Index of stress/strain direction [-]
P	External load on the battery cell [N]
δ	Displacement of the punch head [mm]
S	Area of the battery surface [mm^2]
H	Thickness of the battery cell [mm]
W	Width of the battery cell [mm]
L	Length of the deformation zone [mm]
R	Radius of the punch head [mm]
E	Youngs modulus [MPa]
ε_f	Failure strain [-]
σ_{cut}	Cut-off stress [MPa]
σ_{eff}	Effective stress [MPa]
σ_0	Energy equivalent flow stress [MPa]
ξ	x_1-coordinate of the inflection point [mm]
k	Ratio of radius in the analytical model [-]
Q	Effective shear stress [MPa]
N	Tensile stress [MPa]
V_f^i	Volume fraction of component i [-]
c_1, c_2	Material constants of Mohr-Coulomb model [-],[MPa]
θ	Friction angle of M-C model [rad]

Appendix

Plane-strain case

$$P\dot{\delta} = 2W\int_0^H \int_0^L \sigma_{33}\dot{\varepsilon}_{33}dx_1dx_3 = 2WH\int_0^L B\varepsilon_{33}^2\dot{\varepsilon}_{33}dx_1$$
$$= 2WH\left(\int_0^\xi B\varepsilon_{33}^2\frac{\dot{\delta}}{H}dx_1+\int_\xi^L B\varepsilon_{33}^2\frac{\dot{\delta}}{H}\left(\frac{1+k}{k}\right)\left(1-\frac{x_1}{L}\right)dx_1\right) \tag{A1}$$

Then

$$P = 2WB\left(\int_0^\xi \varepsilon_{33}^2dx_1+\int_\xi^L \varepsilon_{33}^2\left(\frac{1+k}{k}\right)\left(1-\frac{x_1}{L}\right)dx_1\right)$$
$$= 2WB\left(\int_0^\xi \left(\frac{\delta}{H}\left(1-\frac{1}{1+k}\left(\frac{x_1}{\xi}\right)^2\right)\right)^2dx_1 + \int_\xi^L \left(\frac{L^2}{2HR_1}\left(1-\frac{x_1}{L}\right)^2\right)^2\left(\frac{1+k}{k}\right)\left(1-\frac{x_1}{L}\right)dx_1\right) \tag{A2}$$

$$P = 2WB\left(\left(\frac{\delta}{H}\right)^2\xi\int_0^1 \left(1-\frac{1}{1+k}s^2\right)^2ds + \frac{L^4}{(2HR_1)^2}\left(\frac{1+k}{k}\right)\int_{\frac{\xi}{L}}^1 \left(1-\frac{x_1}{L}\right)^5ds\right) \tag{A3}$$

Finally,

$$P = 2WB\sqrt{2RH}\left(\frac{\delta}{H}\right)^{5/2}\frac{\sqrt{1+k}}{(1+k)^3}\left(\frac{5k^3+30k^2+40k+16}{30}\right) \tag{A4}$$

We can look at two particular cases, $k = 0$ and $k = 1$

$$P(k=0) = P_0 = \frac{16\sqrt{2}}{15}WB\sqrt{RH}\left(\frac{\delta}{H}\right)^{5/2} \tag{A5}$$

$$P(k=1) = \frac{91}{60}WB\sqrt{RH}\left(\frac{\delta}{H}\right)^{5/2} \tag{A6}$$

The difference is minimal between those two cases, less than 0.5%, but the force is larger with increasing k value. The function is strictly increasing.

Axisymmetric case

Similar derivation can be performed for the axisymmetric case. The only difference is a presence of factor of $2\pi r$ inside the integrand. In this case the analysis can be generalized directly to any power law.

$$P = 2\pi B\left(\left(\frac{\delta}{H}\right)^n\xi^2\int_0^1 \left(1-\frac{1}{1+k}s^2\right)^n sds + \left(\frac{L^2}{2HR_1}\right)^nL^2\left(\frac{1+k}{k}\right)\int_{\frac{\xi}{L}}^1 (1-s)^{2n+1}sds\right) \tag{A7}$$

$$P = \frac{2\pi}{n+1}BRH\left(\frac{\delta}{H}\right)^{n+1}\left(1+\frac{k^n}{(1+k)^{n+1}}\left(\frac{k(2n+3+k)}{(n+1)(2n+3)}-1\right)\right) \tag{A8}$$

We can look at two particular cases, $k = 0$ and $k = 1$

$$P(k=0) = P_0 = \frac{2\pi}{n+1}BRH\left(\frac{\delta}{H}\right)^{n+1} \tag{A9}$$

$$P(k=1) = \frac{2\pi}{n+1}BRH\left(\frac{\delta}{H}\right)^{n+1}\left(1-\frac{1}{2^{n+1}}\frac{2n^2+3n-1}{(n+1)(2n+3)}\right) \tag{A10}$$

For any n value above $\frac{(-3+\sqrt{17})}{4} \approx 0.28$, the value is lower than for the $k = 0$ case. The minimum can be easily calculated and is evaluated at $k = 0.9$ for $n = 2$. The decrease is then 8%.

Contribution of the discrete aluminum and copper foil to the closed-form load-displacement solution

Table A1
Properties of simplified rigid plastic model of the discrete members

	t [mm]	N [-]	σ_0 [MPa]	V_f [-]	σ_{eff} [MPa]
Cu	0.01	19	290	0.029	21.0
Al	0.02	20	180	0.061	
Separator	0.026	40	10	0.158	

Even though the volume percentage of the current collectors in the entire cell stack is of the order of 8%, their effect on the total resistance to punch indentation must be estimated. The compressive stress-strain curve characterizing the mechanical properties of a cell was obtained from one-dimensional strain test. Because of plastic incompressibility, the aluminum and copper foils must be treated as completely rigid. Therefore, they have no effect on the compressive strength of the cell stack, which was modeled with Equation (3). At the same time, the current collectors transmit tensile and transverse shear stresses. In the theory of moderately large deflections of plates, the leading term in the out-of-plane equilibrium is the so-called effective shear stress Q is given by

$$Q = Nw' \tag{A11}$$

where N is the tensile stress and $w' = \frac{\partial u_3}{\partial x_1}$. The maximum slope occurs at the inflection point of the deformed profile, which occurs at $x_1 = \xi$. There are two approaches to calculate the joint contribution of current collectors and separator to the punch resisting force. One is to sum up all discrete layers, metallic and polymeric, the other one which is taken in the present derivation is to smear the discrete strength of the layers into one average tensile strength of the material.

$$\sigma_{eff} = \sigma_0^{Cu} V_f^{Cu} + \sigma_0^{Al} V_f^{Al} + \sigma_0^{Sep} V_f^{Sep} \tag{A12}$$

where σ_0^{Cu}, σ_0^{Al} and σ_0^{Sep} are the so-called energy equivalent flow stress of the material with low hardening modulus and V_f^{Cu}, V_f^{Al} and V_f^{Sep} are corresponding volume fraction. Specific values of the present type of batteries are reported in Table A1. The effective stress is calculated to be $\sigma_{eff} = 21.0\text{MPa}$.

From Equation (A11) the total reaction force coming from the shear resistance is

$$P_{shear} = 2W \int_0^H \sigma_{eff} w'(x_1 = \xi, z) dz \tag{A13}$$

The coefficient 2 stands for the symmetry of the problem with respect to x_1. After straightforward calculations, the final expression is

$$\Delta P_{shear} = W\sigma_{eff} \sqrt{2R\delta} \frac{H}{R} \frac{1}{\sqrt{1+k}} \tag{A14}$$

For example at a deflection of $\delta = 2$ mm, which is close to the failure point, $\Delta P_{shear} = 2.97$ kN. The resistance force due to compressive stresses is $P = 90.86$ kN by Equation (A6). According to the present assumptions, the discrete layers contribute only about 3.3% to the total resistive force for $k = 1$. Taking $k = 2$, the contribution of the shear resistance drops to 2.3%, which is negligible for practical purposes.

A similar analysis can be performed for the case of axisymmetric solution. The result is

$$\Delta P_{shear} = 2\pi\sigma_{eff} H\delta \frac{1}{1+k} \tag{A15}$$

In terms of numbers, the shear stress correction amounts of 8% and 4% for $k = 0$ and $k = 1$, respectively.

References

[1] E. Sahraei, E. Bosco, B. Dixon, B. Lai, Microscale failure mechanisms leading to internal short circuit in li-ion batteries under complex loading scenarios, J. Power Sources 319 (2016) 56–65.

[2] E. Sahraei, R. Hill, T. Wierzbicki, Calibration and finite element simulation of pouch lithium-ion batteries for mechanical integrity, J. Power Sources 201 (2012) 307–321.

[3] E. Sahraei, M. Kahn, J. Meier, T. Wierzbicki, Modelling of cracks developed in lithium-ion cells under mechanical loading, RSC Adv. 5 (2015) 80369–80380.

[4] E. Sahraei, J. Meier, T. Wierzbicki, Characterizing and modeling mechanical properties and onset of short circuit for three types of lithium-ion pouch cells, J. Power Sources 247 (2014) 503–516.

[5] L. Greve, C. Fehrenbach, Mechanical testing and macro-mechanical finite element simulation of the deformation, fracture, and short circuit initiation of cylindrical lithium ion battery cells, J. Power Sources 214 (2012) 377–385.

[6] C. Zhang, S. Santhanagopalan, M.A. Sprague, A.A. Pesaran, A representative-sandwich model for simultaneously coupled mechanical-electrical-thermal simulation of a lithium-ion cell under quasi-static indentation tests, J. Power Sources 298 (2015) 309–321.

[7] C. Zhang, S. Santhanagopalan, M.A. Sprague, A.A. Pesaran, Coupled mechanical-electrical-thermal modeling for short-circuit prediction in a lithium-ion cell under mechanical abuse, J. Power Sources 290 (2015) 102–113.

[8] H. Wang, S. Simunovic, H. Maleki, J.N. Howard, J.A. Hallmark, Internal configuration of prismatic lithium-ion cells at the onset of mechanically induced short circuit, J. Power Sources 306 (2016) 424–430.

[9] A. Mason, Material Characterization and Axial Loading Response of Pouch Lithium Ion Battery Cells for Crash Safety, Ph.D. thesis Mechanical Engineering, Massachusetts Institute of Technology, 2017.

[10] J. Zhu, X. Zhang, E. Sahraei, T. Wierzbicki, Deformation and failure mechanisms of 18650 battery cells under axial compression, J. Power Sources 336 (2016) 332–340.

[11] T. Kisters, E. Sahraei, T. Wierzbicki, Dynamic impact tests on lithium-ion cells, Int. J. Impact Eng. 108 (2017) 205–216 In Honour of the Editor-in-Chief, Professor Magnus Langseth, on his 65th Birthday.

[12] D.H. Doughty, SAE J2464 “EV & HEV rechargeable energy storage system (RESS) safety and abuse testing procedure”, SAE Technical Paper, SAE International, 2010.

[13] C. Zhang, S. Santhanagopalan, P. Ramadass, IMLB-2008 Tianjin China, Abstract, 2008.

[14] D. Mohr, M. Dunand, K.-H. Kim, Evaluation of associated and non-associated quadratic plasticity models for advanced high strength steel sheets under multi-axial loading, Int. J. Plast. 26 (2010) 939–956.

[15] Y. Bai, T. Wierzbicki, Application of extended mohr–coulomb criterion to ductile fracture, Int. J. Fract. 161 (2009) 1.

[16] Y. Bao, T. Wierzbicki, On fracture locus in the equivalent strain and stress triaxiality space, Int. J. Mech. Sci. 46 (2004) 81–98.

[17] L. Xue, Damage accumulation and fracture initiation in uncracked ductile solids subject to triaxial loading, Int. J. Solid Struct. 44 (2007) 5163–5181.